THE UNIVERSITY *of* EDINBURGH

THE UNIVERSITY
of EDINBURGH

DOCTORAL THESIS

Escherichia coli's response to hyposmotic shocks

Smitha Hegde

A thesis submitted in fulfilment of the requirements
for the degree of Doctor of Philosophy

February 17, 2020

Abstract

Water is central for all living cells; in prokaryotes—also in fungi and plants—osmotic forces regulate the water available for cellular functions. The osmotic pressure inside a cell arises due to the higher concentration of cell membrane impermeable solutes inside the cell than its external environment. During any sudden perturbations in the environmental osmolarity, the primary implications on the cell is swelling or dehydration. The subsequent response of the cell, in the event of dehydration due to a hyperosmotic shock, is to restore the cellular water by actively increasing the solute concentration inside the cell using osmoregulatory network. In the event of swelling due to a hyposmotic shock, resulting increase in cell membrane tension triggers opening of a series of mechanosensitive channels (MSCs), which opens pores through which the solutes and cellular water diffuse out. These two diverse osmoregulatory mechanisms adjust the internal osmotic pressure in a bacterium to maintain a pressure homeostasis. To study osmoregulation, bacteria which live in the gut of animals make an ideal system, as they experience a constantly changing external environment due to the complex feeding habits and metabolic activity of their hosts. And among these bacteria, *Escherichia coli* is one of the simplest and best understood organisms. With a curiosity to understand life in the context of survival to osmotic challenges, in this thesis, I explore the single cell responses of *E.coli* to hyposmotic shocks.

Using epi-fluorescence microscopy and constitutively expressing eGFP as cytoplasm marker, I first characterize the *in-vivo* volume responses of the wild-type *E.coli* to a hyposmotic shock. The characteristic volume response includes fast volume expansion due to water influx and a subsequent slower volume recovery through MSCs, which also overshoots below the initial volume. The fast volume expansion is on the order of 0.5-2s whereas the recovery phase lasts few minutes. To affirm that the volume recovery is through MSCs, I next measure the volume response in a double and hepta MSCs deletion mutants. These two mutants exhibit a fast volume expansion but not the characteristic

volume recovery of the wild-type. The double mutant shows a small volume recovery and hepta-mutant remains swollen throughout the duration of imaging (up to few hours). For a large 960 mOsmol hyposmotic shock, $\approx$ 36 % of the hepta mutant cells survive the challenge. A closer look into the death of hepta-mutant suggests that the quality of cell attachment to the coverslip influences the time of death, poorly attached cells dying sooner. In this thesis I study the dynamics of cell death due to hyposmotic shock and discuss the possible influence of cell-wall mechanics on the survival of the hepta mutant.

In contrast to membrane embedded ion channels MSCs are non-specific to the solutes that pass through them. While this non-specificity helps bacteria restore osmotic pressure during a hyposmotic shock, it can also cause excess loss of solutes, which can also lead to volume overshoot. Given that cell's response to hyposmotic shock is passive, I also investigated the possible additional levels of control that could fine tune *E.coli*'s passive response to hyposmotic shock. Specifically, I looked at co-operative gating of MSCs through clustering in the cell membrane. With a continuum phenomenological model, supported by collaborative results from a coarse-grained model of MSCs aggregation, I demonstrate that the MSCs clustering regulates the whole cell volume during a hyposmotic shock and does it in a way to reduce excessive solute loss without impeding the functionality of MSCs. In the final part of the thesis, I apply the knowledge gained on hyposmotic response of *E.coli* for industrial biotechnology applications. Specifically, I optimize the osmotic extraction of an industrially important periplasmic protein, Hel4, by deleting a replaceable centrifugation step without compromising on yield. Additionally, I address the leakage of the periplasmic Hel4 in industrial fermentation by looking at the role of outer-membrane porins, OmpC and OmpF.

Lay Summary

Osmosis is the movement of water from a region of low solute concentration to a higher one. It is a common, natural process that controls the availability of water in the cells of living organisms, including bacteria, one of the simplest organisms on Earth. Bacteria, like all living organisms are made up of water and solutes, including proteins, DNA, sodium and potassium. A bacterium is capable of withstanding large, and often sudden, variations in the water concentration of its environment. A good example of this is a bacterium living in soil, where the soil, with a relatively low concentration of water, is frequently exposed to rain. When this happens, they initially swell due to osmosis. However, swelling more than their capacity increases the pressure inside the cell and poses a risk of the cell bursting. In order to overcome this, bacteria have a clever protein known as mechanosensitive channels (MSCs) that senses the increase in the pressure inside the cell and opens gate like valves to release it cell's content—similar to the release of content when opening a soda can.

In this Ph.D. thesis, I have studied the role of MSCs in bacterial survival to osmotic swelling. To do this, I used *Escherichia coli* (*E. coli*), a bacterium that lives in the animal gut and using single cell microscopy techniques, I studied the volume changes of single *E. coli* cells during osmosis. The results showed that *E. coli* cells initially swelled as a consequence of water flowing into the cell, which subsequently led to the opening of MSCs to release cellular content. However, when similar experiments were performed with *E. coli* cells which have had the MSCs genetically removed, they were unable to release the pressure caused by the water flowing into the cell. As a result, in these situations, the bacteria died by bursting slowly. The experiments in this thesis demonstrate that the MSCs are a critical components for *E. coli*'s survival to osmosis, offering a potential new target for antibiotics that can treat bacterial infections by stopping MSCs from doing its job.

Declaration

I declare that the thesis has been composed by myself and that the work has not be submitted for any other degree or professional qualification. I confirm that the work submitted is my own, except where work which has formed part of jointly-authored publications has been included. My contribution and those of the other authors to this work have been explicitly indicated below. I confirm that appropriate credit has been given within this thesis where reference has been made to the work of others.

The work presented in Chapter 3 is published in *PNAS* as *Dynamics of Escherichia coli's passive response to a sudden decrease in external osmolarity* by Renata Buda, Yunxiao Liu, Jin Yang, **Smitha Hegde**, Keiran Stevenson, Fan Bai and Teuta Pilizota. I carried out the experiments in the paper along with the co-author Renata Buda.

The work presented in Chapter 6 is published in *PRL* as *Dynamic clustering regulates activity of mechanosensitive membrane channels* by Alexandru Paraschiv, **Smitha Hegde**, Raman Ganti, Teuta Pilizota and Anđela Šarić. I carried out the continuum model section of the paper. The content of the paper is rearranged in the chapter to follow a monograph style of thesis and my contribution in each section has been indicated.

Smitha Hegde
February 17, 2020

Acknowledgements

As I write this section, I find myself in the deepest gratitude to the simplest forms of life that is teaching us about Life, with their existence. Boon or bane, they have been a part of our existence and an object of wonder. These mysterious bacteria have thankfully lured me to pursue this Ph.D.

I am thankful and grateful to my supervisor, Teuta Pilizota, for her support, guidance, encouragement and inspiration throughout these four years. I also extend my sincere acknowledgements to my thesis committee members, David Finnegan and Naomi Nakayama for their constant support and motivation at every stage of my Ph.D. My sincere thanks to Darwin Trust of Edinburgh and IBioIC for providing me funding to pursue this Ph.D.

My former and current colleagues: Alex, Jerko, Ekaterina, Dario, Leonardo, Guillaume, Keiran, Jill, Mark, Marijana and James have been been my closest and dearest company in the last four years from whom I have learnt physics, to swear in their respective mother tongue or to laugh away a difficult day in a Ph.D student's life—I thank them for working with me.

I thank my husband, Adarsh, for encouraging me to pursue this Ph.D. and supporting me in every walk of life. I am grateful to my mom, dad and brother for being my pillars of support. My mother-in-law, both my sister-in-laws and my little nephew have showered me with love and support, I thank them for being my family.

I thank my colleagues from neighbouring groups, Lorna, Benura and Elis for helping with molecular biology techniques. A hearty thanks to George McMillan for ensuring that the laboratory facilities worked without fail, be it a rainy day or a weekend.

List of Abbreviations

MSCs	mechanosensitive channels
MscL	mechanosensitve channel of large conductance
MscS	mechanosensitive channel of small conductance
MscM	mechanosensitive channel of mini conductance
KefA	potassium dependant mechanosensitive channel
PLL	poly-L-lysine
PEG	polyethylene glycol
EDTA	ethylenediaminetetraacetic acid
MM9	modified M9
IPTG	isopropyl-β-D-thiogalactoside
BSA	Bovine serum albumin
CG	coarse grained
PCR	polymerase chain reaction
aa	amino acid
bp	base pair
LB	Luria Bertani
PBS	phosphate buffered saline
AFM	Atomic Force Microscopy

Contents

Chapter 1

Introduction

At the core of all animate objects lies a cell membrane that separates the life processes from their environment. As much as the cell membrane encloses the matter needed for life, it is selective for what enters and leaves the cell. Cell membrane, together with cell wall forms the fortress of a bacterial cell. While cell membrane forms the physical barrier, cell wall provides the mechanical strength and shape to the bacteria. A gram-negative bacteria has an additional outer membrane enclosing the cell wall, whereas a gram-positive bacteria instead has a thicker cell wall than the gram-negative bacteria.

1.1 The rise of osmotic pressure

Cell membrane is permeable to water irrespective of the presence of the membrane protein, Aquaporin (Delamarche et al., 1999). However, solutes in the cytoplasm like ribosomes, proteins, DNA, RNA, metabolites, together with ions that are not permeable through the cell membrane gives rise to a solute concentration gradient between the cell's cytoplasm and the environment. This solute concentration gradient gives rise to positive osmotic pressure (π) in the cytoplasm as defined by Eq. 1.1. The osmotic gradient further drives a flux of water into the cell's cytoplasm (due to higher water potential) to swell and stretch the cell wall up to a certain extent. Beyond this limit, the resisting mechanical stress (also termed turgor pressure) exerted by the cell envelope balances the osmotic pressure to prevent further water flux into the cell.

Osmotic pressure is expressed as below.

$$\pi = \phi RT(C_e - C_i) \tag{1.1}$$

Where R is the ideal gas constant, T is thermodynamic temperature, C_i is the total solute concentration inside the cell and C_e is the solute concentration external concentration. ϕ is the molar osmotic coefficient, which is unity for an ideal solution, but for macromolecules like proteins and non-electrolytes like sucrose, ϕ value is greater than unity. For example, a 33.5 % hemoglobin solution has a $\phi = 2.57$ (Dick, 1966). In addition to bacterial cells, osmotic pressure is known to be present in fungi and plant cells, however is near zero in animal cells.

1.2 Need for turgor pressure

The idea of turgor pressure driving cell growth, although proposed in the early 20th century (Thompson, 1917), models to support this hypothesis were only proposed recently (Koch et al., 1981; Koch, 1990; Jiang et al., 2010). These studies hypothesized that the strain on the cell wall due to positive pressure drives the cell wall elongation for growth. However, Rojas et al. (2014) demonstrated for short time scales (of the order of a few seconds) and at small shock magnitudes that *E.coli* continued to elongate its cell wall even after plasmolysis due to a hyperosmotic shock with sorbitol. Therefore, they suggested that synthesis and addition of peptidoglycan to cell wall was independent of turgor pressure. However, this study does not address the affect of large hyperosmotic shock on peptidoglycan synthesis or long term implications of no turgor pressure on growth which remains an open question.

Where does the turgor pressure act on the cell envelope? Studies have shown that the periplasm of *E.coli* is iso-osmotic with the cytoplasm due to the presence of membrane derived oligo sacharide (MDOs). They are 8-11, highly branched glucose molecules located in the periplasmic space (Schneider et al., 1979; Rumley et al., 1992; Cayley et al., 2000). The concentration of these periplasmic MDOs are regulated depending on the osmolarity of the growth medium such that the periplasm is iso-osmotic with the cytoplasm. The concentration of MDO in the periplasm was shown to reduce with increasing concentration of NaCl in the growth medium (Kennedy, 1982). In concurrence with these studies, Erickson (2017) argued that the force required for FtsZ ring formation during cell septation and division was only possible if the periplasm was iso-osmotic with cytoplasm. These studies suggest that

the osmotic gradient lie on either side of the cell wall, the periplasm and the environment. Rojas et al. (2018) demonstrated that the *E.coli* outer membrane was stiffer than the cell wall and was essential for bearing the turgor pressure. However, the study does not discuss the distribution of the mechanical load between cell wall and outer membrane.

1.3 Measuring turgor pressure in bacteria

Measuring turgor pressure in a bacterium is challenging due to its smaller size and complex architecture of the cell envelope. Also, turgor pressure of a bacterial cell can vary depending on the cell envelope architecture i.e., if they are gram-negative or gram-positive, material properties of the cell wall or growth stages. In the section below, I discuss some of the methods described in the literature to measure turgor pressure.

Walsby first proposed the method to measure turgor pressure in bacteria that have gas vesicles in the cytoplasm (Walsby, 1971; Holland et al., 2009). These vesicles are hollow cylindrical structures formed by certain proteins in the cell which are hydrophobic. Atmospheric gas molecules get filled inside these vesicles making the bacteria buoyant. If the atmospheric pressure increases, at a certain critical pressure the vesicles collapse. The collapse of the vesciles can be estimated as the reduction in the intensity of light scattered by the bacteria. The pressure at which 50% of the vesicles collapse in a turgid cell ($\bar{P}_a$) was estimated. The mean critical pressure at which the isolated vesicle collapse ($\bar{P}_c$) was next estimated. Bacteria that is suspended in hypertonic sucrose solution, lose turgor pressure due to water efflux from the cell. Hence, measuring $\bar{P}_c$ in isolated vescile is similar to measuring it in sucrose solution. The turgor pressure was then estimated as the difference in $\bar{P}_c$ and $\bar{P}_a$. Figure 1.1 shows the set-up of Walsby pressure nephelometer.

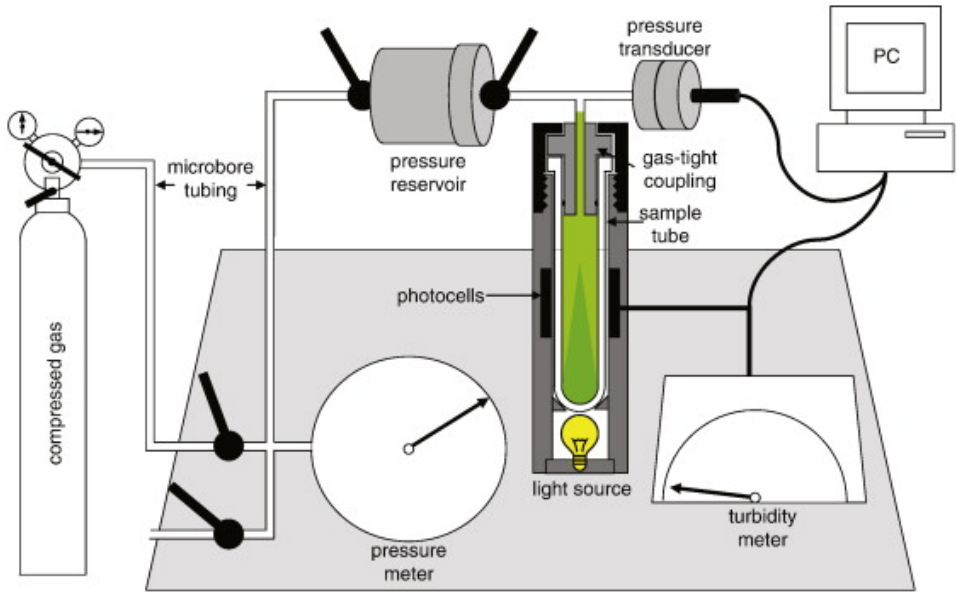

FIGURE 1.1: Schematic pressure nephelometer, figure taken from Holland et al., 2009. Pressure to the sample tube was applied through N_2 gas inlet needle valve. The intensity of scattered light in the sample tube was recorded using a selenium photocell.

This method estimated the turgor pressure of a Cynobacteria, *Anabaena*, to be in the range of 1.7-3.5 atm (Walsby, 1971) and that of *Microcystis* sp. to be in the range of 6.5-10.1 atm (Holland et al., 2009). Walsby's method although applicable to those bacteria that have gas vesicles, various other bacteria can be genetically engineered to express these vesicles. This method of estimating turgor pressure is more robust in a slow growing bacteria as the cell's active response to a hypertonic sucrose solution could be considered to be slow. However, fast growing bacterium like *E.coli*, actively adjust the turgor pressure by pumping K^+ ions within few seconds after suspending in hypertonic solution and hence, the measurement $\bar{P}_c$ should be faster than the cell's response to hypertonic solution.

Cayley et al. (2000) estimated the osmotic pressure of *E.coli* by quantifying the volumes of cytoplasmic and periplasmic water as a function of increasing NaCl concentration in the medium. These volumes were estimated by suspending cells in radioactive water, sucrose or inulin. Sucrose is permeable into the periplasm but not into cell cytoplasm (Gary et al., 1976). Inulin is a large molecule that is not permeable across the outer membrane (Stock et al., 1977). When the cells are suspended in sucrose solution, water diffuses out through cytoplasm and in case of inulin solution, water diffuses out through cytoplasm

and periplasm. This resulted in dilution of radioactivity which then allowed to measure the amount of water released from the cell. With these measurements they demonstrated that the osmotic pressure decreased with increasing growth osmolarities, from ≈ 3 atm at 0.03 Osmol to 0.5 atm above 0.5 Osmol.

In bacteria that do not have gas vesicles, turgor pressure can also be estimated using Atomic Force Microscopy (AFM) (Arnoldi et al., 2000; Deng et al., 2011). Deng et al. (2011) in their method, determined the turgor pressure of a live *E.coli* with the help of an antibiotic vancomycin that inhibits peptide bond formation in cell wall. This resulted in cell wall fractures, through which cell membrane then bulged out, along with cell wall and outer membrane, as shown in Figure 1.2. The radius of the bulge was estimated using cytoplasmic GFP that also occupied the bulge. The stiffness of the bulge encompassing the cell membrane, cell wall and the outer membrane was estimated using AFM. Force was applied through the AFM cantilever tip to indent the bulge, the slope of force-indentation curve was the stiffness of the bulge. Using an appropriate computational model that considers the indentation with a conical tip and cell wall stress stiffening, Deng et al. (2011) then estimated the turgor pressure of a live *E.coli* to be ≈ 0.3 atm.

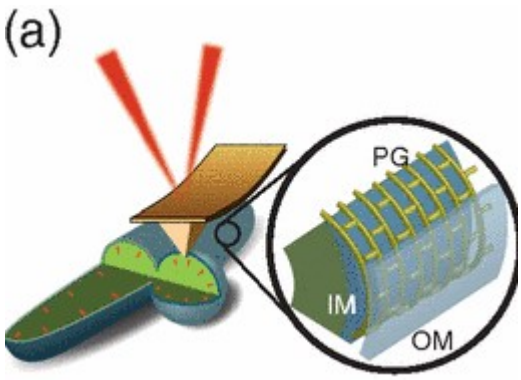

FIGURE 1.2: Measuring turgor pressure of live bacteria using AFM, image taken from Deng et al. (2011). Image shows the formation of a cell membrane (PG) bulge along with cell wall (CW) and outer membrane (OM) after treatment with vancomycin and probing with AFM tip.

1.4 Maintenance of osmotic pressure homeostasis

Bacteria are found anywhere and everywhere on this planet. Thriving in the diverse habitat, they commonly face variety of stress. Of all the stresses, the

changes in environmental osmolarity is the most commonly encountered stress. For instance, *E.coli* residing in an animal gut can experience a constantly varying osmotic pressure attributing to the complex feeding habits of animals. Also, the osmolarity of the illeum from a fasted to a fed state in a healthy human was shown to vary about $\approx$ 190 mOsmol (Reppas et al., 2015). In the case of *E.coli* causing a urinary track infection, it could also experience a fluctuating urine osmolarity of 50-1200 mOsmol throughout the day (Sands et al., 2009). Unlike any other stress, the greatest threat to a bacterium could be exposure to water and consequent bursting due to osmosis. Therefore, in order to cope with the ever changing environmental fluctuations in osmolarity and to maintain a pressure homeostasis that is necessary for growth, bacterial cells constantly adjust their internal solute concentration using osmoregulatory network. The sudden increase of environmental solute concentration is termed hyperosmotic shock and the sudden decrease in the environmental solute concentration is hyposmotic shock. The first passive implication on the cell during hyperosmotic or hyposmotic shock is the flux of water, out or into the cytoplasm, respectively. Consequently, bacterial cells then respond using osmosensors. The term hyperosmotic shock is interchangeably used with upshock and hyposmotic shock with downshock in this thesis.

E. coli is reported to grow in external osmolarity as low as 0.015 Osmol up to 3 Osmol (Baldwin et al., 1995; Cayley et al., 2003). Walsby (1971) and Cayley et al. (2000) showed that the turgor pressure of *E.coli* reduced with increasing growth osmolarity. The growth rate of *E.coli* has also been shown to decrease with increasing osmolarity of the growth medium, starting from 0.28 Osmol (Cayley et al., 2000; Pilizota et al., 2014; Rojas et al., 2014; Dai et al., 2018a). The growth was also reported to reduce below 0.28 Osmol (Cayley et al., 2000; Cayley et al., 2003). The growth rate reduction at higher osmolarity has been due to the increased molecular crowding in the cell and reduced cytoplasmic free water which could have lead to reduced translation elongation rate (Record et al., 1998; Cayley et al., 2003; Cayley et al., 2004; Van Den Berg et al., 2017; Dai et al., 2018b).

1.4.1 Bacterial response to hyperosmotic shock

The mechanism of single *E.coli* cell's passive responses to hyperosmotic shock has been demonstrated by Pilizota et al. (2012), where they observed up to

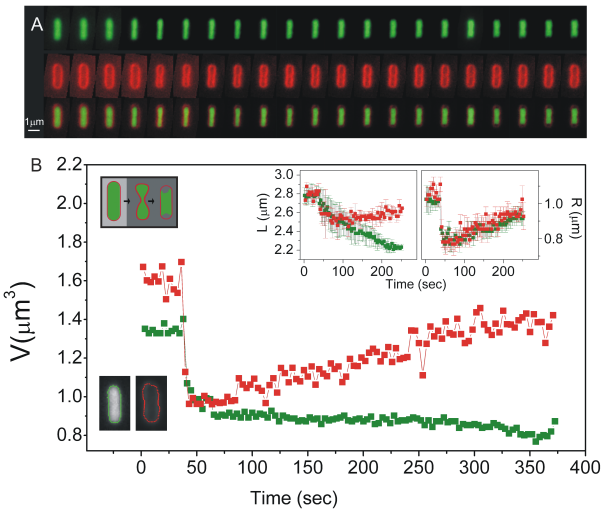

FIGURE 1.3: ***In-vivo* dynamics of *E.coli*'s cell volume, length and radius following a 0.62 mM sucrose hyperosmotic shock.** Image taken from Pilizota et al. (2012). (A) Sequence of fluorescent images that show the cell shape responses from pre-shock to post shock. The green color in top figure shows the cytoplasm area, marked with fluorescent protein eGFP. Red cell boundary in the middle row marks the outer membrane, tagged with FM4-64 dye. The images in the bottom row is the overlay of top and middle images. (B) The dynamics of total (red) and cytoplasm (green) volume, length and radius and following hyperosmotic shock. The top left cartoon shows the cell shape changes post sucrose shock.

40% of cytoplasmic volume reduction when shocked with sucrose. The Figure 1.3 shows the cell shape changes and the dynamics of cell volume, length and width upon 0.62 M sucrose shock. They also showed that the cell shape following a hyperosmotic shock was dependant on the permeability of the solute across the cell envelope (Pilizota et al., 2013).

Following the passive response as shown in Figure 1.3, the subsequent response of a bacterium is to increase the osmolarity of the cytoplasm by actively importing solutes from the environment or synthesizing osmolytes. The first active response is to transiently import K^+ ions using potassium pumps, Trk and kdpFABC. These pumps rely on either proton motive force or ATP to move K^+ into the cell (Dinnbier et al., 1988; McLaggan et al., 1994; Asha et al., 1993). Following the K^+ import, cells synthesize glutamate to neutralize the positive charge of K^+ (Dinnbier et al., 1988; McLaggan et al., 1994) The turgor pressure starts resuming as the import of K^+ further drives water into the cell. However, increasing ion concentration is not favourable to cells and hence they replace K+ and glutamate with trehalose by synthesizing them in the cell. Figure 1.4

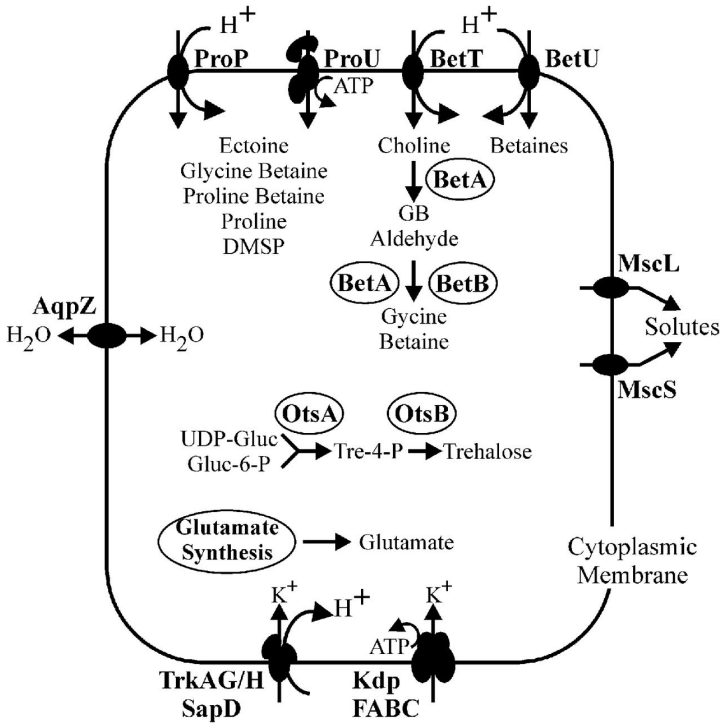

FIGURE 1.4: Osmoregulation in *E.coli*, image taken from Wood (2007). The figure shows the osmosensors present on *E.coli* cell membrane that responds to hyperosmotic or hyposmotic shocks.

summarizes the osmosensors that are identified in *E.coli*, to-date, using *in-vitro* techniques.

In addition to import of K^+, cells also import organic solutes like glycine-betaine, proline, choline or ecotine, if present in the environment. Some of these transporters are ProP in *E.coli*, BetP in *Corynebacterium glutamicum* and OpuA of *Bacillus subtilis* and are present on the cell membrane to import glycine-betaine and proline into the cytoplasm (Racher et al., 2001). One of the well studied sensors is ProP, which is a proton-osmolyte symporter. The loss of water from the cytoplasm during an upshock was shown to increase the cation density around the ProP sensor, which further changed the confirmation of the protein so as to transport glycine-betaine or proline into the cytoplasm (Racher et al., 2001; Wood, 2010; Culham et al., 2018).

1.4.2 Bacterial responses to hyposmotic shock

A bacterium's response to a hyposmotic shock is very different than upshock and because this thesis is focused on *E.coli*'s responses to hyposmotic shock, I

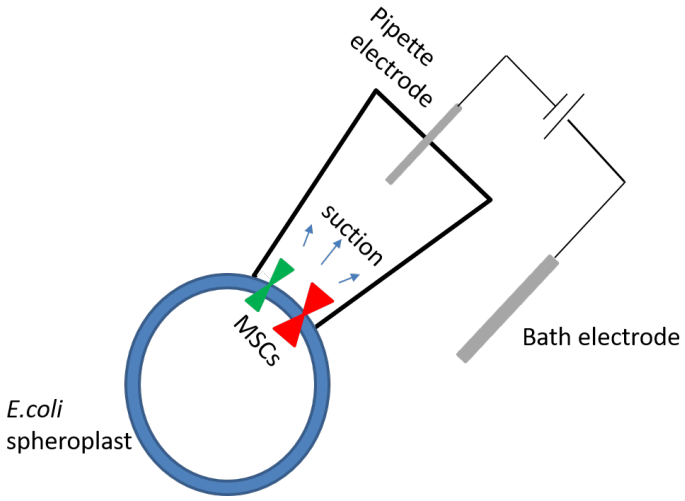

FIGURE 1.5: **Cartoon of patch-clamp technique.** *E.coli* spheroplast containing mechanosensitive channels (MSCs) are tightly sealed to the glass micropipette. A suction is applied through the pipette to gate MSCs. The current passing through channels due to ion flow is then recorded. Recordings of an excised membrane patch with MSCs can be done similarly.

have described this section in detail. During 1960s, studies reported that *E.coli*, when subjected to a downshock to water, released cellular proteins and amino acid pools and gained full viability when transferred back to growth medium (Britten et al., 1962; Neu et al., 1965; Nossal et al., 1966). Though the cellular mechanism of cytoplasmic release was not known, it was hypothesized that transient membrane pores formed during the downshock were responsible for the release. Later on, Martinac et al. (1987) first discovered in *E.coli* spheroplasts, mechanosensitive channels (initially termed pressure-activated channels) that opened to release ions upon application of positive or negative pipette pressure using a patch-clamp technique, as shown in Figure 1.5. Spheroplasts of *E.coli* were formed by growing the cells in presence of an antibiotic, cephalexin, that prevented the formation of cell septum and instead, cells grew as a large snake. The cell wall of these long cells were next dissolved by treating with lyzozyme and EDTA to form giant spheroplasts that could be then used in patch-clamp technique.

At that time, the channels were thought to be present on the outer membrane. The following year, similar channels were discovered in gram-positive bacteria *Streptococcus faecalis* suggesting that the channels could not be present on the outer membrane (Zoratti et al., 1988). Further patch clamp study by

Berrier et al. (1989), fusing the cell membrane of *E.coli* into liposomes, clarified that these channels were indeed found on the inner membrane. The above studies were performed by gating MSCs using pipette suction pressure, Cui et al. (1994) first demonstrated the activation of these channels using an osmotic shock that was delivered through the pipette electrode in *E.coli* (Figure 1.5). Location of mechanosensitive channels (MSCs) in the inner membrane supported the understanding that the osmotic gradient in a cell was not across the outer membrane.

1.5 MSCs, the pressure valves of bacteria

Early patch clamp studies on *E.coli* spheroplast identified 4-5 different channels, with diverse pressure threshold of gating. Of them, two channels with conductance 3 nS and 1 nS were the most frequently encountered channels. These are mechanosensitive channel of large conductance (MscL) and mechanosensitive channel of small conductance (MscS), respectively (Sukharev et al., 1993; Sukharev et al., 1994; Cui et al., 1994; Berrier et al., 1996). While MscL does not show any preference to the charge of the solutes, MscS has a small preference to anions (Sukharev et al., 1993). In addition to these two channels, to date, five more MSCs with different degree of homology with MscS have been identified in *E.coli* (Li et al., 2002; Schumann et al., 2010; Edwards et al., 2012). The five other channels are YbdG, YnaI, YbiO, YjeP (also termed MscM) and MscK (also termed KefA). Though previous patch-clamp techniques identified three to four channels in *E.coli*, channels like Ybio and YnaI were not identified in these studies due to their low expression levels.

The seven MSCs of *E.coli* open a pore of different sizes and gate at varying tension thresholds. While MscL has been shown to open the largest pore of $\approx$ 3 nm diameter (Cruickshank et al., 1997; Perozo et al., 2002b), MscS opens a pore of 1.3-1.4 nm diameter (Francisco et al., 2002; Wang et al., 2008) The Figure 1.6 taken from Edwards et al. (2012) shows the pressure required to gate the seven MSCs relative to the pressure required to gate MscL in *E.coli*. Figure 1.6 shows that MscK requires the least tension to gate compared to six other MSCs but it has been shown to gate only in presence of K^+ ions at the periplasmic side of the channel (Li et al., 1994).

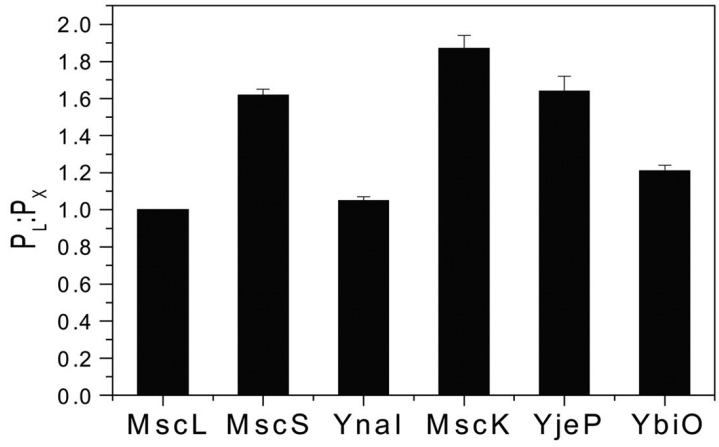

H

FIGURE 1.6: Gating pressures of (P_x) relative to the gating pressure of MscL (P_L), figure taken from Edwards et al. (2012). The figure demonstrates that MscL requires higher pressure than the six other MSCs

1.5.1 Physiological importance of MSCs

The physiological importance of MSCs was observed as the reduction in survivability and cell lysis in MSCs' deletion mutants during hyposmotic shock (Reuter et al., 2014; Bialecka-Fornal et al., 2015). Survival experiments were done by comparing the colony forming units (CFU) upon hyposmotic shock with respect to un-shocked condition. Cell lysis were studied by delivering hyposmotic shocks using a flow-cell or microfluidic devices while imaging using optical microscope. An *E.coli* mutant lacking MscL and MscS showed a < 10% survival for hyposmotic shocks greater than 0.3 M NaCl (Levina, 1999), emphasizing that MscS and MscL are the two important channels for survival. The native levels of YbdG expression improved $\approx$ 50% survival chances of *E.coli* triple-mutant ($MscL^-$, $MscS^-$, $MscK^-$) while compared to a quadruple-mutant ($MscL^-$, $MscS^-$, $MscK^-$, $YbdG^-$) for a 0.15 M NaCl shock (Schumann et al., 2010). Over expression of Ybio, YnaI or MscM in a MSC null mutant have been shown to offer full protection against hyposmotic shock (Edwards et al., 2012). Edwards et al. (2012) and Bialecka-Fornal et al. (2015) noted that the survival of a MSC null-mutant (devoid of all seven MSC genes) was less than 1% upon 0.3 and 0.5 M hyposmotic shocks.

1.5.2 MSCs sense lateral tension on the lipids

Of a great interest to the scientific community is understanding the sensing mechanism of MSCs and if the stimuli is tension or pressure on the cell membrane. The relationship between pressure and tension in a non-planar surface, across the interface between liquid-liquid or gas-liquid is given by Laplace equation: the tension $\sigma = \Delta P \cdot r/2$, where r is the radius of curvature and P is the pressure difference across the interface. Moe et al. (2005) studied the gating of MscL in membrane patches with various radii of curvature and estimated the probability of MscL gating as a function of increasing pressures. From those experiments they evaluated the mean gating pressure i.e., the pressure at which the probability of opening of the channels is half. And then using the Laplace equation, they estimated the tension on the membrane and found that the threshold tension of opening for various radius of curvature was the same. This study supported that the MscL sensed the lateral tension in the lipid and not the pressure across them. They also compared MscL gating in various lipid compositions like phosphatidylcholine (PC), phosphatidylserine (PS), phosphatidylglycerol (PG), or phosphatidylethanolamine (PE) and demonstrated the tension threshold of MscL gating was dependant on the biophysical properties of the lipids and not their interaction with MscL or the charge of the lipid.

Pliotas et al. (2015) showed that purified MscS contained *E.coli* lipids in the TM pockets of the channel. Using MD simulations, they demonstrated that the increase in lipid tension results in repartition of lipid molecules from the MscS's TM pockets to the bilayer and thereby destabilizing the closed state of the channel. The cartoon in Figure 1.7 illustrates the force of lipid in gating MSC.

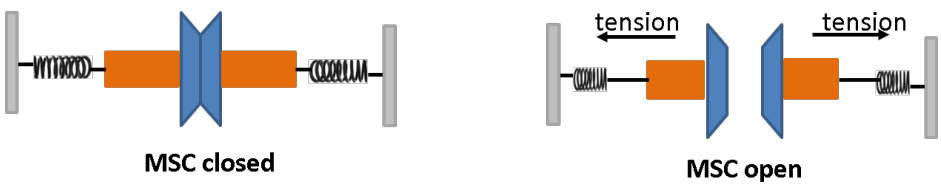

FIGURE 1.7: Illustration of force from lipid in mechanosensation

1.5.3 MSCs gate in milliseconds upon hyposmotic shock

Previous *in-vivo* studies using stopped flow device combined with measuring optical scattering measurement of bacterial suspension demonstrated millisecond time scales for gating of MSCs. Stopped flow device is a rapid mixing instrument that forces liquid from multiple chambers (using a syringe) to a mixing chamber; the hyposmotic shock delivered using technique was as fast as 3-8 ms. Following the hyposmotic shock, the swelling of bacteria due to water influx and consequent solute efflux through MSCs resulted in lowered refractive index of the bacterial cells. The reduction of refractive index of the cell hence lowered the optical scattering OD_{600} . The dynamics of OD_{600} was then used to interpret the events happening in the cell. The swelling of cell was noted to be around 30-50 ms; 100-150 ms following swelling, the OD_{600} plateaued suggesting the closure of the channels or exhaustion of permeable pools of osmolytes in the cytoplasm. This study formed the first evidence demonstrating the *in-vivo* response of *E.coli* to hyposmotic shock

1.5.4 How many MSCs are required to survive a hyposmotic shock?

The expression of MscS and MscL has been reported to depend on the growth media, osmolarity of the media and cell's growth phase (Stokes et al., 2003; Bialecka-Fornal et al., 2012). These studies also demonstrated that the expression of the channels was up-regulated in elevated levels of stress sigma factor, RpoS, whereas a RpoS null-mutant showed cell lysis upon hyposmotic shock. Figure 1.8 shows the *in-vivo* census of MscL copy number found in *E.coli* at different growth medium (Bialecka-Fornal et al., 2012). As shown in Figure 1.8, a cell grown in M9 media supplemented with 0.5 M NaCl expressed $\approx$ 1300 copies of MscL. It can be interpreted from these studies that cells at high osmolarities are prepared in anticipation of a possible hyposmotic shock.

Following these studies one could ask what is the minimum number of channels sufficient for the cells to survive a given hyposmotic shock. Van Den Berg et al. (2016) demonstrated in *E.coli* using colony counting assay and qPALM to count mEos3.2 tagged MscL and MscS that a minimum of 100 copies of MscL or MscS was required to achieve complete survival to a hyposmotic shock of 0.3 M. Another study characterizing the survival in a flow cell showed

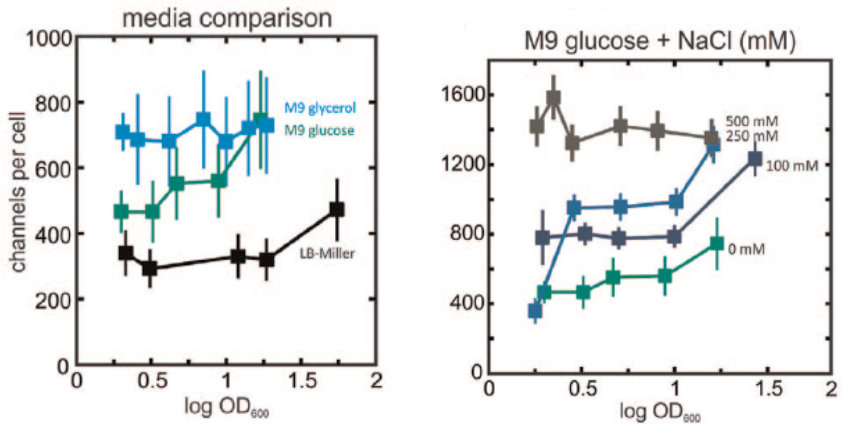

(a) (b)

FIGURE 1.8: **Census of MscL copies expressed in *E.coli* at various growth conditions versus OD_{600} taken from Bialecka-Fornal et al. (2012).** The copies of MscL per cell was estimated using fluorescence microscopy with sfGFP tagged MscL. (a) OD_{600} versus MscL copy number in varying growth media as mentioned in the legends (b) OD_{600} versus MscL copy number in M9 media with increasing NaCl concentration. MscL copies increase with increasing media osmolarity and at OD >1.0. The mean number of channels measured using western blot technique also was in the range as measured here.

that *E.coli* when subjected to fast or slow 0.5 M hyposmotic shock, showed 80% survival chance, if at least 500-700 MscL were present in the cell (Chure et al., 2018). The discrepancies in the number of MscL channels required per cell estimated by the above two studies could have been due to difference in shock magnitude or the uncertainties associated with the technique used to measure the copies of MscL or survival. However, Booth (2014) calculated that 5-10 MscL was sufficient for an *E.coli* grown in 0.5 M to release it's entire osmotic pool. This range of MscL copy number was also in agreement with the previous estimates of MscL copy number (Stokes et al., 2003). The higher number of MscL experimentally measured than the theoretically estimates could suggest that pores of gated MSCs were necessary to accommodate the increase in surface area of the cell due to water influx. However, considering a MscL channel opens a circular pore of 3 nm diameter and with a surface area change of 6 μm^2 per channel, as shown in the Figure 1.9, the total increase in surface area can be calculated as the number of MscL times the area of the opened pore. I estimate that to achieve at least 2% increase in cell surface area during hyposmotic shock, 17400 copies of MscL is required. This value is far higher than

500-1300 MscL measured *in-vivo*. These unanswered questions could further lead to debates on co-operative gating of MSCs and the need for higher number of channels (Ursell et al., 2007; Grage et al., 2011; Van Den Berg et al., 2016; Fernandes et al., 2017). This will be discussed in Chapter 6 of this thesis.

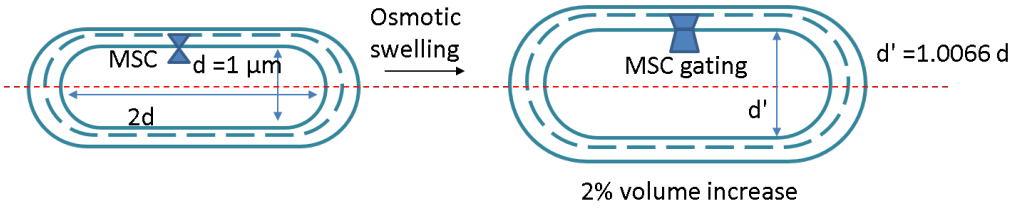

FIGURE 1.9: **Cartoon of *E.coli* swelling upon hyposmotic shock.** The figure demonstrates a 2% increase in cell volume due to swelling during a hyposmotic shock, which leads to the increase in the cell surface area. The elastic properties of the cell wall is thought to allow the cell to maintain the spherocylindrical geometry during volume expansion, without forming cell blebs or bulges.

1.5.5 Structure of MscL and MscS

MscL and MscS are the two most thoroughly studied bacterial MSCs. Crystal structure of MscL was first characterized from *Mycobacterium tuberculosis* using X-ray crystallography as shown in Figure 1.10 (Chang et al., 1998). MscL structure consists of 5 identical subunits (homo-pentamer) where each unit is made of 136 amino acid. The structure has transmembrane (TM) and cytoplasmic domains. Starting from the N-terminal of cytoplasmic side, TM1 helix of each subunit spans across the membrane region to form the pore lining. TM1 joins the TM2-helix through a loop, which dips into the pore and through another loop then extends to a helix into the cytoplasm.

A stable open structure of MscL confirmation was next obtained from *E.coli* using lysophosphatidlycholine (LPC). LPC helped to gate MscL due to curvature stress in phosphatidylcholine (PC) vesicles (Perozo et al., 2002a) at very low turgor pressures. This enabled to study the open structure of MscL as an add-on to that was known about the closed structure (Chang et al., 1998).

MscS is a homo-heptamer with each subunit made of 289 amino acids. The membrane region is made of 3 alpha helices: TM1, TM2 and half of TM3 (TM3A) lines the central pore; the other half of TM3 (TM3B) is bent away from

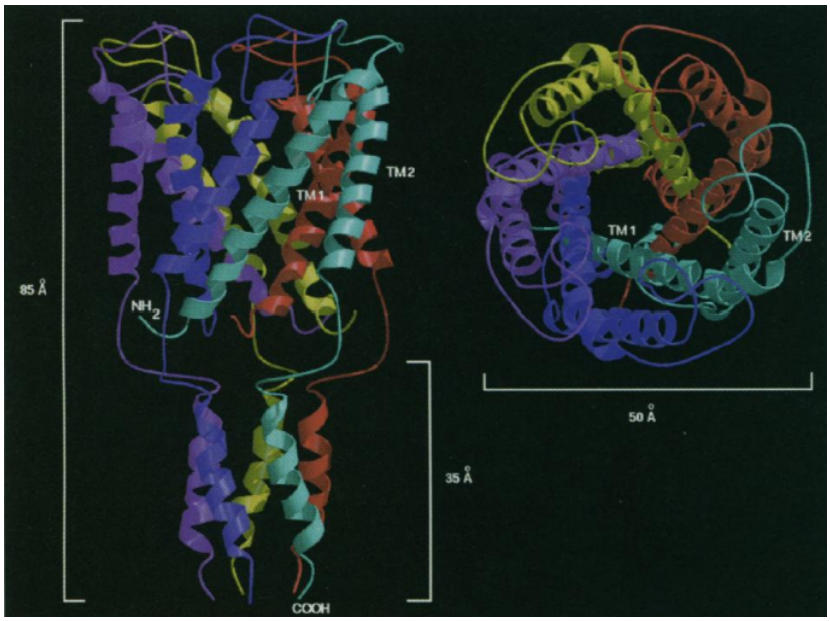

FIGURE 1.10: **Homo-pentameric structure of Tb-MscL taken from Chang et al., 1998.** Model structure of Tb-Mscl showing each subunit represented in individual color and the overall dimensions of MscL structure.

the pore and extends into the cytoplasm along with β containing large cytoplasmic domain as shown in Figure 1.11 (Francisco et al., 2002; Wang et al., 2008). TM1 and TM2 sense the tension and move away such that the linker between TM2 and TM3A twists to arrange in an open state.

1.6 Motivation for this thesis

I am interested to understand the single *E.coli* cell response and survival mechanism to a constantly fluctuating environmental osmolarity. The key components in osmoregulation during hyperosmotic shock have been previously identified (Wood, 2010) and the single cell responses of *E.coli* to hyperosmotic shock has been previously characterized in depth (Pilizota et al., 2012; Pilizota et al., 2013; Pilizota et al., 2014). The survival assays performed using physiological techniques have elucidated the importance of MSCs to survive hyposmotic shocks. Patch-clamp techniques, X-ray crystallography, bioinformatics methods have provided vast information on the structure and functions of MSCs. Previous, the *in-vivo* responses of *E.coli* and *Pseudomonas ariginosa* characterized using light scattering dynamics of bacterial suspension upon step hyposmotic shock, have demonstrated that MSCs gate in milli second time scales

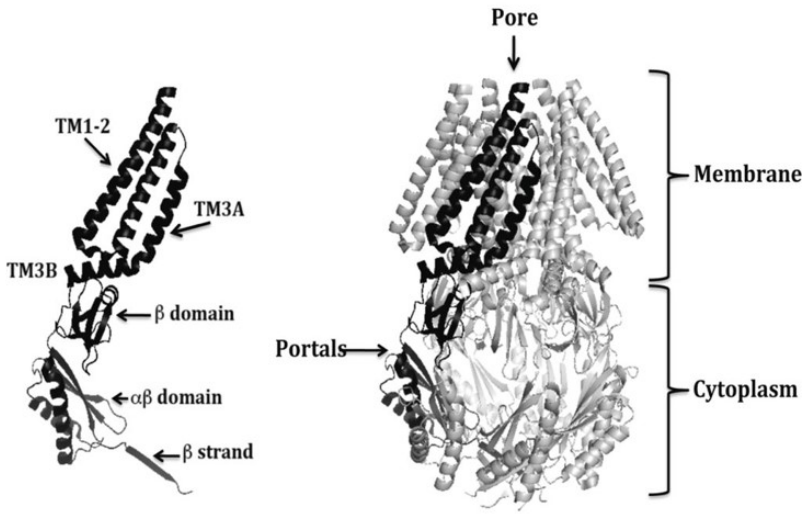

FIGURE 1.11: Homo-heptamer structure of MscS taken from Bootha et al. (2012) shows the structure of closed MscS. A single subunit is colored black and is shown either integrated (left) or separated (right) from the MscS structure

(Boer et al., 2011; Çetiner et al., 2017). These studies have been performed in a scenario when a bacterium encounters a step change in osmolarity. In real life, bacteria on the top surface of the soil could encounter a step change in osmolarity when it rains. But there also exists real life scenarios where the bacteria encounters a gradient change or slow hyposmotic shock (Reppas et al., 2015). For instance, a bacteria living in the animal gut often encounter gradient hyposmotic shock due to the complex gut milieu. A study by Bialecka-Fornal et al. (2015) demonstrated the survival of *E.coli* exposed to varying rates of hyposmotic shock. However, the *in-vivo* responses of the cell to slow hyposmotic shock is not known.

A recent study performed in *E.coli* demonstrated that dihydrostreptomycin (a derivative of streptomycin) was effective in growth inhibition only if MscL was expressed in the cells (Iscla et al., 2014; Wray et al., 2016). Streptomycin is a widely used antibiotic that has been used to target numerous bacterial infections. Streptomycin binds to the 16s rRNA and inhibits protein synthesis in the bacteria. The binding of dihydrostreptomycin to MscL also reduced the gating threshold of MscL in a patch-clamp technique. They observed that the cell survivability also reduced if MscL from *Bacillus subtilis* and *Staphlyococcus aureus* were expressed in *E.coli*. These studies for the first time demonstrated the role of MSCs in the transport of dihydrostreptomycin across the cell. Similar to

these studies, novel antibiotics that bind to MscL have potentials to be further developed. As MscL is a highly conserved protein, structurally and functionally (Balleza et al., 2009; Booth, 2014), broad spectrum antibiotic could be designed. The potential novel antibiotic can be designed to gate MscL at steady-state membrane tensions to render the cell membrane leaky and beyond rescue. The design of novel antibiotics targeting MSCs hold a broad prospect of addressing the current crisis of antibacterial resistance and the study of MSCS and the cells survival mechanism to hyposmotic shock response of bacteria holds broad prospects of developing new drugs. However, a more efficient antibiotics that target the function of MSCs can be designed only if the cell's response to real life fluctuation is osmolarities are understood.

The initial responses of a bacteria when subjected to hyposmotic shock are swelling, opening of MSCs, solute efflux through MSCs, closing of MSCs and thereby recovery of osmotic pressure. The consequence of all these events is reflected as changes in cell volume. Measuring the *in-vivo* single-cell volume allows one to study the detailed dynamics of cellular response upon hyposmotic shock. There are no *in-vivo* single cell studies on the volume response of bacterial cells to hyposmotic shock. In this thesis, using *E.coli* as the model, I characterize the cell's *in-vivo* volume response to hyposmotic shocks and the contribution of MSCs in cell volume dynamics. The studies are useful in understanding the cell's response to slow hyposmotic shock and the knowledge can be applied to design novel antibiotics or other industrial applications discussed in Chapter 7.

1.7 Organization of the thesis

The work presented in this thesis in parts was performed with collaborators and some parts carried out independently. Wherever done in collaboration, my contribution is clearly stated. Following this Introduction chapter is Materials and Methods, where I have summarized all the protocols and techniques used in this thesis.

Chapter 3 was performed in collaboration with a group from Peking University, China and the work is published. In this Chapter, I have contributed in characterizing *E.coli*'s cell volume response to increasing hyposmotic shock. I

also study the response of MscL and MscS deficient mutant to characterize the contribution of MSCs in the volume response.

In Chapter 4 I study the response of *E.coli* with all the MSCs deleted (hepta-mutant). I then characterize the survival of the mutant to varying hyposmotic shock and discuss the effect of mechanical constraints on cell death.

In Chapter 5, I report a novel finding that explains some of the discrepancies that I and other researchers observed while measuring *E.coli*'s response to hyposmotic shocks (Rojas et al., 2017). In these experiments, the cells did not show the characteristic volume recovery of wild-type cells, rather the volume response was similar to that of a hepta-mutant, indicating that the MSCs were not gating in those experiments. I discuss the possible reasons for the observed response and further, demonstrate methods to prepare hyposmotic shock solutions to achieve gating of MSCs.

Chapter 6 was performed in collaboration with the group in University College London, where the collaborators developed a Coarse Grained model of MSCs in lipids and demonstrated the co-operative gating of MSC clusters. I use the results from the Coarse Grained model to study the effect of co-operative gating on cell volume response.

In Chapter 7, I apply the *in-vivo* responses of *E.coli* to simplify the osmotic extraction of periplasmic protein used in industry. I also identify the path through which the periplasmic protein leaks during fermentation and discuss possible designs that could be implemented to genetically engineer recombinant *E.coli* that could overcome the leak and in turn be more efficient to osmotic extraction

In the final chapter, I conclude the thesis by summarizing the observations of this work and discuss future work.

Chapter 2

Materials and Methods

This chapter includes the details on the strains used, experimental procedures and data analysis methods done in this thesis.

2.1 List of strains

E.coli BW25113 (Δ(araD-araB)567 Δ(rhaD-rhaB)568 ΔlacZ4787 (::rrnB-3) hsdR514 rph-1) is the parent strain of Keio single gene deletion collection from Baba et al. (2006) and is used in all the experiments, except for those in periplasmic protein extraction in Chapter 7. This strain is synonymously termed wild-type in this thesis. The double MSC deletion of the wild-type , Δ *mscL* and Δ *mscS*, also termed double-mutant, were made by Renata Buda (Buda et al., 2016) from single knock-out Δ *mscL* and Δ *mscS*, Keio strains using P1 phage method as described below (see Chapter 3 for details on double-mutant cloning done by Renata Buda).

Starting from the double-mutant, I next deleted the remaining five MscS homologous genes, *kefA*, *ybdG*, *yjeP* (synonymous with *mscM*), *ybiO* and *ynaI* to create LSMONGK, also termed hepta-mutant in this thesis. These genes for proteins MscK (1120 aa), YbdG (415 aa), YjeP (1107 aa), YbiO (741 aa) and YnaI (343 aa), respectively .

2.2 Cloning of hepta-mutant mutant

2.2.1 Removing kanamycin cassette from double-mutant

The kanamycin cassette in the double-mutant was removed before the cloning of hepta-mutant using a plasmid pCP20 (Datsenko et al., 2000). The kanamycin

resistance gene is flanked at both ends by FRT sites (that recognized by FLP recombinase enzyme) (Baba et al., 2006). pCP20 plasmid includes temperature sensitive replication, ampicillin and chloramphenicol resistance selection marker, and thermal inducible FLP recombinase. FLP recombinase when induced can flip the FRT sites at the ends of kanamycin cassette leaving behind a 102 bp FRT scar in the site. The protocol for pCP20 transformation and removal of kanamycin cassette is given below.

The double-mutant was first transformed with pCP20 plasmid (Sambrook et al., 1989). The 30°C overnight culture of double-mutant carrying the pCP20 plasmid was 1000 fold diluted into Luria Bertani (LB) broth supplemented with 50 μg/ml of kanamycin and 100 μg/ml of ampicillin and continued to grow with shaking at 220 rpm, at 30°C for few hr. This dilution step was repeated 2-3 times. This step removes the kanamycin cassette by FLP recombinase. The plasmid was then cured by growing the cultures at 37°C. The single colonies that were sensitive to kanamycin were then identified using replica plating and confirmed using boil colony polymerase chain reaction (PCR) using GoTaq polymerase (Promega). The manufactures protocol was used for PCR. The amplified PCR product were then visualized using 1% agarose gel electrophoresis (Sambrook et al., 1989).

2.2.2 Plasmid Mediated Gene Replacement

Plasmid Mediated Gene Replacement (PMGR) method to modify the chromosome was first proposed by Link et al. (1997). This method of chromosome editing depends on *E.coli*'s RecA mediated homologous recombination. In this method, the plasmid, pTOF24, $repA101^{TS}$ encodes a temperature dependant replication initiator protein and two positive antibiotic selection markers, *cat* and *aph*, encoding chloramphenicol and kanamycin. pTOF24 also includes a negative selection marker levin sucrase encoded by *sacB*, which makes *E.coli* sensitive to sucrose (Merlin et al., 2002). To delete a MSC gene, $\approx$ 400-500 bp of each homology arm flanking the gene is first joined together by cross over PCR as shown in Figure 2.1. This fragment and pTOF24 (Figure 2.2a) were then separately digested at PstI and SalI using respective restriction enzyme (Promega or NEB, USA), following the manufacturer's protocol. The digested homology arms and pTOF24 were then ligated using T4 DNA ligase (Promega, USA),

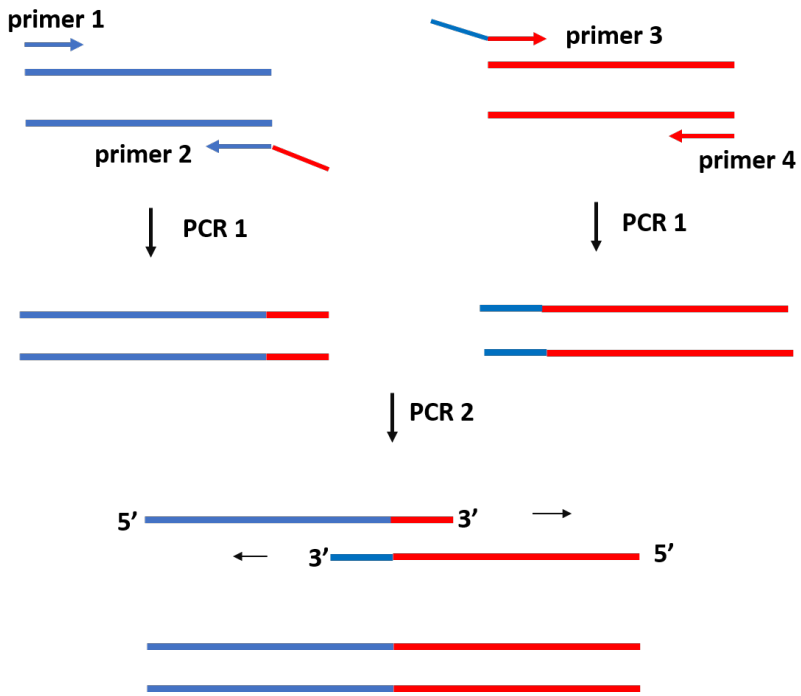

FIGURE 2.1: **Cross over PCR to join the homology arms flanking a gene.** The two homology arms flanking a gene are joined together using two step PCR, PCR1 and PCR2 The reverse primer of the left homology arm, primer 2, has a tail that is reverse compliment of the forward primer of the right homology arm, primer 3. Similarly, the primer 3 has a reverse compliment tail of primer 2. In the PCR1 step, the upstream and downstream homology arm of a gene were amplified using the primers, primer 1, primer 2, primer 3 and primer 4. The amplified product of PCR1 was used as the template for PCR2 along with the end primers, primer 1 and primer 4. The amplified product of PCR2 was the joined homology arms. Phusion polymerase (NEB, USA) was used for PCR amplification using the manufactures protocol

leaving it on a tub of ice, overnight (Figure 2.2b). The homology arm replaced *aph* in pTOF24.

pTOF24 based vector was next transformed to double-mutant (and sequentially deleted MSC mutants) (Sambrook et al., 1989). A few dilutions of the transformants were spread on LB agar supplemented with chloramphenicol for growth of colonies at 30°C, overnight. A successful colony was next streaked into a fresh LB agar plate (also with chloramphenicol) for overnight growth at 42°C. At this temperature, the plasmid loose autonomous replication and can only replicate if they integrate into the chromosome, at one of the homology

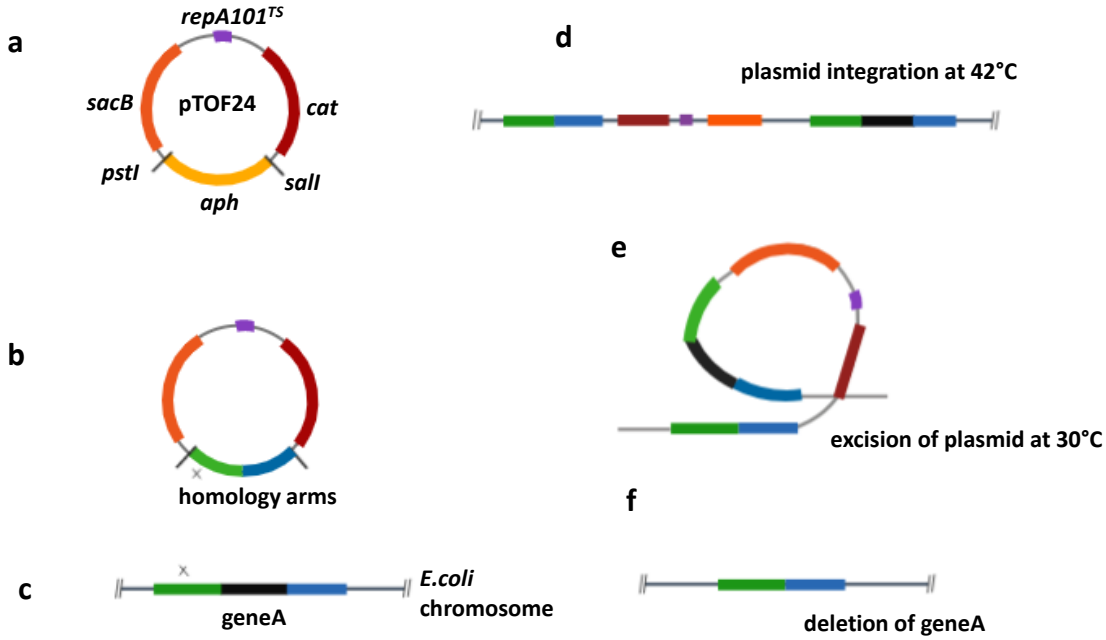

FIGURE 2.2: **PMGR technique to construct MSC deletion mutant**

arms. Those cells that successfully had integrated the plasmid grew in presence of chloramphenicol at 42°C and was re-streaked to grow in the same condition to ensure the purity of the integrants. Next, the integrant was cultured in LB medium with no selection antibiotic, at 30°C with continuous aeration by shaking at 220 rpm. This step excises the integrated plasmid at the second homology arm of the gene, mediated by RecA and while doing so, PMGR occurs to delete the gene. The liquid culture was then replica plated to 5% sucrose and chloramphenicol plates to select the colonies that had lost the plasmid. Sucrose colonies were then checked for successful MSC deletion by boil colony PCR by confirming the right size band in the PCR product.

Starting from the double-mutant, *yjeP, ybiO, ynaI* and *ybdG* were sequentially deleted using pTOF24 to create hexa-mutant. The primers used for cross over PCR and colony PCR are tabulated in AppendixA. The deletion of the final MSC gene, *kefA*, from the hexa-mutant was carried out using *kefA* single deletion Keio strain and P1 virus as described in section below. The PGMR method of deletion is scarless while the P1 method described here leaves a 102 bp FRT scar. The final PCR of the hepta-mutant deletion is shown in Figure 2.3. The PMGR deletions were then sequenced to negate mutations that

could have been caused in the homology arm during cross over PCR.

2.2.3 P1 phage mediated gene replacement

E.coli is a host for P1 virus and during the phage lytic cycle, fragments of host DNA are mispacked into the phage head. These phage carrying fragments of *E.coli* chromosome can be used to edit *E.coli* chromosome by homologous recombination. A donor host cell carrying an antibiotic selection marker in place of the gene of interest is transfected with P1 and then this virus lysate is transfected to the recipient strain. The P1 DNA, homologous with recipient DNA gets recombined and the strains with right edition are selected using the antibiotic marker. While making a double mutant, Keio strains Δ MscS was used as the donor and ΔMscL as the recipient.

Protocol for P1 mediated gene edition BW25113 Δ *kefA* knock-out from the Keio collection was used as the donor strain, where the *kefA* gene is replaced with kanamycin resistance antibiotic marker along with FRT sites at both the ends (Baba et al., 2006). The overnight 37°C, LB culture of the donor strain was 100 fold diluted into 5 mL fresh LB, supplemented with 0.5 % glucose and 5 mM $CaCl_2$, and incubated for 30 min with continuous aeration by shaking at 220 rpm, at 37°C. Then, 0.1 ml of P1 lysate stock was added and incubated for 2-3 hr with continuous aeration, until the cells lyzed and the culture looked less turbid compared to the control flask without the P1. 0.1 ml chloroform was then added to further lyse the unlysed donor cells and this culture was spun down to obtain the supernatant with P1 lysate.

In the second stage, 5 ml of overnight culture of the recipient, hexa-mutant, was spun down to collect the pellets, which was then re-suspended in 2.5 ml of 10 mM Mg_2 SO_4 and 5 mM $CaCl_2$. To 100μl of this re-suspended recipient, different dilutions of the P1 lysate (from 10 to 100μl) was added and incubated for 30 min at 37°C. To this, 1ml of fresh LB with 10 mM sodium citrate was added and incubated for 30 more min. The cells were pelleted and 0.1 ml of 10 mM sodium citrate was added to the tubes and spread on LB agar plate supplemented with kanamycin. The recipient colonies which had successfully replaced the *kefA* gene with kanamycin cassette, received from the donor strain, successfully grew on the kanamycin plate. The successful colonies were then re-streaked several times until the colonies were completely free from P1 phage and looked healthy.

The kanamycin cassette from the hepta-mutant was then removed using pCP20 plasmid as described in the section 2.2.1. After each MSC deletion, the success of cloning was confirmed using colony PCR primers (AppendixA) and agarose gel electrophoresis. At the end of seven deletion, the success was re-confirmed with Keio primers (also tabulated in AppendixA) as shown in Figure 2.3 (Baba et al., 2006). The Figure 2.3 shows the following deletion: 858 bp, *mscS*; 408 bp, *mscL*; 1245 bp, *ybdG*; 1029 bp, *ynaI*; 2223 bp, *ybiO*; 3321 bp, *yjeP* and 3360 bp, *kefA* (::kan, $\approx$ 1000 bp).

2.3 *In-vivo* single cell measurements

In all the single cell experiments, the strains were grown in modified minimal media (MM9). MM9 salts have the similar composition as M9 salts (*M9 minimal medium (standard)* 2010) except KH_2PO_4 is replaced with NaH_2PO_4 so that the amount of potassium in the media can be regulated by adding KCl, without altering the pH of the medium. The final MM9 media has the following components including MM9 salts: MEM amino acids (SigmaAldrich), 1mM KCl, 0.3% glucose, 2 mM Mg_2SO_4, 0.1 mM $CaCl_2$. The final osmolarity of this media is 240 mOsmol and pH is around 7.2 to 7.3. To increase the medium osmolarity, additional NaCl was added to the MM9 media, as tabulated Table 2.1. MM9 buffers were made by diluting 4x stock of MM9 salts and supplementing with 100 mM Mg_2SO_4 for the stability of outer membrane LPS. The composition and osmolarities of MM9 buffer supplemented with varying concentration of NaCl is tabulated in Table 2.1

Osmolarity of the solutions were measured using a Osmometer (Loser, Germany), where the osmolarity is measured using freezing point technique. The unit of measurement is Osmole or Osmol, where a unit Osmole is defined as the osmotic pressure of 1.0 Molal solution.

Wild-type, double-mutant and hepta-mutant frozen glycerol stocks were made from overnight cultures of single colony. These frozen cultures were then diluted 100 times into fresh growth medium supplemented with 100 μg/ml ampicillin and/or 50 μg/ml kanamycin. Following the inoculation, the flask was incubated at 37°C and aerobically stirred at 220 rpm, until the cultures reached an OD_{600} 0.25-0.4. The cultures were then used in room temperature

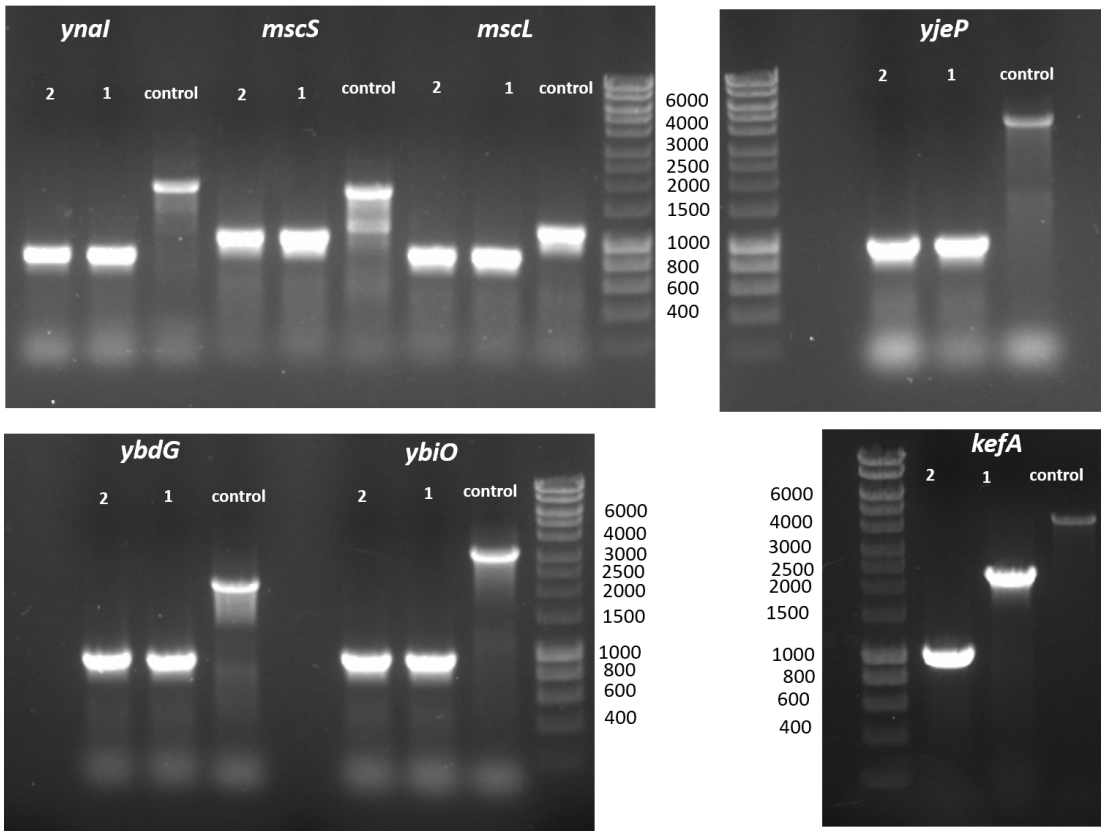

FIGURE 2.3: **Confirmation of the hepta-mutant using PCR and agarose gel-electrophoresis**. The image shows the confirmation of the hepta MSC gene deletions done using PCR and agarose gel electrophoresis. Each set of PCR to test a gene deletion were carried out for 3 samples: control, 1 and 2. Control is a wild-type, BW25113, purified chromosome template. Sample 1 is the hepta-mutant from purified chromosome template. Sample 2 is the hepta-mutant cured of kanamycin cassette in the *kefA* gene location, also from purified chromosome template. The 3 samples are labelled at the top of the corresponding PCR band. The respective MSC deletion confirmed using PCR are labelled at the top of the sample bands. The ladder shown in the image is 1 kb HyperLadder ^{TM} (Bioline). Keio single-knockout primers were used to obtain the deletion confirmation, except for *kefA*, pKCL05 and pKCL06 primers were used in this image (AppendixA). *kefA* shows a deletion of 3360 bp in sample 2 and $\approx$ 2360 bp in sample 1 attributing to the kanamycin cassette.

TABLE 2.1: Osmolarities of growth media and MM9 buffer supplemented with increasing NaCl concentration.

Media/buffers	Osmolarity (mOsmol)
MM9 media	240
MM9 + 50 mM NaCl	343
MM9 + 125 mM NaCl	430
MM9 + 225 mM NaCl	630
MM9 + 300 mM NaCl	700
MM9 + 450 mM NaCl	1030
MM9 + 550 mM NaCl	1200
MM9 + 650 mM NaCl	1370
MM9 Buffer	214
MM9 buffer + 575 mM NaCl	1220
MM9 buffer + 550 mM NaCl	1180
MM9 buffer + 450 mM NaCl	970
MM9 buffer + 225 mM NaCl	570
MM9 buffer + 125 mM NaCl	370

(21°C) for slide preparation for single cell measurements, up to an OD_{600} of 0.65.

2.3.1 Plasmids used for measuring cytoplasmic area

pWR20 plasmid, constitutively expressing cytoplasmic eGFP and kanamycin antibiotic selection marker was used to measure the cytoplasmic area in wild-type (Pilizota et al., 2012). pWR21 was similar to pWR20 except the antibiotic selection marker was ampicillin. pWR21 was used in double-mutant and hepta-mutant cytoplasmic area analysis.

2.4 *In-vivo* hyposmotic shock and imaging

2.4.1 Slide preparation

Tunnel slides for volume analysis were made as shown in the Figure 2.4. Two parallel strips of double sided sticky tape, of $\approx$ 0.1 mm (Scotch Double Sided Tape) was attached to the microscope glass-slide, keeping $\approx$ 4 mm gap in between them. On top of this set-up, the coverslip was attached and pressed to the tape for tight seal. This sandwich of glass-slide, tape and coverslip formed

a tunnel of volume $\approx 8\mu$l. Through the tunnel, first 10μl of 0.1% w/v poly-L-lysine (PLL) (Sigma) was flushed. Immediately, 100 μl of the growth medium was flushed by dropping the solution at one end of the tunnel and wicked through the other end. A 10 μl of 1 μm polystyrene beads (Polybead ®, Polysciences, Inc) was flushed through the tunnel and incubated for $\approx$ 2 min for the beads to attach to PLL. The unattached beads were washed with 100 μl of the growth medium. Next, 10 μl of 5 times concentrated cell culture was flushed through the channel and incubated for 10 min, for the attachment of the cells to PLL. After the incubation, unattached cells were flushed with growth medium and imaged.

The single cell measurements were made using customized epifluorscence microscope from Pilizota lab (Rosko, 2017; Krasnopeeva, 2018) and were controlled with customized LabView program. To image the fluorescent bacteria Nikon CFI Plan Apochromat Lambda 100x objective (NA of 1.45) and single-photon sensitive iXon Ultra 897 EMCCD (Andor,UK) camera was used. In order to reduce photo-bleaching, eGFP was excited with YFP filter (500 nm) and the emitted light was collected at 515 nm. The epifluorescence light was also shuttered between image frames to further reduce the effects of photo-bleaching.

While recording a time-lapse, in order to maintain the field of view stable, the x,y,z position of the slide was stabilized using back focal plane inferometry. A 855 nm laser was focused on to the attached 1 μm polystyrene bead and back-focal-plane of the condenser was imaged onto a Position Sensitive Detector (PSD, Newport USA). The center of the laser beam was noted as the midpoint of the dimensionless X,Y signal range. Using a LabView feedback algorithm, the bead position was maintained at the midpoint of the *x,y,z* of the laser beam (Pilizota et al., 2012).

A field of view was chosen, the *x,y,z* position was fixed, a hyposmotic shock was delivered through the tunnel by flushing 35 μl of the shock solution, while constantly imaging (Figure 2.4). After the hyposmotic shock, in order to overcome the drying of the slide at the ends of the tunnel, 10-50 μl of the solution used for hyposmotic shock was dropped on one side of the tunnel and was constantly replenished when dried. This method was followed in the experiments of Chapter 3. In Chapter 4, this method was instead replaced with a hydrophobic and inert, liquid sealant (CoverGrip ^{TM} Coverslip Sealant, Biotium). The inertness of the sealant was first tested by sealing the tunnel slide

with unshocked cells and monitored for growth of these cells for few hr. The cells grew normally without showing any inhibition to growth.

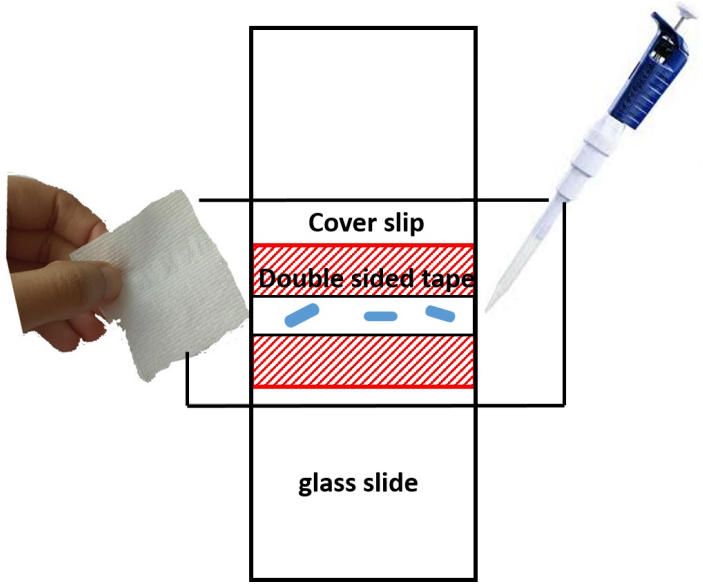

FIGURE 2.4: **Set-up for delivering *in-vivo* hyposmotic shock.** Figure illustrates the tunnel slide set-up and technique of delivering hyposmotic shock.

2.5 Image analysis

2.5.1 Flow calibration

The *in-vivo* hyposmotic shock was delivered as shown in Figure 2.4. To determine the hyposmotic flush rate, fluorescent dye from a Highlighter pen was extracted and suspended in Phosphate Buffer Saline (PBS). The 30 μl of the fluorescent marker was flushed in a PLL coated tunnel slide as shown in Figure 2.4 was flushed back and forth several time while imaging with excitation at 470 nm and emission at 525 nm. From each image in the time lapse, mean intensity was extracted and normalized with the minimum and maximum values. The time taken to complete a hyposmotic shock was estimated by measuring the time taken for the normalized intensity to reach unity. The time taken for the hyposmotic to complete was estimated to 1.75 s.

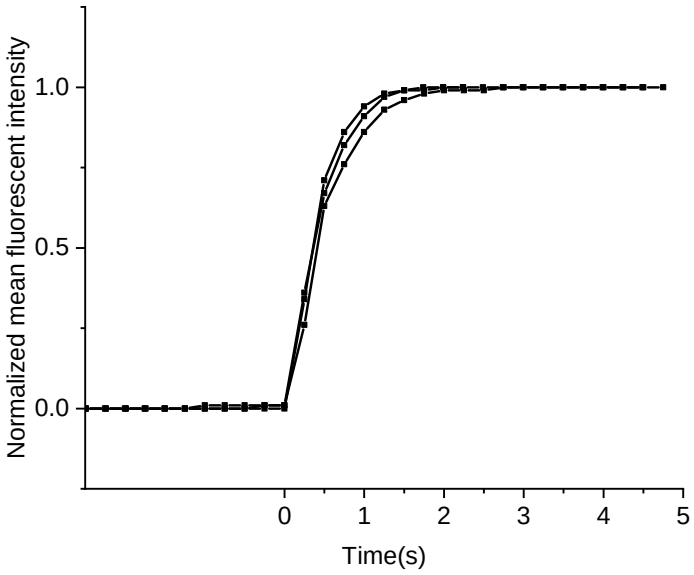

FIGURE 2.5: **Calibration of hyposmotic shock completion time using fluorescent dye.** The hyposmotic shock by manual flush was competed in an average of 1.75 s.

2.5.2 Volume analysis

The images were analyzed using a previously scripted LabView program (Pilizota et al., 2012). From the first image frame, 'flat' cells were chosen by drawing a box around the cell. A flat cell can be defined as a cell that is uniformly attached to the coverslip, decided visually by the uniform fluorescence distribution. A second smaller box covering the background of the cell was drawn to estimate the mean background intensity. The background intensity was estimated for each frame and were subtracted from the respective image frame. Next, from the image frames, minimum and maximum intensity pixel values were extracted. From the background subtracted image frame, if the pixel value was 30% above the difference between the minimum and maximum, the pixel was considered as the part of the cell cytoplasm. The 30% threshold was based on the given point spread function and the blurring caused by the lens. The total number of pixels belonging to the cytoplasm were counted to estimate cell area, $S_{area}(t)$. Considering *E.coli* as a sphero-cylinder (a cylinder capped with hemispheres at ends) with length, twice the diameter, the cell volume was estimated as $V(t) = S_{area}(t)^{\frac{3}{2}} \cdot \frac{\frac{10\pi}{3}}{(4+\pi)^{\frac{3}{2}}}$.

The cell volume from each cell was next normalized as $V_n = V(t)/V_0$, where V_0 is the mean of ten volume points before the hyposmotic shock. The normalized volume sample was then filtered with median filter, with window size 3 in Chapter 3 (done using MATLAB) and window size 5 (done using Python) in Chapter 4, to remove any spurious points. Filtered traces of all the cells in a particular experiment were then aligned at individual cell's time of maximum cell volume expansion and then mean volume response were estimated.

2.5.3 Cell length and width analysis

The program to estimate cell length and width was scripted by Dario Miroli (unpublished). I have used the same program for the analysis of cell length and width analysis of hepta-mutant in Chapter 4. The program was scripted using Python Skimage packages. A flat cell used for volume analysis was as well used for length and width analysis. Each cell was first segmented as described in volume analysis. The edge pixel location on the segmented cell was labelled. Each edge pixel position was examined (clockwise or counter-clockwise) to obtain the curvature of the cell. The pixels at the pole of a cell had the maximum curvature and those at the sides will be a straight line. In order to estimate the curvature, each pixel position and the 2 consecutive pixel position around each pixel was examined. If the pixel was located at the long edge of the cell, the given pixel would be the midpoint between its neighbouring pixel. If the pixel was at the poles, the distance between its neighbouring pixel would drop. So by scanning the curvature of the cell edge, the position of minimum curvature was identified as the poles of the cell. Next, the segmented cell was skeletonized to obtain the cell boundary passing through the identified poles. To estimate the cell length, a second order polynomial was fit through the backbone, poles and truncated using the boundaries of the segmented cell. Cell width was estimated by identifying the midpoint of the length line and a line perpendicular to the midpoint was drawn intersecting the cell boundary.

The cell length and width was normalized with the pre-shock value (by taking an average of the first 10 length or width measurements).

2.5.4 Cell death and growth analysis of hepta-mutant

The analysis of dying and growing cells were performed for all the cells in a fixed field of view and not just the flat cells. To do this, a box was drawn around all the cells and then each cell was analyzed as below. A cell was defined as dead (Chapter 4), if the total intensity of the cell dropped at least 20% the total intensity following the hyposmotic shock and time point at which the cells lost the 20% intensity was noted as the time of death. This threshold value was chosen empirically to include the cells that slowly lost fluorescent intensity, along with shrinkage in volume. To estimate the total intensity, a box was drawn around every cell so that it could be separated from it's neighbouring cell. The minimum intensity value from each frame was subtracted from every pixel to subtract the background. Total fluorescent intensity was then estimated by adding all the fluorescent intensities within the box, for each cell. The time of growth following hyposmotic shock for a hepta-mutant is defined as the time at which cells started increasing cell area. Cell area was first estimated as described in section 2.5.2 and then every 10 contiguous points were averaged. The time of growth was then estimated as follows: if the value of a point in the average was greater than an average of 10 and 20 points preceding it and smaller than an average of 10 and 20 succeeding it, then the time value corresponding to the point was the time of growth.

2.5.5 Analysis of flatness of cell attachment

As performed for section 2.5.4, a box around a cell was drawn for all the cells and then the flatness of cell attachment was estimated by first identifying the poles of a cell as described in the section 2.5.3. The box was then rotated to align the cell's long axis vertically. To subtract the background noise, minimum intensity value in the box was subtracted from every pixel. The pixels with intensities 18% below the difference between the minimum and maximum intensity were set to zero, while those above were used for analysis as shown in Figure 2.6b. Along each longitudinal section of the segmented cell, the intensities were normalized to unity. The Figure 2.6c shows the plot of normalized intensity within each longitudinal section of the cell, each color represents a longitudinal section. Symmetry of the distribution was estimated by measuring the difference between two corresponding pixel points on either

side of the distribution, starting from the tails of the distribution and moving towards the center. This estimation of difference was performed for every longitudinal section of the cell. Next, the sum of these differences were estimated for each longitudinal section of the cell as shown in Figure 2.6d. The sum of difference for a symmetric distribution would be zero and would increase with the level of skewness of the distribution. A flat cell would have a symmetric distribution while the skewness would be higher for non-flat cell. Next, the sum of differences were squared and the mean value was calculated to estimate a flatness score. The flatness score for a flat cell and a not flat cell is shown in Chapter 4 Figure 4.10a.

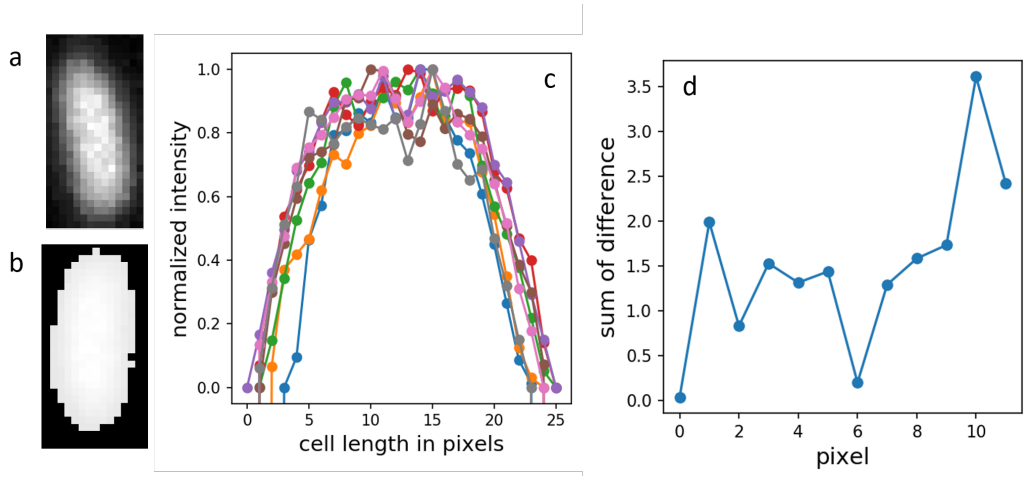

FIGURE 2.6: Estimation of the quality of cell attachment to coverslip. (a) shows a box drawn around a cell (b) cell segmented and rotated to align the long axis of the cell, vertically (c) plot of normalized intensity values of every pixel, sectioned along the long axis of the cell. Here, the intensity distribution of the either side edge of the cell is not shown (d) plot of the sum of the difference between pixel intensities of the distribution in subplot c. The sum of difference is measured by subtracting two corresponding pixel points on either side of the distribution, starting from the tails of the distribution and moving towards the center, for each longitudinal section.

2.6 Periplasmic protein extraction

2.6.1 *E.coli* growth conditions

E.coli W3110 K-12 (CD1441) carrying plasmid pave265 (tetracycline antibiotic selection) with periplasmic expression of Hel4 was used (Lennon et al., 2014).

Th strain and plasmid were obtained from FUJIFILM Diosynth Biotechnologies. The glycerol frozen stock of CD1441 were grown overnight in LB media (25 g/l, osmolarity: 400 mOsm) supplemented with 10 μg/ml of tetracycline antibiotic, with continuous aeration by shaking at 220 rpm at 37°C. The following day, the cultures were 100 fold diluted into to fresh LB media with 10 μg/ml of tetracycline antibiotic and cultured at 37°C with shaking at 220 rpm. Hel4 expression was next induced with 100 μM Isopropyl--D-thiogalactoside (IPTG) when the culture OD $_{600}$ reached $\approx$ 0.5. Post-induction, the cultures were grown for $\approx$ 5 hr until a stationary phase, termed end of fermentation (EOF), in growth was reached.

EOF culture was centrifuged at 8000 rpm for 15 min to obtain the cell pellets, which was then subjected to hyperosmotic shock using 0.58 M sucrose in Tris-HCl buffer and 1.4 mM EDTA, adjusted to pH 8.0. Alternatively, hyperosmotic shock was delivered by adding equimolar sucrose or sodium chloride powder to the EOF culture medium. Following the hyperosmotic shock, in all the protocols, cells were centrifuged at 8000 rpm and then cell pellets was subjected to hyposmotic shock using 5 mM Mg_2SO_4.

2.6.2 Protein estimation using Coomassie stained gels

The estimation of Hel4 was done using 4-12% Bis-Tris, precast gels (Invitrogen NuPAGE). To estimate the amount of Hel4 expressed in cell, known weight of cell pellet was suspended in known volume of RIPA lysis buffer (Santa Cruz) and sonicated in 5 cycles with sonication for 30 s each and alternating on ice for 30 s between the cycles. The lysed cells were centrifuged and the known volume of the supernatant was next diluted with 4x loading buffer (Nupage). A known volume of Hel4 containing samples, osmotic extracted and cell culture supernatant, was mixed with appropriately diluted 4x loading buffer. The samples were next incubated in a water bath at 70° C for 5 min. The cooled samples were then diluted with 10X reducing agent (Nupage) and known volume was loaded into each well of the pre-cast gel. In the every gel a protein ladder (PageRuler ®) and three different volumes of purified Bovine Serum Albumin (100 mg/ml) were loaded. BSA was loaded in each gel to obtain the standard calibration line.

In every experiment, the amount of Hel4 expressed per g of cells was estimated by summing the amount of Hel4 in cells at EOF (by lysing the cells)

and the amount of Hel4 leaked into the fermentation medium. However, the amount of Hel4 leaked in one of the experiments was not estimated, so in the calculations, the average % of Hel4 leaked from all the other experiment was taken for this particular experiment. This was done on the basis that the cells were induced to produce Hel4 at OD 0.5 and were grown for 5 hr, in all the experiments and so the variation in the Hel4 leaked would be consistent.

The gel was first fixed with a mixture of 40% (v/v) methanol and 10% (v/v) acetic acid for 30 min. Next the gels were stained with 0.1% Coomassie R-250 (Abcam) in 40% (v/v) methanol and 10% (v/v) acetic acid for 1 hr. Following which the gels were de-stained with 50% (v/v) methanol and 10% (v/v) acetic acid, until the gel background was clear of Coomassie. The gels were next imaged at 650 nm using UV transilluminator.

The amount of Hel4 was estimated by first imaging the gel and then, the image was analyzed using a customized Python program as described next. A rectangular box was drawn around the protein band in the image. The left and right edge of the rectangle was drawn close to the protein band, in-order to minimize the errors from the background as shown in Figure 2.7a. The minimum pixel intensity value in the box was subtracted from each pixel intensities to subtract the background noise. Figure 2.7a shows the horizontal and vertical axis of the gel that will be referred next. The sum of intensities along each horizontal axis of the box was estimated and plotted against the vertical axis as shown in Figure 2.7b. In Figure 2.7b, region of interest was chosen visually by drawing a box. The sum of the intensity (area under the curve) within the drawn box was estimated to calculate the total pixel intensity of the protein band. Pixel intensities of three known amounts of BSA was estimated and a straight line passing through zero was fit to these points. The amount of Hel4 was then estimated using the BSA line equation and total pixel intensity of respective Hel4 band.

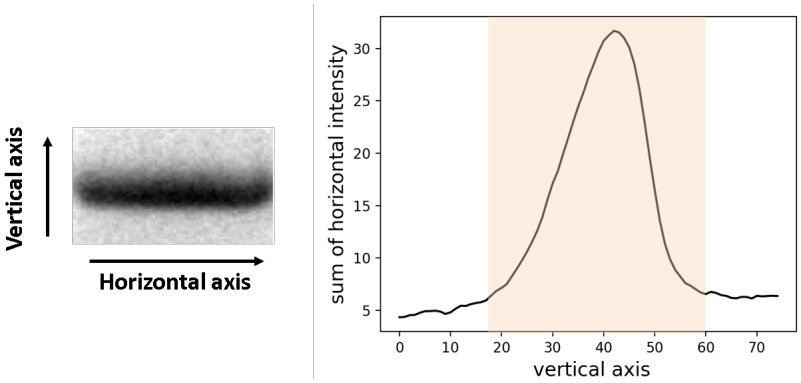

FIGURE 2.7: Estimation of amounts of protein from a Coomassie stained protein gel. (a) Shows the box drawn around the protein band to be analyzed. The box was drawn close to the left and right edge of the protein band to reduce background contributions. (b) The area under the curve marked in orange gives the total pixel intensity.

Chapter 3

Dynamics of *Escherichia coli's* passive response to a sudden decrease in external osmolarity

3.1 Introduction

The work in this Chapter is carried out in collaboration Dr. Bai Fan's group from Peking University, China and Dr. Teuta Pilizota's group. The work is published as *Dynamics of Escherichia coli 's passive response to a sudden decrease in external osmolarity* in PNAS, 2016, and can be found

Buda, Renata et al. (2016). " Dynamics of Escherichia coli 's passive response to a sudden decrease in external osmolarity ". In:Proceedings of the NationalAcademy of Sciences113.40, E5838–E5846.ISSN: 0027-8424.

DOI:10.1073/pnas.1522185113.

The work in the paper can be separated into experimental and model section. The experiments and data analysis were performed by Renata Buda and I. The model section was performed by Yunxiao Liu, Jin Yang and Keiran Stevenson. The contribution of each author in the paper can be found at the end of the publication. My contribution in the paper is towards Figures 2 and 3 in the main paper and Figures S1 and S2 in the supplementary text, where the experiments for these figures were performed by both Renata and I. Following this introduction, the PDF format of the publication is attached along with Supplementary Information.

Dynamics of *Escherichia coli*'s passive response to a sudden decrease in external osmolarity

Renata Buda[a,1,2], Yunxiao Liu (刘云啸)[b,1], Jin Yang (杨津)[b,1], Smitha Hegde[a,1], Keiran Stevenson[a], Fan Bai[b,3], and Teuta Pilizota[a,3]

[a]Centre for Synthetic and Systems Biology, Institute of Cell Biology, School of Biological Sciences, University of Edinburgh, Edinburgh EH9 3FF, United Kingdom; and [b]Biodynamic Optical Imaging Centre (BIOPIC), School of Life Sciences, Peking University, Beijing 100871, China

Edited by Janet M. Wood, University of Guelph, Guelph, ON, Canada, and accepted by Editorial Board Member Herbert Levine July 28, 2016 (received for review November 10, 2015)

For most cells, a sudden decrease in external osmolarity results in fast water influx that can burst the cell. To survive, cells rely on the passive response of mechanosensitive channels, which open under increased membrane tension and allow the release of cytoplasmic solutes and water. Although the gating and the molecular structure of mechanosensitive channels found in *Escherichia coli* have been extensively studied, the overall dynamics of the whole cellular response remain poorly understood. Here, we characterize *E. coli*'s passive response to a sudden hypoosmotic shock (downshock) on a single-cell level. We show that initial fast volume expansion is followed by a slow volume recovery that can end below the initial value. Similar response patterns were observed at downshocks of a wide range of magnitudes. Although wild-type cells adapted to osmotic downshocks and resumed growing, cells of a double-mutant (Δ*mscL*, Δ*mscS*) strain expanded, but failed to fully recover, often lysing or not resuming growth at high osmotic downshocks. We propose a theoretical model to explain our observations by simulating mechanosensitive channels opening, and subsequent solute efflux and water flux. The model illustrates how solute efflux, driven by mechanical pressure and solute chemical potential, competes with water influx to reduce cellular osmotic pressure and allow volume recovery. Our work highlights the vital role of mechanosensation in bacterial survival.

osmotic downshock | bacterial mechanosensing | single-cell imaging

Biology offers an array of intriguing mechanical solutions, both active and passive, often exceeding what is currently possible with man-made methods. Understanding how biological systems achieve different functionalities under mechanical stimuli can inform new, thus-far-unexplored design principles. One such passive control system is the bacterial response to sudden decreases in external osmolarities.

A Gram-negative cell's fluid cytoplasm is separated from the external environment by the inner membrane, the periplasmic space, and the outer membrane. Ordinarily, the total solute concentration within the cytoplasm is higher than that of the environment, resulting in a positive osmotic pressure on the cell wall (termed turgor pressure) (1). *Escherichia coli* is able to respond to both increases and decreases in external concentrations. An increase in external osmolarity (hyperosmotic shock or upshock) results in water efflux from the cell interior, causing cellular volume to shrink and osmotic pressure to drop to zero (2). *E. coli* responds by actively accumulating specific solutes (osmolytes), such as potassium, proline, and glycine-betaine (2). Accumulation of osmolytes in the cell's cytoplasm causes reentry of water, cell volume increase, and recovery of osmotic pressure (3, 4). A downward shift in external osmolarity (termed hypoosmotic shock or downshock) causes fast water influx into the cell's cytoplasm. As a result, the osmotic pressure increases and the cell expands in a nonlinear fashion (5, 6). Turgor pressure in *E. coli* has been estimated to lie between 0.3 and 3 atm (5, 7), rising up to 20 atm upon a large downshock (6). An increase in the inner membrane tension, caused by the expansion, is thought to activate the nonspecific export of solutes through mechanosensitive channels (MSCs), such as MscS and MscL (Fig. 1*A*) (8). As the solutes leave the cell, so does the cytoplasmic water, enabling the cell to recover original volume and pressure (Fig. 1*A*).

Mechanosensitive channels are found in a wide range of cells (9–11), displaying great diversity. The precise gating mechanism of these pressure-controlled channels has attracted a lot of attention from scientific community. Despite the efforts, it remains a challenge (12). To our current knowledge, *E. coli* possesses seven different mechanosensitive channels (13). Of those seven, four play the dominant role: the mechanosensitive channel of small conductance (MscS), the large mechanosensitive channel (MscL) (9, 14, 15), the mechanosensitive channel of miniconductance (MscM) (16), and the potassium-dependent mechanosensitive channel (MscK) (17). Since their discovery in giant spheroplasts of *E. coli* (13, 18), crystal structures of some of the channels have been obtained (19–21), and channel function has been extensively studied in vitro (13, 18, 19, 22–25). The most widely used in vitro technique, electrophysiology, enabled measurements of channels' pressure sensitivity, open dwell time, conductance, as well as ion selectivity (18, 26). For example, in vitro-measured opening time of MscS or MscL is on the order of 20–30 ms (27, 28), and the channels close immediately upon the decrease in tension (13).

Significance

Mechanosensation is central to life. Bacteria, like the majority of walled cells, live and grow under significant osmotic pressure. By relying on mechanosensitive regulation, bacteria can adapt to dramatic changes in osmotic pressure. Studying such mechanical sensing and control is critical for understanding bacterial survival in a complex host and natural environment. Here, we investigate the fundamental design principles of *Escherichia coli*'s passive mechanosensitive response to osmotic downshocks by implementing single-cell high-resolution imaging. We explain the observed cell volume changes by modeling flux of water and solutes across the cell membrane. A better characterization of bacterial mechanosensitive response can help us map their reaction to environmental threats.

Author contributions: T.P. designed research; R.B., S.H., and T.P. performed research; K.S. contributed new reagents/analytic tools; J.Y., F.B., and T.P. developed the model; J.Y. and K.S. fitted the data to the model; R.B., Y.L., S.H., and T.P. analyzed data; and R.B., Y.L., J.Y., S.H., K.S., F.B., and T.P. wrote the paper.

The authors declare no conflict of interest.

This article is a PNAS Direct Submission. J.M.W. is a Guest Editor invited by the Editorial Board.

[1]R.B., Y.L., J.Y., and S.H. contributed equally to this work.

[2]Present address: Laboratory of Cell Biophysics, Division of Molecular Biology, Ruder Boskovic Institute, 10000 Zagreb, Croatia.

[3]To whom correspondence may be addressed. Email: teuta.pilizota@ed.ac.uk or fbai@pku.edu.cn.

This article contains supporting information online at www.pnas.org/lookup/suppl/doi:10.1073/pnas.1522185113/-/DCSupplemental.

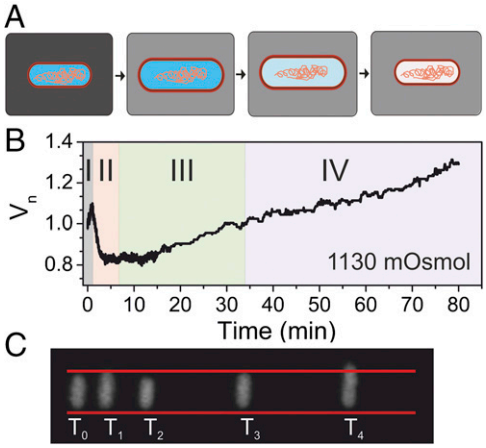

Fig. 1. Characteristic cell volume response to a sudden downshock. (*A*) Upon a sudden decrease in external concentration, cell volume expands, which leads to opening of mechanosensitive channels. Consequently, solutes exit the cell, allowing recovery of cell volume through loss of cytoplasmic water. (*B*) A characteristic single-cell volume response for a 1,130-mOsmol downshock. The trace was normalized by the initial volume, that is, the volume before the downshock. Different phases of the recovery response are indicated with different colors. In gray is the expansion phase (phase I), followed by two volume recovery phases. Phase II (in orange) is characterized by volume decrease, and phase III (in green), by volume increase upon reaching the minimum volume. Phase IV (in purple) indicates recommenced growth. Initial 15 min are sampled at 5 Hz and an additional 1 h at a frame every 5 s. (*C*) Still images from different phases in *B*. T_0 is the very beginning of the recording, before the downshock. $T_1 = 45$ s, $T_2 = 4$ min, $T_3 = 35$ min, and $T_4 = 70$ min. Red lines are drawn to indicate the size of the cell before the downshock. In comparison, the cell size at T_1 is slightly larger (phase I), at T_2 smaller (phase II), at T_3 it reaches the initial size (phase III), and at T_4 it is significantly larger (phase IV).

In contrast to in vitro studies, in vivo studies are rare and mostly focused on estimating bacterial population survival with or without MSCs present (13, 28, 29). For example, we know that, if either MscS or MscL alone is present in the cell membrane, populations of cells can easily survive the abrupt osmotic downshock (28). When both channels are lacking, the survival rate decreases (29, 30). On a single-cell level, a recent study looked at the nature of cells dying upon downshocks and found that it depends on the flow rate with which the shock is administered (29).

However, in vitro studies of mechanosensitive channel gating and population survival studies cannot be easily translated into insights on the passive control of the whole-cell volume and pressure. Here, by looking at the response to hypoosmotic shocks on a single-cell level, we show that the volume recovery after initial fast expansion proceeds on a much slower timescale, on the order of minutes. In addition, cellular volume can decrease below the initial value. We present a theoretical model that explains our experimental observations. A competition between water efflux and influx and solute efflux through mechanosensitive channels gives rise to the observed characteristic slower volume recovery. The chemical potential of water and solutes serve as effective "control" variables in this passive dynamic system.

Results

Characterizing Whole-Cell Downshock Response. *E. coli*'s response to downshocks has previously been characterized using light scattering in a stop flow device and within the first second postshock (28). We applied a single-cell microscopy assay previously developed (3), to extend the length of observation and investigate the response to downshocks in a range of shocks of different magnitudes.

Fig. 1*B* shows a characteristic volume recovery trace of a single wild-type cell subjected to a large osmotic downshock (Δc = 1,130 mOsmol), delivered with a local flow rate of 0.68 μL/min. At this rate, full transition to the lower osmolarity media is completed within 0.8 s (*Materials and Methods*). Cytoplasmic volume was monitored via cytoplasmically expressed eGFP, sampled at a frame every 0.2 s for initial 15 min, and at a frame every 5 s for the rest of the 75-min recording. Characteristic phases were identified and indicated with different background colors as follows: (I) expansion phase, observed immediately after downshock; (II) decrease phase of volume recovery, observed postexpansion, lasting several minutes; as the volume decreases in this phase, a characteristic "overshoot" below the initial volume is often observed; (III) increase phase of volume recovery, observed after minimum volume (V_{min}) has been reached and lasting until initial volume is reestablished, that is, ~30 min; (IV) cell growth phase, observed post-volume recovery. Fig. 1*C* gives raw images corresponding to different phases shown in Fig. 1*B*.

We analyzed volume changes in 609 wild-type cells before, during, and after downshock for the following shock magnitudes: 103, 190, 460, 790, 960, 1,130, and 1,337 mOsmol. Fig. 2, *Left*, shows average traces with SDs of 103- to 1,130-mOsmol shocks. All cells quickly expand in phase I and show characteristic slow volume recovery in phase II. As the shock increases, the length of phase II and the overshoot increase. *SI Appendix*, Fig. S1, *Left*, shows average traces with SDs over longer time periods; phase IV, that is, growth, is visible for all shock magnitudes. *SI Appendix*, Fig. S3, *Left*, shows average trace with SDs of our largest shock, 1,337 mOsmol. We observe expansion in phase I; however, only small recovery in phase II is visible, with no characteristic overshoot and no phase IV. In fact, a large number of cells in 1,337-mOsmol condition lyse during our recording (*SI Appendix*, Fig. S10).

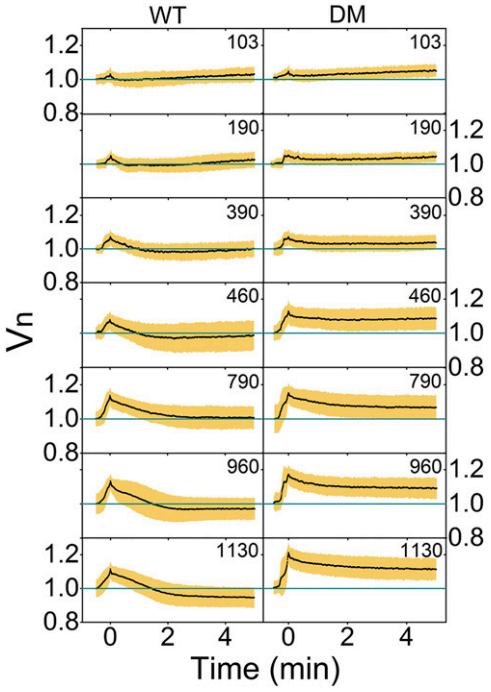

Fig. 2. Cell volume response of the wild-type cells at different downshock magnitudes shows slow volume recovery and an "overshoot." We use descriptive statistics to present our datasets and plot average volume traces with SDs constructed from 609 (WT) and 480 [double mutant (DM)] traces as a function of time. A zoom-in to first 5 min of downshock response sampled every 0.375 s is given. In total, 64 (WT) and 66 (DM) cells were used for 103 mOsmol, 94 (WT) and 52 (DM) cells were used for 190 mOsmol, 66 (WT) and 54 (DM) for 390 mOsmol, 56 (WT) and 80 (DM) for 460 mOsmol, 90 (WT) and 68 (DM) for 790 mOsmol, 116 (WT) and 50 (DM) for 960 mOsmol, and 106 (WT) and 77 (DM) cells for the 1,130-mOsmol downshock. Volume expands in all conditions and increases with the shock magnitude. Slow recovery follows volume expansion. For the wild-type cells, volume drops below the initial value, increasingly so with the larger shocks.

To confirm that the characteristic slow volume recovery after expansion is due to mechanosensitive channels, we characterized the response of a mutant strain lacking the channels contributing the most to downshock response (30), MscS and MscL (double mutant). Fig. 2, *Right*, shows average traces with SDs of the double-mutant cells exposed to downshocks of same magnitudes as in Fig. 2, *Left*. In total, 480 cells were analyzed. The double-mutant strain quickly expands for all shock magnitudes, similarly to the wild type. The response of the double-mutant strain in phase II and phase III is similar to that of the wild type for shocks of <390 mOsmol. For shocks of ≥390 mOsmol, the double mutant shows a smaller decrease in volume postexpansion and no overshoot. In addition, phase IV was not observed within 35 min postdownshock for any of our shocks (*SI Appendix*, Fig. S2). *SI Appendix*, Fig. S3, *Right*, shows average traces with SDs of the double mutant exposed to the largest shock. The response is similar to that of the wild type, where the number of lysing cells during our recording in 1,337-mOsmol condition increased for the double mutant (see also *SI Appendix*, Fig. S10 and analysis of observed lysis in *Growth Rate upon Downshock Does Not Depend on the Shock Magnitude*).

During sample preparation, we attached individual cells to the coverslip surface. To investigate whether the observed characteristic response to a sudden downshock is specific to surface-attached cells only, we repeated the experiment on freely floating cells (*Materials and Methods* and *SI Appendix*, Fig. S4). We were particularly interested in phases II and III, that is, slow volume recovery and overshoot. In the case of free cells, the shock was completed in microfuge tubes. Imaging began 3–4 min postshock and continued at specific time points, giving a population averaged volume (*SI Appendix*, Fig. S4, and *Materials and Methods*). *SI Appendix*, Fig. S4 shows that characteristic phases II–IV are similar to those observed for the individual cell given in Fig. 1*B*. Phase I, that is, expansion, could not be captured with this method as it was completed before the imaging began.

In Figs. 1 and 2, the shock was induced by removing a given osmolarity of NaCl. To examine whether the characteristic response observed is specific to the solute that causes the downshock, we have induced the shock by removing sucrose in *SI Appendix*, Fig. S5. The magnitude of the downshock in *SI Appendix*, Fig. S5 was 590 mOsmol and the response observed is very similar to that of the 790-mOsmol NaCl-induced shock shown in Fig. 2.

Maximum Volume Expansion Occurs Fast, on the Order of Seconds. To quantify the extent of postdownshock volume expansion in the wild-type strain, in Fig. 3*A* (blue) we plot maximum volumes, $V_{n,\max}$, against the magnitude of the downshock. $V_{n,\max}$ increases with the shock magnitude up to 790 mOsmol, at which point it reaches $\approx$ 15% and expansion saturates. The time it takes to reach $V_{n,\max}$ is $\approx$ 30 s (Fig. 3*B*, blue) for all shock magnitudes.

We compare the $V_{n,\max}$ of the wild type to that of the double mutant. $V_{n,\max}$ and $T_{\max}$ for the double mutant are given in Fig. 3 *A* and *B* in red. Similarly to the wild type, the double mutant expands more with increasing shock magnitude. However, for shocks ≥790 mOsmol, $V_{n,\max}$ of the double mutant saturates at a slightly higher value, $\approx$ 20%. The time it takes to reach $V_{n,\max}$ for the double-mutant strain lasts $\approx$ 30 s, similar to the wild type, with the only difference that at higher shock magnitudes full expansion is slightly faster, lasting $\approx$ 20 s.

Upon Expansion, Volume Recovery Is Slow, on the Order of Minutes, and Volume Can Decrease Below the Initial Value. To determine the length of the time volume decreases from $V_{n,\max}$ to $V_{n,\min}$ (minimal, postshock value) in phase II, we identified the time point, $T_{\min}$, at which $V_{n,\min}$ is reached. Fig. 3*C* shows a box plot of $V_{n,\min}$ and Fig. 3*D* of $T_{\min}$ against the downshock magnitude. Wild-type cells (in blue) show increasing overshoot with increasing shock magnitude, reaching $\approx$0.9 for the highest shock. In contrast, the double mutant (in red) does not overshoot in any of the conditions. The time it takes to reach $V_{n,\min}$ increases with the shock magnitude both for the wild type and the double mutant, reaching $T_{\min} \approx$ 8 min for the wild type, and $\approx$ 5 min for the double mutant. $T_{\min}$ is consistently lower at different shock magnitudes for the double mutant compared with the wild type.

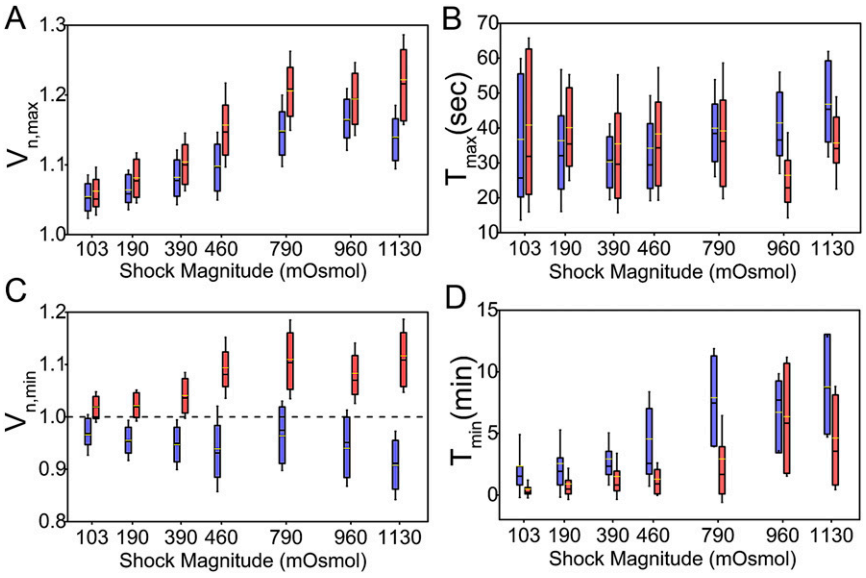

Fig. 3. Analysis of maximum and minimum volume and time. (*A*) Box plot of maximum volume, $V_{n,\max}$, and (*B*) the time at which maximum volume is reached, $T_{\max}$, as a function of shock magnitude. The wild type is shown in blue, and the double mutant, in red. The upper/lower whiskers indicate 1.5× the SD value. The upper/lower edges of the boxes indicate the third/first quartile. The black line indicates the median, and the yellow line, the average value. $V_{n,\max}$ increases with the shock magnitudes and saturates at and above 790 mOsmol. $T_{\max}$ is independent from the shock magnitude for the wild type (blue) and slightly smaller for the double mutant (red) for the two largest shock magnitudes. (*C*) $V_{n,\min}$ and (*D*) $T_{\min}$ plotted against the shock magnitude for wild type (blue) and double mutant (red). $V_{n,\min}$ in *C* is slightly below 1 for the wild type and decreases with the shock magnitude. $V_{n,\min}$ for the double mutant stays above 1 in all conditions. $T_{\min}$ increases with the shock magnitude for both wild-type and double-mutant cells.

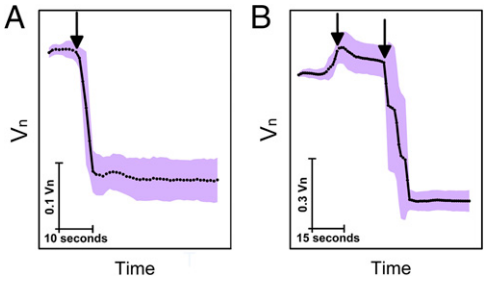

Fig. 4. Cells, either grown at high osmolarities or subjected to a downshock, were exposed to a subsequent upshock. Normalized, average volume of (*A*) 13 and (*B*) 30 cells plotted against time in seconds. SD is given as a shaded area in light purple. (*A*) Cells grown in media of high osmolarity, 1,370 mOsmol, were subjected to a further increase of external osmolarity (upshock of 1,272 mOsmol). Arrow indicates the time at which shock was administered. Cell volume decreased within seconds posthyperosmotic shock. (*B*) Cells grown in the same media were subjected to a 1,130-mOsmol downshock indicated with the first arrow. Upon the downshock, volume expanded. At ≈ 1 min after the downshock, cells were exposed to a strong upshock of 2,160 mOsmol, indicated by the second arrow. Upon the upshock, cell volume decreased within seconds.

Growth at High Osmolarities, Together with Downshock, Do Not Change Membrane Permeability to Water. To gain more information on the physical mechanism behind the slow volume decrease in phase II, we considered the possibility that, despite fast gating of mechanosensitive channels [within tens of milliseconds (27, 28)], water exits the cell slowly. This could be the case if the cell envelope changes during growth at high osmolarities in such a way that water can no longer pass as fast. The change in envelope permeability properties with respect to water could be caused by changes in lipid composition of the bilayers, number of porins present in the outer membrane, aquaporin numbers in the inner membrane (AqpZ), as well as changes in the number of any other channels that might be facilitating water transport across the cell envelope. Alternatively, a change in water flux for any (or a combination of) the above-named reasons could occur after initial expansion immediately postdownshock. Fig. 4*A* shows average volume of 13 cells grown in media of 1,370 mOsmol subjected to a sudden upshock of 1,272 mOsmol. Fig. 4*B* shows the average volume of 30 cells grown at 1,370 mOsmol, subjected to a 1,130-mOsmol downshock followed by an immediate 2,160-mOsmol upshock. In both cases, upon the upshock, the cytoplasmic volume shrinks within seconds. Fast reduction of volume shows that water can exit the cell fast in a postdownshock expanded cell. *SI Appendix*, Fig. S6 shows cells grown in media of a different osmolarity, 1,200 mOsmol, subjected to the same sequence of upshocks as in Fig. 4*A*. Cell volume shrinks fast for these cells as well. Thus, the membrane permeability with respect to water does not change with the osmolarity of the growth media or the downshock magnitude.

Model of *E. coli* Response to Downshock Explains Experimentally Observed Volume Changes. To understand the cellular response to a sudden downshock we observed experimentally, we developed the following model. An *E. coli* cell is separated from its environment by the semipermeable membrane. Normally, the solute concentration in a cell is higher than that of the environment, giving rise to osmotic pressure:

$$\Pi = -\phi(c_i - c_e)RT. \quad [1]$$

Here, c_i, c_e, R, and T denote solute concentration inside the cell, solute concentration in the environment, ideal gas constant, and thermodynamic temperature. The constant ϕ is the molar osmotic coefficient (31) (we use osmotically active solute concentrations and set ϕ to 1).

Osmotic pressure in Eq. **1** strains the cell wall, giving rise to mechanical pressure. To quantify it, we consider the elasticity of the cell wall, defined as follows:

$$E = \frac{\text{True stress}}{\text{True strain}} = \frac{d\sigma/l}{dr/r}, \quad [2]$$

where σ is the cell wall tension. We note that, in our model, we take into account only the elasticity of the cell wall, under the assumption that it is significantly larger compared with bilayer(s) elasticity.

For a bacterial cell represented as a cylinder with a thin wall of thickness l, cell wall tension σ is given as the following:

$$\sigma = P \cdot r, \quad [3]$$

where r denotes the cell radius and P is the pressure applied to the cylindrical cell wall. At a given point in time and for a pressurized cell, the volume is set by the balance between osmotic pressure (Π) and mechanical pressure (P) derived from the cell wall strain.

Water moves across the semipermeable cell membrane in accordance with the chemical potential gradient; therefore, water flux is given as the following:

$$j \propto -\Pi - P. \quad [4]$$

We assume that the periplasmic space is in equilibrium with the external environment throughout our considerations [the outer membrane contains large number of porins (32)].

Given that osmotic pressure is proportional to the solute concentration difference, we can write the following:

$$\frac{dV}{dt} = V_m j A_c = V_m K \cdot (-\Pi - P). \quad [5]$$

Here, t denotes time, V_m is the molar volume of water, and A_c is the superficial area of the cell. K (moles per pascal·second) is an effective "conductivity" coefficient that characterizes the relationship between pressure difference and flow speed in moles. It depends on the nature of the flow process, which we expect to have both diffusive and quasilaminar components (33). Here, we assume that water flows mainly through porins (AqpZ) and that the total number of AqpZ does not change. Under these assumptions, changes in the surface area of the cell will not increase the water conductance and we keep A_c constant.

To derive the expression for mechanical pressure, P, we take into account recent experiments depicting cell wall stress stiffening (5). Deng et al. (5) found that the elasticity of the cell wall in *E. coli* behaves as $E = E_0(P/P_0)^\gamma$, where $\gamma = 1.22$. Here, we assume $\gamma = 1$, in rough agreement with experimental data and to simplify our model. We note that the assumption does not change the model behavior:

$$E = E_0 P / P_0, \quad [6]$$

where E_0 and P_0 denote elasticity of the cell wall and pressure when cell is at its original volume before the downshock (V_0). From Eqs. **2–6** follows:

$$\frac{E_0 l}{P_0} \cdot \frac{dr}{r^2} = \frac{dP}{P}. \quad [7]$$

Combining Eqs. **1–7**, we get the following (*SI Appendix*):

$$P = e^{\sqrt[3]{\frac{10}{3}\pi}\frac{E_0 l\left(V^{\frac{1}{3}} - V_0^{\frac{1}{3}}\right)}{\Delta c_0 RT V^{\frac{1}{3}} V_0^{\frac{1}{3}}}} \cdot \Delta c_0 RT \frac{V_0^{\frac{1}{3}}}{V^{\frac{1}{3}}}. \quad [8]$$

V denotes the cell volume and Δc_0 is the initial, osmotically active solute concentration difference across the cell membrane, that is, before the downshock.

The expression for osmotic pressure (Eq. **1**) and mechanical pressure (Eq. **8**), as well as Eq. **5** enable us to fully characterize cell volume changes caused by the water flux in and of the cell.

Upon a sudden downshock and before the activation of MSCs, the environmental solute concentration is greatly smaller than the cellular solute concentration. Here, we assume the membrane thickness and the cell surface area do not change considerably; thus, the cell will expand at a fast rate and cell volume conforms to the following:

$$\frac{dV}{dt} = V_m K R T \left[\left(\frac{n_i}{V} - c_e \right) - e^{\frac{\sqrt[3]{\frac{10}{3}\pi} \frac{E_0 l \left(V^{\frac{1}{3}} - V_0^{\frac{1}{3}} \right)}{\Delta c_0 R T V^{\frac{1}{3}} V_0^{\frac{1}{3}}}} \cdot \Delta c_0 \frac{V_0^{\frac{1}{3}}}{V^{\frac{1}{3}}} \right]. \quad [9]$$

Upon reaching a critical value, V_{th}, mechanosensitive channels open and cell volume can be described as follows:

$$\frac{dV}{dt} = (A+1) \cdot \frac{dV'}{dt}, \quad [10]$$

where dV'/dt is the dV/dt given in Eq. **9** and we use A to characterize the relative conductivity of the membrane with opened channels. For example, $A = 2$ gives 3 times higher conductivity compared with the cell membrane with closed mechanosensitive channels.

At the point of channel opening, the water chemical potential difference is still large, with the inside lower than the outside. Thus, more water rushes into the cell through newly opened holes (Fig. 5*B*, *Left*). We note that water can flow both in and out of the cell through the channels, whose individual size reaches $\approx$ 3 nm upon opening (34, 35). During this period, the osmotic pressure inside the cell further increases, as the inward flow of water exceeds the outward flow of cytoplasmic solutes (Fig. 5*B*, *Left*). At the critical point at which Eq. **10** equals zero, inward pressure starts pushing both the water and the solutes out of the cell.

Simultaneously, the opening of mechanosensitive channels rendered the cell membrane permeable to solutes, which causes solute flux down the solute chemical potential:

$$j_s = D_s \frac{\partial c_s}{\partial x}, \quad [11]$$

where D_s is the diffusion coefficient of solutes and c_s is solute concentration. Taking into account the number of mechanosensitive channels (N_{MSC}) and the cross-sectional area of a representative mechanosensitive channel (a_{MSC}), we get the inner solutes outward flow (Fig. 5*B* and *SI Appendix*):

$$\frac{dn_i}{dt} = -AV_m K \cdot \frac{n_i}{V} \cdot e^{\frac{\sqrt[3]{\frac{10}{3}\pi} \frac{E_0 l \left(V^{\frac{1}{3}} - V_0^{\frac{1}{3}} \right)}{\Delta c_0 R T V^{\frac{1}{3}} V_0^{\frac{1}{3}}}} \cdot \Delta c_0 R T \frac{V_0^{\frac{1}{3}}}{V^{\frac{1}{3}}} - AD_s N_{MSC} a_{MSC} \cdot \frac{\frac{n_i}{V} - c_0}{l_M}, \quad [12]$$

where n_i denotes the total amount of internal solutes in moles and l_M is the thickness of the cell membrane. We substitute the unknown parameters of the solute diffusion (D_s) and channel number (N_{MSC}) with a combined chemical flow parameter α normalized to the initial volume V_0:

$$\alpha = \frac{D_s N_{MSC} a_{MSC}}{l_M \cdot V_0}. \quad [13]$$

We thus have the following:

$$\frac{dn_i}{dt} = -AV_m K \cdot \frac{n_i}{V} \cdot e^{\frac{\sqrt[3]{\frac{10}{3}\pi} \frac{E_0 l \left(V^{\frac{1}{3}} - V_0^{\frac{1}{3}} \right)}{\Delta c_0 R T V^{\frac{1}{3}} V_0^{\frac{1}{3}}}} \cdot \Delta c_0 R T \frac{V_0^{\frac{1}{3}}}{V^{\frac{1}{3}}} - A\alpha V_0 \cdot \left(\frac{n_i}{V} - c_0 \right). \quad [14]$$

As the solutes exit, the outward flow becomes larger than the inward flow of water and the cell begins to shrink. At the same time, the overall concentration difference decreases further (Fig. 5*B*).

V_{th}, the volume at which MSCs open and close, is expected to be the same (13). Thus, our model predicts that, to reach the cell volume that is smaller than initial, as experimentally observed in Figs. 2 and 3, V_{th} needs to be small.

The qualitative predictions of our model are given in Fig. 5*B* and results of the fit to the Eqs. **10** and **14** in Fig. 5*D*, *Top*, and *SI Appendix*, Table S2. We chose a representative trace of 960-mOsmol downshock and used four parameters during the fitting routine (*Materials and Methods*): A, V_{th}, α, and K. Some of the parameters in our equations are physical quantities that have been experimentally estimated, and we used these estimates to fix them (*SI Appendix*, Table S2). For example, we experimentally measured $V_0 = 1.3 \pm 0.1$ μm^3. The initial difference between internal and external concentration we used, $\Delta c_0 = 0.04$ Osmol/L, is based on the experimental estimates of turgor pressure and the thickness of the cell wall, l. Measured values for turgor pressure are 300 kPa (7) and 29 kPa (5), so we use the in-between value, 100 kPa, to fix Δc_0. Thickness of the cell wall was measured to be $\approx$ 5 nm (36). For the normalized volume at which the mechanosensitive channels open, best fit yields $V_{th} = 1.04 \pm 0.01$. Fig. 5*C* gives predictions of our model in a scenario where one of the model parameters changes, whereas others are kept fixed. For example, the double-mutant strain is expected to have smaller A and α, as these parameters describe the water and solute conductivity of the membrane with mechanosensitive channels opened. Our model predicts that with smaller A and α, the cell volume expansion increases and overshoot decreases (Fig. 5*C*), as is seen in the double mutant's response to the downshocks (Fig. 2, *Right*). To test our model predictions further, we performed the fit to a representative trace of the double-mutant strain, considering the same shock magnitude as for the wild type (960 mOsmol). Fig. 5*D*, *Bottom*, and *SI Appendix*, Table S3 show the results of the fit. In line with our expectations, A and α obtained from the best fit are smaller in comparison with the wild type. The best fit yields V_{th} for the double mutant is 1.083 ± 0.001. Increase in V_{th} in Fig. 5*C* results in higher cell volume expansion, but smaller overshoot, consistent with double-mutant response in Fig. 2, *Right*. *SI Appendix*, Fig. S7 shows the fit to all of the average traces obtained for the wild type and the double mutant at different shock magnitudes (Fig. 2). Good agreement between the experimental results and the fits are visible across all of the conditions. Fit parameters are plotted against the shock magnitude at the *Bottom* of *SI Appendix*, Fig. S7. A and α are higher for the wild type than the double mutant across all shock magnitudes. The inverse is true for the V_{th}, which is higher for the double mutant compared with the wild type. V_{th} obtained for the wild type at higher shock magnitudes saturates, in agreement with expectations.

Fig. 6*B*, *Left*, shows a prediction from the fit against the experimental data of the representative, wild-type cell volume trace shown in Fig. 5*D* at later time points, that is, minutes after the downshock. At later time points, experimental data show disagreement with the fit predictions.

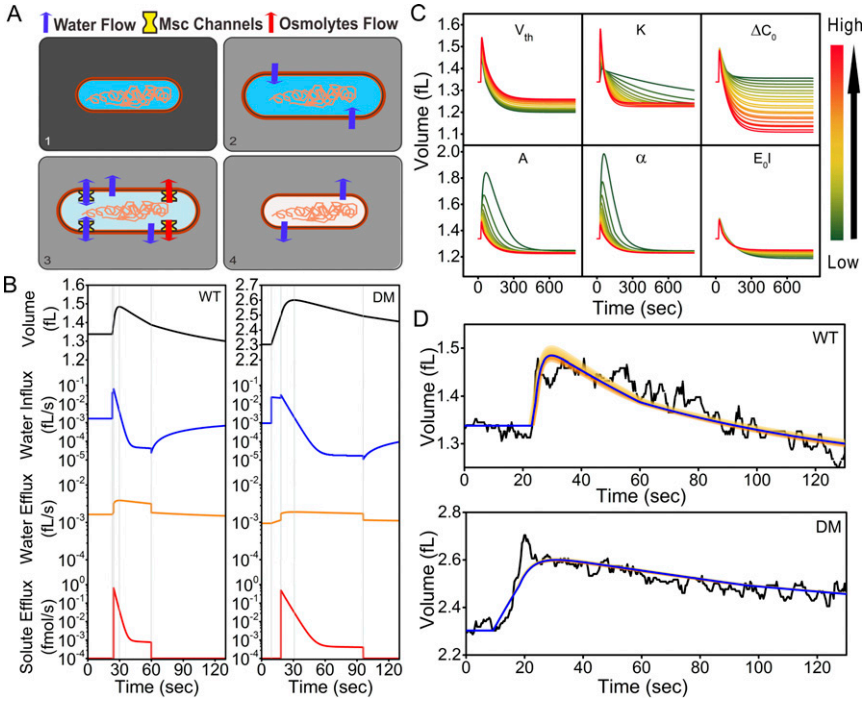

Fig. 5. Model of cellular response to a sudden downshock. (*A*) A sudden decrease in external osmolarity leads to cell volume expansion and opening of mechanosensitive channels (panels 1 and 2). Upon channel opening, the water flux into the cell increases, as the water now flows inward through the channels as well (panel 3, blue arrow). Consequently, solutes exit the cell down the solute chemical potential and due to increased pressure inside the cell (panel 3, blue and red arrows). Solute efflux through the channels tips the competition between water influx and efflux toward efflux, which allows the recovery of cell volume to proceed (panel 4, blue arrow). (*B*) Cell volume (black), water influx (blue), water efflux (orange), and solute efflux (red) are given against time for the wild type (*Left*) and the double mutant (*Right*). All are solutions to the mathematical model equations using four free parameters obtained from the best fit to the representative cell volume trace in 960-mOsmol downshock condition. Eq. **10** was used to plot the cell volume. The first part of Eq. **10** was used for the water influx and the second part of Eq. **10** for the water efflux. Eq. **14** was used for solute efflux. Vertical gray lines indicate following events in sequential order: osmotic shock, opening of the mechanosensitive channels, the point in time when V_{max} is reached, and closing of the channels. (*C*) Cell volume as predicted by the mathematical model given as a function of time. Parameters used in the best fit to the average cell volume in 960-mOsmol downshock condition were varied by ±100% for all parameters. Only one parameter is varied at a time, and the others are kept fixed. Green color indicates the lowest value used, and red, the highest (color scale is given on the *Right*). Increasing V_{th} increases V_{max}, but lowers V_{min}. Increasing α and A decreases V_{max} but increases V_{min}, whereas increasing K and ΔC_0 increases V_{max} and decreases V_{min}, with a stronger effect on the V_{min} reduction. $E_0 l$ increase has little effect on V_{max}, but it decreases V_{min}. (*D*) Representative trace of the wild type (*Top*) and the double mutant (*Bottom*) for the 960-mOsmol condition is given in black. Blue line shows the result of best fit to the average trace. Shaded orange regions show fit confidence intervals; from lighter to darker orange, these are as follows: 50%, 90%, 95%, and 99%. There is a good agreement between the model and the experimental data.

To examine the possibility that the observed disagreement is due to the contribution of active transport processes, we exposed *E. coli* grown in media of 1,130 mOsmol to a sudden downshock by transferring them into sodium phosphate buffer supplemented with 5 mM potassium chloride (Fig. 6*A*). As *E. coli* cannot grow in 5 mM KCl only, the increase of volume observed in phase III in Fig. 6*A* is likely due to active potassium import, presumably by some of the components of the osmoregulatory network responsible for the recovery from a hyperosmotic shock, such as Trk, Kup, and Kdp pumps (2). We also hypothesize that, if the disagreement between our model predictions and the experimental observation is due to active transport processes, cells subjected to a downshock in buffer media will not show an increase in cell volume upon reaching V_{min}. Traces in *SI Appendix*, Fig. S8 show the downshock response of cells in rich modified M9 (MM9) media (taken from Fig. 2) against the cells subjected to the same shock magnitude in the buffer only. Four different shock magnitudes were selected, and in each, phase III of the recovery response is absent in the buffer, in agreement with our hypothesis. We further examined whether the addition of active transport component into our model (*SI Appendix*) recovers phase III observed in the experimental trace in Fig. 5*D*. Fig. 6*B*, *Right*, shows the result of the fit to the extended model. The fit is in very good agreement with the representative experimental trace.

Growth Rate upon Downshock Does Not Depend on the Shock Magnitude. *SI Appendix*, Fig. S9 shows growth rates of individual cells after experiencing and recovering from the downshock of a given magnitude (phase IV, *SI Appendix*, Fig. S2), as well as population growth curves and growth rates of cells grown at high osmolarities (up to OD of 0.25–0.4) and subjected to a sudden downshock (*Materials and Methods*). In both cases, growth rate does not depend on the magnitude of the downshock. Doubling time of individual cells observed in the microscope tunnel slide and the population growth rate measured in the plate reader are similar, 0.6 h^{-1}. *SI Appendix*, Fig. S9*C* shows lag time of population growth curves upon a downshock of a given magnitude. Both the wild type and the double mutant exhibit longer lag times with higher shock magnitudes, where the double-mutant lag time sharply increases for the two largest shocks.

We examined the survival rate of the wild-type and the double-mutant strain to compare them with previous reports (29, 30). We consider a cell to be lysed if during the experimental time its total fluorescent intensity drops to background levels (*Materials and Methods*). *SI Appendix*, Fig. S10*A* shows probability density of a cell lysing during 75-min experimental recording time, for each shock magnitude. In *SI Appendix*, Fig. S10*B*, we classify the wild type, and in *SI Appendix*, Fig. S10*C*, double-mutant cells, into bursters, faders, rupturers, and blebers following previously

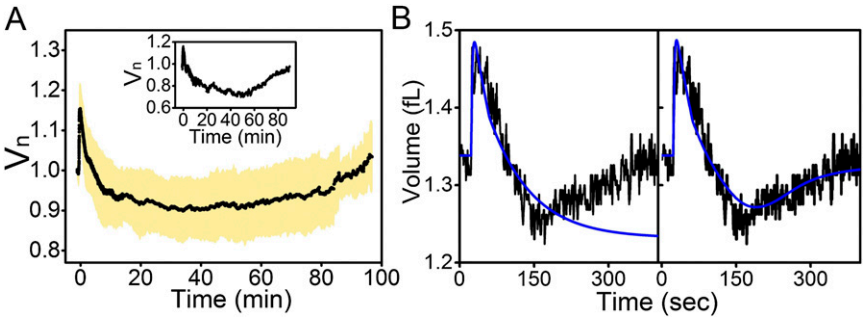

Fig. 6. Active response and postshock growth rates. (*A*) Black line shows average volume against time of 36 wild-type strains exposed to a 1,310-mOsmol downshock. Cells were grown in MM9 supplemented with NaCl and transferred into sodium phosphate buffer supplemented with 5 mM KCl. Shaded orange region indicates SD. Cell volume expanded and recovered, dropping below the initial volume. Within the last 30 min, volume increase is visible. *Inset* shows an example of an individual trace, where volume increase occurs after V_{min} is reached at ≈ 60 min postdownshock. (*B*, *Left*) Wild-type representative trace (black) and the result of the global fit (blue) taken from Fig. 5*D* and shown on a longer timescale. (*Right*) The fit (blue) is performed with the addition of the active pumping component (see *SI Appendix* for details on the extended model) and plotted against the same wild-type representative trace shown on the *Left* and in Fig. 5*D* (black).

described definitions (29). The percentage and type of cell lysis at our local flow rate of 0.68 μL/min is consistent with previously published studies (29). The number of lysed cells is larger for the double mutant, and for the double mutant, lysis starts at lower downshock magnitudes in agreement with previous reports (29, 30).

Discussion

By monitoring changes in volume of individual cells, we were able to explain *E. coli*'s response to sudden decreases in external osmolarity. We found that, upon a sudden downshock, cell volume expands within ≈30 s irrespective of the shock magnitude. The volume expansion increased with shock magnitude and saturated at ≈ 15%. Previous estimates of the material properties of the cell wall used atomic force microscopy to show peptidoglycan expansion of ≈ 12% per 1 atm (37). This estimate is in agreement with our observation. Our results indicate that *E. coli*'s membrane can expand beyond what is expected for a lipid vesicle. The result is in line with a recent study that showed *E. coli*'s spheroplasts can increase their volume by more than three times, presumably by maintaining membrane reservoirs (38).

Despite the fact that mechanosensitive channels open on millisecond timescales, as observed in in vitro experiments (27, 28), the total cell volume recovery is significantly slower, taking minutes to complete. We reasoned that this could be caused by either hindered water transport across *E. coli*'s membrane, as a result of growth at high osmolarity or as a consequence of the downshock, or by slow solute efflux. We found evidence for the latter. Our mathematical model considers postdownshock water and solute transport according to chemical potential difference, and takes into account cell wall stress stiffening properties. The model is in agreement with experimental data and suggests that, postdownshock, water rushes into the cell cytoplasm down the chemical potential gradient. Cell volume expands and increases tension in the cell wall, which results in opening of MSCs. At the point of channel opening, even more water flows into the cell, further increasing wall tension. This effectively pushes the solutes, as well as the water, out of the cell. Furthermore, opening of the channels renders the membrane permeable to the solutes, which now move down the solute chemical potential as well. At a critical point, water no longer enters the cell but starts to exit.

Our experimental traces show clear overshoot during volume recovery that increases with shock magnitude. The observation suggests relatively low threshold for channel opening and closing. The fit of the representative trace in Fig. 5*D* to the equations in our mathematical model predicts that MSC channels open/close at 4% volume expansion in the wild-type strain. This is a relatively small value given the extent of maximum volume expansion we observe (15%). In the model we have assumed, guided by the in vitro studies, that MSCs open and close at the same lipid bilayer tension (13). The V_{th} value predicted by the model is thus a result of balancing the observed $V_{n,max}$ with V_{min}. However, it is possible that, in a live cell, the V_{th} at which the channels open and close is not the same; in particular, because the response is the combined effect of seven different MSCs, where the number of individual channels of a given type can vary, and cooperative channel gating effects are possible (39–41).

When comparing the volume expansion of the mutant strain lacking MscL and MscS to that of the wild type, we found no difference for shocks up to 790 mOsmol, at which point the double-mutant strain expanded slightly more (≈ 20%) and slightly faster. Larger and faster expansion is consistent with our model. In the wild-type strain, the peak volume expansion is reached several seconds later compared with the double mutant, as upon opening of MSCs water influx competes with solute efflux and water efflux. In the double mutant, there is far less of such competition. Consequently, the water influx upon the downshock is larger and the cell volume expands more.

Overall, we found the most obvious differences between the double-mutant and the wild-type response at large shocks. The result is in agreement with previous population studies (30). However, small differences between the response of the wild-type and the double-mutant strain are visible even for smaller shocks. For example, some overshoot is observed even for smaller shocks in the wild-type strain, but none is visible in the double-mutant response. For shocks of ≥790 mOsmol, double mutant showed no growth within the 35-min observation period. At this point, we do not understand the nature of the damage caused by the absence of MscS and MscL, nor whether it is reversible. However, our results show that lack of MscS and MscL does not result solely in instant rupture or bursting. In fact, most of the nongrowing double-mutant cells that were subjected to 960- and 1,130-mOsmol downshock do not show any obvious damage as observed by fluorescent microscopy. It is possible that these cells continue growth, but at a later time.

Based on our fit parameters in the case of the wild-type trace given in Fig. 5*D*, MSCs will open at 4% volume increase, which corresponds to an increase in cell wall and membrane tension of ≈ 7 mN/m, which is in rough agreement with the in vitro measurements of channel opening membrane tensions, usually 5–15 mN/m (42, 43). At our measured V_{max}, and based on our fit parameters, the cell wall and the inner, outer membrane tension increases by ≈ 30 mN/m.

Our study reveals the main characteristics of *E. coli*'s passive response to downshock, namely, fast volume expansion followed by a

slow volume recovery that can overshoot below the preshock volume. Additionally, we observed a degree of cell-to-cell variability, not only for cells exposed to a given downshock but also when comparing the trends between different shock magnitudes. The observed heterogeneity may be expected, as recent studies show significant variation in MscL numbers within the population, as well as between different growth conditions (including growth on glucose in different external osmolarities) (39). Apart from MscL, the case could be similar for the six other MSCs in *E. coli*. Additionally, for the large number of MscL channels measured (up to $\approx$ 1,000) (39), cooperative gating is possible (40) and could further increase cell-to-cell variability in the overall downshock responses.

Materials and Methods

Construction of *E. coli* Strains. Strains BW25113 with pWR20 and ΔMscLΔMscS (double mutant) with pWR21 plasmid were used in the study for single-cell fluorescent microscopy experiments. BW25113 is the Keio collection parent strain (44). The plasmids pWR20 and pWR21 carry genes for constitutive expression of enhanced green fluorescent protein (eGFP) and kanamycin (kan) or ampicilin (amp) resistance, respectively (3). ΔMscLΔMscS strain was constructed from BW25113 single-knockout strains with the *mscL* or *mscS* genes replaced with kan cassette (available from Keio collection) (44). After PCR verification of both single mutants, kan resistant *mscL* mutant was transformed with pCP20 plasmid to eliminate the antibiotic resistance (45). The deletion of the kan cassette and the plasmid curing was verified by kanamycin, chloramphenicol, and ampicillin sensitivity tests. Subsequently, P1 vir lysate was prepared from ΔMscS strain carrying kan cassette, here used as the donor, for the transfection of the recipient strain, ΔMscL. P1 transductants were plated onto selective media (LB containing 50 $\mu g \cdot mL^{-1}$ kanamycin). ΔMscLΔMscS strain was verified by PCR and transformed with pWR21 plasmid.

***E. coli* Growth and Culturing.** *E. coli* strains were grown from frozen stocks (made from single colonies) in MM9 medium with 0.3% glucose, MEM essential amino acids (Sigma Aldrich), and supplemented with 0, 50, 125, 225, 300, 450, 550, 650, or 750 mM NaCl at 37 °C to an OD of 0.2–0.4, aerobically with shaking (see also *SI Appendix* for media osmolarities). MM9 is of the same composition as M9 (46) except sodium phosphate buffer only was used, and the media were supplemented with 1 mM KCl. MM9 was chosen over M9 to allow adjustment of potassium concentration from zero to the desired value. Media was supplemented with 50 μg/mL kanamycin. Upon reaching OD of 0.2–0.4, cells were kept at room temperature and used for sample preparation for up to 4 h (up to maximum OD of 0.65). For *SI Appendix*, Fig. S5, cells were grown as above except in MM9 supplemented with 450 mM sucrose. Growth curves in *SI Appendix*, Fig. S9 were obtained as follows: 300 μL of MM9 medium supplemented with 50, 125, 225, 300, 450, 550, 650, or 750 mM NaCl was inoculated with 2 μL of wild-type and double-mutant cells from frozen stock. OD was measured in a plate reader (BMG) every 7.5 min at 37 °C, until stationary phase. To obtain growth curves after the downshock, cells were initially inoculated as above. At an early exponential phase (OD, 0.2–0.35), 2 μL of cells from each growth media were transferred into a well with MM9 medium with no additional salt. OD was measured every 7.5 min until stationary phase.

Microscopy. Cells were observed in epifluorescence using a Nikon Eclipse Ti microscope with perfect focus (4) at 21 °C. At the beginning of each experiment, a field of view with 10 or more "flat" cells was chosen as described in ref. 3 (*SI Appendix*). Images of cells expressing eGFP were acquired at an exposure time of 0.1 s using a 512 × 512 pixel back-thinned electron-multiplying charge-coupled device camera (Andor Technologies). Epi-illumination light was shuttered in-between image recordings to reduce photobleaching (*SI Appendix*, Fig. S11). Images were captured at every 0.2 or 0.375 s during the first 15 min and every 5 s for the rest of the recordings. Total recording time was up to 75 min.

Sample Preparation and Osmotic Shock. Microscope tunnel slide was prepared as in ref. 47; cells were attached to the coverslip surface as in ref. 48; and to administer a sudden osmotic shock (either downshock or upshock), the tunnel is flushed with 25 μL of the low- or high-osmolarity medium, with an average rate of 2.5 μ/L as in refs. 3 and 47. To characterize the characteristic noise in the downshock experiment, we performed a control flush. The 3D histogram in *SI Appendix*, Fig. S11, obtained from cells grown in MM9 and flushed with MM9, shows that the noise magnitude is small for the scale of volume changes we are observing. Osmotic shocks in microfuge tubes were performed in two different ways as follows. (*i*) Cells from grown cell culture were imaged in a tunnel slide before the downshock; no attachment was used. A volume of 1.3 mL of cell culture was then spun down, and growth medium was removed. Tunnel slide was prepared as above and placed in the microscope. Cells were downshocked by adding 0.1 mL of MM9. A volume of 10 μL of downshocked cells was flushed into the tunnel slide. Thirty different fields of view were chosen, and cells were imaged at a frame every 1 min for 1.5 h. (*ii*) Several different tunnel slides were prepared before start of the experiment. Cells from the growth culture were imaged before the downshock with no attachment. A volume of 1 mL of cell culture was spun down, and growth medium was removed. Cells were shocked into 1 mL of MM9 and kept in the microfuge tube. At 2.5, 10, 20, and 30 min postdownshock, samples were added to the prepared tunnel slides for imaging.

Speed of Local Flow for Downshock Delivery. A green fluorescent dye [10 μM Sodium Green (Molecular Probes) prepared in 10 mM Tris buffer] was used to determine the local speed of downshock delivery. Microscope tunnel slide was prepared as described above. A sudden shock was administered by flushing 25 μL of Sodium Green dye through the channel at an average flow rate of 2.5 μL/s while recording at a frame every 0.2 s. The dye was both flushed in and subsequently flushed out several times. To obtain the local flow rate close to the coverslip surface, we started with transforming fluorescent intensity in arbitrary units to microliters by taking into account the size of the field of view, the number of pixels in the image frame, and the size of the channel. Next, the difference in intensity between two adjacent frames was calculated to get the flux across a unit surface. We obtained the local flow rate of 0.68 μL/min as an average of the linear fits of the intensity profiles given in *SI Appendix*, Fig. S12.

Image Analysis. Data analysis was performed on cells uniformly attached to the coverslip surface ("flat" cells) by a process of background subtraction and thresholding as described in ref. 3 and *SI Appendix*. Cells stuck to the surface were assumed to be a spherocylinder (2 μm long and 1 μm in diameter) and cell area obtained from image analysis was converted to volume according to the following formula: $V(t) = S(t)^{3/2} \cdot (((10/3) \cdot \pi)/((4+\pi)^{3/2}))$ (*SI Appendix*, Fig. S11). When analyzing cells that were downshocked in the microfuge tube and imaged with no surface attachment, cells that were close to the coverslip surface and did not move significantly were chosen for time-lapse analysis.

Singe-Cell Data Analysis. Traces recorded at a frame every 0.2 s were resampled to 0.375 s and further analyzed with the traces recorded at 0.375 s. Volume traces obtained upon image analysis were normalized. We used average volume of first five data points, corresponding to the first 1.8 s of recording. Next, normalized traces were passed through a median filter with the width of 5 points per window frame. Normalized and filtered traces were aligned by T_{max} in phase I. Total of 609 cells was analyzed for the wild type, and 480 for the double mutant. To obtain the growth rate from single-cell measurements in *SI Appendix*, Fig. S9*B*, we analyzed the phase IV part of the average traces given in *SI Appendix*, Fig. S1. The part of the trace starting at the beginning of phase IV, that is, when cell volume reaches 1, was fitted to an exponential. To obtain the cumulative bar diagrams in *SI Appendix*, Fig. S10, we used definitions of cell lysis types described before (29). We assumed a cell to be lysed if the cell's fluorescent intensity dropped to background level during our observation. The cells that lysed during our recording were included in the V_{max} analysis only, but excluded from the rest of our analysis. $V_{n,max}$ is the average value around the absolute maximum value identified in each trace (we averaged 5 points either side of the maximum value). T_{max} is the difference between the start of the shock and the point in time $V_{n,max}$ is reached. To identify $V_{n,min}$ and T_{min} in the wild-type traces, we apply a running window (10 points wide) starting from T_{max} and identify the minimum position within the trace. The double-mutant traces often leveled off rather than continuously decreased. Thus, we modified our algorithm and identified if the average value of the current running window decreases below the average value plus 3 SDs of the neighboring window. Once the condition is no longer satisfied, $V_{n,min}$ (and T_{min}) in the trace has been reached.

Growth Curve Analysis. OD measurements were converted to cell density as follows. Thirty wells of 200 μL of bacterial culture were grown to OD of 0.15 in MM9 medium. The wells were pooled, and 125 μg/mL chloramphenicol was added to inhibit further cell division or growth. Cells were then concentrated to ~20× initial concentration, diluted down to 0.0625, 0.125, 0.25, 0.5, 1, 2, 3, 5, 7, 10, and 11 times initial concentration. OD was measured in the plate reader using the same conditions as the growth curves. Cells at 1× concentration were counted using bright-field illumination and in a tunnel slide of known height (100 μm) to give the true cell density. Obtained calibration curve is given in *SI Appendix*, Fig. S13. A second-degree

polynomial was used to convert the growth curve ODs to cell number ($N = 2.2 \cdot 10^8 OD^2 + 1.45 \cdot 10^9 OD + 2 \cdot 10^6$) (49). Calibrated growth curves were fitted using a Gaussian fitting algorithm (50) to give both the maximum growth rate and lag time as defined by the tangent to the inflection point in each condition shown in *SI Appendix*, Fig. S9.

Model Fitting Procedures. To simulate the model, Eqs. **10** and **14** were used to calculate the volume and moles of internal solute during the downshock. To provide the initial volume for the model, we used the measured V_0, and the initial value for n_i was based on previously published results (7). The opening of mechanosensitive channels was simulated by a conditional statement such that when $V/V_0 > V_{th}$ A is positive, and zero otherwise. An adaptive Markov chain Monte Carlo sampling procedure (51) was used to fit the model to the averaged wild-type and double-mutant traces for the 960-mOsmol downshock. During fitting, simulation of the model was performed by the ode function in Matlab (52). Fig. 5*D* shows the posterior confidence intervals of 50,000 simulations that comprised the Markov chain for the final parameters listed in *SI Appendix*, Tables S2 and S3. Upon obtaining the best fit, we used the fit parameters to generate Fig. 5*B*. Water influx was obtained from the first part of the Eq. **9** before channels open and Eq. **10** after. Similarly, water efflux was obtained from the second part of Eq. **9** and Eq. **10**. Solute efflux was obtained from Eq. **14**. To obtain Fig. 5*C*, we have varied the parameters obtained from the best fit to the wild-type data by ±100% for all parameters, with a step size of 10%. Total cellular volume was plotted by solving Eq. **10**.

ACKNOWLEDGMENTS. We thank all of the members of T.P. and F.B. laboratories for their comments and support, and Meriem El Karoui for granting access to her microscope during the course of the project. R.B. was supported through a Biotechnology and Biological Sciences Research Council (BBSRC) Crossing Biological Membranes Network (CBMNet) Scholarship; Y.L., J.Y., and F.B. by National Natural Science Foundation of China Grant 31370847, Recruitment Program of Global Youth Experts, and Human Frontier Science Program Grant RGP0041/2015; T.P. by BBSRC CBMNet and Human Frontier Science Program Grant RGP0041/2015; S.H. by the Darwin Trust and Industrial Biotechnology Innovation Centre grant (to T.P.); and K.S. by the BBSRC Industrial Collaborative Awards in Science and Engineering grant (to T.P.).

1. Koch AL (1985) How bacteria grow and divide in spite of internal hydrostatic pressure. *Can J Microbiol* 31(12):1071–1084.
2. Wood JM (2015) Bacterial responses to osmotic challenges. *J Gen Physiol* 145(5): 381–388.
3. Pilizota T, Shaevitz JW (2012) Fast, multiphase volume adaptation to hyperosmotic shock by *Escherichia coli*. *PLoS One* 7(4):e35205.
4. Pilizota T, Shaevitz JW (2014) Origins of *Escherichia coli* growth rate and cell shape changes at high external osmolality. *Biophys J* 107(8):1962–1969.
5. Deng Y, Sun M, Shaevitz JW (2011) Direct measurement of cell wall stress stiffening and turgor pressure in live bacterial cells. *Phys Rev Lett* 107(15):158101.
6. Booth IR, Blount P (2012) The MscS and MscL families of mechanosensitive channels act as microbial emergency release valves. *J Bacteriol* 194(18):4802–4809.
7. Cayley DS, Guttman HJ, Record MT, Jr (2000) Biophysical characterization of changes in amounts and activity of *Escherichia coli* cell and compartment water and turgor pressure in response to osmotic stress. *Biophys J* 78(4):1748–1764.
8. Corry B, Martinac B (2008) Bacterial mechanosensitive channels: Experiment and theory. *Biochim Biophys Acta* 1778(9):1859–1870.
9. Kung C, Martinac B, Sukharev S (2010) Mechanosensitive channels in microbes. *Annu Rev Microbiol* 64:313–329.
10. Martinac B, Kloda A (2012) Mechanosensory transduction. *Comprehensive Biophysics*, ed Egelman EH (Elsevier, Amsterdam), pp 108–141.
11. Sackin H (1995) Mechanosensitive channels. *Annu Rev Physiol* 57:333–353.
12. Pak OS, Young YN, Marple GR, Veerapaneni S, Stone HA (2015) Gating of a mechanosensitive channel due to cellular flows. *Proc Natl Acad Sci USA* 112(32):9822–9827.
13. Edwards MD, et al. (2012) Characterization of three novel mechanosensitive channel activities in *Escherichia coli*. *Channels (Austin)* 6(4):272–281.
14. Berrier C, Besnard M, Ajouz B, Coulombe A, Ghazi A (1996) Multiple mechanosensitive ion channels from *Escherichia coli*, activated at different thresholds of applied pressure. *J Membr Biol* 151(2):175–187.
15. Booth IR, Edwards MD, Miller S (2003) Bacterial ion channels. *Biochemistry* 42(34): 10045–10053.
16. Schumann U, et al. (2010) YbdG in *Escherichia coli* is a threshold-setting mechanosensitive channel with MscM activity. *Proc Natl Acad Sci USA* 107(28):12664–12669.
17. Li Y, Moe PC, Chandrasekaran S, Booth IR, Blount P (2002) Ionic regulation of MscK, a mechanosensitive channel from *Escherichia coli*. *EMBO J* 21(20):5323–5330.
18. Martinac B, Buechner M, Delcour AH, Adler J, Kung C (1987) Pressure-sensitive ion channel in *Escherichia coli*. *Proc Natl Acad Sci USA* 84(8):2297–2301.
19. Chang G, Spencer RH, Lee AT, Barclay MT, Rees DC (1998) Structure of the MscL homolog from *Mycobacterium tuberculosis*: A gated mechanosensitive ion channel. *Science* 282(5397):2220–2226.
20. Bass RB, Strop P, Barclay M, Rees DC (2002) Crystal structure of *Escherichia coli* MscS, a voltage-modulated and mechanosensitive channel. *Science* 298(5598):1582–1587.
21. Perozo E, Cortes DM, Sompornpisut P, Kloda A, Martinac B (2002) Open channel structure of MscL and the gating mechanism of mechanosensitive channels. *Nature* 418(6901):942–948.
22. Sukharev SI, Sigurdson WJ, Kung C, Sachs F (1999) Energetic and spatial parameters for gating of the bacterial large conductance mechanosensitive channel, MscL. *J Gen Physiol* 113(4):525–540.
23. Sukharev S, Betanzos M, Chiang CS, Guy HR (2001) The gating mechanism of the large mechanosensitive channel MscL. *Nature* 409(6821):720–724.
24. Blount P, et al. (1996) Membrane topology and multimeric structure of a mechanosensitive channel protein of *Escherichia coli*. *EMBO J* 15(18):4798–4805.
25. Ou X, Blount P, Hoffman RJ, Kung C (1998) One face of a transmembrane helix is crucial in mechanosensitive channel gating. *Proc Natl Acad Sci USA* 95(19):11471–11475.
26. Hamill OP, Marty A, Neher E, Sakmann B, Sigworth FJ (1981) Improved patch-clamp techniques for high-resolution current recording from cells and cell-free membrane patches. *Pflugers Arch* 391(2):85–100.
27. Chiang CS, Anishkin A, Sukharev S (2004) Gating of the large mechanosensitive channel in situ: Estimation of the spatial scale of the transition from channel population responses. *Biophys J* 86(5):2846–2861.
28. Boer M, Anishkin A, Sukharev S (2011) Adaptive MscS gating in the osmotic permeability response in *E. coli*: The question of time. *Biochemistry* 50(19):4087–4096.
29. Bialecka-Fornal M, Lee HJ, Phillips R (2015) The rate of osmotic downshock determines the survival probability of bacterial mechanosensitive channel mutants. *J Bacteriol* 197(1):231–237.
30. Levina N, et al. (1999) Protection of *Escherichia coli* cells against extreme turgor by activation of MscS and MscL mechanosensitive channels: Identification of genes required for MscS activity. *EMBO J* 18(7):1730–1737.
31. Dick DAT (1966) *Cell Water* (Butterworths, London), pp 16–25.
32. Hancock RE (1987) Role of porins in outer membrane permeability. *J Bacteriol* 169(3):929–933.
33. Mauro A (1957) Nature of solvent transfer in osmosis. *Science* 126(3267):252–253.
34. Wang Y, et al. (2014) Single molecule FRET reveals pore size and opening mechanism of a mechano-sensitive ion channel. *eLife* 3:e01834.
35. Louhivuori M, Risselada HJ, van der Giessen E, Marrink SJ (2010) Release of content through mechano-sensitive gates in pressurized liposomes. *Proc Natl Acad Sci USA* 107(46):19856–19860.
36. Yao X, et al. (2002) Atomic force microscopy and theoretical considerations of surface properties and turgor pressures of bacteria. *Colloids Surf B Biointerfaces* 23(2):213–230.
37. Yao X, Jericho M, Pink D, Beveridge T (1999) Thickness and elasticity of Gram-negative murein sacculi measured by atomic force microscopy. *J Bacteriol* 181(22):6865–6875.
38. Sun Y, Sun TL, Huang HW (2014) Physical properties of *Escherichia coli* spheroplast membranes. *Biophys J* 107(9):2082–2090.
39. Bialecka-Fornal M, Lee HJ, DeBerg HA, Gandhi CS, Phillips R (2012) Single-cell census of mechanosensitive channels in living bacteria. *PLoS One* 7(3):e33077.
40. Ursell T, Huang KC, Peterson E, Phillips R (2007) Cooperative gating and spatial organization of membrane proteins through elastic interactions. *PLoS Comput Biol* 3(5):e81.
41. Grage SL, et al. (2011) Bilayer-mediated clustering and functional interaction of MscL channels. *Biophys J* 100(5):1252–1260.
42. Belyy V, Kamaraju K, Akitake B, Anishkin A, Sukharev S (2010) Adaptive behavior of bacterial mechanosensitive channels is coupled to membrane mechanics. *J Gen Physiol* 135(6):641–652.
43. Sukharev S (2002) Purification of the small mechanosensitive channel of *Escherichia coli* (MscS): The subunit structure, conduction, and gating characteristics in liposomes. *Biophys J* 83(1):290–298.
44. Baba T, et al. (2006) Construction of *Escherichia coli* K-12 in-frame, single-gene knockout mutants: The Keio collection. *Mol Syst Biol* 2:2006.0008.
45. Datsenko KA, Wanner BL (2000) One-step inactivation of chromosomal genes in *Escherichia coli* K-12 using PCR products. *Proc Natl Acad Sci USA* 97(12):6640–6645.
46. Cold Spring Harbor Laboratory (2010) M9 minimal medium (standard). *Cold Spring Harb Protoc*, 10.1101/pdb.rec12295.
47. Pilizota T, Shaevitz JW (2013) Plasmolysis and cell shape depend on solute outer-membrane permeability during hyperosmotic shock in *E. coli*. *Biophys J* 104(12):2733–2742.
48. Pilizota T, et al. (2009) A molecular brake, not a clutch, stops the *Rhodobacter sphaeroides* flagellar motor. *Proc Natl Acad Sci USA* 106(28):11582–11587.
49. Koch AL (1970) Turbidity measurements of bacterial cultures in some available commercial instruments. *Anal Biochem* 38(1):252–259.
50. Swain PS, et al. (2016) Inferring time-derivatives, including cell growth rates, using Gaussian processes. *BioRxiv*, 10.1101/055483.
51. Haario H, Laine M, Mira A, Saksman E (2006) DRAM: Efficient adaptive MCMC. *Stat Comput* 16(4):339–354.
52. The MathWorks, Inc. (2015) *MATLAB and Statistics Toolbox Release* (The MathWorks, Inc., Natick, MA).

Supporting Information

Deduction of mechanical pressure. The deduction of mechanical pressure in main text is as follows. Cell wall tension is given as:

$$\sigma = P \cdot r \tag{1}$$

where we annotate tension before the downshock as

$$\sigma_0 = P_0 \cdot r_0 \tag{2}$$

Cell wall elasticity as given in the main text is:

$$E = E_0 P / P_0 \tag{3}$$

Thus, we have:

$$E \cdot \frac{dr}{r} = \frac{d\sigma}{l} \tag{4}$$

After integrating the above, we get:

$$\frac{E_0 \sigma \cdot dr}{P_0 r^2} = \frac{d\sigma}{l} \tag{5}$$

With rearrangement we have:

$$\frac{E_0 l \cdot dr}{P_0 r^2} = \frac{d\sigma}{\sigma} \tag{6}$$

Upon integrating (6) we have:

$$ln(\sigma/\sigma_0) = \frac{E_0 l}{P_0} \cdot \frac{r - r_0}{r_0 r} \tag{7}$$

The equation (7) is then written in the exponential form:

$$\sigma/\sigma_0 = e^{\frac{E_0 l}{P_0} \cdot \frac{r - r_0}{r_0 r}} \tag{8}$$

We assume a typical cell is a cylinder with length of $2r$ which is capped by two hemispheres with the radius of r. Thus, the volume of such a cell is:

$$V = \frac{10}{3}\pi r^3 \tag{9}$$

Similarly, initial cell volume is

$$V_0 = \frac{10}{3}\pi r_0^3 \tag{10}$$

From equation (9) and (10) we get

$$r = \frac{V^{\frac{1}{3}}}{\sqrt[3]{\frac{10}{3}\pi}} \tag{11}$$

$$r_0 = \frac{V_0^{\frac{1}{3}}}{\sqrt[3]{\frac{10}{3}\pi}} \tag{12}$$

Combining equation (8), (11) and (12) we get:

$$\sigma/\sigma_0 = e^{\sqrt[3]{\frac{10}{3}\pi}\frac{E_0 l}{P_0} \cdot \frac{V^{\frac{1}{3}} - V_0^{\frac{1}{3}}}{V_0^{\frac{1}{3}} V^{\frac{1}{3}}}} \tag{13}$$

From (1), (2) and (13) we further have:

$$(P \cdot V^{\frac{1}{3}})/(P_0 \cdot V_0^{\frac{1}{3}}) = e^{\sqrt[3]{\frac{10}{3}\pi}\frac{E_0 l}{P_0} \cdot \frac{V^{\frac{1}{3}} - V_0^{\frac{1}{3}}}{V_0^{\frac{1}{3}} V^{\frac{1}{3}}}} \tag{14}$$

The initial pressure is determined by the initial difference between cellular and environmental solute osmolarity:

$$P_0 = \phi \cdot \Delta c_0 RT \tag{15}$$

Finally, combining equation (14) and (15) we have:

$$P = e^{\sqrt[3]{\frac{10}{3}\pi}\frac{E_0 l}{P_0}\cdot\frac{V^{\frac{1}{3}}-V_0^{\frac{1}{3}}}{V_0^{\frac{1}{3}}V^{\frac{1}{3}}}}\cdot\Delta c_0 RT\frac{V_0^{\frac{1}{3}}}{V^{\frac{1}{3}}} \tag{16}$$

Deduction of the time dependent cell volume change. Water flows across the cell membrane in accordance with the water chemical potential gradient, thus the water flux is given as follows:

$$j \propto -\Pi - P \tag{17}$$

The molar speed of water flux across the whole cell membrane is given as:

$$\frac{dn_W}{dt} = jA_c \tag{18}$$

After multiplication with the molar volume of water, the molar water flux becomes the cell volume change:

$$\frac{dV}{dt} = V_m\frac{dn_W}{dt} = V_m jA_c \tag{19}$$

Given that we assume A_c is constant through out the experiments, we write:

$$jA_c = K\cdot(-\Pi - P) \tag{20}$$

Combining (19) and (20) we get:

$$\frac{dV}{dt} = V_m K\cdot(-\Pi - P) \tag{21}$$

Given the expression for osmotic pressure:

$$\Pi = -\phi(c_i - c_e)RT \tag{22}$$

and the expression for mechanical pressure on the cell wall:

$$P = e^{\sqrt[3]{\frac{10}{3}\pi}\frac{E_0 l(V^{\frac{1}{3}}-V_0^{\frac{1}{3}})}{\Delta c_0 RTV^{\frac{1}{3}}V_0^{\frac{1}{3}}}}\cdot\Delta c_0 RT\frac{V_0^{\frac{1}{3}}}{V^{\frac{1}{3}}} \tag{23}$$

For the case of closed MSCs we get the expression for cell volume change by combining (21), (22) and (23):

$$\frac{dV}{dt} = V_m KRT((\frac{n_i}{V} - c_e) - e^{\sqrt[3]{\frac{10}{3}\pi}\frac{E_0 l(V^{\frac{1}{3}}-V_0^{\frac{1}{3}})}{\Delta c_0 RTV^{\frac{1}{3}}V_0^{\frac{1}{3}}}}\cdot\Delta c_0\frac{V_0^{\frac{1}{3}}}{V^{\frac{1}{3}}}) \tag{24}$$

When MSCs open, water conductivity across the membrane is A times higher compared to the case when MSCs are closed:

$$\frac{dV}{dt} = (A+1)\cdot V_m KRT((\frac{n_i}{V} - c_e) - e^{\sqrt[3]{\frac{10}{3}\pi}\frac{E_0 l(V^{\frac{1}{3}}-V_0^{\frac{1}{3}})}{\Delta c_0 RTV^{\frac{1}{3}}V_0^{\frac{1}{3}}}}\cdot\Delta c_0\frac{V_0^{\frac{1}{3}}}{V^{\frac{1}{3}}}) \tag{25}$$

Deduction of inner solute outward flow. Flow of solutes upon MSCs opening is driven by (1) mechanical pressure, which is the second part in equation (21) multiplied by the concentration of solutes, and (2) diffusion.

$$\frac{dn_i}{dt} = AV_m K\cdot(-P)\cdot\frac{n_i}{V} - Aj_s S \tag{26}$$

Here j_s is the diffusion flux of solutes per surface area (S).

$$j_s = D_s\cdot\frac{\partial c_x}{\partial x} \tag{27}$$

$$S = N_{MSC}\cdot A_{MSC} \tag{28}$$

After combining (23), (26), (27) and (28) we get:

$$\frac{dn_i}{dt} = -AV_m K\cdot\frac{n_i}{V}\cdot e^{\sqrt[3]{\frac{10}{3}\pi}\frac{E_0 l(V^{\frac{1}{3}}-V_0^{\frac{1}{3}})}{\Delta c_0 RTV^{\frac{1}{3}}V_0^{\frac{1}{3}}}}\cdot\Delta c_0 RT\frac{V_0^{\frac{1}{3}}}{V^{\frac{1}{3}}} - AD_s N_{MSC}a_{MSC}\cdot\frac{\frac{n_i}{V}-c_0}{l_M} \tag{29}$$

Expanding the model to include active transport component. We assume that when cell volume drops to a certain value below the initial volume, V_{AT}, the cell starts to import solutes via active transport. The active transport 'speed' is given by the constant K_{AT}, which is proportional to the difference between cell volume and the threshold volume for active pumping ($V_{AT} \cdot V_0 - V$). Thus the speed at which active pumping occurs can be written as:

$$\frac{dn_{AT}}{dt} = K_{AT} \cdot (1 - \frac{V}{V_{AT}V_0}) \tag{30}$$

Combining the active pumping with the former deduced solute flow, the total solute flow when cell volume is smaller than V_{AT} is:

$$\frac{dn_i}{dt} = AV_mK \cdot (-P) \cdot \frac{n_i}{V} - Aj_sS + \frac{dn_{AT}}{dt} \tag{31}$$

The fit in Fig. 6 B, right is performed using the equation:

$$\frac{dn_i}{dt} = -AV_mK \cdot \frac{n_i}{V} \cdot e^{\sqrt[3]{\frac{10}{3}}\pi \frac{E_0 l(V^{\frac{1}{3}} - V_0^{\frac{1}{3}})}{\Delta c_0 RTV^{\frac{1}{3}}V_0^{\frac{1}{3}}}} \cdot \Delta c_0 RT \frac{V_0^{\frac{1}{3}}}{V^{\frac{1}{3}}} - AD_sN_{MSC}a_{MSC} \cdot \frac{\frac{n_i}{V} - c_0}{l_M} + K_{AT} \cdot (1 - \frac{V}{V_{AT}V_0}) \tag{32}$$

Growth Media Osmolarities. Growth media osmolarities were measured with an osmometer (Micro-Digital Osmometer MOD200 Plus, Camlab, Cambridge, United Kingdom) and are given in Table S1.

Definition of 'flat' cells. 'Flat' cells were chosen for analysis as described before [1]. Briefly, 'flat' cells appeared to be uniformly attached to the cover slip surface, as indicated by a uniform fluorescent intensity of cytoplasmic eGFP across the cell area for a given focal position. These flat cells are less likely to move in z when the media is exchanged, ensuring a more accurate estimate of changes in cell volume.

Background subtraction and thresholding procedure for image analysis. The process of background subtraction and thresholding was as described before [1]. Briefly, Upon choosing a flat cell, the cell's long axis is manually aligned either vertically or horizontally with the image axis. A rectangle is chosen around the cell (Image Rectangle). Inside the Image Rectangle, a second rectangle, covering only background pixels near the cell is selected (Background Rectangle). The pixel intensities were extracted from the Image and Background Rectangle and the mean intensity of the Background Rectangle was subtracted from all the pixel values in the Image Rectangle in each individual frame. For each frame, pixel values were normalized and scanned for minimal and maximal value. The pixels whose intensity was above 30% of the difference between the two values was chosen as belonging to the cell cytoplasm. The number of pixels above this threshold was recorded for each frame. In such a way our estimates of cell area were least sensitive to photobleaching. In addition, in between recordings epi-fluorescence was shuttered to minimize photobleaching effects. Fig. S11 gives the intensity against the recording time of the pixel with maximum intensity, showing photobleaching to be within 5-10%.

Fit Parameters. The model was fitted to experimental data as described in *Methods*. The resulting best fit parameters obtained for wild type and double mutant cells are given in Table S2 and S3 respectively.

Primers, plasmids and strains used in this study. We list the primers, strains and plasmids used in this study in Table S4 and Table S5.

Supporting Figures. Supporting Figures to the main text are given with captions.

Table 1. Media osmolarities

Media	Osmolarity (mOsmol)
MM9	240
MM9+50 mM NaCl	343
MM9+125 mM NaCl	430
MM9+225 mM NaCl	630
MM9+300 mM NaCl	700
MM9+450 mM NaCl	1030
MM9+550 mM NaCl	1200
MM9+650 mM NaCl	1370
MM9+750 mM NaCl	1577
MM9+1 M NaCl	2402
MM9+450 mM sucrose	780
MM9 Buffer	214

Reserved for Publication Footnotes

Table 2. Model fit parameters for the wild type

Variable	Units	Fitted value	Std Dev	Lower limit	Upper limit
A	-	0.72858	0.027281	0.7	1.0
V_{th}	-	1.0372	0.0053052	1.03	1.08
α	s^-1	0.74632	0.043314	0.7	1.0
K	$molPa^{-1}s^{-1}$	9.0157x10^{-22}	4.9617x10^{-23}	1.0x10^{-25}	1.0x10^{-21}

Variable	Units	Fixed value
E_0l	Nm^-1	0.52
V_0	fL	1.3380
Δc_0	M	0.04034

Table 3. Model fit parameters for the double mutant

Variable	Units	Fitted value	Std Dev	Lower limit	Upper limit
A	-	0.49087	0.0074371	0.4	0.5
V_{th}	-	1.0825	0.0012429	1.075	1.085
α	s^-1	0.49072	0.0086498	0.4	0.5
K	$molPa^{-1}s^{-1}$	5.1761x10^{-22}	1.0229x10^{-23}	5.0x10^{-22}	1.0x10^{-21}

Variable	Units	Fixed value
E_0l	Nm^-1	0.52
V_0	fL	2.3030
Δc_0	M	0.04034

Table 4. List of primers

GENE	FORWARD PRIMER	REVERSE PRIMER
mscL727::kan	TGATCCCTTATTCCGACAGC	ACGATGACGAGGCCAATATC
mscS775::kan	TCCAAGAAACACAACCTGCC	AAAGCATTTTGTGGACCGAG

Table 5. List of strains and plasmids

Strain	Description	Reference
BW25113	[F-, (araD-araB)567, lacZ4787(del)::rrnB-3, LAM-, rph-1, (rhaD-rhaB)568, hsdR514 derived from the K12 strain] with pWR20	[2] and [3]
JW3252-1 (ΔmscL)	[F-, (araD-araB)567, lacZ4787(del)::rrnB-3, LAM-, mscL727::kan, rph-1, (rhaD-rhaB)568, hsdR514 derived from the K12 strain]. Keio Collection.	[2]
JW2891-2 (ΔmscS)	[F-, (araD-araB)567, lacZ4787(del)::rrnB-3, LAM-, mscS775::kan, rph-1, (rhaD-rhaB)568, hsdR514 derived from the K12 strain]. Keio Collection.	[2]
ΔmscLΔmscS	[F-, (araD-araB)567, lacZ4787(del)::rrnB-3, LAM-, rph-1, (rhaD-rhaB)568, mscL727::kan, mscS775::kan, hsdR514 derived from the K12 strain] with pWR21.	This study.
Plasmid		
pWR20 and pWR21	Constitutive expression of enhanced green fluorescent protein (EGFP) and kanamycin (kn) or ampicilin (amp) resistance respectively.	[1]
pCP20	Has the yeast Flp recombinase gene, FLP, chloramphenicol and ampicillin resistant genes, and temperature sensitive replication.	[2] and [3]

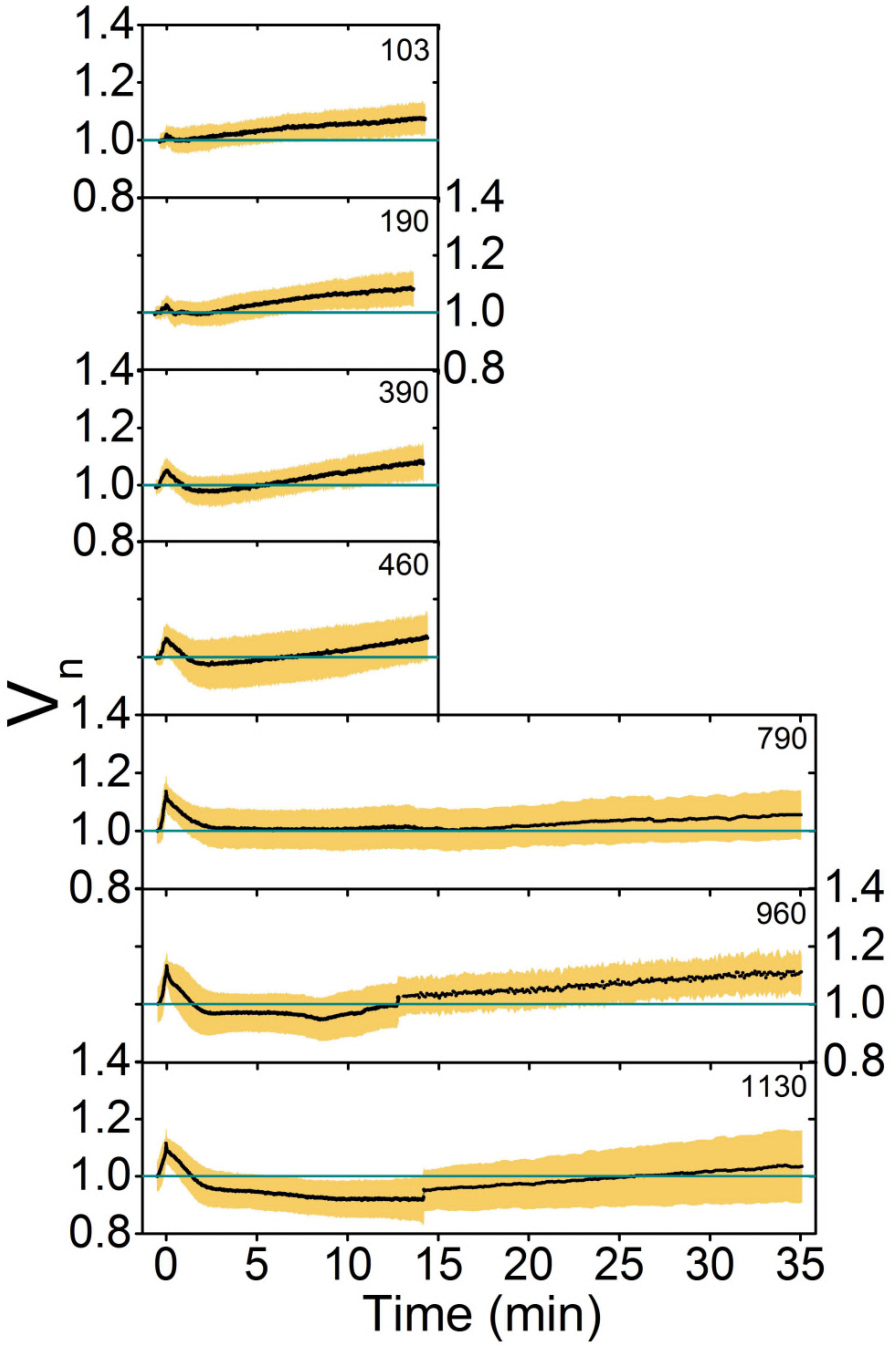

Fig. S 1. Average volume traces with standard deviations (orange shaded area) of wild type cells exposed to different shock magnitudes. The traces are the same as shown in Figure 2 of the main text, except here longer time periods are plotted; 15 min or 35 min depending on the shock magnitude. For 15 min traces the entire data set shown in Figure 2 is plotted (total of 609 cells). A sub-set was recorded for longer period. Thus, the 35 min average trace for the 790 mOsmol shock contains 90 cells in the first 15 min and 44 after, the 960 mOsmol shock contains 116 cells and 84 cells respectively and 1130 mOsmol shock 106 and 52 cells. For all shock magnitudes shown, growth is visible.

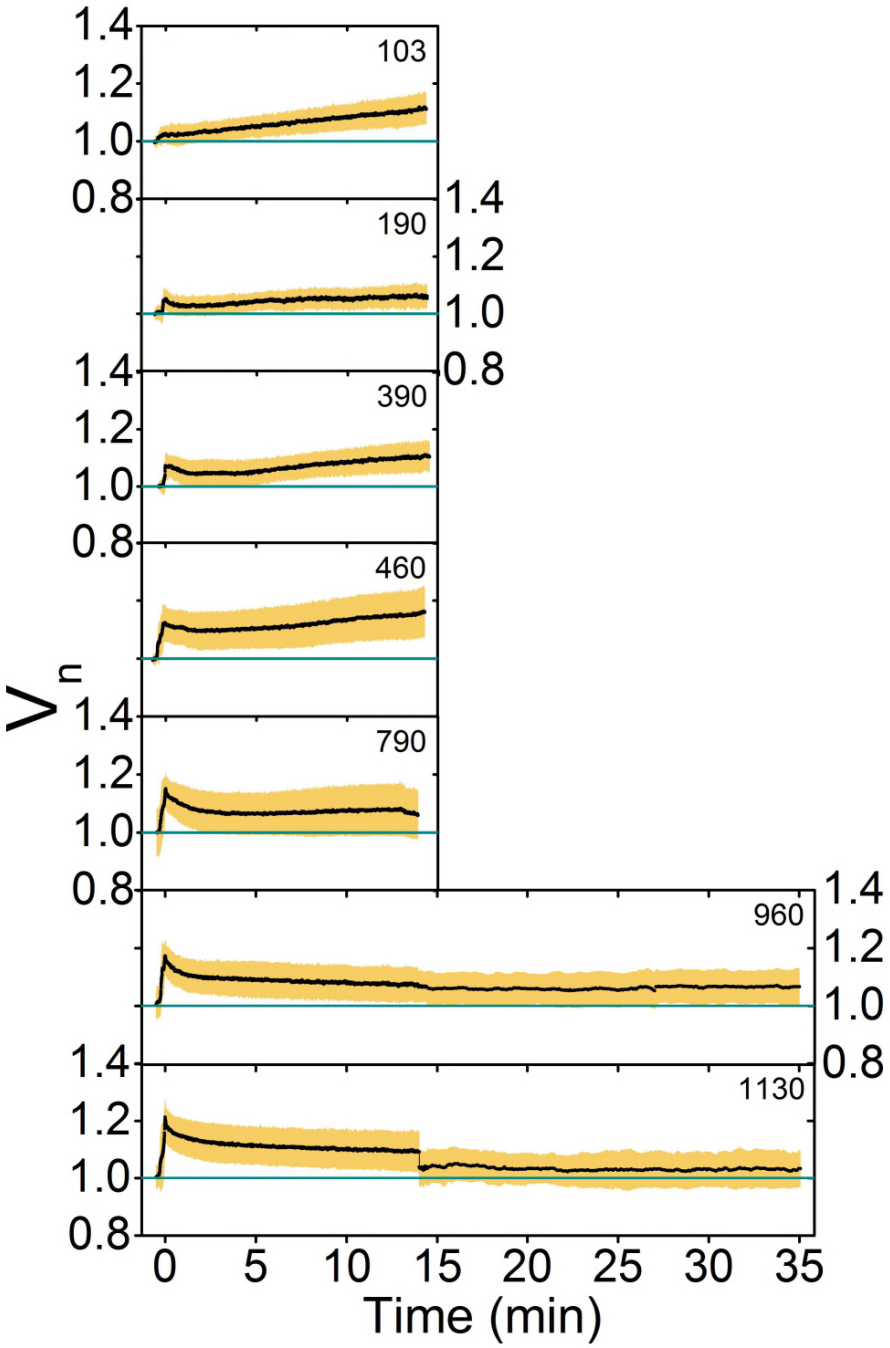

Fig. S 2. Average volume traces with standard deviations (orange shaded area) of double mutant cells exposed to different shock magnitudes. The traces are the same as shown in Figure 2 of the main text, except here longer time periods are plotted; 15 min or 35 min depending on the shock magnitude. For 15 min traces the entire data set shown in Figure 2 is plotted (total of 480 cells). A sub-set was recorded for longer period. Thus, the 35 min average trace for the 960 mOsmol shock contains 50 cells in the first 15 min and 15 after and the 1130 mOsmol shock contains 77 cells and 29 cells respectively. Unlike the wild type strain, for higher shock magnitudes growth is not observed even within 35min post downshock.

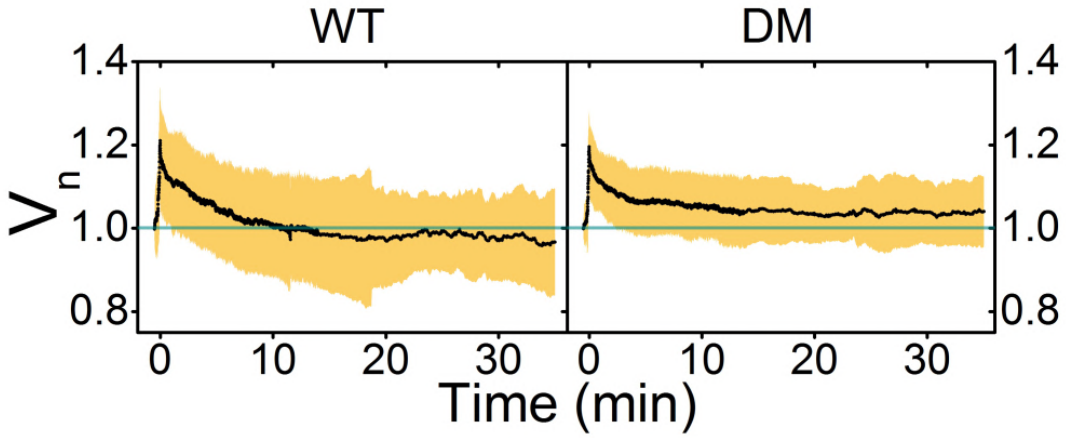

Fig. S 3. Average volume trace of cells exposed to the largest (1337 mOsmol) downshock. Left shows the wild type and right the double mutant. Orange shaded areas show standard deviation. 7 cells were analyzed for the wild type and 33 for the double mutant trace within the first 15 min, and 13 and 15 cells respectively were recorded for longer. At this shock magnitude 8 wild type and 12 double mutant cells died during the recording and were excluded from the analysis. Cell expansion s visible in Phase I, with very small volume recovery in Phase II and no Phase III or Phase IV for either wild type or double mutant strain.

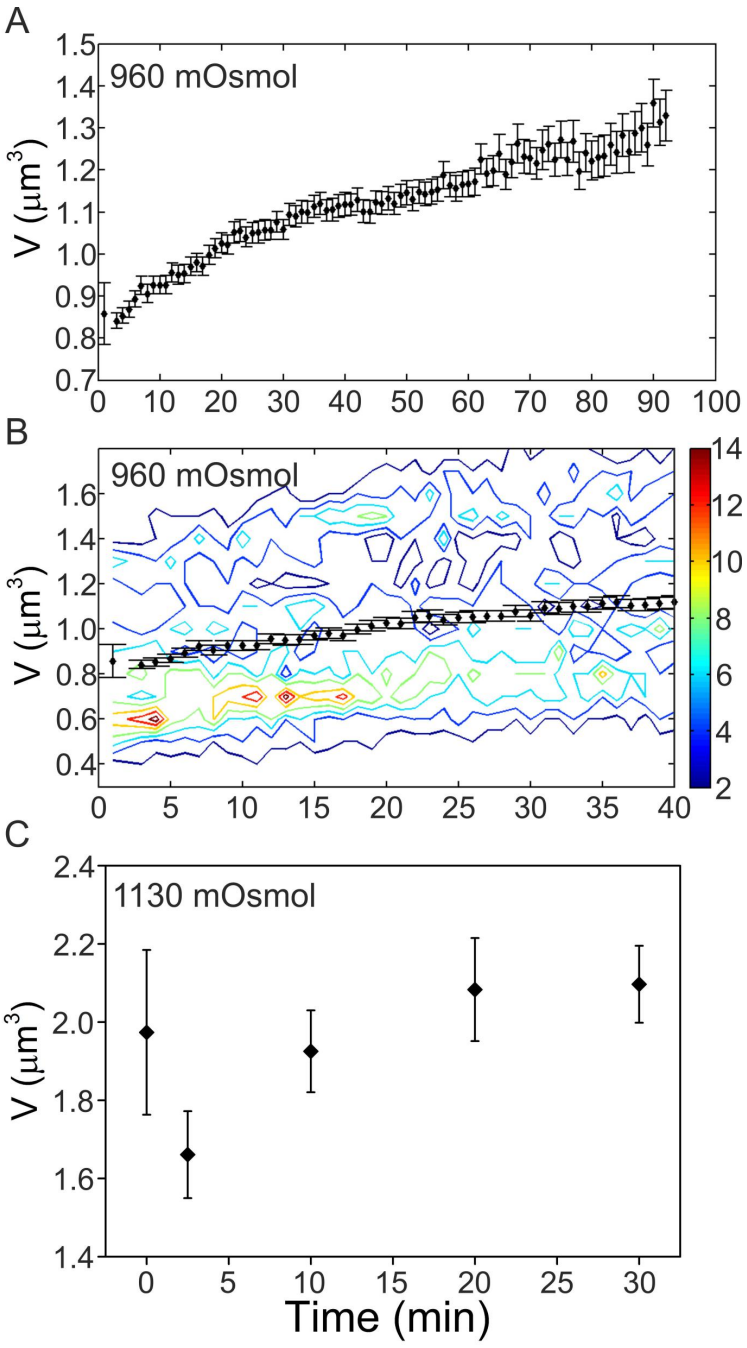

Fig. S 4. Downshock with no surface attachment. (A) Average volume with standard errors of 59 cells subjected to a 960 mOsmol downshock. Initial volume was measured prior to the downshock (shown at t=0). Cells were shocked in a microfuge and the imaging began ≈ 4min after the shock. Time lapse of the cell volume was taken at a frame every 1 min. Cells that settled close to the surface were used for analysis. (B) The data set in (A) shown as a 3D contour histogram with the average trace from (A) overlaid. Z scale is given on the right and represents cell numbers. Upon the downshock volume is smaller then initial volume, corresponding to the 'overshoot' observed in the surface attached cells. Phase III and Phase IV of the response are similar to those of the surface attached cells. (C) Average volume with standard errors plotted against time. Cells were subjected to a 1130 mOsmol downshock in a microfuge and kept in the microfuge during the recovery. Cells were imaged before the downshock (t=0) and at 2.5, 10, 20, 30 min after the shock. Post-shock 'overshoot' and Phase III of volume recovery is visible, similar to the surface attached cells.

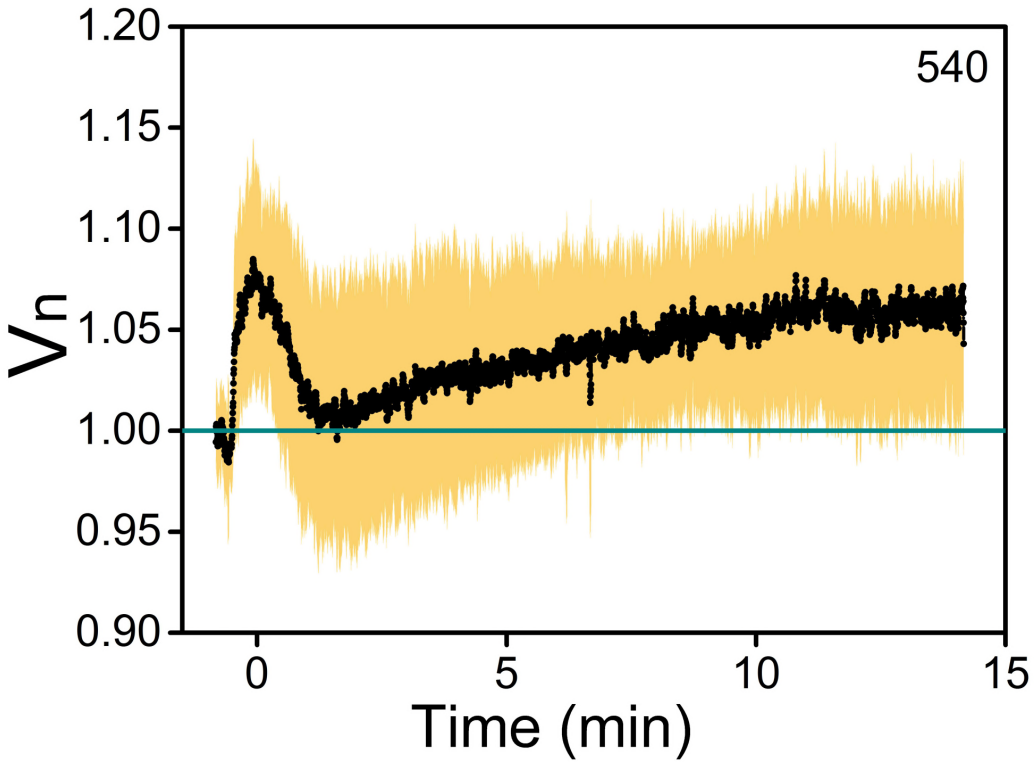

Fig. S 5. Downshock due to the reduced sucrose concentration. Average trace of 17 cells that were grown in MM9 media supplemented with 450 mM sucrose and then subjected to a 540 mOsmol downshock. Shaded yellow area indicates standard deviation. Cell volume expands and slowly recovers post downshock. The response is qualitatively similar to those observed for the NaCl induced downshocks of similar magnitudes.

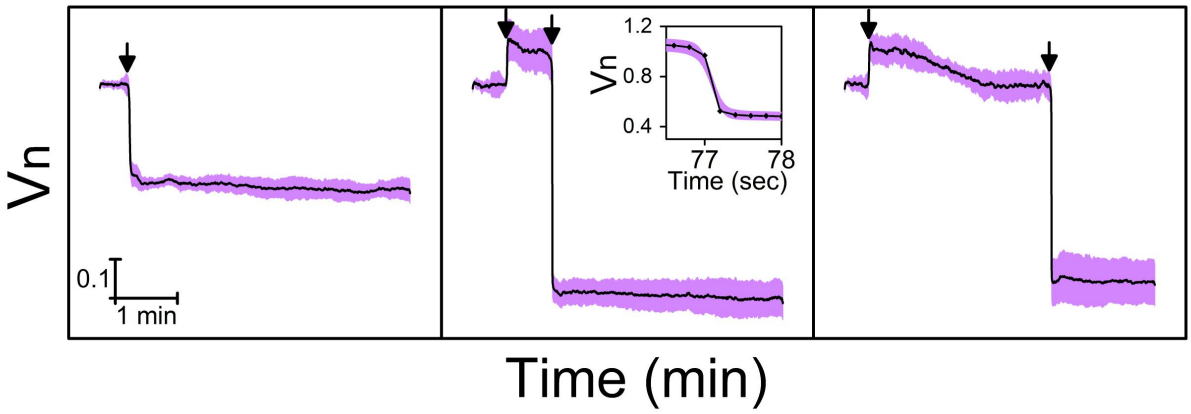

Fig. S 6. Cellular water can leave the cytoplasm fast for cells that were either grown at high osmolarities or when subjected to a downshock. Averaged normalized volume trace of 14 cells is shown on the left, 9 in the center and 13 cells on the right, plotted against time. On the left, cells were grown at 1200 mOsmol and subjected to a 1202 mOsmol upshock. In the middle, cells were subjected to an downshock of 960 mOsmol and immediately after, to an upshock of 2162 mOsmol. On the right, the same sequence of shocks was administered as in the center. However, instead of immediately upon the downshock, the upshock was administered 3 min after the downshock. The arrows indicate the point in time when the shock was administered. Shaded purple areas indicate standard errors. Upon each of the upshocks cellular water left the cell within a second (inset, center), indicated by the fast reduction in cell volume.

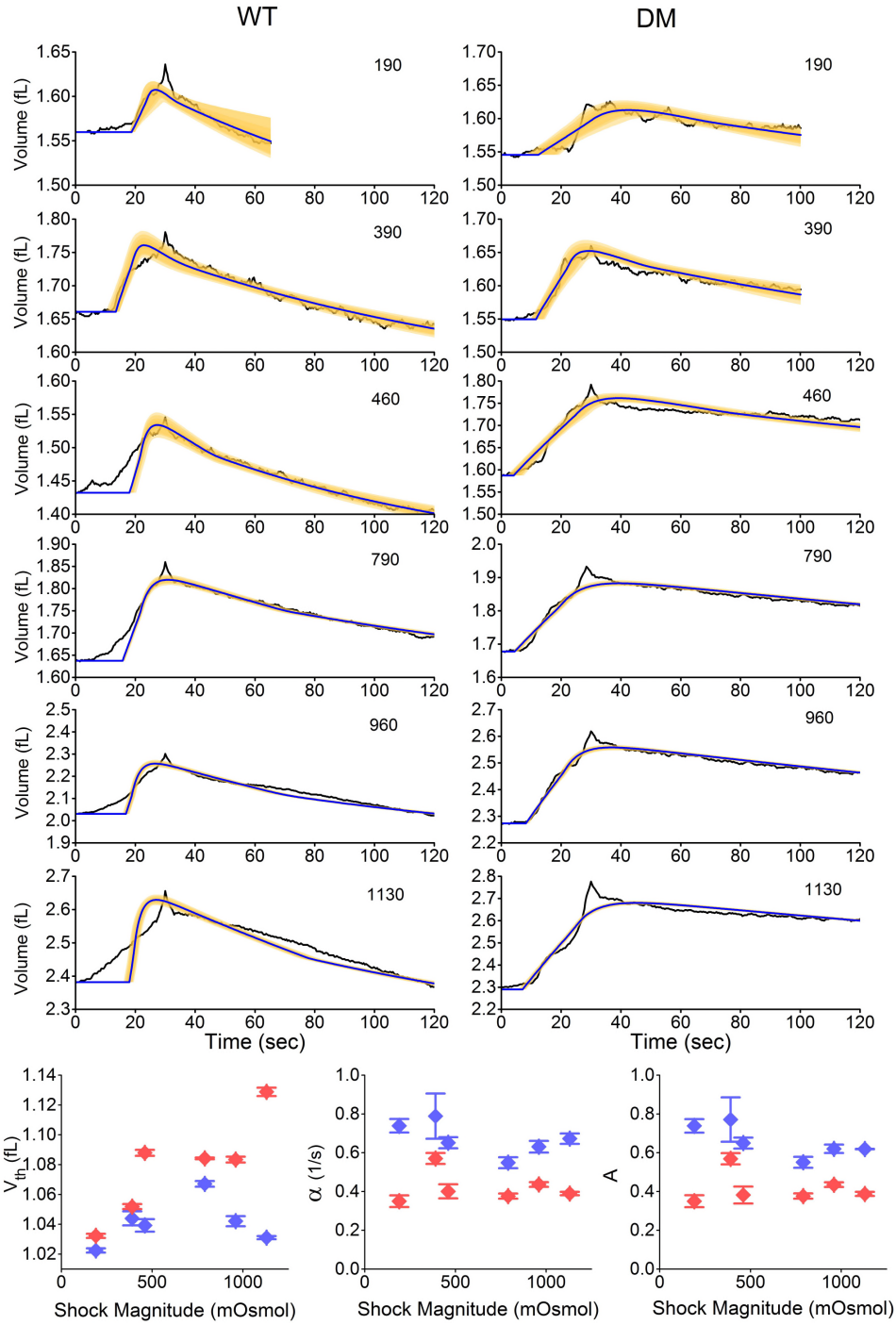

Fig. S 7. Fits to average volume traces taken from Fig. 2. Left shows the wild type and right the double mutant. Average traces for each shock magnitude are given in black. Blue line shows the result of best fit to the average trace. Shaded orange regions show fit confidence intervals, from darker to lighter orange these are: 50%, 90%, 95%, and 99% . There is a good agreement between the model and the experimental data. Fit parameters obtained are plotted against the shock magnitude at the bottom of the figure for both wild type (blue) and double mutant (red).

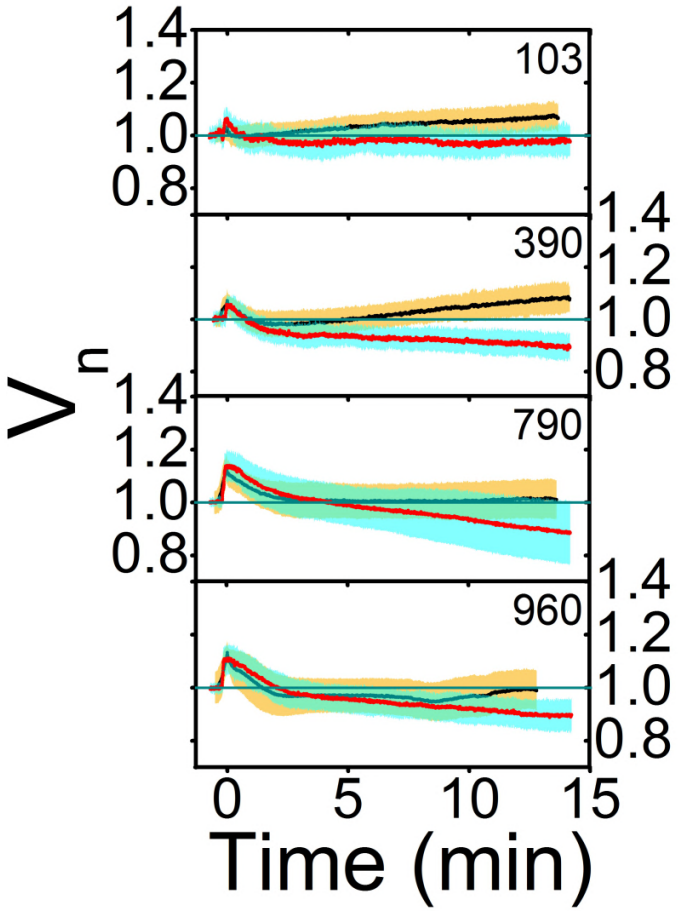

Fig. S 8. Average volume trace of cells exposed to 103, 390, 790 and 960 mOsmol downshocks. Average traces of downshocks performed in rich media are given in black, with orange shaded areas showing standard deviation. These traces are taken from Fig. 2 for the shock magnitudes shown. In red are the average traces of cells subjected to the same downshock, but the shock was performed in buffer only. Cyan shaded areas show standard deviations. 17 (wt) and 28 (dm) cells were used for the 103 mOsmol downshock in buffer, 22 (wt) and 23 (dm) for the 390 mOsmol, 35 (wt) and 52 (dm) for the 790 mOsmol and 33 (wt) and 25 (dm) for the 950 mOsmol downshock.

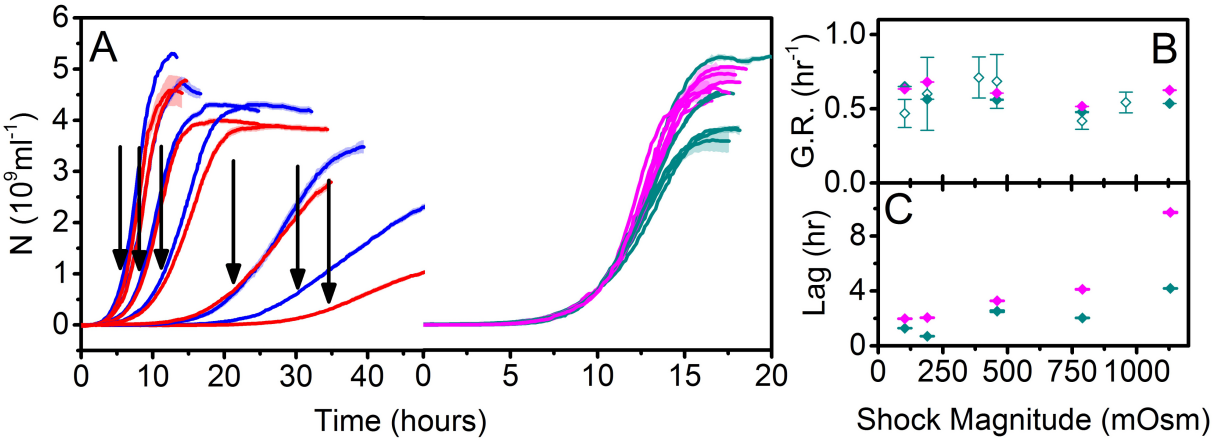

Fig. S 9. Population and single cell growth rates. (A) Cell number (obtained from OD measurements as described in *Methods*, see also Fig. S13 below) is plotted against time. Cells of the wild type (blue) and the double mutant strain (red) were inoculated in MM9 media with a given amount of NaCl (as described in *Methods*). The osmolarities of MM9 media were 343 to 1577mOsm. At higher osmolarities of the growth media cells in the culture grew slower. At the point in time indicated with an arrow, cells (2 μl) were transfered from high osmolarity MM9 to MM9 only, to induce a downshock. The remaining culture was left to grow in MM9 of high osmolarity. Culture growth post downshock is shown in cyan for the wild type and pink for the double mutant. Post downshock growth curves were aligned to the beginning of observable growth for easier growth rate comparison. Corresponding lag times are shown in C. (B) Growth rates obtained from growth curves in A and from single cell data in Fig. S2. Growth rates are plotted against the shock magnitudes: in cyan the wild type growing in MM9 post downshock and in pink the double mutant growing in MM9 post downshock. Cyan open symbols show growth rates obtained for the wild type from single cell data (as described in *Methods*). Post downshock both the wild type and the double mutant strains grow at a same rate irrespective of the shock magnitudes. (C) Lag times of post downshock cultures plotted against shock magnitude. Cyan shows the wild type and pink the double mutant. Lag time increases with higher downshock, particularly so for the double mutant at higher shock magnitudes.

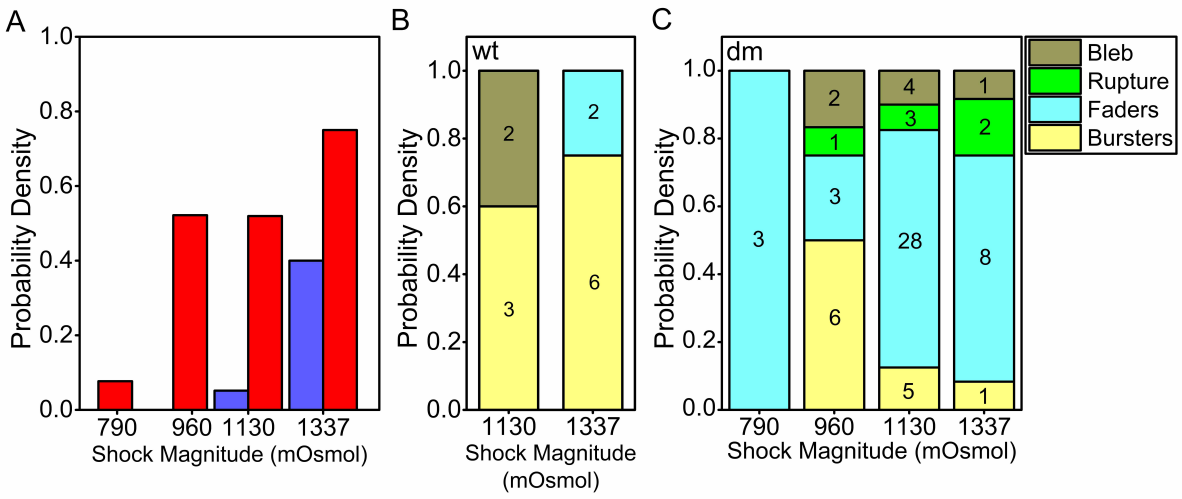

Fig. S 10. Cell survival analysis. (A) Probability density of lyses is given against the shock magnitudes. Wild type is in blue and double mutant in red. Analysis of the nature of cell death is given for the wild type (B) and the double mutant (C). The definitions of cell death types used are based on morphological changes and as defined in a previous study [4]. Faders are shown in cyan, bursters in yellow, rupture in green and bleb in dark yellow. Blebing cells are those with spherical like, inner membrane bulges that protrude through the cell wall and outer membrane. Bursting cells abruptly lost fluorescence intensity down to background level. Fading cells are characterized by gradual, but substantial loss of fluorescence intensity. Cells classified as being ruptured show characteristic irregular shapes with no blebs [4].

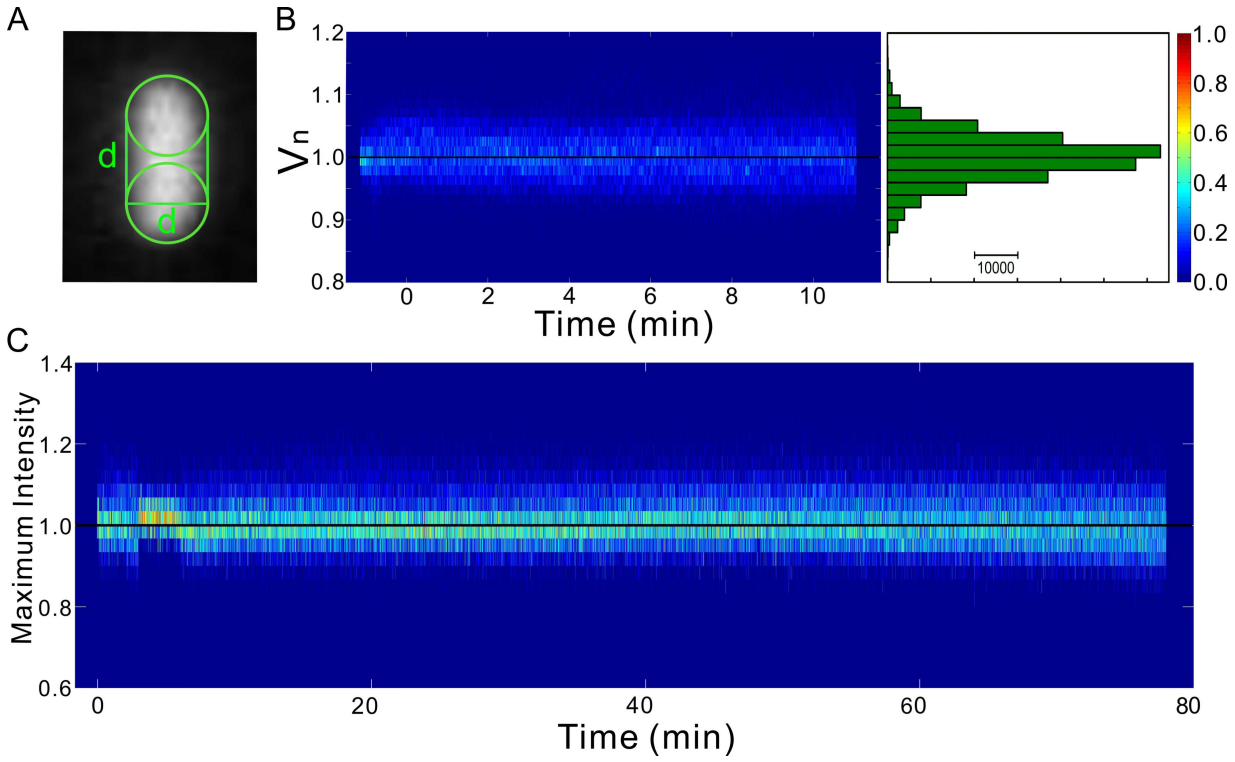

Fig. S 11. (A) A representative spherocylinder (in green) of 2:1 length to diameter ratio is given over an image of an example cell (imaged prior to the downshock). d indicates cell diameter. (B) Noise analysis. 3D histogram of normalized cell volumes is given against time on the left. Z color scale is given on the far right. 2D histogram of the traces plotted on the left is given on the right. Cells were flushed with growth media (MM9) using the same flow rate as for the downshocks, except no shock was administered. No volume changes were observed during the control flush. The noise in the experimental data is below the volume changes we observe during the downshocks. (C) Photobleaching estimate. Photobleaching was minimized by shuttering the epi-fluorescence in between recordings. Additionally, the image analysis algorithm of background subtraction and thresholding, described in *Methods* and Supporting Information text above, is only sensitive to large losses in fluorescence. The photobleaching was estimated in the following way. Pixel of maximum intensity ($\mathrm{I_{max}}$) was monitored over time for the entire duration of the recording. 3D histogram of $\mathrm{I_{max}}$ is given for a total of 24 cells exposed to 1130 mOsmol downshock. The 1130 mOsmol shock magnitude was chosen as this condition showed all characteristic response phases observed in Fig. 1 B. Over time ≈5% of fluorescent intensity is lost, which is well below the sensitivity of our image analysis algorithm (the intensity loss would need to approach ≈ 70% to affect the estimate of the cell area during the recording).

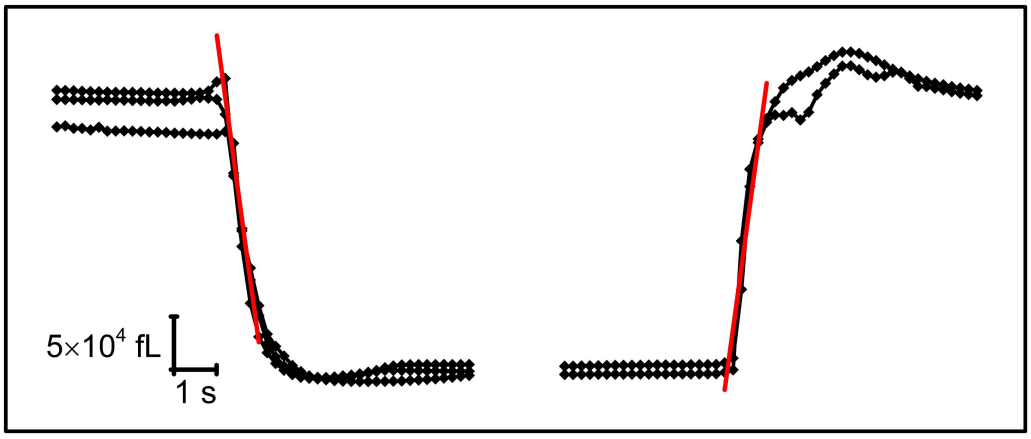

Fig. S 12. Flow rate calibration. Local flow rate close to the surface against time. Local flow rate was estimated from several calibration flushes using a fluorescent dye (see *Methods*). The dye was both flushed in (right, in black) and out (left, in black) of the channel. Linear fits were performed for each direction of the flush and then averaged (shown in red lines)

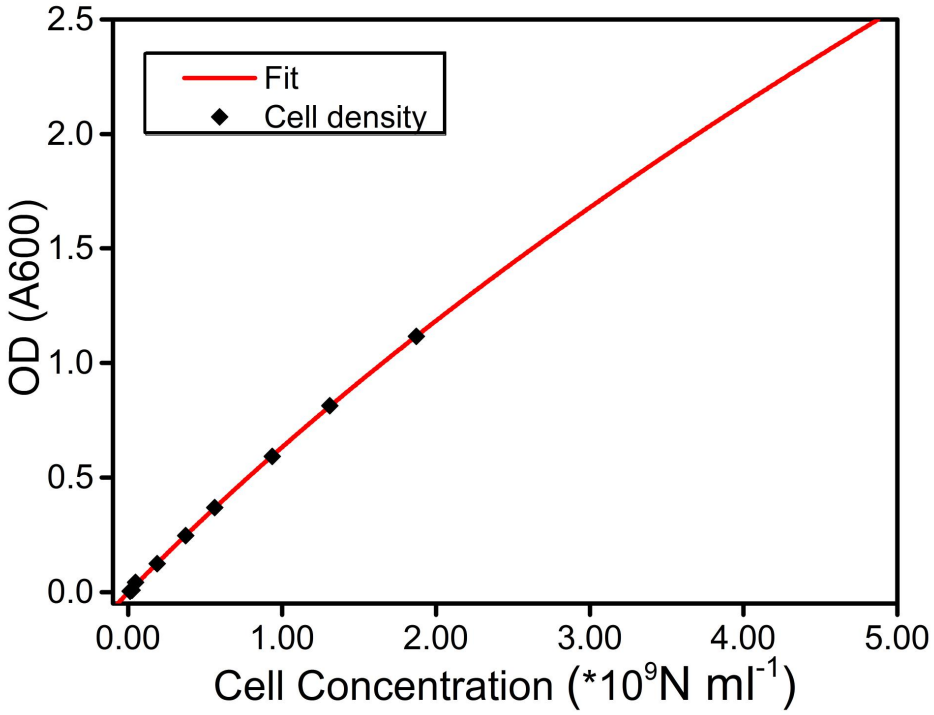

Fig. S 13. Calibration curve for the optical density measurements. Optical density measurements are performed under the assumption that for a single scattering event absorbance measurement is equivalent to the turbidity measurement. This assumption breaks down when cell number increases and multiple scattering events start occurring, effectively lowering the OD reading. Here we calibrate for this effect. Optical density measured at 600 nm is plotted against the cell concentration (as obtained by cell counting in a microscope, see also $Methods$). Second order polynomial is fitted to the obtained curve and used for OD measurements calibration. The fit gave $\mathrm{N} = 2.2 \cdot 10^8 \mathrm{OD}^2 + 1.45 \cdot 10^9 \mathrm{OD} + 2 \cdot 10^6$ [5].

1. Pilizota T, Shaevitz JW (2012) Fast, multiphase volume adaptation to hyperosmotic shock by Escherichia coli. PLoS One 7(4):e35205.
2. Baba T et al (2006) Construction of Escherichia coli K-12 in-frame, single-gene knockout mutants: the Keio collection. Mol Syst Biol 2:2006.0008.
3. Datsenko KA, Wanner BL (2000) One-step inactivation of chromosomal genes in Escherichia coli K-12 using PCR products. Proc Natl Acad Sci USA 97(12):6640-6645.
4. Bialecka-Fornal M, Lee HJ, Phillips R (2015) The rate of osmotic downshock determines the survival probability of bacterial mechanosensitive channel mutants. J Bacteriol 197(1):231-237.
5. Koch AL (1970) Turbidity measurements of bacterial cultures in some available commercial instruments. Ana Biochem 38(1):252-259.

3.4 Conclusions

In this thesis chapter, I have demonstrated the *in-vivo* single cell volume responses of *E.coli* to increasing hyposmotic shock. Previously characterized *in-vivo* responses of *E.coli* to hyposmotic shock that was fast as ≈8 ms demonstrated that the MSCs gate in 150-200 ms (Boer et al., 2011; Çetiner et al., 2017). The hyposmotic shock in those studies can be considered as a step-change, and fast with respect to time scales of MSC gating. However, in real life scenario the changes in osmolarity is most likely to be a slow gradient. In this study, I have studied the single cell response to a slow hyposmotic shock (≈2 s) that is slower than the time scales of MSC gating, as shown in Figure 2.5 and Fig S12. Additionally, Chapter 8 Figure 8.1, captures the cell volume response to a further pronounced slow hyposmotic shock.

The volume response showed characteristic phases upon hyposmotic shock (Fig 2). In the first phase, upon hyposmotic shock, the cell volume increased due to water influx to reach a maximum volume expansion. Following this, the cell showed volume recovery that overshot below the initial volume. To evaluate the contribution of MSCs in the volume response, I next characterized the volume response of a MscL and MscS deleted mutant, double-mutant (Fig. 2). The double-mutant exhibited the fast volume expansion but showed only partial volume recover (V_{min} in Fig. 3C).

To assert that the partial volume recovery observed in the double-mutant is through remaining MSCs and not through the cell membrane, further characterization of volume response in the absence of MSCs is necessary. Gadolinium (Gd^{3+}), a rare earth element has been shown to block MSCs reversibly (Berrier et al., 1992; Cui et al., 1994). However, Gd^{3+} was successful in blocking larger channels only (Berrier et al., 1992), at high concentrations. A hepta MSC deletion is necessary to understand the contribution of MSCs in volume recovery and to characterize the role of MSCs in survival. In the next chapter, I demonstrate the cell volume dynamics of a hepta MSC deletion mutant.

As shown in Fig.2, the cell 'overshoot' volume as much as 1- 10% lower than initial volume for a 100 to 1130 mOsmol hyposmotic shock. If the MSCs closed when the tension relaxed during volume recovery, how would the cell continue to lose volume leading to overshoot? This can be explained using the phenomenological model detailed in this chapter (Buda et al., 2016). In addition to water/solute fluxes as shown in Fig.5b, the Figure 3.1 here shows

the dynamics of osmotic pressure and Laplace pressure during hyposmotic shock. Following the closure of channels (marked by 4th grey vertical line), the Laplace pressure (P in Eq. 8, Chapter 3) is still higher than the initial pre-shock value and hence, the strained cell wall continues to slacken. As a result the volume continues to reduce and only reaches a steady-state when the Laplace pressure equates osmotic pressure. This could suggest that following the closure of MSCs, the cell continues to lose water from the cytoplasm leading to volume overshoot. The overshoot further increases with increasing channel number (as noted by increasing osmolarity) as shown in Fig.3 because of excessive loss of solutes that requires further shrinking of the cell to equilibriate the two pressures. It is also important to note that, Figure 3.1 does not include the import of ions through active pumping. Hence, the osmotic pressure of the cytoplasm could only be raised by losing cell water and reducing cell volume. This continuum model also does not consider the effect of co-operative gating of channels on cell volume response, which will be further discussed in Chapter 6

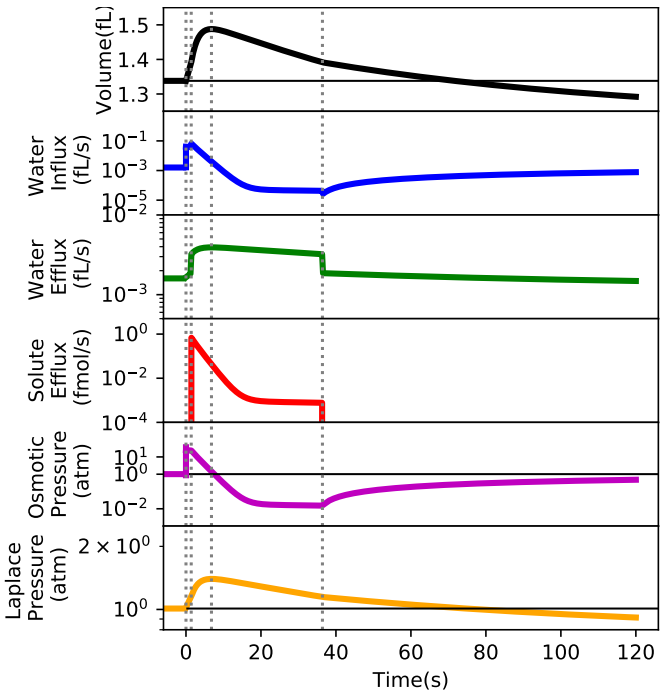

FIGURE 3.1: Cellular responses to a 960 mOsmol hyposmotic shock predicted by the model (see Chapter 3, Fig. 5b)

The model considers a fixed threshold of gating for all the channels in a cell,however, Edwards et al. (2012), Martinac et al. (1987), and Cui et al. (1994)

have demonstrated varied threshold of gating for the seven kinds of MSCs in *E.coli*. Further, the threshold of gating for each kind could be further influenced by co-operative gating as studied in detail in Chapter 6. Thus, the parameter in A in Eq. 10 & 12, could be a non-linear function of V_{th}, channel number, shock magnitude and channel cross section area.

Figure 3.1 shows that the turgor pressure on the cell wall is 0.5 atm for a 15% increase in volume, upon 960 mOsmol hyposmotic shock. An osmolarity of 960 mOsmol corresponds to an osmotic pressure of $\approx$ 25 atm. The continuum model predicts that due to the presence of MSCs an *E.coli* can only experience a turgor pressure increase of 0.5 atm for an osmotic shock of 25 atm.

Chapter 4

Life and death of an inflated *E.coli*

4.1 Introduction

Chapter 3 demonstrated the *in-vivo* cell volume dynamics of *E.coli* wild-type and double-mutant ($\Delta mscS$ and $\Delta mscL$), to increasing hyposmotic shocks. The wild-type response consisted of fast volume expansion followed by a slow volume recovery that overshot below the initial volume. Whereas, the double-mutant exhibited the fast volume expansion but recovered only an average of 50.5% of the expanded volume upon a hyposmotic shock of 960 mOsmol. This volume response of double-mutant suggested that while MscL and MscS were necessary for complete volume recovery, attributing to the presence of five other MSCs (MscK, YbdG, YjeP, YbiO and YnaI) or water leaking through membrane led to partial volume recovery.

Several studies have demonstrated the importance of these five 'minor' MSCs in cell's survival to hyposmotic shocks. For instance, the native levels of YbdG expression improved ≈50% survival chances of *E.coli* triple-mutant ($MscL^-$, $MscS^-$, $MscK^-$) while compared to a quadruple-mutant ($MscL^-$, $MscS^-$, $MscK^-$, $YbdG^-$) for a 0.15 M NaCl shock (Schumann et al., 2010). The over expression of either Ybio, YnaI or YjeP in a MSC deletion mutant (termed hepta-mutant in this thesis) conferred full protection against a 0.3 mM NaCl hyposmotic shock (Edwards et al., 2012). Bialecka-Fornal et al. (2012) demonstrated 0-90% survival of various combinations of *E.coli* MSC mutants when exposed to hyposmotic shocks of various rates.

While the above studies demonstrated the importance of various MSCs in *E.coli*, Edwards et al. (2012) and Bialecka-Fornal et al. (2012) demonstrated a < 1% survival chance in hepta-mutant following a 0.3 and 0.5 M NaCl down-shock. Bialecka-Fornal et al. (2015) demonstrated that the cell death in the

hepta-mutant occurred in multiple ways due to damage the on the cell envelope. They noted that while some cells showed fast fading due to leakage of cytoplasmic content— similar to that observed by Reuter et al. (2014)—others exhibited slow fading or blebing that lasted up to several minutes to an hour. In that study they hypothesized that the swelling of the cells resulted in fracture of a few layers in the cell wall, which then propagated with time to completely damage the cell wall— this led to the formation of blebs or complete loss of cellular content.

The studies on hepta-mutant survival were performed at higher hyposmotic shocks where the impact of shock on the cell damage were significant. These studies lead to an open question as to how much of the osmotic swelling can an *E.coli* sustain without cell envelope damage and beyond what magnitudes of cell swelling would it start affecting cell envelope integrity, which I address in this part of the thesis using a hepta-mutant. In the first part of the Chapter, I characterize the first 5 minutes cell volume response of the hepta-mutant to increasing hyposmotic shocks and compare the maximum cell volume expansion against wild-type and double-mutant. To understand the extent of elevated osmotic pressures a hepta-mutant sustains, I next study the cell survivability and the dynamics of cell volume response that leads to cell death or survival, at three increasing hyposmotic shock. In the final part, I demonstrate the possible impact of cell surface attachment on the dynamics of cell death.

4.2 Results

Starting from a double-mutant (cloning done by Renata Buda, details are in Chapter 3, Materials and Methods), I created a hepta-mutant by deleting the remaining five MSC genes using Plasmid Mediated Gene Replacement technique and P1 phage (details of cloning in Chapter 2 section 2.2.2 and 2.2.3).

4.2.1 Hepta-mutant shows no cell volume recovery

Hepta-mutant was first grown in MM9 media supplemented with increasing concentration of NaCl (Chapter 2 section 2.3 for growing conditions) and then hyposmotic shock was delivered using MM9 media. The first 5 minutes of

average cell volume response of the hepta-mutant to hyposmotic shock of increasing magnitudes is shown in Figure 4.1. Individual traces were aligned at the first point of maximum volume expansion and then average values are plotted as shown in Figure 4.1. The maximum volume expansion of individual cell was as fast as 0.33 s (camera frame rate) to 1.32 s. Unlike the wild-type, the average V_n in Figure 4.1 does not show the characteristic volume recovery . Figure 4.2 compares the normalized maximum volume expansion ($V_{n,max}$) across the three strains: wild-type, double-mutant and hepta-mutant. $V_{n,max}$ of the hepta-mutant is greater than the wild-type and the double-mutant, for a given hyposmotic shock.

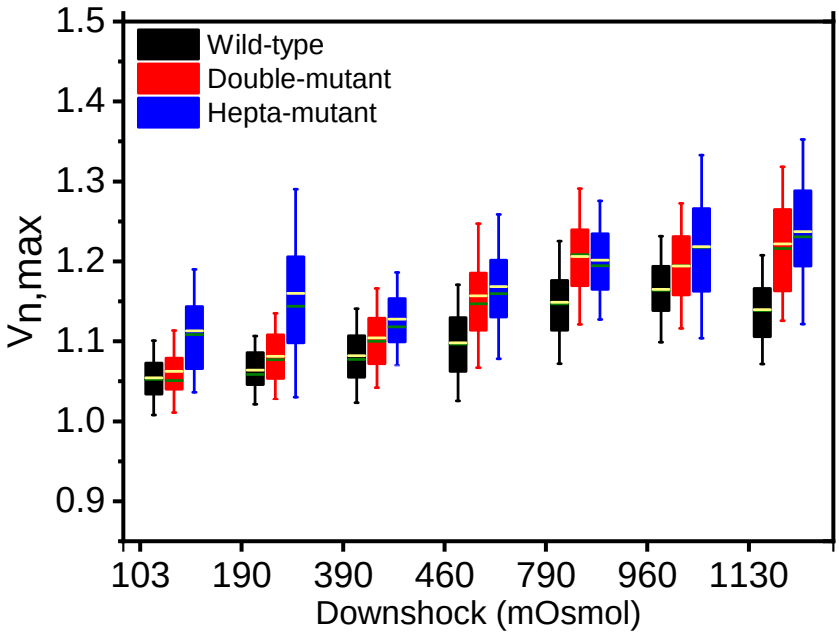

FIGURE 4.2: Comparison of maximum volume expansion across wild-type (black), double-mutant (red) and hepta-mutant (blue). Whiskers indicate 1.5x SD value and the upper and lower edges of the boxes indicate the third and first quartile, respectively. The green line shows the median and the yellow line shows the mean. The sample size for each condition is same as that shown in Fig 4.1 and Chapter 3 Figure3a

4.2.2 Longitudinal expansion upon hyposmotic shock

Analysis of cell's average radial and longitudinal expansion profiles during the event of hyposmotic shock, Figure 4.3 shows the changes in cell length and

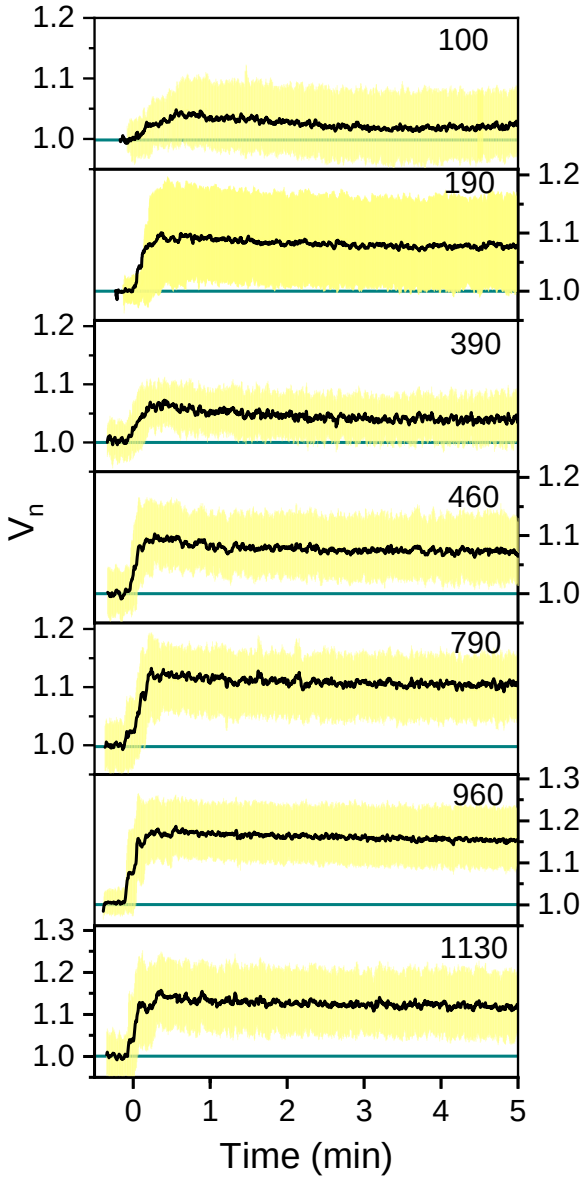

FIGURE 4.1: **Average volume response of hepta-mutant upon increasing hyposmotic shocks.** The figure legends indicate the magnitude of hyposmotic shock in mOsmol. The first 5 minutes following a hyposmotic shock shows no volume recovery that is characteristic of MSCs, as seen in wild-type, Chapter 3. The individual cell volume response are first filtered with a median filter of window size 5 and then aligned at the first point of maximum volume expansion. Black curve shows the average response of individual single cell volume response and yellow shaded region indicate 1SD. The sample sizes for each shock is 61 (100 mOsmol), 99 (190 mOsmol), 44 (390 mOsmol), 87 (460 mOsmol), 69 (790 mOsmol),99 (960 mOsmol) and 40 (1130 mOsmol).

width upon hyposmotic shock to three varying conditions. Fig 4.3(b) indicates that the radial expansion of cell is negligible and the volume expansion due to water influx mainly occurs by longitudinal stretching of the cell.

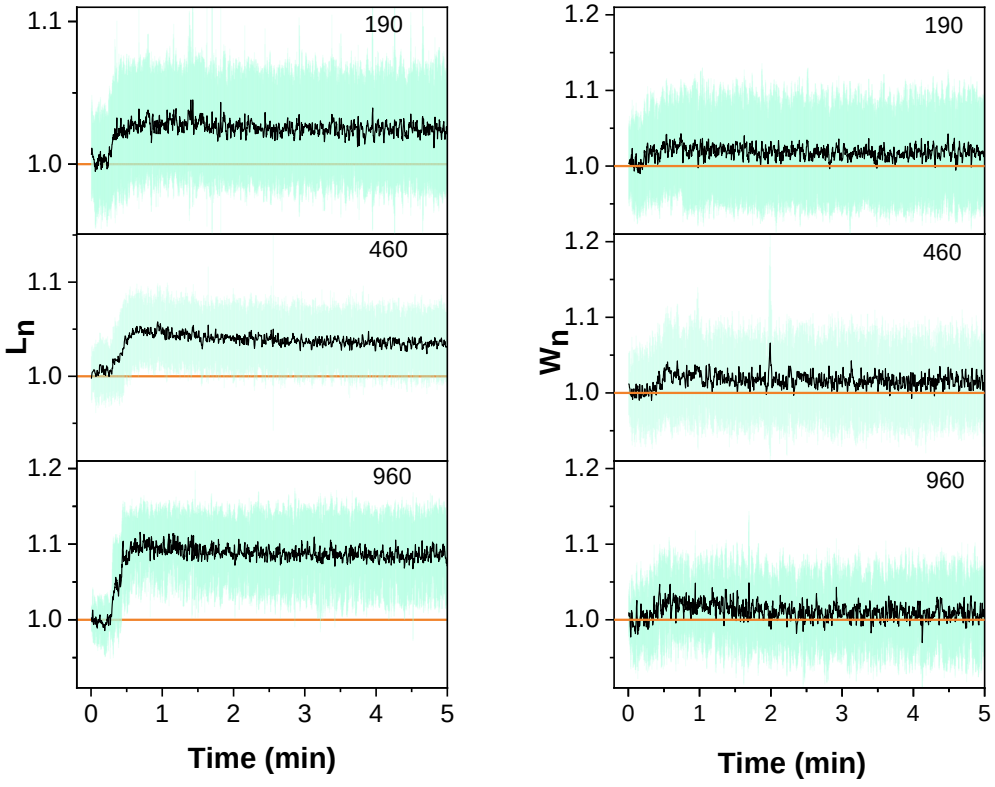

(a) (b)

FIGURE 4.3: Average length and width response of hepta-mutant to hyposmotic shock. (a) Average response of normalized cell length L_n (b) Average response of normalized cell width or diameter (W_n). The data was filtered with median filter of window size 3. Blue shaded region is 1SD. The sample size for 190, 460 and 960 mOsmol are 112, 90 and 94, respectively. The individual traces were averaged without aligning at maximum expansion due to large noise in measuring length and width.

4.2.3 Hepta-mutant survives small magnitude hyposmotic shock

The first 5 minutes of the cell volume response following a hyposmotic shock showed no volume recovery and to understand the impact of this swelling on the cell's ability to survive, two slides for each condition were imaged

overnight. The slides following the hyposmotic shock were sealed. The first 15 minutes of imaging, the frame rate was to capture every 0.3 s and following that the frame rate was set to every 15 s to reduce photo-damage. In a field of view, the cells which were isolated or in other words, unattached to any neighbouring cells were visually chosen for fluorescence intensity and area estimation. Dying cells were identified as those which lost at least 20% of total fluorescence intensity (see Chapter 2 2.5.4 for details). Figure 4.4 shows the loss of fluorescence, which marks the dying event. The total fluorescence intensity was constant until the event of dying, ensuring that the loss in fluorescence was due to leakage of GFP from cytoplasm and not due to photo-bleaching of GFP, as shown in Figure 4.5. The fluorescence intensity drop in most cases was between 15 s to 2 min and few cases it took 15-20 min. The cells died mainly as fading cell and only 1-2 cells showed an inner membrane 'bleb'. The cells that showed an increase in cell area/volume are categorized as growing/surviving. The remaining non-separable cells in the field of view were visually inspected for loss in fluorescence intensity or increase in cell area to include in Figure(4.6).

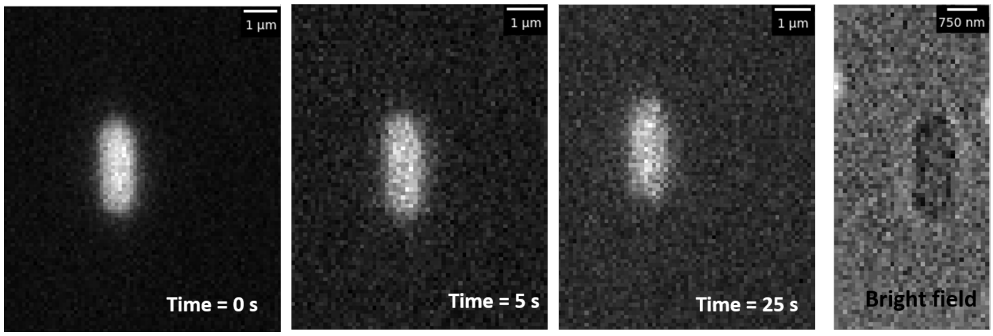

FIGURE 4.4: **Depiction of cell dying event in hepta-mutant during hyposmotic shock**. Time series of images show the loss of cytoplasm fluorescence intensity during a 460 mOsmol hyposmotic shock. The start of the cell lysis event was at some point following hyposmotic shock and is set to Time= 0s. Loss in fluorescent intensity stops at 25 s. Bright field image of the cell was captured at the end of imaging showing the presence of a 'ghost' cell. These cells appeared less denser than the growing cell due to loss of cellular solutes.

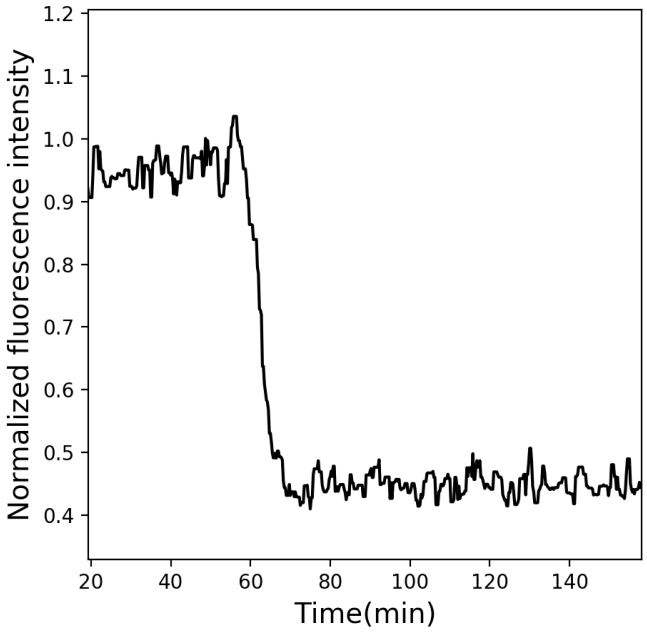

FIGURE 4.5: **Fluorescent intensity sample trace of a hepta-mutant during cell lysis.** The total fluorescent intensity is normalized with the intensity at maximum volume expansion. The total fluorescent intensity is filtered with median filter with window size 5.

A survey of dying or surviving cells is shown in Fig 4.6 for a hyposmotic shock 190, 460 and 960 mOsmol. At 190 mOsmol hyposmotic shock, 75.8 $\pm$ 6.65 % of the cells survived the challenge and 3.3 $\pm$ 0.75 % died during the event. The percent difference between the dying and survival events is the uncertainty in measuring if the cells died or survived in the time observed. One of cause for uncertainty was because of those cells that attached to the coverslip at the pole end and appeared disc like. In case if the cells grew, the changes in cell area during elongation due to growth was negligible along the short axis and also, the total fluorescence intensity either remained constant or diluted with the increasing cell volume but did not show an increase. These discrepancies were also true for those cells that were partly attached at one end of the pole and the other end of the pole sticking out to another focal plane. A few cells, remain unchanged in cell volume or intensity during the entire time of imaging. For increasing hyposmotic shock, the chance of cell survival reduced as shown in Figure 4.6

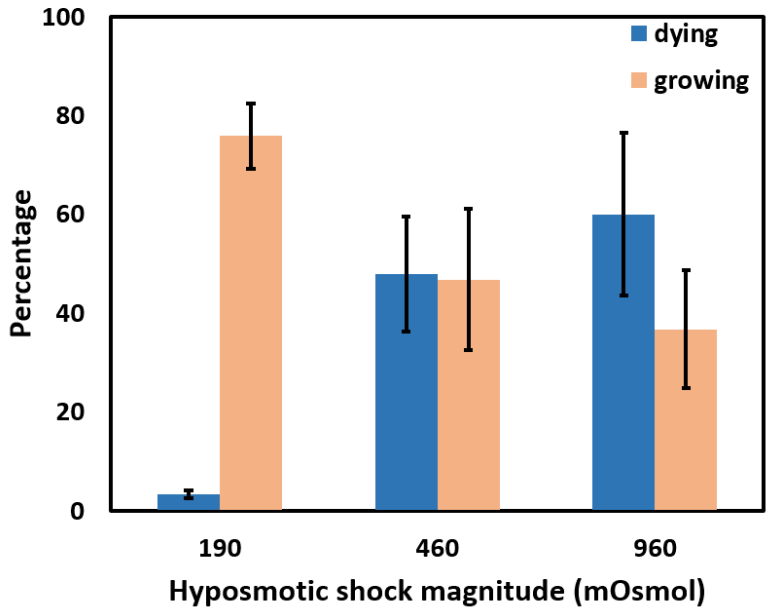

FIGURE 4.6: **Analysis of hepta-mutant survival and death at three different hyposmotic shocks.** The bar graph shows the percent of cell surviving upon 190, 460 and 960 mOsmol hyposmotic shock (orange bars). Blue bars show the percent of cells dying after hyposmotic shocks. Error bar show 1SD. The total number of cells observed for 190, 460 and 960 mOsmol hyposmotic shock are 124, 255 and 129, respectively. The difference in the dying and surviving percent gives the uncertainty in estimating either of the two events.The number of uncertain cells are respectively 25, 14 and 4 for 190, 460 and 960 mOsmol shock.

4.2.4 At a larger shock, hepta-mutant takes longer time to die

The distribution of time taken to survive or die following the hyposmotic shock is shown in Figure 4.7. The time of growth is the time point of inflection at which the cell area starts increasing (see Chapter2 for details). Figure 4.7a shows an increasing lag time with increasing hyposmotic shock. Time of death was estimated as the time at which the cells lost at least 20% of its total intensity. The cells that experienced a large 960 mOsmol downshock died later than those that experienced 460 mOsmol, Figure 4.7b. At 960 mOsmol downshock, a $\approx$ 10% of the data set died 15-20 hours after the hyposmotic shock, where in these cases the composition of the environment would have significantly changed. For eg., the dissolved oxygen or nutrients in the environment would have been depleted due to their consumption by those that survived, hence impeding any chances of survival for those cells categorized as outliers.

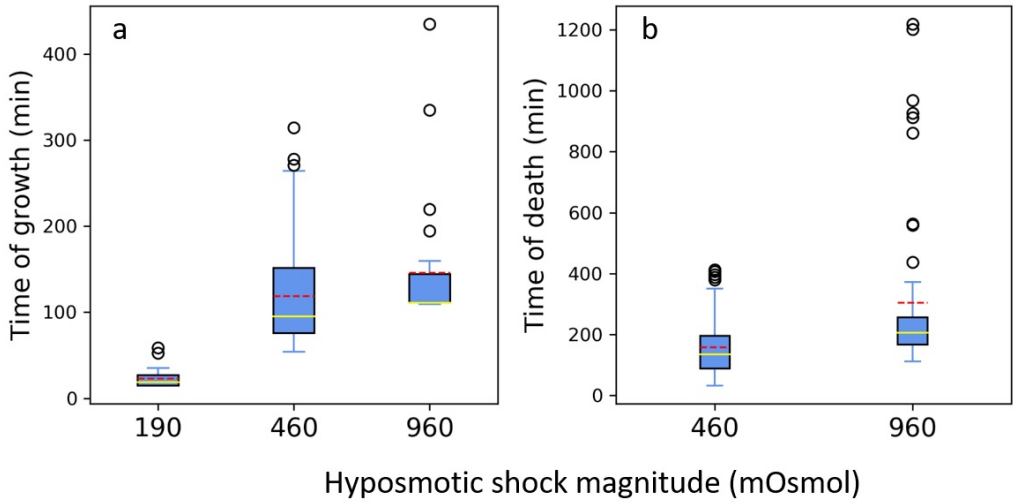

FIGURE 4.7: **Distribution of time taken to survive or die during hyposmotic challenge.** A boxplot of time (min) taken to (a) survive hyposmotic shock of magnitude 190, 460 and 960 mOsmol with sample size 35,58 and 26 respectively (b) time of death, i.e., the time at which cells lost at least 20% of the total fluorescent intensity for 460 and 960 mOsmol hyposmotic shock (sample size 62 and 55, respectively). Whiskers indicate 1.5x SD value and the upper and lower edges of the boxes indicate the third and first quartile, respectively. The yellow line shows the median and the red line shows the mean. The round markers indicate the outliers.

4.2.5 Volume response of surviving cells show varying survival mechanisms

Figure 4.8 shows the long volume trace of individual cells that survive the hyposmotic shock and exhibit volume increase. For 190 mOsmol shock (Fig 4.8a), $\approx$ 40 min after the volume expansion, the cells start showing an increase in volume that can be attribute to growth and double to 2-3 generations in the time imaged . However, for a shock of 460 mOsmol and 960 mOsmol, the cells show different mechanisms of survival to the shock. In these two shocks, some cells start losing cell volume within 15 minutes and continue to lose volume for an hour or longer until they started exhibiting volume increase. This continued long drop in volume suggests a loss of internal solute through damaged cell membrane and cell wall. However, the fluorescent intensity did not drop during this volume reduction, which suggests that the cell did not lose larger solutes.

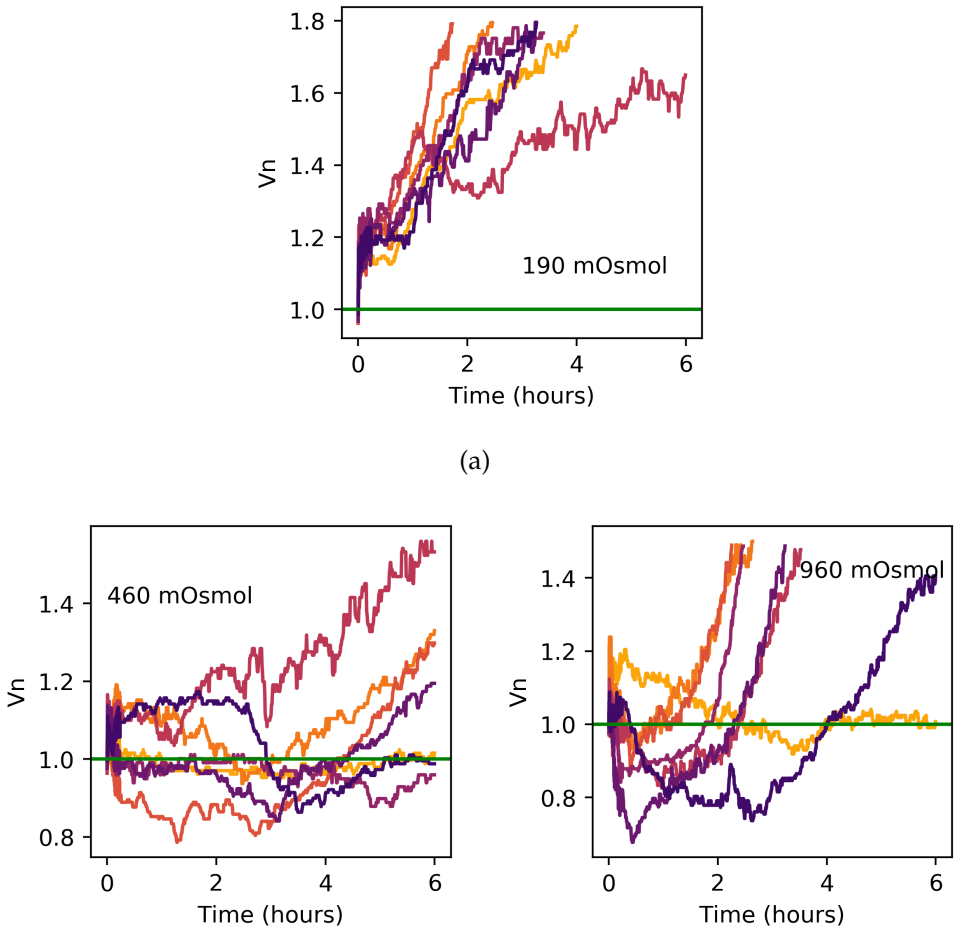

FIGURE 4.8: **Volume response of growing cells.** The individual V_n response of cells that grow following the (a) 190 mOsmol (b) 460 mOsmol (c) 960 mOsmol hyposmotic shock. To represent just the trend in volume response, the individual volume traces are filtered with median filter with window size of 15.

The volume response of the dying cell for 460 mOsmol and 960 mOsmol hyposmotic shock is shown in Figure4.9. Similar to the response of those cells that grew, some cells lost volume far below the pre-shock volume. After a certain time, the fluorescence intensity dropped below 20% , marking them as dead. A few cells remained swollen, without much change in the cell volume until they died.

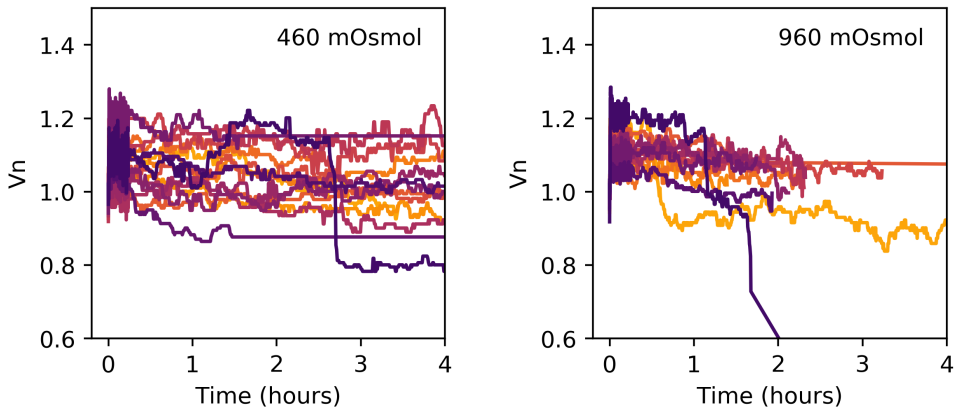

(a) (b)

FIGURE 4.9: **Volume response of dying cells.** The individual V_n response of cells that died following the (a) 460 mOsmol (b) 960 mOsmol hyposmotic shock. In these traces, the cell would have died at any point when they lost fluorescence, however,if the cell did not lose fluorescence completely, the cell volume can be observed.

4.2.6 Quality of surface attachment affects time of death

During the dying events, those cells that were not 'flat' or in other words, poorly attached to the coverslip died sooner than those that were 'flat'. The quality of attachment was measured as a flatness score. The details of the estimation are in Chapter 2 section 2.5.5. Briefly, to estimate the flatness score, cell's poles were identified and the intensity distribution along sections of cell's long axis were obtained. The distribution was symmetric about the two halves for a flat cell whereas a non-flat cell had a skewed distribution. Flatness score was then estimated from the skewness of the distribution. Poorer the cell's attachment to the surface, lower the score. Figure 4.10a exemplifies a 'flat' cell and 'non-flat' cell with the estimated flatness score. It is important to note that estimating flatness score has an error in the accuracy of measurement which could be due to the size of the cell, the maximum fluorescence intensity of a cell or also in identifying the poles of the cell. A plot of time of death versus flatness score for 460 and 960 mOsmol hyposmotic shock (Figure 4.10b) shows that the cells with lower flatness score died later.

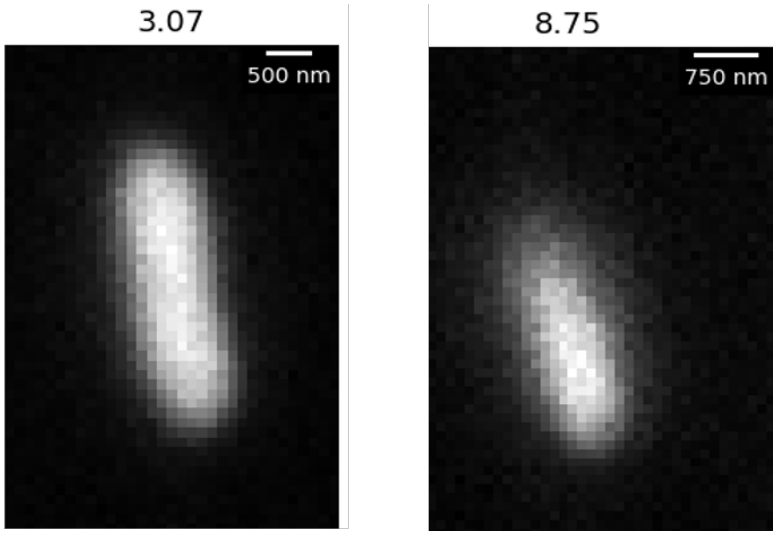

(a)

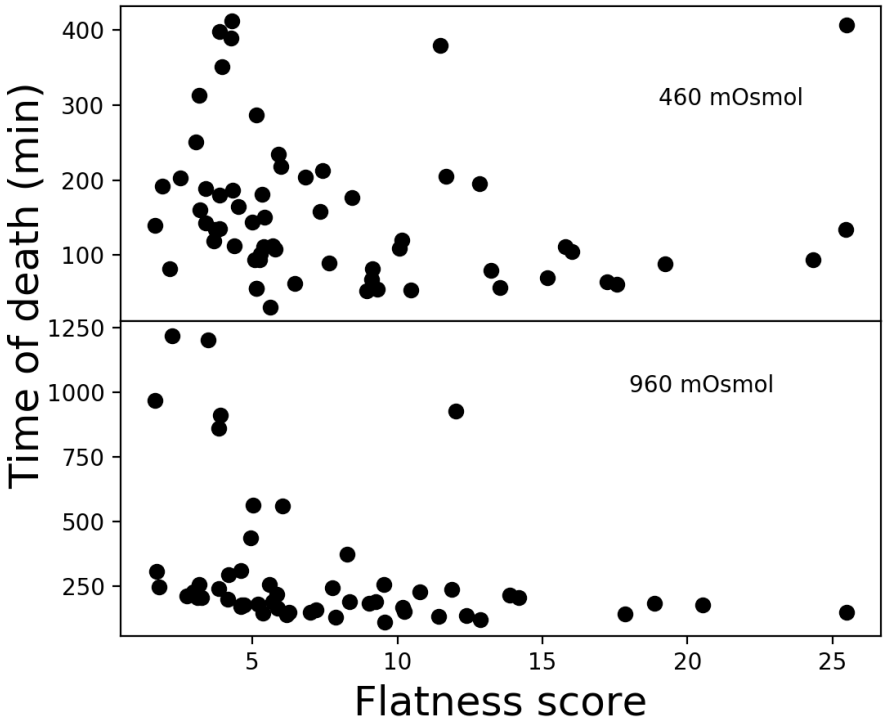

(b)

FIGURE 4.10: **Effect of surface attachment on death.**(a) Sample of two cells showing different quality of attachment to the surface. Cell on left is a well attached or 'flat' cell with a flatness score of 3.07. Cell on right is a poorly attached cell with a flatness score of 8.75. (b) Scatter plot of time of death (as shown in Figure4.7b) versus the flatness score for 2 varying hyposmotic shock (legend)

4.2.7 Growth media could influence survival to hyposmotic shock

Previously, using colony counting method, Edwards et al. (2012) observed a 0.4% chances of survival when hepta-mutant was grown in LB supplemented with 0.3 M NaCl and then subjected to hyposmotic shock with LB. In line with their results, for a 0.5 M NaCl (also in LB) downshock, Bialecka-Fornal et al. (2015) observed <1 % survival chance. However, in this chapter, an average of 46.07 and 36.76 % chances of survival was observed for 0.3 and 0.55 M NaCl hyposmotic shock (Figure 4.6). These differences in survival chances could be influenced by the composition of the growth media, prior or after the hyposmotic shock. For instance, wild-type cells in LB supplemented with 0.3 M or 0.4 M NaCl, I observed various wild-type cell phenotype that looked like blebs to that formed long chains as shown in Figure 4.11.

In Figure 4.11 a and b, frozen glycerol stocks (overnight cultures grown in MM9) were 10^5 diluted into fresh LB media with 0.3 M NaCl (Figure 4.11 c and d were grown with 0.4 M NaCl) and supplemented with 100 ug/ml of kanamycin. These cultures were then grown to early exponential phase OD_{600} with continuous aeration at 37°C. For Figure 4.11 e and f, cells were cultured similar to that done by Bialecka-Fornal et al. (2015). In this condition, overnight cultures of LB with 0.4 M NaCl were diluted 1:500 to fresh LB medium with 0.4 M NaCl and grown aerobically at 37°C until early exponential (OD_{600} of 0.2-0.3). However, substituting NaCl with sucrose as the osmolyte did not show cell chaining or blebs (Dario Miroli, unpublished). Though these experiments were tested in wild-type, similar morphologies can be expected in hepta-mutant. These differences in the cell morphology could indicate varying cell envelope properties and could lead to different chances of cell survival.

4.3 Discussion

In this chapter of the thesis, I have established the volume response of an *E.coli* that does not have any MSCs. The average volume response of hepta-mutant shows a fast swelling but not the characteristic recovery of the wild-type (Figure 4.1). Also, the maximum volume expansion of the hepta-mutant was higher than the wild-type or double-mutant for a given downshock magnitude (Figure 4.2). The highest $V_{n,max}$ for the hepta-mutant was ≈124% for

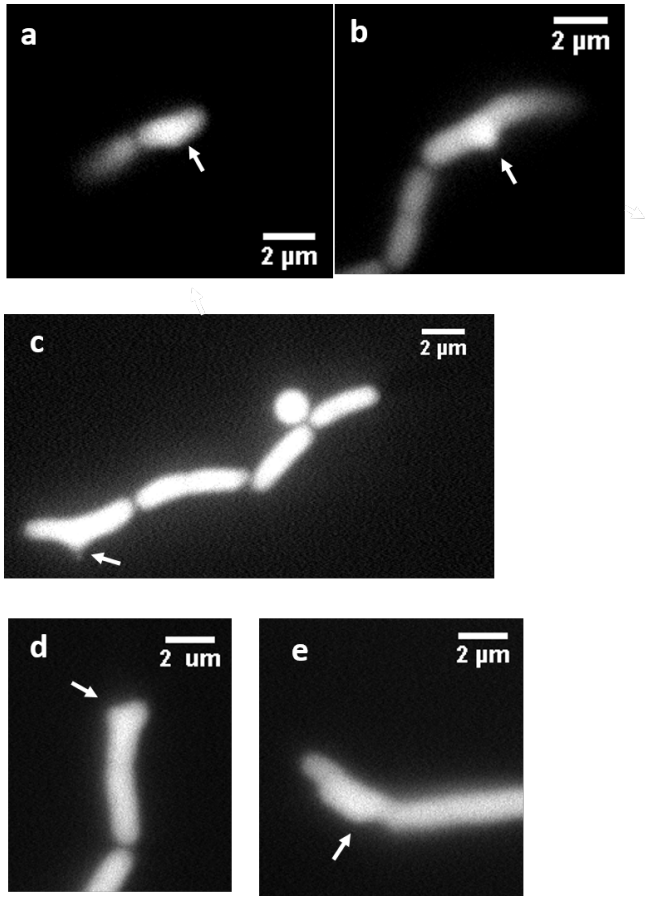

FIGURE 4.11: **Various morphologies of wild-type grown in LB supplemented with NaCl.** The cells grown in LB supplemented with NaCl showed various morphologies that looked like blebs, chaining and circular cells. (a) and (b) wild-type grown in LB with 0.3 M NaCl (c) wild-type cells cultured in LB with 0.4 M NaCl. The cells in a,b,c and d were 10^5 diluted from a glycerol stocks into fresh LB supplemented with 0.3 or 0.4 M NaCl (kanamycin as the selection marker) and grown with continuous aeration at 37 ° C until early exponential OD_{600}. (d) and (e) wild-type cells grown in LB supplemented with 0.4 MNaCl. The frozen glycerol were grown overnight in LB (with kanamycin) and 1:500 diluted into fresh LB supplemented with 0.4 M NaCl and grown until early exponential OD_{600} with continuous aeration at 37 ° C. Arrow points the location of cell bulging or blebs. *E.coli* BW25113 with cytoplasmic eGFP was used for these experiments.

a maximum shock of 1130 mOsmol. Starting from a hyposmotic shock of 100 mOsmol, for every 100 mOsmol increase in hyposmotic shock, the hepta-mutant showed ≈ 1% increase in cell volume as shown in Figure 4.2. Analysis of radial and length dynamics following three hyposmotic shocks show the volume increase due to longitudinal elongation. This could be due to the elastic anisotrophy exhibited by *E.coli* to axial and hoops stress (Yao et al., 1999; Deng et al., 2011).

A survival analysis of the hepta-mutant for three increasing shocks showed (Figure 4.6) an average of 3.3% chance of lysis for 190 mOsmol hyposmotic shock (corresponding to 0.125 M NaCl). To estimate the osmotic pressure of the cell at maximum cell volume expansion ($V_{n,max}$) following a 190 mOsmol shock, let's consider *E.coli* with a resting osmotic pressure of ≈ 1 atm (refer Chapter 3), so the osmotic gradient across the cell membrane/ cell wall (ΔC_0) is 0.04 Osmol/L (Buda et al., 2016). At a hyposmotic shock corresponding to 190 mOsmol (5.7 atm), $V_{n,max}$ of the hepta-mutant is ≈ 16% due to water influx and this swelling further dilutes the internal solute concentration by 16%. As the hepta-mutant shows no trace of solute efflux or volume recovery, the osmotic pressure across the cell membrane at $V_{n,max}$ estimates to 4.1 atm. The cell's remain in this pressure for ≈ 40 min, following which they show increase in cell volume due to growth (Figure 4.8a) without exhibiting any volume recovery. At this point it is not clear if the cells adjust the osmotic pressure before they start growing or continue synthesizing cell envelope materials even at cell's elevated osmotic pressure. However, the lag time exhibited by the hepta-mutant to survive a 4.1 atm hyposmotic shock is longer than that taken by the wild-type or double-mutant, which was less than <5 min (Figure 4.8a). A study of the cell wall properties using AFM, predicts a possible 12% stretching of the cell wall for an increase of 1 atm pressure (Yao et al., 1999) and a study on *E.coli*'s spheroplasts demonstrates that the lipid bilayer can increase area by 2.4 times attributing to the presence of membrane reserves (Sun et al., 2014). These studies could indicate that the hepta-mutant could withstand a 16% volume expansion following a 190 mOsmol hyposmotic shock and survive without the aid of MSCs to release the osmotic pressure.

The consequence of large hyposmotic shock on hepta-mutant's survival only starts affecting when the cell envelope undergoes irreparable damages. Similar to that observed by Reuter et al. (2014) and Bialecka-Fornal et al. (2015), the event of cell death at 460 and 960 mOsmol hyposmotic shock was noted

as the fading of cells due to loss of cytoplasmic fluorescence. Molecular Dynamics simulations demonstrate that the lipid bilayer at critical tensions form water pores which further enlarge to rupture the bilayer (Leontiadou et al., 2004). AFM studies demonstrate that the *E.coli* cell wall is a porous structure with a mean pore size of 10 nm Turner et al., 2013. These pores on the cell wall are large enough for an eGFP molecule (3-4 nm in diameter) to diffuse out of the cell. Damage in cell wall or not, the leakage of GFP from cytoplasm could be mainly due to the ruptures in the cell membrane. Additionally, the bright-field image of the died cell at the end of imaging time showed the appearance of 'ghost' cell (Figure 4.4d) indicating the loss of other larger molecules from cytoplasm and further suggesting possible cracks in cell wall through which these larger molecules diffused out. Reuter et al. (2014) demonstrated using electron microscopy the presence of similar ghost cells following a hyposmotic shock in a *E.coli* triple mutant ($MscL^{-}$, $MscS^{-}$, $MscK^{-}$). The mechanism of cell death was mainly due to the fading of the cell as shown in this Chapter and only 1-2 cells showed blebs following a hyposmotic shock. An average volume expansion for 460 and 960 mOsmol was 20 and 22%, respectively. At this increase in cell volume, lipid reserves could be used up to increase the cell surface area and hence limit their availability required for the formation of blebs.

While the volume response of some of the growing cells at 460 and 960 mOsmol show an increase in cell volume without fully recovering following the swelling, a few others showed a different mechanism of survival where they continued to lose cell volume for 1-4 hours before they started growing. The continued and gradual loss of cell volume for 1-4 hours could indicate damage to the cell envelope, leaking smaller solutes (as there was no loss in fluorescence). At some point (i) cells show increase in cell volume possibly suggesting damage control Figure 4.8a and b (ii) cells show a loss of fluorescence and death suggesting that the damage on the cell envelope was irreparable as shown in Figure 4.9a and b. These responses indicate that the role of MSCs starts becoming significant at higher hyposmotic shocks.

The faster dying of the poorly attached cells than the flat cells suggest a favourable chemical interactions between the cell envelope and poly-L-lysine (PLL), Figure 4.10. Strahl et al. (2010) demonstrated that PLL interacted with cell membrane and affected the proton motive force (PMF). However, it is not clear yet, the influence of PMF on pressurized cell death in my experiments.

Lonergan et al. (2014) compared the effect of surface attachment to PLL or gelatin on the permeability of fluorescent dyes Syto9 and Propidium Iodide (PI) in *E.coli* Dh5α. The permeability to Syto9 indicated a normal membrane integrity and the increased permeability to PI indicated damaged membrane. That study showed that higher permeability to PI in cells attached to PLL in comparison to those attached to gelatin, following a hyposmotic shock to 0.01 PBS and 0.1 PBS.

In conclusion, this Chapter shows that *E.coli* can survive a hyposmotic shock of 0.125 M NaCl without the MSCs. However, the longer lags in resuming growth than those cells that have MSCs can pose a risk of washing out in an environment with multiple competitors for nutrients. At larger hyposmotic shock, MSCs are important to release the cell envelope tension to overcome the damage to cell envelope.

Chapter 5

Influence of the environment composition on MSC gating

5.1 Introduction

Early studies on *E.coli* showed that they release cellular proteins and amino acid pool when downshocked to water (Britten et al., 1962; Neu et al., 1965; Nossal et al., 1966). The release of these solutes were later shown to happen via diffusion through the MSCs (Martinac et al., 1987; Sukharev et al., 1999). However, one study reported that *Pseudomonas ariginosa* released no cytoplasmic content upon hyposmotic shock (Glick et al., 1983) even though they have one MSC like *E.coli*'s MscL and two MSCs like Ec-MscS (Çetiner et al., 2017), suggesting that the MSCs did not gate during those experiments. Another study on *Bacillus subtilis* showed no recovery of cell length, following the cell length expansion upon hyposmotic shock with sorbitol. They noted that the recovery of cell length was observed when 500 mM KCl was added to the hyposmotic shock solution and the growth media (Rojas et al., 2017), indicating that MSCs were gating in that condition. In all these reports, there was no consensus as to why in some cases MSCs gate and do not in others.

In line with these studies, I report similar discrepancies observed during *in-vivo* measurement of cell volume response of *E.coli* to hyposmotic shock. In these experiments, wild-type cells did not show the characteristic volume recovery when downshocked to specific media components. The volume response was similar to that observed in hepta-mutant cells. The characteristic volume response was observed only when the wild-type cells were downshocked with solution made in a certain way. In this chapter, I report these seeming inconsistencies in the volume responses I observed and then identify

an ideal way to prepare buffers for hyposmotic shock experiments.

5.2 Results

5.2.1 *E.coli*'s hyposmotic shock response to MM9 buffer

In Chapter 3, to characterize the response of *E.coli* to increasing hyposmotic shocks, the cells were first grown in MM9 media supplemented with varying NaCl concentrations and then subjected to a hyposmotic shock with MM9 media as illustrated in Figure 5.1a. However, growing *E.coli* in varying NaCl concentrations introduces heterogeneity in the number of MSCs expressed (Bialecka-Fornal et al., 2012). Additionally, increasing NaCl concentration has been shown to affect the cell membrane composition, which thereby could affect the gating of MSCs (Romantsov et al., 2009; Sévin et al., 2014). To reduce this heterogeneity and to characterize the cell volume response to varying magnitude of hyposmotic shock, the cells were grown in MM9 medium supplemented with 650 mM NaCl, as illustrated in Figure 5.1b. Varying hyposmotic shock was next delivered using MM9 buffer (See Chapter 2 for buffer details) supplemented with increasing concentration of NaCl. The buffer was also supplemented with 100 mM Mg_2SO_4 for outer-membrane stability.

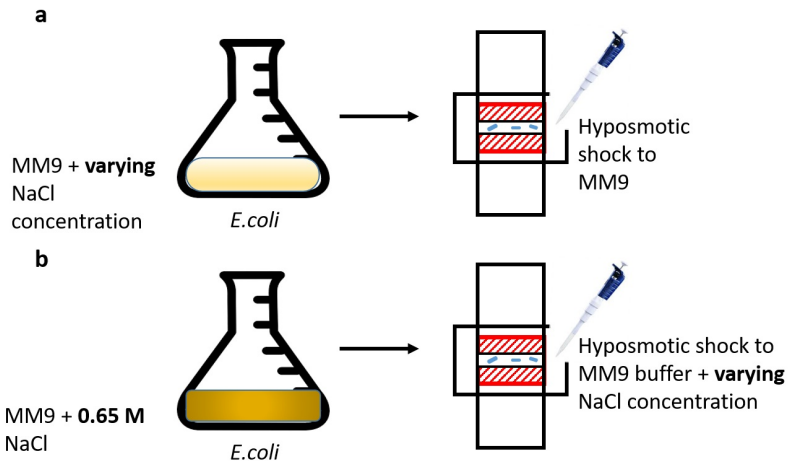

FIGURE 5.1: **Illustration of the experimental set-up for hyposmotic shock**

The Figure 5.2 shows the normalized cell volume responses to increasing hyposmotic shock. The V_n response for hyposmotic shocks 90, 180, 390 and

1114 mOsmol shows a response similar to the hepta-mutant, where following the cell volume expansion, the cells show no recovery of cell volume. A shock of 960 mOsmol shows a partial volume recovery, similar to that observed in the double mutant. A shock of magnitude 790 mOsmol shows volume recovery and signs of MSCs gating but on an average take longer time to reach the initial volume. The water used for preparing the MM9 buffers in Figure 5.2 was obtained from Purite (Suez Water Purification Systems, formerly Purite Ltd.) of purity 15 MΩcm.

5.2.2 Irreproducibilty of previous experiments

To assure that the response in Figure 5.2 was not due to the affect of growing cells at high NaCl on the cell membrane mechanical properties (Romantsov et al., 2009; Sévin et al., 2014) and in-turn its affect on MSCs gating, I next repeated the experiments in Chapter 3 Fig.SI8 by growing wild-type cells in MM9 media supplemented with varying NaCl concentrations and then shocked to MM9 buffer with no additional NaCl. Figure 5.3 compares the cell volume response to that has been done previously by Renata Buda, co-author Buda et al. (2016), in Chapter 3 Fig.SI8. Unlike that observed in Renata's experiments, the cell volume shows some volume recovery after hyposmotic shock, however, the average cell volume response was inconsistent with Renata's results.

5.2.3 No recovery of cell volume when downshocked to ultra-pure water

Between the two experimental set-up, the difference was the water filter unit in the laboratory. So the irreproducibility in volume response as shown in Figure 5.3 could have been due to the source of water used to prepare MM9 buffers. Nevertheless, a swollen cell with an increased cell membrane tension due to hyposmotic shock, ideally should gate MSCs unless there are channel inhibitors in the solution. To deconstruct the source of this ambiguity and to reduce the impurities in the hyposmotic solution, I next recorded the response of *E.coli* when hyposmotic solution was made from MiliQ water from Millipore (Merck). Generating MiliQ water includes two step purification. In the first step, water is passed through a Reverse Osmosis (RO) membrane, which results in a water with a purity of 15 MΩcm. In the second step, water is

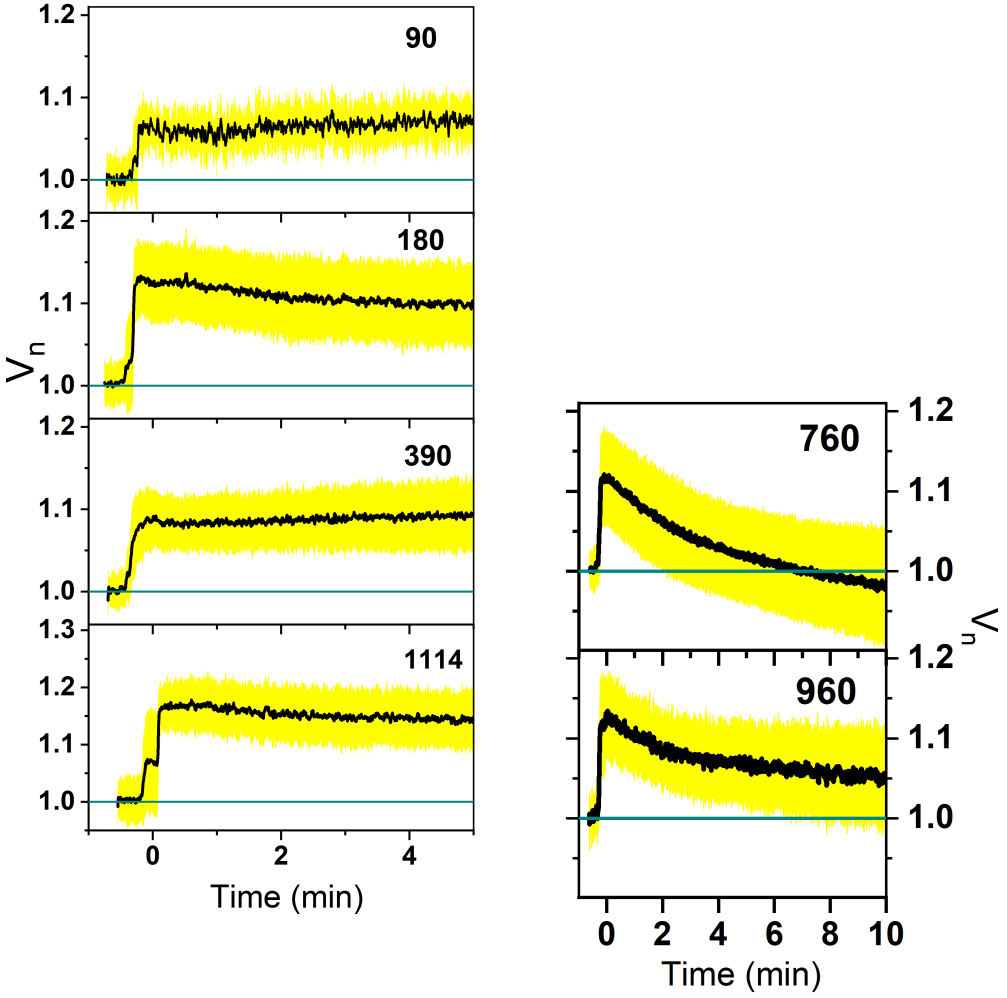

(a) (b)

FIGURE 5.2: **Average cell volume response to varying hyposmotic shocks**. *E.coli* grown in MM9 media with 0.65 M NaCl was subjected to varying hyposmotic shock using MM9 buffer with 0, 0.125, 0.225, 0.425, 0.55 and 0.575 M NaCl to deliver a final shock (mOsmol) and sample size respectively as follows: 1114, n=50 ; 960, n=19; 760, n=71; 390, n=71; 180 ,n=70 and 90, n=29. V_n is the cell volume normalized with initial volume. Black curve is the average of single cell volume response and yellow shaded region is 1 SD. The individual volume traces are filtered with median filter with window size 5 and aligned at maximum volume expansion before averaging.

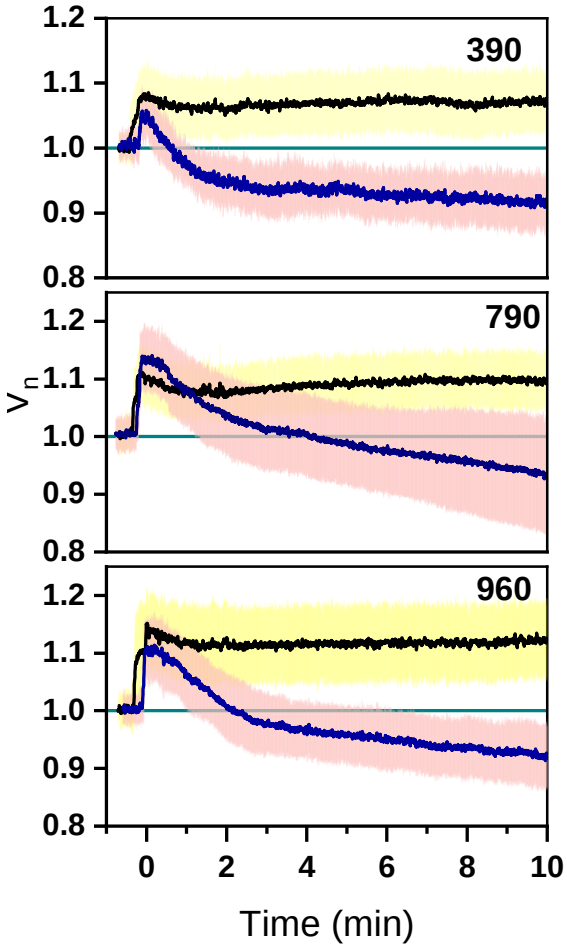

FIGURE 5.3: **Irreproducible cell volume response upon hyposmotic shock to MM9 buffer.** Cell volume experiments with MM9 buffer compared to the response as in by Renata's experiments. Blue curve is average V_n (n= 22, 35, 33 respectively for 390, 790, 960 mOsmol hyposmotic shock in legend) of previous experiment, Chapter 3 Fig.SI8. Black curve is the average V_n (n= 48, 40, 47 respectively for 390, 790, 960 mOsmol hyposmotic shock) response of the same experiment that I performed. Red and yellow shaded region is 1 SD. The individual cell volume is filtered with median filter of window size 5.

passed through ion exchange resins that remove traces of cations and anions contaminants in water up to a final water purity of 18 MΩcm (also termed ultra-pure water). Figure 5.4a, b and c show the cell volume response when downshocked to MiliQ water, phosphate buffer and MM9 media, both made using MiliQ water. Figure 5.4a, b and c show no volume recovery following the hyposmotic shock.

Figure 5.4b shows a comparison of maximum volume expansion ($V_{n,max}$) of wild-type, double-mutant and hepta-mutant grown in MM9 media supplemented with 0.55 M NaCl and then subjected to hyposmotic shock to MM9 media or MM9 buffer. $V_{n,max}$ of cells that do not gate in MM9 buffer (WT-B(1)) show higher volume expansion than those that gate in MM9 buffer (WT-B(2)). In this case, $V_{n,max}$ is comparable to that of hepta-mutant and double-mutant.

5.2.4 Recovery of cell volume in autoclave water, in presence of $CaCl_2$

Next, the water from Purite filter unit that was autoclaved in borosilicate glass was used for testing of volume response. Hyposmotic shock to this water did not show gating of MSCs. However, addition of 0.1 mM $CaCl_2$ to this water showed volume recovery as shown in Figure 5.5a. Phosphate Buffer Saline (PBS) from the same water source did not show gating of MSC and gating was only observed when supplemented with 0.1 mM $CaCl_2$. The volume response shows full volume recovery and characteristic volume overshoot as observed in Chapter 3 Fig.2. Due to the presence of K^+ in PBS, the cells in Figure5.5b also show increase in volume following the overshoot by actively pumping K^+ into the cytoplasm (Chapter 3 Fig. 6a).

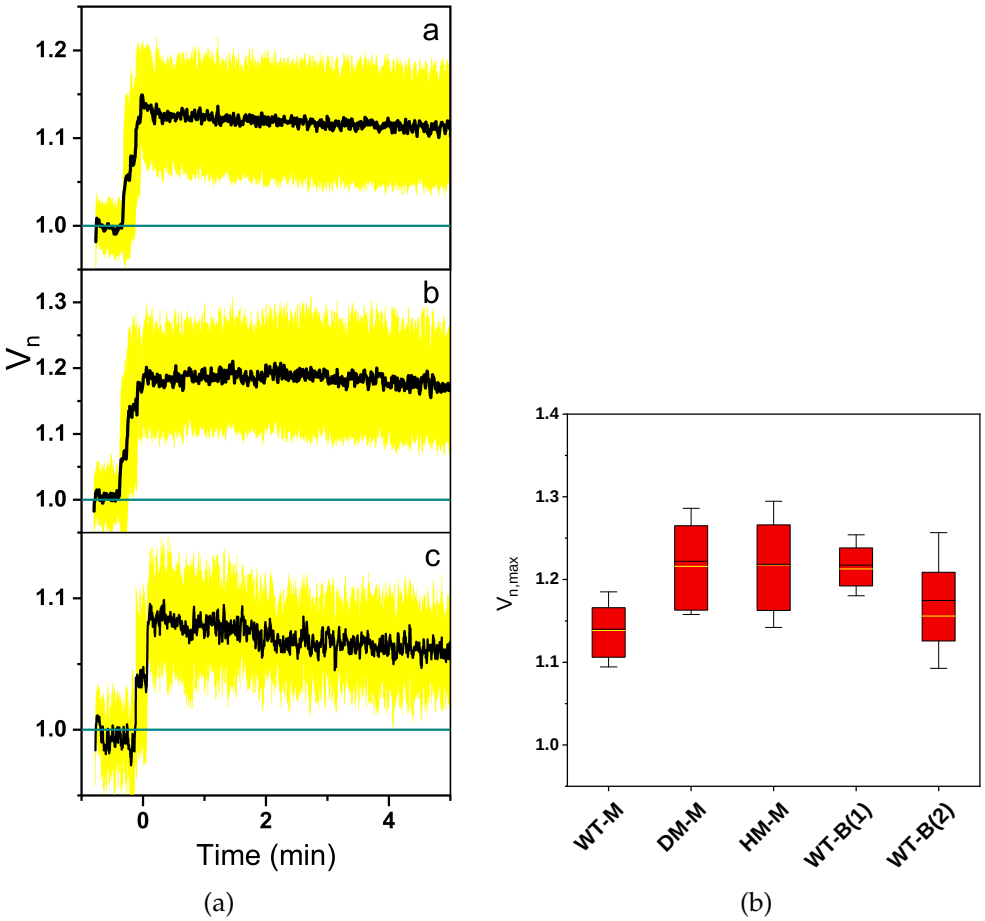

FIGURE 5.4: **Downshock to solution made from ultra-pure water shows no volume recovery** The average cell volume response upon hyposmotic shock to (a) water (n=32) (b) phosphate buffer (n=12) (c) MM9 media (n=9). The source of water used is 18 MΩcm MiliQ (Millipore). (d) Comparison of maximum volume expansion ($V_{n,max}$) when cells were grown in MM9 media supplemented with 0.55 M NaCl (1200 MOsmol) and shocked to either MM9 media (240 mOsmol) or MM9 buffer (214 MOsmol). WT-M: wild-type shocked to MM9 media (Chapter 3), n=119; DM-M: double-mutant shocked to MM9 media (Chapter 3), n=50; HM-M: hepta-mutant shocked to MM9 media, n=99; WT-B(1): WT shocked to MM9 buffer (experiment I repeated, black curve Fig 5.2b), n=47 ; WT-B(2): WT shocked to MM9 buffer (experiment performed by Renata, blue curve Fig 5.3b), n=33

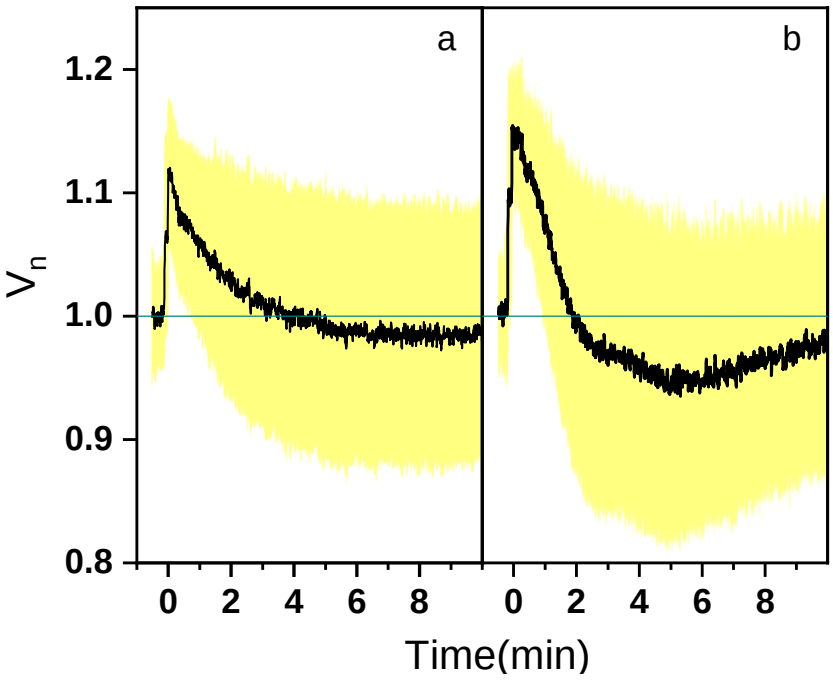

FIGURE 5.5: **Distinct gating of MSCs.** Average cell volume response of wild-type grown in 0.65 M NaCl, upon hyposmotic shock to (a) water with 0.1 mM $CaCl_2$, n=19 (b) phosphate buffer saline with 0.1 mM $CaCl_2$, n=17. The source of water in the shock solution is 15 M Ωcm water, from Purite water unit and then autoclaved in borosilicate glass bottle before use.

5.3 Discussion

In this Chapter, I have discussed the discrepancies I have observed in volume responses of *E.coli* upon hyposmotic shock.The cells showed fast volume expansion following a hyposmotic shock but no volume recovery that was characteristic of MSCs gating. This was observed later during the course of Ph.D, after completion of the work in the Chapter 3. However, this inconsistency in volume responses was not observed while studying the response to MM9 media in Chapter 3, Fig. 2, by the co-author or me. The MM9 media for these experiments were prepared using MM9 salts solution made by the media preparation facility in the building, provided by the School of Biological Sciences at the University. The facility used 15 MΩcm Purite water for preparation of MM9 salt solution and these were then autoclaved in the facility for use.

The initial plan of the work flow for this chapter was to study the hyposmotic shock response of culturing *E.coli* as shown in Fig 5.1. For these experiments, I prepared 18 MΩcm MiliQ water to culture cells and deliver hyposmotic shock solutions. The inconsistency in cell response noted in this chapter directs to the switching of water sources used in these experiments. While MSCs did not gate in buffers or MM9 media made from MiliQ water, channel gating was recovered when downshocked to water or PBS that was prepared from autoclaved water from Purite filter unit (from media preparation facility) and supplemented with 0.1 mM $CaCl_2$ (Figure 5.5). The goal of this chapter is not to compare the performances of the two filter units (Merck and Purite) or to identify the path through which the tracer solutes were introduced or eliminated in the final downshock solutions but to merely report the observation that could be further useful for science community in future.

Previously, Tomasek et al. (2018) observed that during dilution of *E.coli* to PBS solution for flow-cytometry analysis, the mean fluorescent signal of various intracellular fluorescent protein dropped over time and affected cell survival. In that study, the cells initially grown in LB media were diluted in to PBS, so this resulted in a hyposmotic shock. If the fluorescent proteins were to diffuse through MSCs that opened following a downshock to PBS, the loss of solute should have not lasted longer than 5 min for this hyposmotic shock. However, the loss of fluorescence was on the order of 100-180 min. The slow loss of fluorescence and loss of viability of these cells suggest that the loss of fluorescence occurred through the damaged cell envelope, similar to that observed in the hepta-mutant (Chapter 4 4.6). The study also hints that the MSCs were not gating in their experiments. The authors also noted that the addition of outer-membrane stabilizing ions, Mg^{2+} and Ca^{2+} to PBS overcame the loss of fluorescence and loss of viability. This study supports the ambiguity in MSC gating that I observed in this chapter. The source of this discrepancy indicate the presence of certain kind of solute in the buffer that could potentially block the gating of MSCs and the addition of Ca^{2+} was necessary to undo this effect (Figure 5.5). It is not clear yet the effect of Ca^{2+} on membrane properties or it's role in MSC gating. However, it is important to note that the previous downshock experiment into MM9 buffer, which showed MSCs gating (performed by Renata, Fig 5.3 blue curves) do not include Ca^{2+} in MM9 buffer. At the same time, MM9 media also includes $CaCl_2$, however, MM9 media made from

MiliQ water did not show MSC gating. Thus, these evidences suggest the existence of a synergistic interaction between certain ions in the autoclaved water and Ca^{2+} that interferes with the gating mechanism of MSCs.

The inability of MSCs to gate when downshocked to ultra-pure water or MM9 media made from ultra-pure water (Figure 5.4 a,b and c) suggests that the filter unit was unsuccessful in removing tracer impurities that was potentially blocking the channel gating. It has shown previously that Gadolinium (Gd^{3+}) inhibited larger MSCs in *E.coli* (Berrier et al., 1992) and other rare earth elements including Gd^{3+} were shown to inhibit stretch activated channels in *Xenopus* oocyte (Yang et al., 1989). A recent geographical survey identified the presence of Gd^{3+} in tap water and water bodies in various locations, globally (Ebrahimi et al., 2019). The contaminant was as high as 0.23 nmol/kg in tap water from Hinze Dam, Australia and a similar content was found in Västerdalälven river, Sweden. Though, it is not known about the presence of rare earth elements in Scottish water, the inability of MSCs to gate suggests a possible presence of Gd^{3+} or other rare earth elements in this water.

A cation and anion chromatography analysis of commonly found ions in ultra-pure water and the autoclave water are tabulated in Table. 5.1. Due to the unavailability of standards of known concentrations of Ca^{2+} or Gd^{3+} in the chromatography facility, the analysis was limited to those controls available as shown in Table. 5.1. The ion concentration in both the water source were comparable except 1.458 ppm of phosphate ion and 0.446 ppm of sodium ion found in ultra-pure water. Gd^{3+} has a ionic radius of 0.938 Å and that of Ca^{2+} and Na^{+} are 0.99 Å and 0.97 Å, respectively (Yang et al., 1989). The lower ionic radius of Gd^{3+} indicate a possibility of finding it in ultra-pure water in comparable levels to that of Na^{+}, provided there is presence of Gd^{3+} in the water before filtration. An estimation of theoretical concentration of NaCl alone in water at 25 $^{\circ}$C is 0.2 ppb corresponding to 18 M Ωcm (Whitehead, 1997). However, the concentration of ions found in Table 5.1 is significantly higher than that expected for water of 18 MΩcm. This overestimation of ions could be possibly introduced by the level of cleaning of glassware used to prepare elution buffers for chromatography analysis in the facility. A further detailed study on the content of trace impurities using mass-spectrophotometry or ion-chromatography is necessary to further elucidate the nature of impurities found in water.

Using differential scanning calorimetry, lanthanides and calcium ions bound

TABLE 5.1: **Analysis of some of the commonly found ions in water, using ion chromatography** The water samples from MiliQ and autoclaved Purite water filters were analyzed for commonly found ions in water. The MiliQ water sample shows a presence of higher NaCl and phosphate ion than the water sample from Purite water filter

Ions	**ppm MilliQ (18 MΩcm)**	**ppm Purite autoclaved (15 MΩcm)**
Fluoride	0.493	0.483
Chloride	0.689	0.585
Nitrite	0.088	0.093
Nitrate	0	0
Phosphate	1.458	0
Sulfate	0	0
Lithium	0	0
Sodium	0.446	0
Ammonium	0	0
Potassium	0	0

to phospholipid, DPPC, have been shown to increase the phase transition temperature of DPPC by increasing the order and compaction of individual lipid molecules (Li et al., 1994). This order is also noted to reduce the fluidity of the membrane. Ermakov et al. (2010) hypothesized that the increase in the compaction of the lipid molecules could increase the lateral pressure across the hydrophobic core and stabilize the closed-state of MSCs. There are no evidences on the effect of lipid physical properties on the gating of MSCs. A study on the effect of cholesterol on the viscoelastic properties of DPPC have been previously demonstrated using amplitude-modulation-frequency-modulation (AM-FM) technique of multifrequency AFM (Al-Rekabi et al., 2018). A similar analysis can be applied to study the effect of tracer impurities on the *E.coli*'s membrane and gating of MSCs.

Chapter 6

Dynamic clustering regulates activity of MSCs

6.1 Introduction

In-contrast to membrane embedded ion channels, MSC are largely non-specific to the solutes that can pass through them. While this non-specificity helps bacteria restore osmotic pressure during a hyposmotic shock, it can also cause excess loss in solute, which can also lead to volume overshoot during recovery (Chapter 3). Cell's passive response to hyposmotic shock opens a question of another level of control that could fine tune cell's responses to hyposmotic shock. Possible answers to this question directs at the debate on co-operative gating of MSCs clusters in the cell membrane (Fernandes et al., 2017; Ursell et al., 2007). Evidences of clustering of MscL was first demonstrated by Grage et al. (2011) using multiple techniques like fluorescent microscopy, patch-clamp, AFM and small angle neutron scattering (SANS). Their patch-clamp results indicated that clustering resulted in non-linear gating in MscL. However, Van Den Berg et al. (2016) demonstrated that the clustering of MscL could be an artifact of fluorescent tags as these fluorescent proteins exhibit high inter-protein interaction. Therefore, assessing the extent of MscL aggregation using *in-vivo* imaging techniques has proven to be difficult and hence opens a need to explore orthogonal ways to investigate the aggregation phenomenon.

The consequences of non-linear gating of MSCs due to clustering (Grage et al., 2011) could impact the dynamics of cell volume and pressure, during hyposmotic shock. Hence, the *in-vivo* volume analysis can be developed as a tool to assess the clustering of MSC. In this study, I first consider the evidences

of MscL clustering demonstrated by the large MscL clusters in AFM and patch-clamp technique (Grage et al., 2011). Next, develop a minimal *in-silico* model that captures the co-operative gating of MscL clusters and its implications on cell responses during hyposmotic shock. The model could be further used to make experimentally testable predictions.

This work is done in collaboration with Dr.Andela Saric and Alexandru Paraschiv from University College of London, UK. They developed a Coarse Grained (CG) model of MSCs interacting with each other and the lipids. I use their results of the CG model to apply it to the previously developed phenomenological model, described in Chapter 3 (Buda et al., 2016). With these minimal computer model, I demonstrate that the coupling between the membrane tension, MSC confirmation changes and clustering produces a tightly controlled gating system that serves to protect the cells from excessive gating during cell volume recovery, upon hyposmotic shock and also in steady-state. This collaborative work is currently published in PRL (also can be found in bioRxiv) as *'Dynamic clustering regulates activity of mechanosensitive membrane channels* and can accessed as below. The paper along with the supplementary information is included in AppendixB.

Paraschiv, Alexandru et al.(2020).“Dynamic clustering regulates activity of mechanosensitive membrane channels”. In:Phys. Rev. Lett.124, 048102
DOI:10.1103/PhysRevLett.124.048102
URL:https://journals.aps.org/prl/abstract/10.1103/PhysRevLett.124.048102

In the first section of this Chapter, I briefly introduce and summarize the results of the CG model that is relevant to develop the phenomenological model. With the phenomenological model as described in Chapter 3 as the foundation, in the second section of the Chapter, I further develop the phenomenological model that includes the MSC co-operative gating and it's implications on cell volume responses. Some of the content of this Chapter has been adopted from the manuscript Paraschiv et al. (2020) and certain content has been rewritten to follow the monograph style of the thesis.

6.2 Summary of CG Model

The CG model developed by the co-authors Alex and Andela is briefly summarized in this section. The results relevant for the development of the phenomenological model is included in the section, further details of the model can be referred in Paraschiv et al. (2020) or in AppendixB. The MSC in the model is a rod-shaped where the 5 subunits connected by weak springs (Figure 6.1a) and each rod is made of 7 core hydrophobic and two hydrophilic head beads. The rods were maintained longer than the membrane thickness to reproduce the hydrophobic mismatch between the protein and the lipid layer. The beads in a rod were connected by strong elastic bonds and angular potential. The lipid bilayer was a three-beads-per-lipid model, where the single rod diameter was twice the radius of a lipid bead and the inner part of the channel was lined with hydrophilic beads to overcome lipids from overflowing inside the channel. The explicit non-specific inter-protein attractions was modelled by including an attractive patch of beads on the external side of each rod.

A gas of inert "solute" beads was placed on one side of the membrane to generate hyposmotic shock and the collisions of the beads with the membrane created membrane tension (γ), which was linearly proportional to the solute concentration difference across the membrane. Upon hyposmotic shock, the transmembrane components of the MSC interacted attractively with the hydrophobic layer of the membrane while maintaining the contact with the expanding lipid bilayer. This led to channel rods tilting with respect to one another, resulting in the lateral expansion of the channel. The gating of MSC was measured by measuring the MSC radius of gyration tensor ($R_G^{xx^2} + R_G^{yy^2}$). Upon application of hyposmotic shock, the pore size increased immediately to allow for the passage of the solutes. The pore size increased sharply around the membrane tension of $\gamma = 0.50$ mN/m, which was taken as the threshold MSC opening tension (Figure 6.1b) and above this threshold, the channels were set as 'open' and below as 'closed'. The non-specific inter-protein attraction lead to the formation of clusters of MSC of sizes between 2 and ~ 15 MSCs. They observed that MSCs clusters exhibited cooperative gating as shown in Figure 6.1c . The Figure 6.1c demonstrates that pore size of the 2 channels increased with increasing separation with each other. Figure 6.1d demonstrates that at lower membrane tensions ($\gamma = 0.70$ mN/m), the channels remained in cluster but at higher membrane tension ($\gamma = 1.70$ mN/m) channels were isolated,

which further led to increased probability of gating (Figure 6.1d inset)

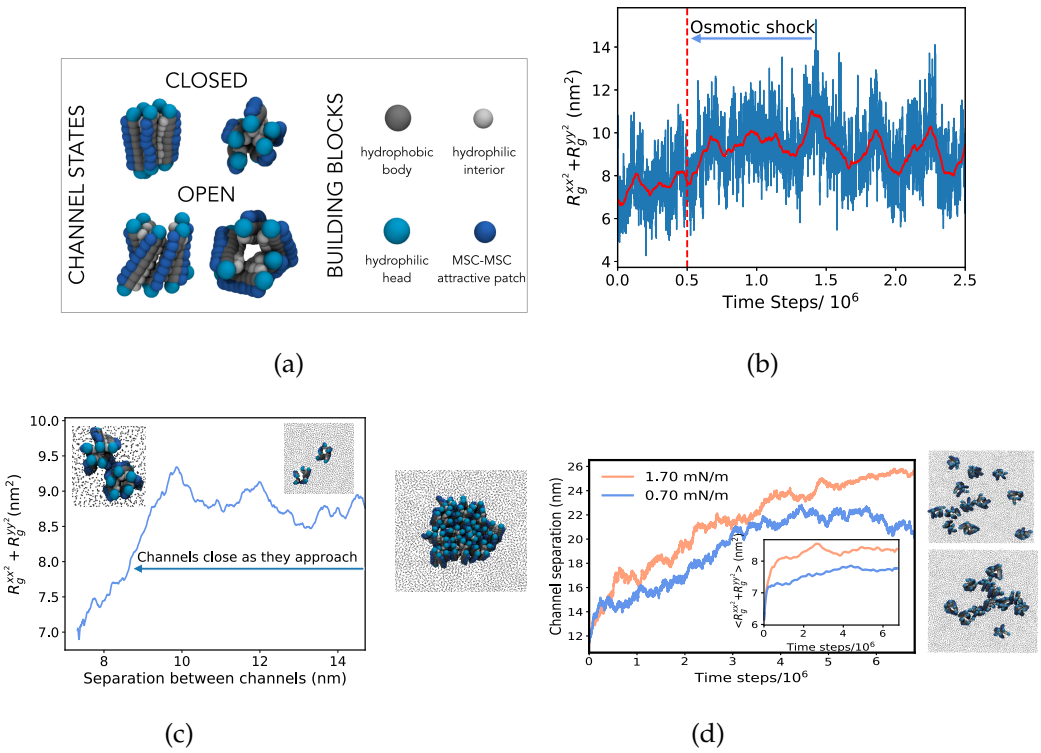

FIGURE 6.1: **MSC clustering leads to co-operative gating that is dependant on membrane tension. The figures and captions are adopted from Paraschiv et al. (2020).**MSC is presented as a collection of rods connected by weak springs. Each rod consists of overlapping hydrophobic beads (depicted in gray) and hydrophilic heads (in cyan) and is $\approx$ 10 nm long. Channel inside is lined with hydrophilic stripes (silver).Explicit inter-channel attractions can be turned-on via an external hydrophobic patch (dark blue). (b) Pore size oscillations of a single MSC. The dashed vertical red line marks the occurrence of an instantaneous osmotic shock corresponding to the membrane tension of γ = 1.2 mN/m, which leads to an increase in the average pore size. (c)Average pore size of two MSCs as a function of distance between them (γ = 1.30 mN/m). (d)The average distance between the channels increases in time and is larger for higher membrane tension (γ = 1.70 mN/m, shown in orange versus γ = 0.70 mN/m, shown in blue) Far right: The snapshot of the cluster configuration in the last time-frame. Inset: The probability of channel opening increases as the simulation progresses.

6.3 *In-vivo* model development and bridging with CG model

To capture the effect of MSC clustering on whole cell responses, the results of CG model can be summarized as *(i)* the probability of opening ($P_{opening}$) of a channel is dependant on membrane tension and decreases with the increasing size of the MSC cluster *(ii)* clustering of MSC is reduced at higher membrane tensions. At a given membrane tension, the number of clusters of a given size is given by probability of cluster formation $P_{formation}$. These results formed the basis of the phenomenological model. The details of the model described in this section is the collaborative work of the co-author, Alex and I, the description of the model details are adopted from Paraschiv et al. (2020).

The probability of opening of a channel in a cluster of size N, $P_{opening}(N, \gamma)$, is given as:

$$P_{opening}(N, \gamma) = a_1 \cdot (1 - a_2 \cdot e^{-C_1\gamma})e^{-C_2 N} \tag{6.1}$$

The functional form was chosen to agree with the results of CG simulations, where a numerical fit gave $a_1 = 1.68 \pm 0.14,\ a_2 = 0.92 \pm 0.06,\ C_1 = 0.93 \pm 0.22,\ C_2 = 0.49 \pm 0.06$.

$P_{formation}(N, \rho, \gamma)$ is the probability of formation of cluster of size N and at a given membrane tension and channel packing fraction (ρ) is given as below.

$$\rho = N_{MSC} \cdot a_{MSC}/A_c \tag{6.2}$$

N_{MSC} is the total number of MSCs and a_{MSC} is the surface area of an MSC and A_c is the surface area of *E.coli*.The functional form of $P_{formation}$ was obtained by considering the probability of formation to be a geometric distribution and CG simulations indicated that the $P_{formation} \propto \rho/\varepsilon$, where ε is the interaction energy between two channels. For brevity and to be in the context of my contribution to the work, the details of $P_{formation}$ derivation are not included here Paraschiv et al. (2020). The final form of $P_{formation}(N, \rho, \varepsilon)$ is given below.

$$P_{formation}(N, \rho, \varepsilon) = e^{((1-N)A/\rho\varepsilon + ln(1/\rho\varepsilon) + B)} \tag{6.3}$$

The constants $A = 0.009 \pm 0.001kT$ and $B = -8.32 \pm 0.054$ were estimated by fitting the results to the CG simulations. To derive an expression for ε,

a correlation between the effective interaction energy between two channels with tension was assumed, as higher tensions lead to conformations that are more tilted, the channels are less likely to interact with each other. As the tension increased,the tilting of the subunits reduced the contact area between the neighbouring channels in the cluster, reducing the interaction energies between the two channels as shown in Appendix II, Fig S10. Paraschiv et al. (2020), also reported that higher tensions also suppressed membrane thermal fluctuations, which resulted in unbinding of two channels. The dependence of channel interaction on tension was noted be sigmoid, as given below.

$$\varepsilon = a/(1 + e^{-c(\gamma - d)}) + b, \tag{6.4}$$

where a, b, c and d are the parameters determined from the fitting the data to the CG model ($a = 0.59 \pm 0.067kt$, $b = -1.97 \pm 0.17kT$, $c = 18.43 \pm 0.40$ m/mN, $d = 0.74 \pm 0.14$ mN/m).

Scaling the parameters between the two models. It is important to make a note that the functional forms of $P_{opening}$ and $P_{formation}$ were obtained by fitting to CG model, which captures the phenomenon of MSC clustering, considering the mechanical properties of membrane. However, the CG model does not include the effects of cell wall on the membrane mechanical properties or does not capture the exact *in-vivo* osmotic gradient across the cell envelope. For instance, in CG model, a tension increase of ≈ 3 mN/m ruptured the membrane, whereas, *in-vivo* values of membrane tension increase has been found to be between 1-25 mN/m (Evans et al., 2003). The tension on the cell membrane can be estimated as shown in the Figure 6.2.

For an *E.coli* cell, with a resting osmotic pressure of 1 atm and cell radius of $\approx$0.5 um, the lateral tension on the cell membrane is 50 mN/m and for a 15% volume increase during a hyposmotic shock, this tension can rise upto 80 mN/m. Thus, the overall increase in membrane tension is 30 mN/m. Previous *in-vitro* studies report that the probability of MscL opening is half for a membrane tension ranging from 8-14 mN/m (Belyy et al., 2010). In order to scale the *in-vivo* membrane tension with the tensions in the coarse-grained model, I chose a mid-value of 11 mN/m.

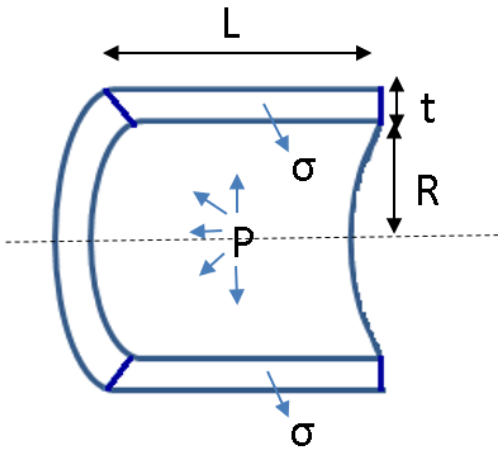

FIGURE 6.2: Diagrammatic representation of stress (σ) in a section of a pressurized thin-walled cylinder. Hoop stress acting on the cylinder is given by $\sigma = PR/t$, where R is the radius of the cylinder, t is the thickness, P is the turgor pressure on the wall. Hence, the wall tension (γ) can be estimated as $\gamma = PR$

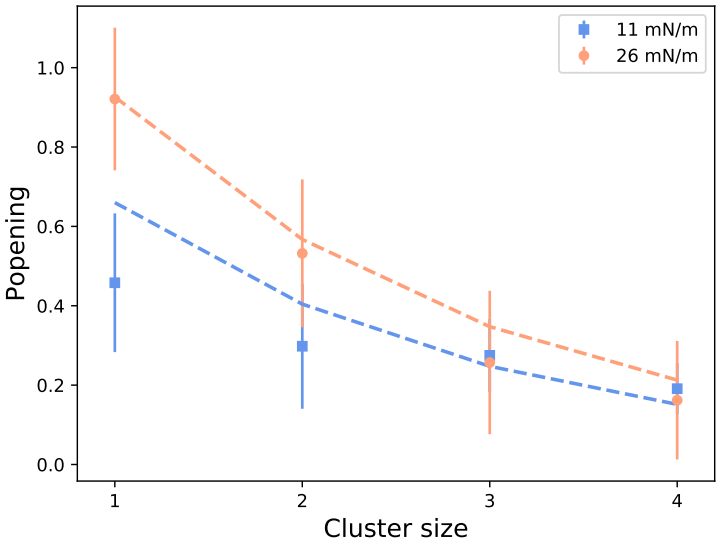

FIGURE 6.3: **Probability of opening per channel versus cluster size at two *in-vivo* values of membrane tension.** As the cluster size increases and the tension decreases, the probability of opening per channel decreases.

Similarly, from the Chapter 3 experimental results and cell volume recovery model, I scale the parameters of $P_{formation}$ in CG model such that at 4%

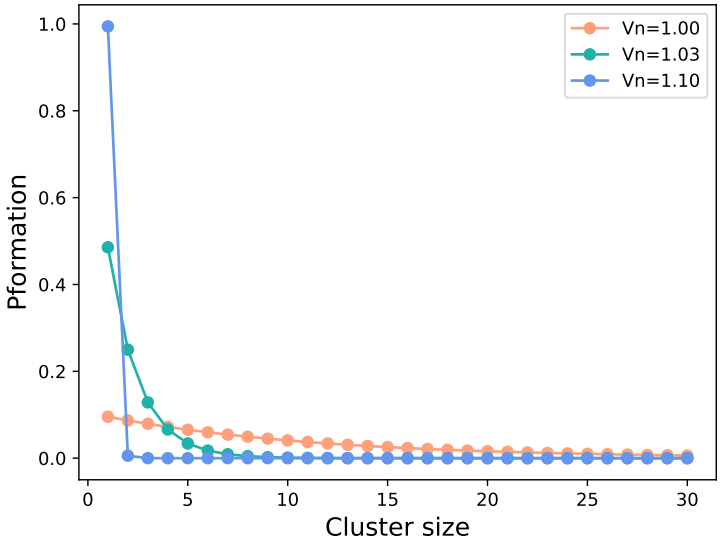

FIGURE 6.4: **Probability of formation of a channel cluster at varying membrane tension.** The probability of formation of a cluster,$P_{formation}$, calculated using Eq 6.3 at varying normalized cell volumes (V_n), at 0.5% packing fraction.

cell volume increase all the channels are monomers (Buda et al., 2016) The 4% increase in cell volume was estimated as the threshold of MSCs gating in Chapter 3 for a 960 mOsmol shock.The constants of $P_{formation}$ are then $a = 19.371kT$, $b = -19.73kT$, $c = 1.675$ m/mN, $d = 3.715$ mN/m, respectively.

The above two key results of CG model (Eq. 6.1 and 6.3) was then connected to the phenomenological model using a feedback parameter $\beta(N, \rho, \gamma)$. Where β is the effective probability of gating of all the MSCs in a cell at a given membrane tension. β is given as below,

$$\beta = \sum_{N=1}^{30} P_{opening}(N, \gamma) \cdot P_{formation}(N, \rho, \gamma) \tag{6.5}$$

$P_{opening}$ is given by Eq. 6.1 and $P_{formation}$ is given by Eq. 6.3. We group together clusters larger than *N=30* as $P_{opening}$ and $P_{formation}$ were negligibly small for *N>30*.

I next included channel clustering into the previously developed phenomenological model of *E.coli*'s cell volume recovery upon hyposmotic shock (Chapter 3). In Eq.9 Chapter 3, A is a continuous variable, A=0 when the channels are closed and A=1, when the channels are open. The channels were approximated

as open or closed according to a certain cell volume threshold, which was estimated by the experimental fit. The effect of clustering on cell volume and solute can be included by introducing β in place of A. The Master equations (Eq.9 and 14 of Chapter 3) for the cell volume change and solute concentration change can be written as below:

$$\frac{dV}{dt} = (\beta + 1)V_m K RT \left[(\frac{n_i}{V} - c_e) - e^{\sqrt[3]{\frac{10}{3}\pi} \frac{E_0 l (V^{\frac{1}{3}} - V_0^{\frac{1}{3}})}{\Delta c_0 RT V^{\frac{1}{3}} V_0^{\frac{1}{3}}}} \cdot \Delta c_0 \frac{V_0^{\frac{1}{3}}}{V^{\frac{1}{3}}} \right] \tag{6.6}$$

$$\frac{dn_i}{dt} = -\beta \cdot (V_m K \cdot \frac{n_i}{V} \cdot e^{\sqrt[3]{\frac{10}{3}\pi} \frac{E_0 l (V^{\frac{1}{3}} - V_0^{\frac{1}{3}})}{\Delta c_0 RT V^{\frac{1}{3}} V_0^{\frac{1}{3}}}} \cdot \Delta c_0 RT \frac{V_0^{\frac{1}{3}}}{V^{\frac{1}{3}}} + \alpha(\frac{n_i}{V} - c_0)). \tag{6.7}$$

I fitted the parameter values K and α to an experimental representative singe cell volume response as these two parameters were associated with the properties of channels and expected it to be different from the previous estimations and fixed rest of the parameters at values previously determined (Buda et al., 2016). The fitting was performed using Scipy packages in Python. The 0.96 Osmol hypoosmotic shock was achieved by growing *E.coli* in media with elevated NaCl concentration and then suddenly exposing the cells to the same media but without NaCl. Growing in elevated NaCl (specifically 550 mM) results in expression of $\approx$ 1300 MscL (Bialecka-Fornal et al., 2012). The packing fraction at this experimental condition is 0.5%, calculated based on the area of a single MscL (24 nm^2 (Grage et al., 2011)) and surface area of *E.coli* (6 μm^2 based on the experimentally obtained cell volume of 1.338 fL (Buda et al., 2016)). The obtained fit values for K and α were 7.0$\times$10^{-22} molPa^{-1}s^{-1} and 0.37 fls^{-1}.To predict the cell responses when the channels existed solely as isolated channels or dispersed, $P_{formation}$ and $P_{opening}$ in Eq.6.5 was calculated for $N = 1$.

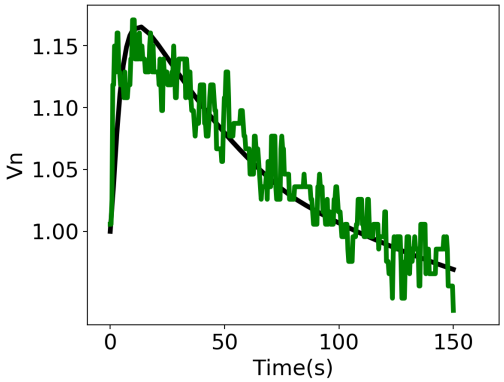

FIGURE 6.5: Model fit (black) to a representative experimental volume trace (green) at 960 mOsmol hyposmotic shock and ρ=0.5%

Model fit to an experimental trace assumed that MSCs cluster *in-vivo* and this was done only to visualize the *in-vivo* dynamics of MSC cluster aggregation and dis-aggregation during a hyposmotic shock. The fit to model also allowed to predict the cell volume response in a scenario where the MSCs did not cluster.

6.4 Dynamic MSC clustering regulates cell volume

Figure 6.6 illustrates the predicted dynamics of cluster aggregation and dis-aggregation as the cell volume expands and recovers during a hyposmotic shock. Probability of observing channels as isolated monomers ($N = 1$) and as aggregates (shown here for for $N = 5$) are given as in color scale. The Figure 6.6 demonstrates that larger clusters were less likely to form at the point of maximum volume expansion i.e., when the tension was largest on the cell membrane and was more likely to re-aggregate as the membrane tension relaxed during volume recovery.

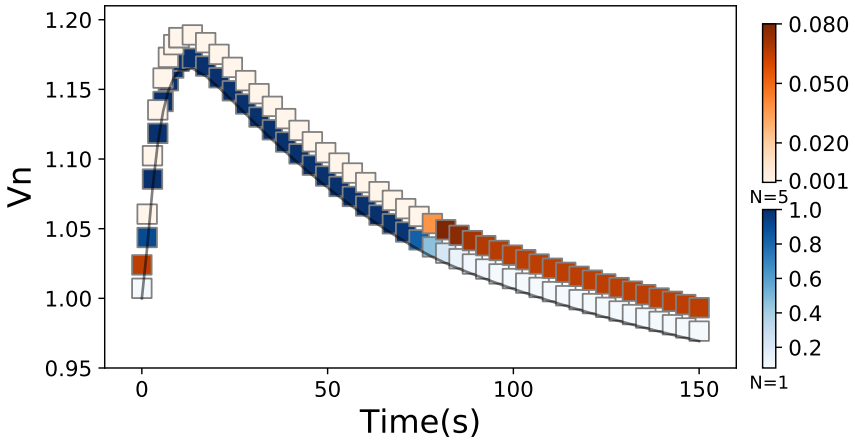

(a)

FIGURE 6.6: **Illustration of channel aggregation and dis-aggregation.** Dynamics of channel clustering during cell volume recovery (gray faded line), V_n, upon 0.96 Osmol hyposmotic shock and 0.5% channel packing fraction. Colorbars: $P_{formation}$ or probability of finding a single isolated channel (blue) and a cluster of 5 channels (orange)

The cell volume response if the channels never clustered and existed solely as dispersed channels can be compared to that if they clustered as shown in Figure 6.7a. The difference between the clustered and dispersed model can be observed during the volume recovery, where the clustering reduced the volume overshoot. To understand this further, Figure 6.7b compares the probability of channel opening (β) with time, for a clustered and dispersed model. β for dispersed model was calculated by considering *N=1* in Eq.6.5. β in the clustered model showed an earlier closing of the channels due to the re-aggregation of channels during volume recovery. This early closing of channels resulted in lesser volume overshoot while compared to the dispersed model.

6.4.1 Trade-off analysis of clustering on cell volume and membrane tension regulation

To further illustrate the effects of increasing amount of clusters on cell volume response, the amount of clusters in the cell was further increased by increasing the interaction energy between 2 channels in Eq. 6.4. This was done by increasing the scaled constants a and b up to 10 times. This Figure 6.8a demonstrates the cell volume response as the level of clustering increases. Figure 6.8b further

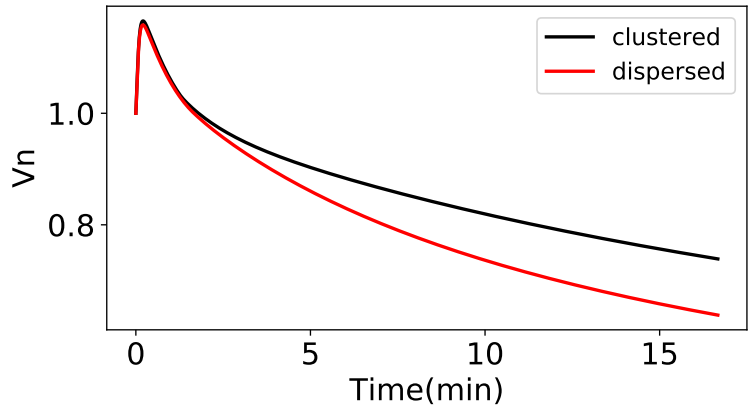

(a)

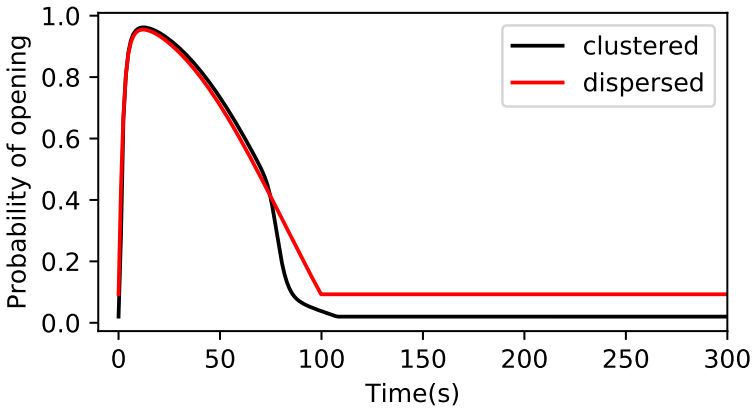

(b)

FIGURE 6.7: **Clustering regulates channel closing to overcome leaky cell membrane.**Comparison of (a) cell volume dynamics (b) probability of opening (β) dynamics between a clustered model (black line) and dispersed model (red line) during a 0.96 Osmol hyposmotic shock and 0.5% channel packing

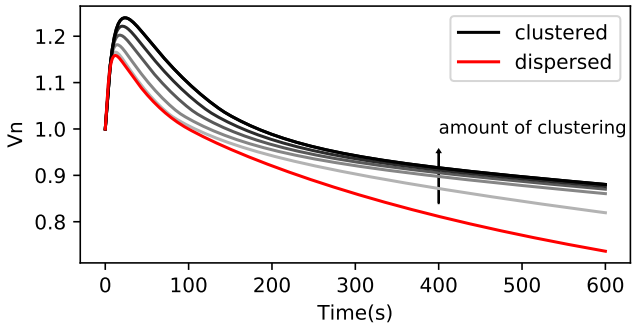

(a)

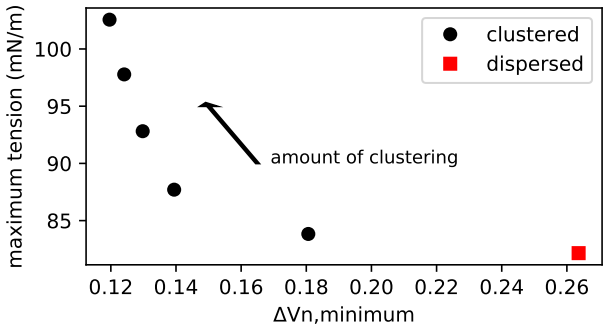

(b)

FIGURE 6.8: **Effect of increased amount of clustering on the cell tension and overshoot upon hyposmotic shock.** (a) Effect of increasing the extent of clustering (increasing the protein-protein attractions in Eq. 6.4), on cell volume dynamics (grey and black lines) in comparison to dispersed channels (red line) (b)Maximum tension on the cell membrane at maximum volume expansion is plotted against difference in volume overshot below the initial volume ($\Delta V_{n,min}$). The osmotic shock is 0.96 Osmol and packing fraction is set to 0.5%.

shows the maximum tension on the cell membrane at maximum volume expansion (Figure 6.7a) plotted against the minimum cell volume ($\Delta V_{n,minimum}$) during volume recovery. At lower amount of channel clustering, the cells benefited by reducing the volume overshoot while compared to the dispersed model. But at higher amount of clusters, the benefit of reducing $\Delta V_{n,minimum}$ was traded off by the burden on cells due to increased cell membrane tension, risking cell lysis.

6.5 Discussion

In this study, supported with the results of CG model, I have demonstrated that spontaneous aggregation and dis-aggregation of MSC clusters during a hyposmotic shock, regulates the cell volume response. The feedback parameter β (Eq. 6.5) regulates the the probability of a channel opening, depending on the tension on the membrane and the channel surface packing fraction (Eq. 6.2), which in turn controls the cell volume response during hyposmotic shock (Fig: 6.6). The MSC clustering controls unnecessary gating of the MSCs as shown in Figure 6.7b and reduces the volume overshoot when they encounter a hyposmotic shock Figure 6.7a. These results align well with the study by Grage et al. (2011) in which the aggregation of *E.coli* MscL reconstituted in lipid vesicles led to a significant decrease in the total gating activity. Their patch-clamp experiments showed that a number of active channels in a patch was consistently lower than the total number of channels. These results were further reinforced by SANS measurement of the total membrane area increase when the channels were open, which was smaller than what would have been expected if the channels were behaving independently.

The model prediction of the effect of clustering on cell volume regulation can be probed experimentally by studying the volume recovery following hyposmotic shock for varied levels of the clustering. Van Den Berg et al. (2016) demonstrated that the MscL can be clustered by tagging each individual MscL subunit with fluorescent protein and clustering can be reduced by reducing the number of fluorescent tags per MscL channel. Using these results, a comparison of volume response of native MscL with fluorescence-tagged MscL could provide evidences on the importance of clustering on cell volume regulation. Also, cluster aggregation and dis-aggregation dynamics upon hyposmotic shock as shown in Figure 6.6 can be further visualized by tagging MscL. The amount of clustering can also be increased by increasing the surface fraction of MSC by expressing them with additional copies of the MSC gene, in the cell.

The dis-aggreagtion of clusters at higher membrane tension (Figure 6.1d) enables the channel to gate with higher probability, without impeding it's function during hyposmotic. However, if the amount of clustering was increased more than that predicted by CG model, the clusters could not disaggregate completely, resulting in lower probability of MSC gating and excessive volume

expansion during hyposmotic shock (Figure 6.8a). The increased volume expansion could pose a threat to damage cell envelope, similar to that observed in hepta-mutant (Chapter 4).

The value of β at steady-state show a 2% and 10% chances of gating if clustered or dispersed model(Figure 6.7b) . These were also observed in the CG model which showed that isolated channels have a non-zero probability of gating even at zero tension (Paraschiv et al., 2020). These results can be supported with results of patch-clamp experiments on single-channel gating, where it is evident that the channel opening does not follows a step function (Belyy et al., 2010). This gating of channels could be crucial when MSCs are over-expressed, e.g. when bacteria grow under hyperosmotic conditions or when they enter stationary phase (Stokes et al., 2003; Bialecka-Fornal et al., 2012), the probability of single channel gating even under quiescent conditions would be sufficiently high to cause a potentially significant loss of cytoplasmic content. For example, a 10% gating of dispersed channels at steady-state, could lead up to 20% volume loss in a period of 10 min. This could be significant, especially for a dormant cell in stationary phase; thus channel aggregation, which is more pronounced at higher channel numbers, could be a natural self-defence mechanism of bacteria against unnecessary gating, contributing to bacterial survival. Along the same lines, our results indicate that the MSC expression *in-vivo* is possibly finely tuned (Figure 6.7a), such that it enables efficient cell volume recovery, but prevents unnecessary volume loss.

Chapter 7

Optimizing osmotic extraction of periplasmic protein

7.1 Introduction

Global Biologics markets that include recombinant proteins like mAbs, vaccines, gene therapy etc., rely on living cell factories, prokaryotic and eukaryotic cells for production of biologics. Over a third of the biologics market uses *E.coli* as the cell factory and these proteins can be either intracellular (cytoplasmic or periplasmic) or extracellular. Routinely, cytoplasmic proteins are extracted from cells by lysing the cells, resulting in higher protein yields but proves to be costly due to the rigorous downstream processing needed to eliminate the impurities endogenous to the cell. On the other hand, periplasmic proteins can be easily extracted using osmotic shock, resulting in cleaner extraction but lower periplasmic extraction yields. The efficiency of extraction of periplasmic proteins can be improved by understanding cell's responses to osmotic shock.

The osmotic extraction of periplasmic protein involves a hyperosmotic shock with sucrose as the solute and followed by a hyposmotic shock to water (Nossal et al., 1966). Sucrose is slowly permeable through outer membrane and cell wall of *E.coli* but is not permeable through the cell membrane. A hyperosmotic shock with sucrose results in plasmolyzed cells due to water diffusion out of the cell (Pilizota et al., 2013). The water flow also drags the periplasmic content out through the outer membrane. *E.coli* cell wall has an effective pore size of 10 nm (Turner et al., 2013) and hence is permeable to large molecules and proteins. The outer membrane of *E.coli* act as molecular sieve, that limits the permeability of larger molecules (Hancock, 1987; Vázquez-Laslop et al., 2001). The size exclusion of outer membrane is through proteins that belong to the

category of porins. OmpC and OmpF are the two important porins that allow passive diffusion of ions and larger molecules, like nutrients, antibiotics, etc. across the outer membrane. Crystal structures of OmpC and OmpF are found to be very similar (Baslé et al., 2006) and studies have revealed pore diameter of $\approx$ 1.0-1.2 nm (Benz et al., 1985). *E.coli* outer membrane has been shown to exclude proteins larger than 100 kDa (Vázquez-Laslop et al., 2001).During the subsequent hyposmotic shock, as the plasmolyzed cell membrane starts recovering tension due to water influx, it starts pushing the periplasmic contents out of the cell. These two osmotic shocks enables the extraction of periplasmic protein.

In this chapter, I address some of the challenges of periplasmic protein extraction from *E.coli*, faced by the industry collaborator, FUJIfilm Diosynth Biotechnologies. As a model periplasmic protein, I use a human antibody protein, Hel4—used in FUJIfilm. Hel4 is a single domain antibody (dAbs) isolated from phage library of human dAbs whose molecular weight is 13kDa (Jespers et al., 2004). Hel4 was found to be soluble without forming aggregates upto a concentration of 38 mg/ml. Thermal unfolding monitored using circular dichroism indicated that unfolding of secondary structure started at 65°C, that was reversible when the temperature was brought back to 25°C and the protein completely denatured at 85°C. These thermal properties are beneficial for manufacturing processes like lyophilization and additionally, it's human origin makes it an excellent candidate for therapeutic uses.

Hel4 is expressed using pAVEway ^{TM} system (Lennon et al., 2014) that can be induced using IPTG and is tagged with OmpA secretion system to assist the transfer into the periplasm. FUJIfilm follows a standard two-step osmotic shock protocol for extraction of periplasmic proteins at the end of the fermentation as illustrated in Figure 7.1. Centrifugation step prior to hyperosmotic and hyposmotic shocks add additional cost to the company. In first part of this Chapter, I demonstrate that the first centrifugation step can be removed by directly adding sucrose to the fermentation medium. I next compare the yields of extraction if sucrose was replaced with NaCl. In the second part of the Chapter, I address the issue faced by FUJIfilm in the production of Hel4, which is it's leakage during fermentation. I identify the path of Hel4 leakage during fermentation and their role in Hel4 extraction.

7.2 Results

7.2.1 Simplification of osmotic extraction

E. coli W3110 K-12 (termed CD1441 for in-house use) is used in FUJIfilm to produce Hel4 and Hel4 is estimated using Coomassie stained protein gels. The details on culturing CD1441 and protein estimation protocol are in Chapter 2 section 2.6 and 2.6.2. When following FUJIfilm fermentation and extraction protocol as shown in Figure7.1, I proceeded as follows: (i) CD1441 is induced with IPTG to express Hel4 and is cultured upto stationary phase (end of fermentation or EOF) in LB medium (ii) EOF culture is next centrifuged to obtain cell pellet (iii) Cell pellets were subjected to a hyperosmotic shock of 880 mOsmol using a 0.58 M sucrose in Tris buffer, pH 8.0 (iv) the shocked solution was centrifuged to separate the cell pellets and the supernatant was used for Hel4 estimation using Coomassie stained gels (v) hyposmotic shock of 1280 mOsmol was administered to the cell pellets using 5 mM Mg_2SO_4 in MiliQ water (vi) hyposmotic shock solution containing Hel4 was then centrifuged to separate the cell pellets and the supernatant was then used for Hel4 estimation. This extraction protocol is termed Standard protocol.

The total amount of protein extracted is defined by yield in Eq. 7.1. The amount of Hel4 expressed for a gram of biomass is estimated by lysing cells at EOF (Step1, Figure 7.1). The amount of Hel4 leaked during the fermentation was estimated from the supernatant of EOF. In the yield estimation, the amount of Hel4 leaked was included in the estimation of total Hel4 expressed. I have not characterized the correlation between Hel4 leaked to Hel4 expressed which is beyond the scope of this project. The final yield which is the sum of yields after hyperosmotic and hyposmotic shock for Standard Protocol is 0.1961. In other words, 19.61% of total Hel4 expressed by cells was extracted using Standard Protocol (Table 7.1). An average of 15.87% of the total Hel4 was lost through leakage during fermentation (see Chapter 2 section 2.6.2 for details on protein estimation using Coomassie staining).

$$yield = \frac{Hel4\ extracted(\mu g)}{biomass(g) \cdot \frac{Hel4\ expressed(\mu g)}{biomass(g)}} \tag{7.1}$$

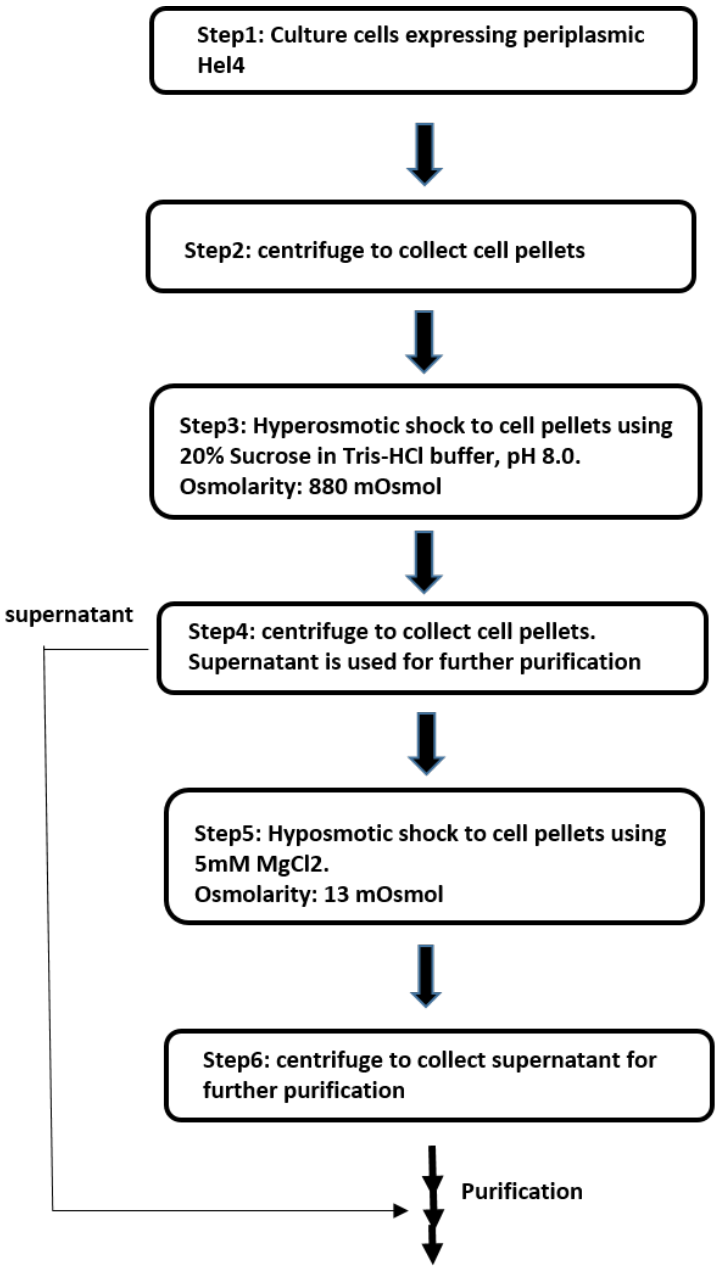

FIGURE 7.1: Standard protocol for osmotic extraction of periplasmic Hel4

TABLE 7.1: Comparison of yields of osmotic extraction of Hel4 following hyperosmotic and hyposmotic shock. Standard Protocol is the routine method of Hel4 extraction in FUJIfilm (Figure 7.1). In 2 and 3, sucrose or NaCl (equimolar with sucrose in Standard Protocol) is added to the fermentation medium to deliver hyperosmotic shock. A step of centrifugation is skipped in 2 and 3 while rest of the steps following the hyperosmotic shock are similar to Standard Protocol. The error in the box is 1SD. Total yield is the sum of yields from hyperosmotic and hyposmotic shock. The error in total yield is estimated using error propagation.

Osmotic shock protocol	Hel4 yield (hyperosmotic)	Hel4 yield (hyposmotic)	Total yield
1.Standard Protocol	0.10 ± 0.02	0.10 ± 0.02	0.12 ± 0.03
2.Sucrose added directly to EOF culture	0.02 ± 0.005	0.15 ± 0.03	0.17 ± 0.03
3.NaCl added directly to EOF culture	0.03 ± 0.02	0.25 ± 0.07	0.28 ± 0.07

To simplify the Standard Protocol and reduce the cost of periplasmic protein extraction, I looked into eliminating the centrifugation step before the hyperosmotic shock in the Standard Protocol (step (ii) of Standard protocol). A hyperosmotic shock in Step (iii) can be delivered by adding solutes directly to the EOF culture medium, bypassing the step of centrifugation. I here compared the effects of adding equimolar concentrations of sucrose or a cheaper substitute like NaCl to the EOF culture. The osmolarity of sucrose and NaCl at a concentration of 0.58 M were comparable. Following this hyperosmotic shock, the steps of standard protocol were followed. The total yields of Hel4 following the hyperosmotic and hyposmotic shock are tabulated in Table 7.1. Total yields were comparable to that of Standard Protocol and addition of NaCl resulted in 8% higher yield than the Standard Protocol.

7.2.2 Leakage of Hel4 through OmpC

The leakage of Hel4 during could have been occurring through the outer-membrane porins, OmpC and OmpF. To investigate this, *E.coli* Δ*ompC* or Δ*ompF* Keio mutants expressing periplasmic Hel4 were used. The mutants were grown and induced as followed for CD1441. Growth rates of Δ*ompC* and Δ*ompF* mutants respectively are 0.466 h^{-1} and 0.689 h^{-1} before induction. Following the induction with 100 uM IPTG the growth rates dropped to 0.321 h^{-1} and 0.537

h^{-1}, respectively. Growth rates of CD1441 before and after induction are 0.855 h^{-1} and 0.599 h^{-1}, respectively. An overall growth reduction of $\approx$ 30% is observed in both CD1441 and $\Delta ompC/\Delta ompF$ mutant, suggesting that the expression of Hel4 in these mutant did not affect any other physiological process under the present experimental conditions.

The culture supernatant at EOF of $\Delta ompC$ Figure7.2 lane 4 shows no leakage of Hel4 into the fermentation medium. On the other hand, $\Delta ompF$ mutant shows no control over Hel4 leakage (Figure 7.3 lane2). These two experiments indicate that Hel4 was leaking through the porin OmpC.

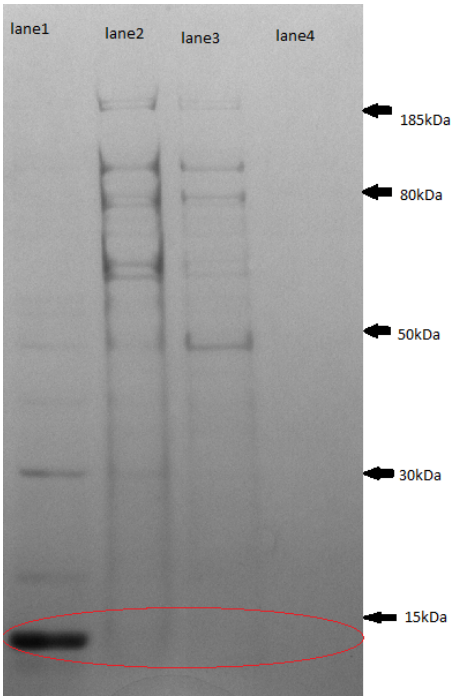

FIGURE 7.2: Coomassie stained protein gel with samples from $\Delta ompC$ mutant. Lane 1: cell lysate supernatant from EOF. Lane2: 480 mOsmol upshock with 0.58M sucrose in Tris-HCl. Lane3: 880 mOsmol downshock following the upshock in lane2. Lane 4: EOF culture supernatant, showing no leakage of Hel4 into the growth medium. The red ellipse in the image indicates the location of Hel4 in the gel, where the size of Hel4 is 12kDa.

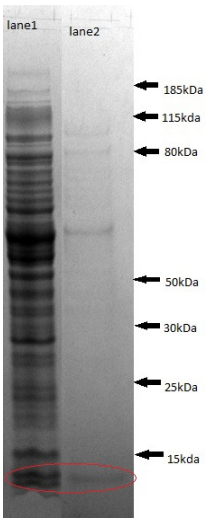

FIGURE 7.3: Coomassie stained protein gel with samples from Δ*ompF* mutant. Lane 1: Cell lysate from EOF. Lane 2: cell culture supernatant at EOF showing leakage of Hel4 through OmpC. The red ellipse in the image indicates the location of Hel4 in the gel, where the size of Hel4 is 12kDa.

7.2.3 Extraction of Hel4 in Δ*ompC* mutant

A 480 mOsmol upshock, followed by 880 mOsmol downshock in Δ*ompC* mutant (Standard Protocol) showed no success in extraction of Hel4 protein, Figure7.2 lane2 and lane 3. However, a very high hyperosmotic shock of $\approx$ 3100 mOsmol (7.4.2 lane 2) using 1.85M sucrose solution showed extraction of Hel4.

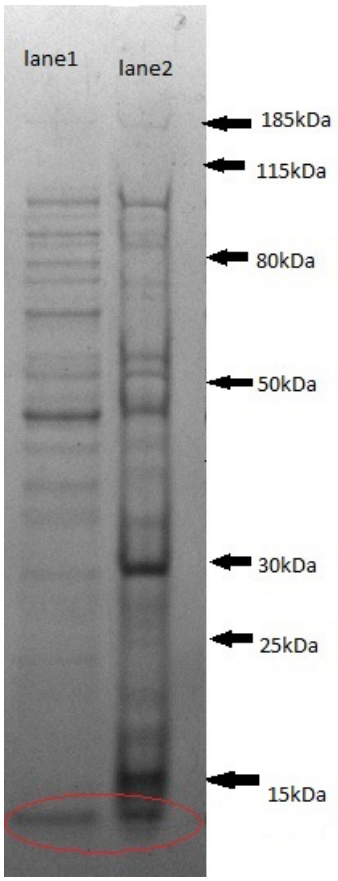

FIGURE 7.4: Coomassie stained protein gel with samples from Δ*ompC* mutant. Lane 1: EOF cell lysate. Lane 2: EOF cell pellet subjected to hyperosmotic using 1.85M sucrose solution. Presence of high concentration of sucrose makes the sample very viscous resulting in higher background noise as seen in lane 2. The red ellipse in the image indicates the location of Hel4 in the gel, where the size of Hel4 is 12kDa.

7.3 Discussion

In this Chapter of the thesis, I have explored the industrial applications of osmotic shock to extract periplasmic protein, Hel4. In the first part, I have demonstrated that the centrifugation Step (ii) in the Standard Protocol can be deducted by directly adding sucrose or NaCl to the EOF culture, without compromising on yields of extraction. The direct addition of NaCl resulted in 8% higher total yield (Table 7.1). Even though the yield estimated after hyperosmotic shock includes Hel4 leaked into the fermentation medium, the yields are five-fold lower than that of Standard Protocol. This could be due to the slower dissolution of salts into the solution, inducing a slow hyperosmotic

shock. This could be addressed by diluting a concentrated sucrose or NaCl solution into the EOF culture. The hyposmotic shock that followed a hyperosmotic shock resulted in a higher yield due to the reduced extraction of Hel4 in hyperosmotic shock. Additionally, the plasmolyzed cells in LB medium (400 mOsmol), following a hyperosmotic shock are capable of recovering cell volume and osmotic pressure through active import and synthesis of osmolytes (Pilizota et al., 2014). The cells as a result could have possibly experienced higher hyposmotic shock than the Standard Protocol.

The total yield in Standard Protocol does not include Hel4 lost through leakage. Addition of solutes directly to EOF culture, not only could deduct a centrifugation step but also recover the leaked Hel4 into the final yields. The effect of adding NaCl on three different kinds of monoclonal antibodies (mAb) were shown to stabilize the mAb in the solution by reducing their aggregation and reducing the viscosity of the solution (Sudrik et al., 2017). The stability of the protein was hypothesized due to the exclusion of water molecules by electrostatic interactions of NaCl at protein surface. In agreement with this study, addition of NaCl upto 1.5M was shown to have no effect on mAb aggregation at pH range of 5-8; aggregates were shown to form at pH lower than 5, which was reversible when the salt was removed (Bickel et al., 2016). These studies support that the addition of 0.58M NaCl could improve the stability of the Hel4 during the extraction. However, the cost saved by skipping the centrifugation step needs to be weighed against (a) the cost of processing large scale culture at the end of hyperosmotic shock, while in the Standard protocol the volume of hyperosmotic solution was scaled down and so resulted in lower volume that was processed further (b) the cost on the amount of NaCl needed to introduce a 880 mOsmol hyperosmotic shock. The result from these experiments were discussed with FUJIfilm for further implementation in industrial set-up.

In the second part of this work, I have identified that Hel4 leakage occurs through the porin OmpC (Figure 7.2). Previous studies have identified that the growth at higher osmolarity media results in increased OmpC expression than OmpF (Hall et al., 1981). It is uncertain at this point that if the leakage of Hel4 through OmpC is due to it's physical properties like charge, hydrophilicity or due to the higher copies of OmpC in LB media than OmpF. The evidence for latter is stronger here as Figure 7.4 suggests a larger osmotic shock was successful in extracting Hel4 in a $\Delta ompC$ mutant and the inhibition in extracting

was possibly limited by the copies of OmpF porins. An optimal concentration of sucrose in the hyperosmotic shock buffer could be estimated to extract Hel4 in Δ*ompC* mutant without comprising on its yields compared to its wild-type counter-part. Alternatively, *E.coli* can be genetically engineered to introduce *ompC* under the regulation of an externally inducible promoter, whose expression can be induced at EOF and before osmotic extraction. Inducing higher copies of OmpC could also increase the permeability of Hel4 through outer membrane and in-turn increase the total yield of extraction. This study opens possibility to engineer a recombinant *E.coli* that can solve the leakage of periplasmic protein, a commonly faced challenge of biotechnology industry during high density fermentation (Rinas et al., 2004).

Chapter 8

Discussion and future work

In this thesis I have explored the cell volume regulation of *E.coli* during hyposmotic shocks. I have first characterized the *in-vivo* responses of *E.coli* to 50 to 750 mM NaCl shocks. The hyposmotic shock was completed in an average of 1.75 s. The characteristic volume response of a cell was fast volume expansion, reaching a maximum expansion in 20-30 s. Following the volume expansion was a slow volume recovery which lasted up to 2-5 minutes. Subsequently, cells started showing increase in cell volume due to growth. The initial cell volume shows an increase within 1-2 s, in agreement with the rate of hyposmotic shock. However, it took 20-30 s to reach maximum volume expansion as seen in Figure 5d in Chapter 3. As the volume increased within few seconds of hyposmotic shock, it led to an increase in membrane tension and thereby triggered the opening of MSCs. Once the MSCs were opened, more water diffused into the cell while solutes diffused out of the cell. This competition of fluxes resulted in longer time to reach maximum volume expansion. Following this, the solute efflux dominated the water influx, which resulted in volume recovery. The phenomenological model developed with collaborators supported the reasoning of the slow volume recovery as shown in Chapter 3, Figure 5b.

The *in-vivo* cell response as observed by Boer et al. (2011) and Çetiner et al. (2017) showed that MSCs opening and closing event upon hyposmotic shock was completed in 150-200 ms. The difference in times scale of events between theirs and my experiments could have been due the rate of hyposmotic shock. They have used stopped flow device to deliver hyposmotic shock, which completed the shock in ≈ 8 ms. The rate of shock could influence the rate of volume expansion and thereby effect MSC gating. Akitake et al. (2005) demonstrated that the gating of MscS was dependant on the rate of application of pipette pressure in patch-clamp experiment. They showed that channels responded only to a fast change and remained inactive to a ramp increase in pressure,

even if the pressure was above the gating threshold. They called this 'dashpot' mechanism. This work suggest that the responses of a cell depends on the rate of hyposmotic shock.

The question of how fast should the solute in the medium change for the cell to perceive it as shock remains open for further studies. The rate of hyposmotic shock influences the rate of water influx and hence the stress-loading rate. The stress-loading rate could influence the extent of cell wall expansion or opening of MSCs. A preliminary experiment of a slow hyposmotic shock is shown in Figure 8.1b. The slow hyposmotic shock was delivered using a syringe pump at flow rate 10 μl/min using a flow cell as illustrated in Figure 8.1a. The average volume response shows a slow volume expansion that takes $\approx$ 6 min to reach a maximum volume increase of $\approx$ 12%. A further pronounced slow shock could elucidate the minimum osmotic gradient that is sensed as a 'shock'. These studies could mimic the real life changes in osmolarities, leading to a deeper understanding on the need for seven MSCs in *E.coli* and address the concerns of channel redundancy.

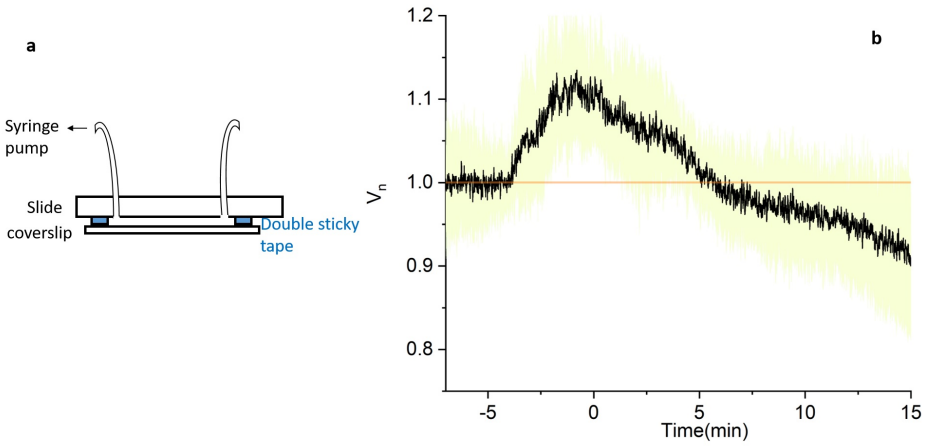

FIGURE 8.1: Average volume response of a slow 0.96 M hyposmotic shock. (a) A set-up of a flow cell used to deliver slow hyposmotic shock. (b) Average volume response of a slow hyposmotic shock of 960 mOsmol (n=8). Black line shows the average volume and blue line indicates 1SD. Pump flow rate is 10 ul/min.

In the second part of the thesis (Chapter 4), using a hepta MSC mutant, I have demonstrated *in-vivo* that the volume recovery during hyposmotic shock occurs through MSCs. The hepta-mutant showed an average of 3.3% lysis for

a shock of 0.125 M NaCl, corresponding to an osmotic pressure of 5.7 atm. Hepta-mutant under a hyposmotic shock of 0.55 M NaCl, corresponding to 25 atm, showed that 40% of the cells survived the challenge and exhibited cell growth. This suggests that the those that survived had reparable or minimal damage to the cell wall. The cell wall of those that lysed could have undergone plastic deformations beyond repair, as illustrated in Figure 8.2. The nature and extent of deformation could be further assessed by subjecting the hepta-mutant to a 0.96 mOsmol hyposmotic shock to induce cell wall damage, followed by a hyperosmotic shock with an outer membrane impermeable solute. The hyperosmotic delivered using an outer membrane impermeable solute like PEG or inulin, causes cell wall and cell membrane to shrink. If the cell wall of the hepta-mutant after a hyposmotic shock is ruptured or stretched beyond the elastic range of the material, then the cell wall would not be able to shrink, as illustrated in Figure 8.2. The changes in cell wall can be viewed using markers like Wheat Germ Aglutinnin. These studies could further provide valuable insights into the contribution of cell wall mechanics in survival to elevated osmotic pressures.

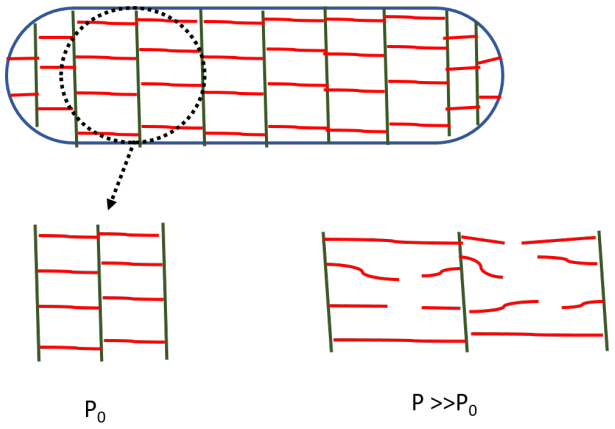

FIGURE 8.2: Illustration of hepta-mutant cell wall under strain after hyposmotic shock. Green lines illustrate the glycan strands and red lines illustrate peptide bonds. P_0 is the turgor pressure before hyposmotic shock, P is the pressure after. The figure illustrates the strain on the cell wall and plastic deformations during a hyposmotic shock ($P >> P_0$).

In Chapter 6, using a phenomenological model supported by Coarse Grained model, developed by the collaborators, demonstrated that clustering and cooperative gating of MSCs could reduce the unnecessary solute leakage and volume overshoot. These model predictions could be further strengthened by

experiments as discussed in the chapter. In Chapter 5, I have discussed the discrepancies while measuring *E.coli*'s response to hyposmotic shocks.These results suggested presence of traces of MSC inhibitors like Gadolinium and other rare earth elements. These findings could be further supported by analysis of trace elements using Mass Spectroscopy. If successful in identifying the trace elements, *E.coli* cell volume analysis could be further developed as bio-sensors that could detect the presence of impurities in water.

In the final result Chapter 7, I have simplified the osmotic extraction of a periplasmic protein relevant to the industry collaborator. The method of simplifying osmotic extraction was developed tailoring to the industry's demands. I suggested removal of the centrifugation step by direct addition of solutes to the cell culture so as to deliver hyperosmotic shock. Deduction of a centrifugation step before osmotic extraction could reduce the additional cost on the process. Additionally, the simplification can reduce the processing time and shear on the cells due to centrifugation. I have also identified a novel mechanism by which this protein leaked during the fermentation process and have discussed the genetic engineering designs that could be developed to overcome the leakage.

Appendix A

List of primers

Plasmid	Sequence	Function
pKCL05	CAACAGGCACAACGTAATCT	Forward primer for *kefA* colony PCR
pKCR06	GTGAAGTGGAAGCCTATGAA	Reverse primer for *kefA* colony PCR
pMUL01	TTTTTCTGCAG AAGATCGCGATGGTAAACG	*yjep* upstream homology forward primer for cross over PCR
pMUR02	CCATCAAAGGAAACGCTGACGTTTGTGTGCCGGATGAAC	*yjep* upstream homology reverse primer for cross over PCR
pMDL03	GTTCATCCGGCACACAAACGTCAGCGTTTCCTTTGATGG	*yjep* downstream homology forward primer for cross over PCR
pMDR04	TTTTTGTCGAC CGTGATTTGCCTTTTCGATAC	*yjep* downstream homology reverse primer for cross over PCR
pMCL05	GATACGGCGATTTGTTTCGT	Forward primer for *yjeP* colony PCR
pMCR06	GATTGTTGGCAGCATTGAGA	Reverse primer for *yjeP* colony PCR
pGUL01	TTTTTCTGCAGGTGCCGATTAACTCGCTGAT	homology forward primer for *ybdG* cross over PCR
pGUR02	CTGTTGTATAAAGGAGACGTTTTAAAAAAACCGCTCTCATCG	*ybdG* upstream homology reverse primer for cross over PCR
pGDL03	CGATGAGAGCGGTTTTTTTAAAACGTCTCCTTTATACAACAGC	*ybdG* downstream homology forward primer for cross over PCR
pGDR04	TTTTTGTCGACAACGATAAAGGTCGCAAGT	ybdG downstream homology reverse primer for cross over PCR
pGCL05	GTAATGCGCCGAAGTTTTTG	Forward primer for *ybdG* colony PCR
pGCR06	ATGTCTGGCTGAAGCTGGTT	Reverse primer for *ybdG* colony PCR
pOUL06	TTTTTCTGCAGAAGAGAGTGGGGCGATTTTT	*ybiO* upstream homology forward primer for cross over PCR
pOUR02	TATTTTCTCACTGGAGGAGTCTTTAACGCTGGCGATTGACAAA	*ybiO* upstream homology reverse primer for cross over PCR

Plasmid	Sequence	Function
pODL03	TTTGTCAATCGCCAGCGTTAAAGACTCCTCCAGTGAGAAAATA	*ybiO* downstream homology forward primer for cross over PCR
pODR07	TTTTTGTCGACATGAAGTGCTGAAGGTTATGC	*ybiO* downstream homology reverse primer for cross over PCR
pOCL05	AACGGCATCATCCATAAAAA	Forward primer for *ybiO* colony PCR
pOCR06	ATGCTGTTTGATGAACCGACTT	Reverse primer for *ybiO* colony PCR
pYNDL01	TTTTTCTGCAGGGAAAAAGAACCTTGGCGTA	*ynaI* upstream homology forward primer for cross over PCR
pYNDR02	CTGGAGGAGCCTGATAAAACAATCAGACATCACTGGCGTT	*ynaI* upstream homology reverse primer for cross over PCR
pYNUL03	AACGCCAGTGATGTCTGATTGTTTTATCAGGCTCCTCCAG	*ynaI* downstream homology forward primer for cross over PCR
pYNUR04 PCR	TTTTTGTCGACTTTCGTACAGAGCATCTTCCA	*ynaI* downstream homology reverse primer for cross over
pYNCL05	TGGTTATGGTCCGCAAAAAC	Forward primer for *ynaI* colony PCR
pYNCR06	CAGCGATTGATGGTCTTGAA	Reverse primer for *ynaI* colony PCR
pTOFL	AGGGCAGGGTCGTTAAATAGC	Forward primer to check homology arm insertion in pTOF24
pTOFR	AGGGAAGAAAGCGAAAGGAG	Reverse primer to check homology arm insertion in pTOF24

TABLE A.1: Keio primers used for final colony PCR (Baba et al., 2006)

Primer	Sequence	Function
MscL_A1	ACGATGACGAGGCCAATATC	Forward primer for *mscL* colony PCR
MscL_C2	TGATCCCTTATTCCGACAGC	Reverse primer for *mscL* colony PCR
MscS_A1	TCCAAGAAACACAACCTGCC	Forward primer for *mscS* colony PCR
MscS_C2	AAAGCATTTTGTGGACCGAG	Reverse primer for *mscS* colony PCR
YnaI_A1	TTGCTGCTCTTTGTTCTTGG	Forward primer for *ynaI* colony PCR
YnaI_C2	GTGGCTGAAAGGTTATCCCA	Reverse primer for *ynaI* colony PCR
YbiO_A1	CCAGGAAGCAGGTATGGTGT	Forward primer for *ybiO* colony PCR
YbiO_C2	CGAAGCAGGTGATGTGGTTT	Reverse primer for *ybiO* colony PCR
YbdG_A1	AAAACTTACCCCGGAACAGG	Forward primer for *ybdG* colony PCR
YbdG_C2	CGTTCGGCAACTATCTCTGC	Reverse primer for *ybdG* colony PCR
MscK_A1	TTCTCACAGCAGGGGGTATC	Forward primer for *kefA* colony PCR
MscK_C2	AAAACTGCCTGATGCGCTAC	Reverse primer for *kefA* colony PCR
MscM_A1	CCGATCCGAATGTACTGGTC	Forward primer for *yjep* colony PCR
MscM_C2	ACGATACCCGTGATGTTGGT	Reverse primer for *yjep* colony PCR

Appendix B

BioRxiv:Dynamic clustering regulates activity of mechanosensitive membrane channels

Dynamic clustering regulates activity of mechanosensitive membrane channels

Alexandru Paraschiv[1], Smitha Hegde[2], Raman Ganti[3], Teuta Pilizota[2], Anđela Šarić[1,*]
[1] *Department of Physics and Astronomy, Institute for the Physics of Living Systems University College London, London, UK*
[2] *Centre for Synthetic and Systems Biology University of Edinburgh, Edinburgh, UK*
[3] *Institute for Medical Engineering and Science Massachusetts Institute of Technology, Cambridge, MA, USA*
*

Experiments have suggested that bacterial mechanosensitive channels separate into 2D clusters, the role of which is unclear. By developing a coarse-grained computer model we find that clustering promotes the channel closure, which is highly dependent on the channel concentration and membrane stress. This behaviour yields a tightly regulated gating system, whereby at high tensions channels gate individually, and at lower tensions the channels spontaneously aggregate and inactivate. We implement this positive feedback into the model for cell volume regulation, and find that the channel clustering protects the cell against excessive loss of cytoplasmic content.

Both eukaryotic and prokaryotic cells harbour a phospholipid membrane packed with proteins, which enables separation of cellular content from the external environment. This physical barrier facilitates transport of signals and materials between the cell and its environment, thus sustaining life [1]. In addition, membranes of unicellular organisms separate the cell from the outside world, and need to be able to respond quickly and efficiently to sudden changes in the cell's surroundings. One of the ways the membranes respond to external stimuli is by reorganising associated macromolecules [2]. A characteristic example of such a behaviour are membrane mechanosensitive channels (MSCs), which respond to mechanical cues from the cell's surrounding, and are central to senses of hearing, balance, and touch, as well as for ensuring cell osmotic homeostasis [3–5].

The best studied MSCs are those of bacterium *Escherichia coli*, whose role is to protect the cell against sudden drops in the environmental solute concentration, so called hypoosmotic shock [6, 7]. Upon hypoosmotic shock water rushes into the cell, resulting in the cell swelling and increased tension in the bacterial envelope, which apart from the protein-filled phospholipid membranes, consists also of a stiffer material called the cell wall [6, 7]. If left unchecked, this pressure can lead to cell death by rupturing the envelope [8, 9]. To prevent it, a portfolio of MSC in *E. coli's* inner membrane act as "pressure release valves" that open and create a nano-sized pore at the centre of the protein. This in turn enables solute and water efflux, reestablishing desired osmotic pressure inside the cell [10–12]. This response is fast and solely regulated by the membrane tension and chemical potential of water and solutes [12].

Bacterial MSCs consist of closely-packed transmembrane helices connected by loops [13, 14]. Driven by membrane tension, the helices are thought to tilt with respect to one another, creating a space between them (up to 3 nm in diameter) for small solutes to non-selectively pass through [15]. Recent studies debate the existence and the role of spontaneous clustering of one of the MSCs found in *Escherichia coli*, MSC of large conductance (MscL) [16, 17]. Indeed, membrane clustering appears to be a common mechanism in cellular signaling, and has been observed for many transmembrane proteins and signaling receptors [18]. Clustering of MSC *in vitro* has been shown to result in collective, non-linear gating behavior [16], suggesting that it could tamper with cell's passive response during a hypoosmotic shock recovery. However, assessing the extent of MscL aggregation via imaging techniques *in vivo* has proven to be difficult due to the potential artifacts of the MscL tags on the process [17], and hence opens a need to explore orthogonal ways to investigate the aggregation phenomenon. Here, by developing a minimal computer model of MSCs embedded in a fluid membrane, we investigate the physical mechanisms behind the MSC cluster formation and cooperative gating, and their implications on cell-volume regulation.

Guided by the known structures of single iso-

*Electronic address: a.saric@ucl.ac.uk

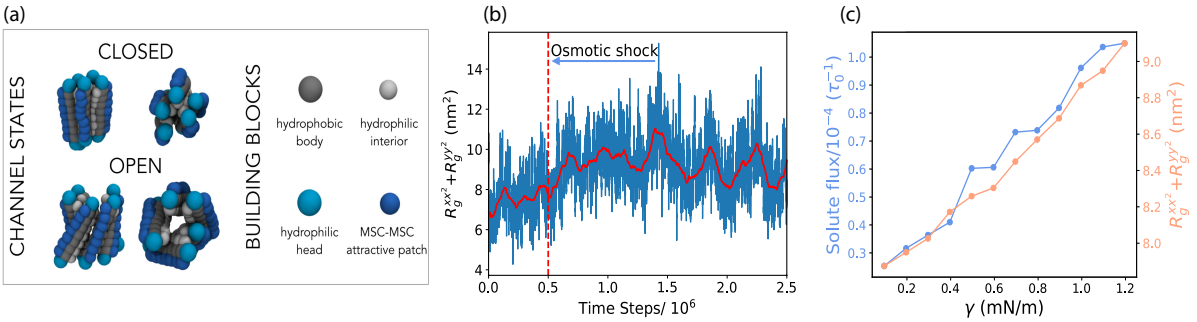

FIG. 1: **Coarse-grained model and single channel properties.** (a) MSC is presented as a collection of rods connected by weak springs. Each rod consists of overlapping hydrophobic beads (depicted in gray) and hydrophilic heads (in cyan), and is $\sim$ 10 nm long. Channel inside is lined with hydrophilic stripes (silver). Explicit inter-channel attractions can be turned-on via an external hydrophobic patch (dark blue). (b) Pore size oscillations of a single MSC. The dashed vertical red line marks the occurrence of an instantaneous osmotic shock corresponding to the membrane tension of $\gamma = 1.2$ mN/m, which leads to an increase in the average pore size. The solid red line represents the moving time average (window size 10^5 time steps). (c) The variation of the pore size, quantified by the in-plane components of the MSC radius of gyration tensor $R_G^{xx^2} + R_G^{yy^2}$, and subsequent solute flux though the channel as a function of the membrane tension.

lated MSCs [13, 14, 19], we built a generic MSC model out of rod-shaped subunits connected by weak springs (Fig. 1a). While bacterial MSCs possess varying number of repetitive helical subunits [7], without loss of generality, we choose to include five rod-shaped subunits. Each rod is made of seven core hydrophobic, and two hydrophilic head beads (Fig. 1a). The rods are longer than the membrane thickness to reproduce a positive hydrophobic mismatch of $\sim$ 0.5nm between the protein and the lipid layer found in structural studies [13]. The lipid bilayer is described by a previously published three-beads-per-lipid model [20] (Fig. S1 and S2). The single rod diameter is twice the radius of a lipid bead, and the inner part of the channel is lined with hydrophilic beads to prevent lipids from overflowing inside the channel. Finally, to be able to include direct inter-protein attractions, an attractive patch of beads is added on the external side of each rod. Hypoosmotic shock is generated by placing a gas of inert volume-excluded "solute" beads on one side of the membrane. The collisions of the solute beads with the membrane create membrane tension, which is linearly proportional to the solute concentration difference across the membrane (Fig. S5). For further details on simulations see Supplementary Information.

We first focus on the behaviour of a single MSC. Application of a hypoosmotic shock causes an increase in the membrane tension and area. Since the transmembrane components of the MSC interact attractively with the hydrophobic layer of the membrane, they maintain contact with the expanding lipid bilayer. Consequently, channel rods tilt with respect to one another, resulting in the overall lateral expansion of the channel, as shown

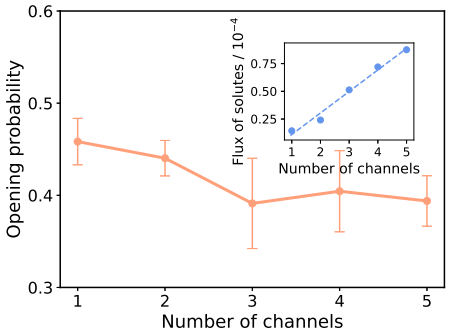

FIG. 2: **Multiple channels interacting via membrane-mediated interactions only do not cluster and hence gate independently.** The probability of channel pore opening versus the number of channels present in the system. Inset: total flux of solutes through the channels versus the number of channels in the system. Channel area fraction ranges from 0.03 ($N = 1$) to 0.15 ($N = 5$).

in Fig. 1 and Video 1. To quantify the channel pore size we measure the in-plane components of the MSC radius of gyration tensor (see Supplementary Information). We find that the pore size oscillates stochastically, and that the application of hypoosmotic shock leads to an immediate increase in the pore size (Fig. 1b), allowing for the passage of the solutes and channel gating (Video 2). As shown in Fig. 1c, the pore size and the flux of solute through the pore increase with the increase in the shock magnitude. For the purpose of our analysis solely, we chose $\gamma = 0.45$ mN/m as the threshold tension for the pore opening; channels whose pore size is above 8.2 nm^2 we consider as open, while those below this size we deem as

closed (Eq. (S5)).

We now analyze the behavior at multiple MSCs interacting only via volume exclusion and effective membrane-mediated interactions. Fig. 2 shows the gating properties of such MSCs as a function of the number of channels in the system. In this case we did not observe any channel clustering and it is evident that each channel behaves independently. Indeed, we find that the membrane-mediated interactions between fluctuating channels in our system are negligible (Fig. S7). Rigid symmetric inclusions of the same hydrophobic mismatch in our model experience attraction of ~ 0.5kT (Fig. S8), in agreement with previous simulation studies [21–23]. redAs we did not observed any MSC clustering due to pure membrane-mediated interactions, we chose a top-down strategy. We know that: (i) MSC aggregation has been reported *in vitro* [16], and *in vivo* while working with MSCs labelled with a small covalent dye [17], (ii) direct inter-protein interactions, such as polar and electrostatic interactions and packing of small apolar side chains [24–29], can lead to attractions of trans-membrane proteins [18]. In addition, local lipid phase separation around the protein can yield effective inter-protein attraction and protein aggregation. Therefore, to drive MSC aggregation we included weak direct inter-protein attractions, which we modelled via an attractive stripe on the outer side of the channel (Fig. 1a).

Incorporating weak direct inter-protein attraction leads to the assembly of MSCs into small clusters of sizes between 2 and $\sim$ 15 MSCs, and we now find that the clusters exhibit strong cooperative gating. Fig. 3(a) shows that the pore sizes of two attractive channels varies as a function of the separation between them. Sharp decrease in the pore sizes at $\sim$9.5 nm of inter-channel separation corresponds to the cooperative closure of individual MSC (Video 3). The reason for this is purely geometrical: two closed channels can achieve larger contact area between them, maximizing their attraction. For multiple channels diffusing in the bilayer we observe dynamic rearrangement and aggregation into larger clusters that leads to decreased gating activity per channel, which scales with the cluster size (Fig. 3b). The clusters are dynamic in nature, whereby individual channels within the clusters oscillate between the closed and open states, can move within, leave the cluster, or join another. Since the channel activity depends on the number of neighbours, individual channel activity within a single cluster is consequentially inhomogeneous. The channels on the cluster interior will on average gate less than the channels sitting at the aggregate rim (inset in Fig. 3b). The average channel activity will hence depend not only on the cluster size, but also on its shape.

We now perform a computational experiment to mimic the situation in which a bacterial cell, living under quiescent conditions, encounters a sudden hypoosmotic shock. We start our simulation with a membrane that contains channels all aggregated into a single cluster. We then applied a sudden tension of 1.5 mN/m, and monitored the system in time. As a control, the same simulation was repeated at zero tension (Fig. 3c). We find that the high magnitude shock breaks up the MSC cluster into individual channels, switching the system from the clustered to the mixed state (Video 4 and 5). Such isolated channels open with higher probability (inset in Fig. 3c), enabling efficient gating at high membrane tensions, when it is needed most. On the contrary, at low tensions the channels remain in a cluster, albeit the cluster shape dynamically elongates (Fig. 3c).

These findings suggest that the spontaneous formation of liquid-like MSC clusters enables an additional level of control over their gating and signal transduction. This control is implemented in the system in a passive way, hard-wired in the system's physical properties. On average, single channels are more closed at low membrane tensions, making the channels more aggregation-prone, which in turn further deactivates their gating. When the cell encounters a hypoosmotic shock, the membrane tension increases and channels open, making them less aggregation prone, which results in spontaneous dispersion of clusters and further opening of individual channels. The positive feedback between the membrane tension and the cluster formation hence dynamically adjusts the extent of channel clustering, as well as their gating properties.

We now include the observed effect of channel clustering into our previously developed continuum model of *E. coli* cell volume recovery upon hypoosmotic shock [12]. Experimentally, we observed total cell volume expansion within seconds after the hypoosmotic shock, followed by a period of slower, minutes-long volume recovery (despite the fact that MSCs open on miliseconds time scales) that exhibits a characteristic "overshoot" below the value of initial volume (Fig. S11). Our continuum model explained the slow recovery and the volume recovery overshoot by considering the change of the cellular volume (V_n) and solute concentration in time. The volume changes, and consequentially the cell membrane tension, are governed by the flux of water, proportional to the difference between osmotic pressure and Laplace pressure on the cell wall. Solute concentration changes are governed by the diffusive fluxes through the MSCs, enhanced by the tension build up (see Supplementary Information).

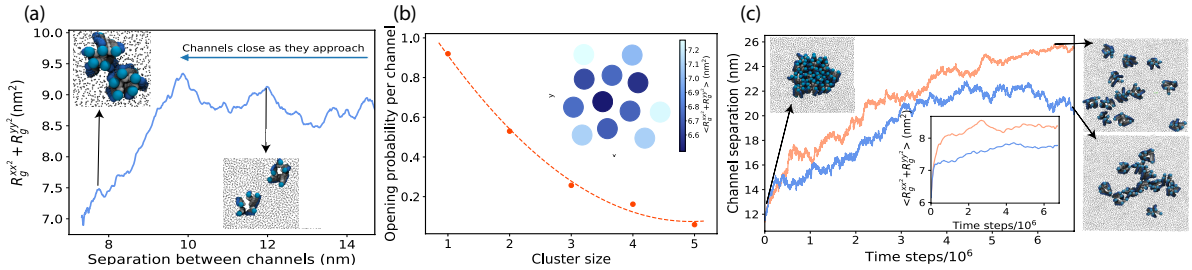

FIG. 3: **Channels interacting via explicit attractive interactions exhibit cooperative gating.** (a) Average pore size of two MSCs as a function of distance between them ($\gamma = 1.30$ mN/m). (b) Opening probability per channel versus aggregate size ($\gamma = 1.70$ mN/m and the channel area fraction is 0.16). Inset: The average pore size of channels within a single cluster formed of twelve MSCs. (c) The average distance between the channels increases in time and is larger for higher membrane tension ($\gamma = 1.70$ mN/m, shown in orange versus $\gamma = 0.70$ mN/m, shown in blue) Far right: The snapshot of the cluster configuration in the last time-frame. Inset: The probability of channel opening increases as the simulation progresses. In all the subfigures $\varepsilon_{protein-protein} = 0.9$kT.

Thus, when MSCs are open the solute flux through the cell membrane increases, which was described in the model with a single fitting parameter that characterizes channels as either open or closed (Eq. (S10)). To link our coarse-grained model predictions with the continuum model we now replace that parameter with a continuous function, capturing that the channel clustering: *(i)* decreases at higher membrane tensions, *(ii)* decreases opening probability per channel and *(iii)* increases for higher MSCs surface fractions. The introduced function hence depends on the number of channels in the cluster (N), bilayer tension (γ), and the channel surface density (ρ), and any constants are fixed by fitting to the results of the coarse-grained model (see Supplementary Information).

Next, we fit the experimental volume trace to the master equations (Eq. (S23) and (S24)) that describe the changes in cellular volume and solute concentration with the results of the coarse-grained model incorporated (Fig. S11). The fit enables us to predict the dynamics of cluster aggregation and disaggregation as the cell volume expands and recovers after hypoosmotic shock, Fig. 4a. Probability of observing channels as monomers ($N = 1$) and as aggregates (shown for $N = 5$) is given as a color scale for each time point post-hypoosmotic shock, showing that larger clusters are less likely to form at the point of maximum volume expansion (largest tension), and more likely to form as the volume recovers and the membrane tension decreases. This gives a clear prediction of our model, which can be tested by imaging the extent of the channel clustering in the membrane at different times post-hypoosmotic shock.

To demonstrate the consequence of MSCs clustering on the cell volume recovery, we show what the volume dynamics would look like if the channel were prevented from clustering and if the clustering differed from that of the fitted data (Fig. 4b and Fig. S12). This allows us to see that, within a specific range, channel clustering can reduce the volume "overshoot" commonly found upon recovery, without jeopardizing channel opening at the point of maximum tension. Fig. 4b and Fig. S13 show that further decreasing the overshoot by MSC clustering can lead to detrimental increase in the maximum tension in the cell envelope, suggesting that the channel clustering is finely-tuned in the cell. Our prediction on the role of clustering for the cell volume regulation can be probed experimentally by tracing the volume recovery post-hypoosmotic shock for different extents of the clustering. The MSC clustering can be enhanced by tagging the channels with fluorescent proteins [17] or modulated by expressing the channels to different levels.

In conclusion, we showed that spontaneous aggregation of mechanosensitive membrane channels results in liquid-like clusters that exhibit lower gating activity than dispersed clusters. Our findings align well with the study by Grage et al. [16] in which the aggregation of *E. coli* MscLs reconstituted in lipid vesicles led to a significant decrease in the total gating activity. The patch-clamp experiments in [16] showed that a number of active channels in a patch was consistently lower than the total number of channels. These results were further reinforced by small angle neutron scattering measurements of the total membrane area increase when the channels were open, which was smaller than what would have been expected if the channels were behaving independently.

Previous continuum models predicted that, due to hydrophobic mismatch, membrane-mediated interactions between perfectly rigid symmetric mechanosensitive channels will lead to their collective opening [30–34]. This is not what we have ob-

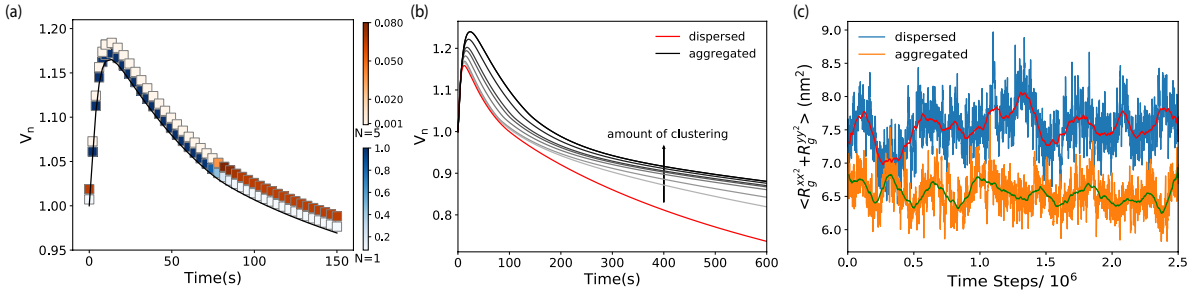

(c) Oscillations in the average MSC pore size at zero membrane tension for a system of 12 MSCs in a dispersed (blue line) and aggregated (orange line) states. Red and green lines show the moving time average in each case (10^5 time steps window).

FIG. 4: **Clustering regulates channel closing to overcome leaky cell membrane.**(a) Dynamics of channel clustering during cell volume recovery (gray faded line). Normalized cell volume, V_n, upon 0.96 Osmol hypoosmotic shock and 0.5% channel packing fraction. Colorbars: Probability of finding a single isolated channel (blue) and a cluster of 5 channels (orange).(b) Effect of increasing the extent of clustering (here by changing protein-protein attractions), on cell volume dynamics (grey and black lines) in comparison to dispersed channels (red line) for the same conditions as in (a).

served in our coarse-grained model. Our channels are not perfectly symmetric or rigid, but can dynamically acquire different conformations, which can render membrane-mediated interactions between two channels both attractive and repulsive. It is likely that this effect erases any membrane-mediated interactions. Interactions between perfectly rigid inclusions of hydrophobic mismatch of 0.5 nm in our model are attractive, albeit weak (Fig. S8). It is possible that the high stiffness of the coarse-grained lipids prevents lipid stretching needed for membrane-mediated interactions. Nevertheless, since membrane-mediated interactions due to hydrophobic mismatch have never been directly experimentally quantified, it is hard to assess their importance in driving MSC aggregation observed in experiments [16, 17]. There is however a growing body of evidence that direct protein-protein interactions drive aggregation of transmembrane helices, and also stabilize helix-helix interactions within a single protein [24–29]. It is likely that the same forces could also drive weak helix-helix interactions between different proteins should they be found close to each other.

We demonstrated that coupling between the membrane tension, channels' conformational change and clustering produces a controlled gating system, whose positive feedback is encoded purely in the system's physical properties. Based on these results, we predict the effects of the feedback on the cell volume regulation. We suggest that MSC aggregation serves to protect the cell from excessive gating, both in steady-state and during its post-shock volume recovery. Indeed, our simulations show that isolated channels have a non-zero probability of gating even at zero tension (Fig. 4c). This agrees with experimental characterisation of a single-channel gating, where it is evident that the channel opening does not follow a sharp step function [35]. Hence, if MSCs are over-expressed, e.g. when bacteria grow under hyperosmotic conditions or when they enter stationary phase [36], the probability of single channel gating even under quiescent conditions would be sufficiently high to significantly increase the effective membrane permeability to ions, making it hard to maintain electrochemical gradients across the cell membrane, which serve as one of the main energy sources for the cell [37–42]. Furthermore, loss of volume by 8-10 % has been experimentally reported to lead to the loss of turgor pressure that the cell actively maintains[43]. Thus channel aggregation, which is more pronounced at higher channel numbers, could be a natural self-defence mechanism of bacteria against unnecessary gating, contributing to bacterial survival, especially in scares environments (alike post-hypoosmotic shock). The MSC model developed identifies the basic physical mechanisms behind mechanosensing of membrane channels. Due to their generality, our results can also be helpful in guiding the design of synthetic nanomechanosening systems [44] and artificial membrane channels [45, 46].

Acknowledgments

We thank Samantha Miller, Bert Poolman, and the members of Šarić and Pilizota laboratories for useful discussion. We acknowledge support from the Engineering and Physical Sciences Research

Council (A.P. and A.Š.), the UCL Institute for the Physics of Living Systems (A.P. and A.Š.), Darwin Trust of University of Edinburgh (H.S.), Industrial Biotechnology Innovation Centre (H.S. and T.P.), BBSRC Council Crossing Biological Membrane Network (H.S. and T.P.), BBSRC/EPSRC/MRC Synthetic Biology Research Centre (T.P.), and the Royal Society (A.Š.).

[1] J Lee Kavanau. Structure and functions of biological membranes. *Nature*, 198(4880):525, 1963.

[2] Alba Diz-Muñoz, Daniel A Fletcher, and Orion D Weiner. Use the force: membrane tension as an organizer of cell shape and motility. *Trends in cell biology*, 23(2):47–53, 2013.

[3] Andriy Anishkin, Stephen H Loukin, Jinfeng Teng, and Ching Kung. Feeling the hidden mechanical forces in lipid bilayer is an original sense. *Proceedings of the National Academy of Sciences*, 111(22):7898–7905, 2014.

[4] Peter G Gillespie and Richard G Walker. Molecular basis of mechanosensory transduction. *Nature*, 413(6852):194–202, 2001.

[5] Niels Eijkelkamp, Kathryn Quick, and John N Wood. Transient receptor potential channels and mechanosensation. *Annual review of neuroscience*, 36:519–546, 2013.

[6] Boris Martinac. Mechanosensitive ion channels: molecules of mechanotransduction. *Journal of cell science*, 117(12):2449–2460, 2004.

[7] Elizabeth S Haswell, Rob Phillips, and Douglas C Rees. Mechanosensitive channels: what can they do and how do they do it? *Structure*, 19(10):1356–1369, 2011.

[8] Michelle D Edwards, Susan Black, Tim Rasmussen, Akiko Rasmussen, Neil R Stokes, Terri-Leigh Stephen, Samantha Miller, and Ian R Booth. Characterization of three novel mechanosensitive channel activities in escherichia coli. *Channels*, 6(4):272–281, 2012.

[9] Maja Bialecka-Fornal, Heun Jin Lee, and Rob Phillips. The rate of osmotic downshock determines the survival probability of bacterial mechanosensitive channel mutants. *Journal of Bacteriology*, 197(1):231–237, 2015.

[10] Christopher C Cruickshank, Rodney F Minchin, AC Le Dain, and Boris Martinac. Estimation of the pore size of the large-conductance mechanosensitive ion channel of escherichia coli. *Biophysical journal*, 73(4):1925–1931, 1997.

[11] Sergei I Sukharev, Wade J Sigurdson, Ching Kung, and Frederick Sachs. Energetic and spatial parameters for gating of the bacterial large conductance mechanosensitive channel, mscl. *The Journal of general physiology*, 113(4):525–540, 1999.

[12] Renata Buda, Yunxiao Liu, Jin Yang, Smitha Hegde, Keiran Stevenson, Fan Bai, and Teuta Pilizota. Dynamics of escherichia coliâĂŹs passive response to a sudden decrease in external osmolarity. *Proceedings of the National Academy of Sciences*, 113(40):E5838–E5846, 2016.

[13] Geoffrey Chang, Robert H Spencer, Allen T Lee, Margaret T Barclay, and Douglas C Rees. Structure of the mscl homolog from mycobacterium tuberculosis: a gated mechanosensitive ion channel. *Science*, 282(5397):2220–2226, 1998.

[14] Randal B Bass, Pavel Strop, Margaret Barclay, and Douglas C Rees. Crystal structure of escherichia coli mscs, a voltage-modulated and mechanosensitive channel. *Science*, 298(5598):1582–1587, 2002.

[15] Eduardo Perozo, D Marien Cortes, Pornthep Sompornpisut, Anna Kloda, and Boris Martinac. Open channel structure of mscl and the gating mechanism of mechanosensitive channels. *Nature*, 418(6901):942–948, 2002.

[16] Stephan L Grage, Asbed M Keleshian, Tamta Turdzeladze, Andrew R Battle, Wee C Tay, Roland P May, Stephen A Holt, Sonia Antoranz Contera, Michael Haertlein, Martine Moulin, et al. Bilayer-mediated clustering and functional interaction of mscl channels. *Biophysical journal*, 100(5):1252–1260, 2011.

[17] Jonas Van Den Berg, Heloisa Galbiati, Akiko Rasmussen, Samantha Miller, and Bert Poolman. On the mobility, membrane location and functionality of mechanosensitive channels in escherichia coli. *Scientific reports*, 6, 2016.

[18] P Andrew Chong and Julie D Forman-Kay. Liquid–liquid phase separation in cellular signaling systems. *Current opinion in structural biology*, 41:180–186, 2016.

[19] Christopher Maffeo, Swati Bhattacharya, Jejoong Yoo, David Wells, and Aleksei Aksimentiev. Modeling and simulation of ion channels. *Chemical reviews*, 112(12):6250–6284, 2012.

[20] Ira R Cooke, Kurt Kremer, and Markus Deserno. Tunable generic model for fluid bilayer membranes. *Physical Review E*, 72(1):011506, 2005.

[21] Ulrich Schmidt, Gernot Guigas, and Matthias Weiss. Cluster formation of transmembrane proteins due to hydrophobic mismatching. *Physical review letters*, 101(12):128104, 2008.

[22] Frédérick de Meyer and Berend Smit. Comment on âĂIJcluster formation of transmembrane proteins due to hydrophobic mismatchingâĂİ. *Physical review letters*, 102(21):219801, 2009.

[23] Frederick Jean-Marie De Meyer, Maddalena Venturoli, and Berend Smit. Molecular simulations of lipid-mediated protein-protein interactions. *Biophysical journal*, 95(4):1851–1865, 2008.

[24] David T Moore, Bryan W Berger, and William F DeGrado. Protein-protein interactions in the membrane: sequence, structural, and biological motifs. *Structure*, 16(7):991–1001, 2008.

[25] Dieter Langosch and Isaiah T Arkin. Interaction and conformational dynamics of membrane-spanning protein helices. *Protein Science*,

18(7):1343–1358, 2009.

[26] Marco Mravic, Jessica L Thomaston, Maxwell Tucker, Paige E Solomon, Lijun Liu, and William F DeGrado. Packing of apolar side chains enables accurate design of highly stable membrane proteins. *Science*, 363(6434):1418–1423, 2019.

[27] Yoshiaki Yano, Arisa Yamamoto, Mai Ogura, and Katsumi Matsuzaki. Thermodynamics of insertion and self-association of a transmembrane helix: a lipophobic interaction by phosphatidylethanolamine. *Biochemistry*, 50(32):6806–6814, 2011.

[28] Xiaorong Ou, Paul Blount, Robert J Hoffman, and Ching Kung. One face of a transmembrane helix is crucial in mechanosensitive channel gating. *Proceedings of the National Academy of Sciences*, 95(19):11471–11475, 1998.

[29] Yoshiaki Yano and Katsumi Matsuzaki. Measurement of thermodynamic parameters for hydrophobic mismatch 1: self-association of a transmembrane helix. *Biochemistry*, 45(10):3370–3378, 2006.

[30] Tristan Ursell, Kerwyn Casey Huang, Eric Peterson, and Rob Phillips. Cooperative gating and spatial organization of membrane proteins through elastic interactions. *PLoS computational biology*, 3(5):e81, 2007.

[31] Osman Kahraman, Peter D Koch, William S Klug, and Christoph A Haselwandter. Architecture and function of mechanosensitive membrane protein lattices. *Scientific reports*, 6, 2016.

[32] Douwe Jan Bonthuis and Ramin Golestanian. Mechanosensitive channel activation by diffusio-osmotic force. *Physical review letters*, 113(14):148101, 2014.

[33] Ksenia Guseva. Collective response of self-organised clusters of mechanosensitive channels. In *Formation and Cooperative Behaviour of Protein Complexes on the Cell Membrane*, pages 31–67. Springer, 2012.

[34] Lucas D Fernandes, Ksenia Guseva, and Alessandro PS De Moura. Cooperative response and clustering: Consequences of membrane-mediated interactions among mechanosensitive channels. *Physical Review E*, 96(2):022410, 2017.

[35] Vladislav Belyy, Kishore Kamaraju, Bradley Akitake, Andriy Anishkin, and Sergei Sukharev. Adaptive behavior of bacterial mechanosensitive channels is coupled to membrane mechanics. *The Journal of general physiology*, 135(6):641–652, 2010.

[36] Maja Bialecka-Fornal, Heun Jin Lee, Hannah A. DeBerg, Chris S. Gandhi, and Rob Phillips. Single-cell census of mechanosensitive channels in living bacteria. *PLoS ONE*, 7(3), 2012.

[37] Ekaterina Krasnopeeva, Chien-Jung Lo, and Teuta Pilizota. Single-cell bacterial electrophysiology reveals mechanisms of stress-induced damage. *Biophysical journal*, 2019.

[38] Peter Mitchell. Coupling of phosphorylation to electron and hydrogen transfer by a chemi-osmotic type of mechanism. *Nature*, 191(4784):144–148, 1961.

[39] SI Sukharev, B Martinac, VY Arshavsky, and CHING Kung. Two types of mechanosensitive channels in the escherichia coli cell envelope: solubilization and functional reconstitution. *Biophysical journal*, 65(1):177–183, 1993.

[40] PF Costa, Mg G Emilio, PL Fernandes, H Gil Ferreira, and K Gil Ferreira. Determination of ionic permeability coefficients of the plasma membrane of xenopus laevis oocytes under voltage clamp. *The Journal of physiology*, 413(1):199–211, 1989.

[41] Keith D Garlid and Petr Paucek. Mitochondrial potassium transport: the k+ cycle. *Biochimica et Biophysica Acta (BBA)-Bioenergetics*, 1606(1-3):23–41, 2003.

[42] David E Goldman. Potential, impedance, and rectification in membranes. *The Journal of general physiology*, 27(1):37–60, 1943.

[43] Teuta Pilizota and Joshua W Shaevitz. Plasmolysis and cell shape depend on solute outer-membrane permeability during hyperosmotic shock in e. coli. *Biophysical journal*, 104(12):2733–2742, 2013.

[44] Julia F Doerner, Sebastien Febvay, and David E Clapham. Controlled delivery of bioactive molecules into live cells using the bacterial mechanosensitive channel mscl. *Nature communications*, 3:990, 2012.

[45] Andrew R Thomson, Christopher W Wood, Antony J Burton, Gail J Bartlett, Richard B Sessions, R Leo Brady, and Derek N Woolfson. Computational design of water-soluble α-helical barrels. *Science*, 346(6208):485–488, 2014.

[46] Kozhinjampara R Mahendran, Ai Niitsu, Lingbing Kong, Andrew R Thomson, Richard B Sessions, Derek N Woolfson, and Hagan Bayley. A monodisperse transmembrane α-helical peptide barrel. *Nature chemistry*, 9(5):411, 2017.

Supplementary Information: Dynamic clustering regulates activity of mechanosensitive membrane channels

This Supplementary Information provides details related to implementation of the coarse-grained model for lipids and mechanosensitive channels (Section I), details regarding the simulation set-up (Section II), details on the model of cell volume dynamics during hypoosmotic shocks (Section III) and supportive results and figures in Section IV.

I. COARSE-GRAINED MODEL

A. Lipids

The lipid bilayer was simulated using a highly coarse-grained model developed by Cooke and Deserno [1]. In this model, each lipid is made of three beads: one hydrophilic "head" bead and two hydrophobic "tail" beads. The beads are joined together by finite extensible nonlinear elastic (FENE) bonds described by the bond potential $V_{bond}(r) = -\frac{1}{2}k_{bond}r_\infty^2 \log\left[1-\left(\frac{r}{r_\infty}\right)^2\right]$, where r is the distance between atoms and r_∞ is the maximum bond extent, in this case taken to be 1.5σ. We used $k_{bond} = 30kT/\sigma^2$. σ is the Lennard-Jones unit of length and corresponds to approximately 1 nm. The angle between the three beads is enforced by a harmonic angular potential $V_{angle}(r) = k_{angle}\left(\theta-\theta_0\right)^2$, with $k_{angle} = 5kT/deg^2$ and $\theta_0 = \pi$.

The intermolecular interactions between the lipid beads are determined by a perturbed Weeks-Chandler-Andersen (WCA) potential [2]. All beads interact via a truncated-shifted Lennard-Jones potential described in equation (S1). The parameter b gives the relative size of the lipid beads and r_c is a cutoff parameter. In our simulations we used $\varepsilon = 1kT$, $r_c = 2^{1/6}\sigma$, $b_{head,head} = b_{head,tail} = \sigma$, $b_{tail,tail} = 0.95\sigma$ as described in [1].

$$V_{rep}(r,b) = \begin{cases} 4\varepsilon\left[\left(\frac{b}{r}\right)^{12} - \left(\frac{b}{r}\right)^{6} + \frac{1}{4}\right], & r \le r_c \\ 0 & r > r_c \end{cases} \tag{S1}$$

An additional attractive potential is enforced between the hydrophobic tail beads [1]. The membrane is kept intact only through the attractive interactions between the hydrophobic tail beads. This perturbative potential is described in equation (S2):

$$V_{attr}(r) = \begin{cases} -\varepsilon, & r < r_c \\ -\varepsilon cos^2\frac{\pi(r-r_c)}{2w_c}, & r_c \le r \le r_c + w_c \\ 0, & r > r_c + w_c \end{cases} \tag{S2}$$

The cosine term is meant to soften the potential which makes the membrane more fluid and ensures the self-assembly and membrane's structural integrity. The adjustable parameter w_c controls decay range of the potential. In our simulations, we used $w_c = 1.4\sigma$. All the parameters were chosen such that the membrane is positioned well into the fluid phase of the phase diagram reported in the original paper [1].

B. Mechanosensitive Channels

We designed a similar coarse-grained model for the mechanosensitive channel of large conductance (MscLs). A single channel is made from five rod-shaped subunits, inspired from the protein's oligomeric structure (Fig. S1). Each subunit mimics the alpha-helices from the transmembrane domains TM1 and

TM2. A representation of a channel is given in Figure S1. The rods are interconnected by a series of weak harmonic bonds of spring constant $k_{spring} = 1.5kT/\sigma^2$, with an equilibrium length set to $r_{eq} = 2.5\sigma$. Each rod is made of seven core hydrophobic beads and two hydrophilic head beads. The rods are slightly longer than the membrane thickness in order to replicate the hydrophobic mismatch between the protein and the lipid bilayer. All the beads are connected by a strong harmonic potential ($k = 100kT/\sigma^2$, $r_{eq} = 2.5\sigma$) meant to ensure the channel's rigidity. The channel is kept straight by a similar angular harmonic potential $k_\theta = 100kT/deg^2$, $\theta_0 = \pi$.

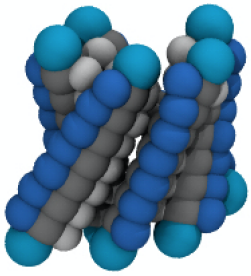

FIG. S1: **Coarse-grained model of a single mechanosensitive channel**. There are four different types of beads in a channel: hydrophilic head beads (cyan), hydrophobic core beads (grey), hydrophilic interior beads (silver), attractive MscL-MscL beads (blue).

The channel head and core beads interact with the lipids and with themselves through the same potential described in equations (S1) and (S2). The size of these protein beads was chosen to be 2σ, giving the relative parameters $b_{protein,protein} = 2\sigma$ and $b_{protein,head} = b_{protein,tail} = 1.5\sigma$. The head beads interact only with WCA potential (S1). The interactions of the core beads contain both the attractive and repulsive parts of the potential (S1 and S2). These beads are hydrophobic so they are attractive towards the lipids and keep the channel embedded within the membrane. Attempts of using solely a Lennard-Jones potential for the channel-membrane interaction, without the soft cosine tail, led to unstable structures that quickly fractured at the point of contact between the protein and the lipids. This suggests that a careful tuning in the interaction between proteins and membrane is crucial for functionality of MscLs.

A hydrophilic patch was added on the channels' interior side to prevent lipids from overflowing inside (silver beads in Figure S1). They interact with the lipids purely through the repulsive part of the Lennard-Jones potential. Their diameter was chosen to be 0.5σ and the potential depth was taken to be $\varepsilon = 50kT$. Since these beads are not attractive to the lipids, they prevent them from flowing inside the channel. Another attractive patch of beads is added on the external side of the channels (blue beads in Figure S1). This patch drives the interaction between proteins via a long-range Lennard-Jones potential (with a cutoff of 3σ) with adjustable depth $\varepsilon_{protein,protein}$. Both these types of beads were connected with the main core beads via a spring with spring constant $k = 1.5kT/\sigma^2$ and equilibrium length $r_{eq} = 1.5\sigma$. The attractive patch is essential to drive the aggregation of channels into clusters and controls the cooperative gating effects described in the paper.

II. SIMULATION DETAILS

The channels were inserted vertically in a lipid membrane placed in the centre of the simulation box. The lipids were initially organised into a square patch on a lattice which further reorganises in a typical bilayer-like structure. The membrane was tethered to the centre of the simulation box with a weak spring of spring constant $k = 1.0kT/\sigma^2$ to prevent its drift under the collisions with the solutes. The simulation box is cuboidal in shape with the initial dimensions $L_x = L_y = \frac{1}{3}L_z$. The side length of the box is allowed to fluctuate in the x and y directions with periodic boundary conditions applied. The simulation box was kept fixed in size in the z direction with weak Lennard-Jones walls at both ends, and with the wall depth $\varepsilon = 1.0kT$.

Our system contained 6024 lipids, each of which is made of 3 particles. We simulated at most 12 channels, where each is made of 115 particles. Number of solute particles was varied between 0 and 1200, where each solute is made of 1 particles. Hence the largest simulation we ran contained 20,652 particles.

The simulations were run in the isoenthalpic-isobaric (NPH) ensemble with zero lateral pressure $P_x = P_y = 0$. The membrane tension is controlled by inserting external osmolyte particles that collide with the membrane. This mechanical interaction between the solutes and the membrane leads to a subsequent expansion of the membrane in the xy plane and a small thinning in the z direction. In order to replicate the stochastic dynamics of the real system, we used a Langevin thermostat with the friction coefficient η set to unity: $\eta = m/\tau_0$, where m is the particle mass (set to unity for all particles) and τ_0 the simulation unit of time. The simulation time step was taken to be $\tau = 0.008\tau_0$, where τ_0 is the simulation unit of time. We used the LAMMPS molecular dynamics package to run the simulations [3] and the VMD package to visualise the trajectory files [4].

A. Membrane tension

Membrane tension is controlled by the number of solute particles impinging on the membrane. The aim of these particles is to mimic the chemical concentration gradient that a channel is exposed to during an osmotic downshock. The solute particles are modelled as hard spheres of diameter 0.5σ that interact with the other particles in the system (including themselves) only through the WCA potential with $\epsilon = 50kT$ (SI). The size of the solutes was chosen carefully so they can flow through the open channels, but not through channels with more contracted conformations or through the membrane itself.

The surface tension was mapped to the number of solute particles as follows: A number of solute particles, $N_{solutes}$, were placed in a box containing a square patch of a lipid membrane of the side length 40σ (in the absence of any mechanosensitive channels). All the solute particles were placed on the same side of the simulation box with respect to the membrane patch. The membrane tension, γ, was calculated by integrating the normal and tangential components of the pressure tensor using the relationship S3 as described in [5]:

$$\gamma = \int [P_{zz} - \frac{1}{2}(P_{xx} + P_{yy})]\mathrm{d}z \tag{S3}$$

Further results are given in Section IV.

B. Channel radial expansion

The radial expansion of a channel is tracked using the xx and yy components of the gyration radius tensor as described in equation

$$R_G^{xx^2} + R_G^{yy^2} = \frac{1}{M}\sum_i m_i(r_{ix} - r_{CMx})^2 + \frac{1}{M}\sum_i m_i(r_{iy} - r_{CMy})^2 \tag{S4}$$

where i is the index of the given protein bead, m_i is its mass and M is the total channel mass. r_{ix} and r_{iy} are the Cartesian coordinates of the particles in the x and y directions. r_{CMx} and r_{CMy} are the coordinates of the channel's centre of mass.

We assigned a state function to the channel, depending on the corresponding gyration radius components. The channel can be considered either "open" or "closed" depending on its radial expansion. As such, the state of a channel is defined as:

$$\text{Channel state} = \begin{cases} \text{open}, & \text{if } R_G^{xx^2} + R_G^{yy^2} \geq R_t \\ \text{closed}, & \text{otherwise} \end{cases} \tag{S5}$$

where R_t is the a threshold value above which the channel is considered open. In this case, it was chosen to be 8.2 nm^2, relying on the sharp transition observed in the pore size with increasing membrane tension (Fig. 1c in the main text). The opening probability was further calculated as P_{open} = open states/total states, where the state of the channel is recorded at every time step.

C. Single channel

A single channel was inserted in a square membrane patch of side length 40σ. The system was equilibrated for 500,000 time steps and a hypoosmotic shock was applied by inserting $N_{solutes}$ solute particles in the system. Multiple simulations were run by varying $N_{solutes}$ between 0 and 1000 in increments of 100 particles. The simulations were run for 2.5 million time steps each. The radial expansion of the channels was recorded at every step during the simulation. Figure 2(a) shows how the radial expansion of the channel is affected during a downshock corresponding to a tension of approximately 1 mN/m. The fluctuations of the radial expansion are increased to higher values immediately after the application of the downshock, indicating that the channel acts like a pressure sensor capable of sensing small changes in the surrounding membrane tension.

D. Non-interacting channels

N channels were inserted inside a membrane patch, where $N = 1, 2, 3, 4, 5$. $N_{solutes} = 800$ were added to the system. Both the probability of opening and the flux of solutes (the flow rate of the solute through the membrane) were recorded for 2.5 million time steps, similarly to the single channel simulation. Five different random seeds in the initial channel geometry were used for each simulation. Results are presented in Fig. 2 of the main text. It was revealed that the number of channels had no influence on the opening probability of individual channels and that the flux of solutes is linear in the number of channels. These results indicate that the channels do not influence each other's gating properties in the absence of a direct interaction. The model does not adequately capture any potential membrane-mediated interactions. Therefore, an attractive patch (blue beads, Fig S1) was added in order to investigate the effect of nonspecific protein interaction on gating.

E. Interaction between two channels

To measure the influence of two adjacent channels on one another, we fixed them in the membrane patch at a $d = 10\sigma$ distance with very weak springs of elastic constant $k_{\text{spring}} = 0.5kT/\sigma^2$. The weak springs serve to maintain the channels in each other's proximity and also limit their lateral diffusion. The interaction between the attractive patches located on the two channels was increased from $\varepsilon = 0kT$ to $\varepsilon = 2.0kT$ in increments of $0.1kT$. The influence of two channels interacting on their radial expansion is described in Fig. 3a of the main text. There is a clear tendency for adjacent interacting channels to reduce each other's radial expansion, and force each other to adopt a more closed conformation. Conformational changes require a higher activation energy necessary to overcome the attractive homophilic protein interactions. The effect of interaction energy on the opening probability of adjacent channels is described in section IV.C. The simulations with two channels were run for 2 million steps and five random seeds were used for the initial geometry. The effect of protein interactions was studied at two different membrane tensions 1.30 mN/m, 0.70 mN/m.

F. Aggregates of MscLs

Twelve MscLs were inserted in a membrane patch of side length 60σ at random initial locations. The membrane patch was equilibrated for 500,000 time steps. Two different membrane tensions (1.70 mN/m, 0.70 mN/m.) were applied. The depth of the interaction potential between the attractive protein patches was set to be $\varepsilon = 1.0kT$ to drive the aggregation of proteins into clusters (Fig. S2). A clustering

algorithm was used to keep track of the MscL clusters formed during the simulation as follows: A channel was considered as being part of a cluster if it was found at a distance less than 10σ from a neighbouring channel, the distance at which two channels start interacting. A single channel radius is $\approx 4\sigma$. Changing the threshold to 9σ and 12σ did not make a significant difference in the distribution of the cluster sizes. The simulation was run for seven million time steps. The pore size was tracked at every time step and the average opening probability per channel per cluster was computed as a function of the cluster size (Fig. S3).

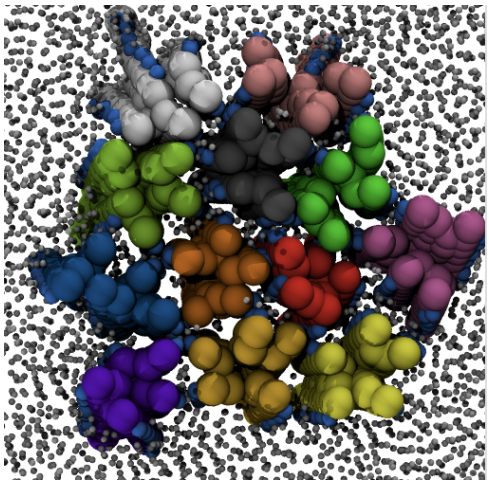

FIG. S2: **A cluster with twelve MscLs**, each presented with a different colour. The attraction between channels leads to the eventual aggregation of channels into large ensembles which show different gating behaviour from the individual channels. The attractive patches on the channels are coloured in light blue and the lipids in grey. Some of the channel beads are shown in a larger size than they are.

The formation of dimers was tracked throughout the simulation and the average interaction energy between the channels within a dimer was calculated at every time step. This allowed the estimation of the tension-dependent interaction between two channels. Further details are given in section IV.C.
For simulations that started with pre-formed clusters (Fig. S2), a single cluster was formed by slowly pulling all the twelve channels toward the centre of the membrane with weak springs. The springs were then released, but the attractive interaction between channels kept the cluster stable as long as no tension was applied to the membrane (Fig. 3b inset). A large osmotic downshock was then applied (corresponding to approximately 1.70 mN/m in one simulation and 0.70 mN/m in another). Both the separation between the channels and the pore size were tracked during seven million steps (Fig. 3c).

III. CELL VOLUME DYNAMICS DURING HYPOOSMOTIC SHOCK

A. A brief description of the previous model

We implement our previously developed model to deduce cellular volume (V) and solute (n_i) dynamics of *Escherichia coli* [6] upon a hypoosmotic shock. Water flux (j) across the cell membrane depends on the difference between the osmotic pressure (Π) and the Laplace pressure (P) of the cell wall, $j \sim -\pi - P$. Where π is defined by Morse Equation given as below:

$$\Pi = -\phi(c_i - c_e)RT \tag{S6}$$

The molar osmotic co-efficient (ϕ) is set to 1 because we osmolarities of solutions measured with an osmometer. Constants c_i, c_e, R and T are cytoplasmic and media solute concentrations, ideal gas constant and thermodynamic temperature, respectively. To derive P we consider cell wall elasticity that has been experimentally demonstrated to exhibit stress-stiffening, thus $E = E_0(P/P_0)^\kappa$ [7], where E_0 and P_0 are the pre-shock steady-state elasticity and pressure and κ is the set to 1 (experimentall it was

measured as 1.22) [6, 7]. We then write:

$$E = \frac{True \quad stress}{True \quad strain} = \frac{d\gamma/l}{dr/r} = E_0 \frac{P}{P_0} \tag{S7}$$

where γ is the membrane tension, and r and l are the radius of the cell and the thickness of the cell wall (note that we effectively merge the contribution from the wall and the membranes into one, thus l can be considered the whole envelope thickness). Considering *E.coli* as thin cylinder, we can write $\gamma = Pr$. At pre-shock steady-state, osmotic pressure gives rise to Laplace pressure, $P_0 = RT\Delta c_0$, where Δc_0=0.04 Osmol/l is the pre-shock osmotically active solute gradient across the cell membrane determined based on experimental estimates of turgor pressure [6]. Solving equation S7 for P gives:

$$P = e^{\sqrt[3]{\frac{10}{3}\pi \frac{E_0 l (V^{\frac{1}{3}} - V_0^{\frac{1}{3}})}{\Delta c_0 RT V^{\frac{1}{3}} V_0^{\frac{1}{3}}}}} \cdot \Delta c_0 RT \frac{V_0^{\frac{1}{3}}}{V^{\frac{1}{3}}} \tag{S8}$$

V_0 is the pre-shock cell volume which is experimentally found to be 1.338 $\pm$ μm^3 [6]. The molar water flux during an osmotic shock leads to change in cell volume and hence:

$$\frac{dV}{dt} = V_m j A_c = V_m K \cdot (-\Pi - P) \tag{S9}$$

A_c is the surface area of the cell (considering the cell as a spherocylinder of 2:1 length to diameter ration with d=1μm). V_m is the molar volume of water and K is the effective water conductivity. Gating of MSCs upon a hypoosmotic shock increases the permeability of the cell membrane to water, which we capture with a constant A

$$\frac{dV}{dt} = (A+1) \cdot V_m K \cdot (-\Pi - P) \tag{S10}$$

$A = 2$ means 2 times higher conductivity compared to the cell membrane with closed MSCs (when $A = 0$). The channels are set open if V is greater than the volume threshold of opening (V_{th}). To deduce the dynamics of cytoplasmic solute concentration we allow the diffusive flow of solutes through the open MSCs, as well as take into account the build up of Laplace pressure in the cell wall due to the large influx of water:

$$\frac{dn_i}{dt} = -A \cdot \left(V_M K \cdot \frac{n_i}{V} \cdot P + D_s N_{MSC} \cdot a_{MSC} \cdot \frac{\frac{n_i}{V} - c_e}{l_M V_0} \right) \tag{S11}$$

where N_{MSC} is the sum of all the MSCs in the cell, a_{MSCL} is the total MSCs pore area, D_s is the average diffusion constant of osmotically active solutes and l_m is the thickness of cell membrane, both have been experimentally estimated and we use the same values as previously [6]

.

B. Including MscL clustering into the model

The channel we built for our course-grained simulations (Fig. S1) is based on the structure of MscL. In a wild type *E. coli* strain there are 7 different MSCs [8]. However, for simplicity we will apply the results of the course-grained simulations to them all and will for now exclude any differences. We thus use MSCs and MscLs interchangeably from here on. The gating activity of the channels will depend on the probability of opening of single channels and the extent of their clustering, which both depend on the membrane tension and the number of channels in the system. To include the effect of channel clustering on cell volume, we introduce a parameter β that captures the total probability of the channel gating in the system, defined as below:

$$\beta = \sum_{N=1}^{30} P_{opening}(N, \gamma) \cdot P_{formation}(N, \rho, \gamma) \tag{S12}$$

The probability of opening of a channel in a cluster of size N, $P_{opening}(N)$, is given as:

$$P_{opening}(N,\gamma) = a_1 \cdot (1 - a_2 \cdot e^{-C_1\gamma})e^{-C_2 N} \tag{S13}$$

The functional form was chosen to agree with the results of simulations given in Fig. S3, where a numerical fit gave $a_1 = 1.684$, $a_2 = 0.91$, $C_1 = 0.9274$, $C_2 = 0.49$. The *in vivo* values of membrane tension are calculated as before, from $\gamma = P \cdot r$ and equation S8. For a resting turgor pressure of 1 atm and cell radius of 0.5 um, the lateral tension on the cell membrane ranges from 50 to 80 mN/m for 15% volume increase during a hypoosmotic shock. Thus, the overall increase in membrane tension is 30 mN/m. Previous *in-vitro* report that the probability of MscL opening is half for a membrane tension ranging from 8-14 mN/m [9]. In order to scale the lateral membrane tension with the tensions in the coarse-grained model, we chose a mid-value of 11 mN/m.

Here it is important to keep in mind that our coarse-grained membrane model is phenomenological in nature, and while it produces the correct mechanical properties of biological membranes in general (bending rigidity and fluidity), it is not meant to reproduce the exact experimental membrane system. For instance, the membrane in our simulations ruptured at tensions greater than 3 mN/m, while experimentally reported values range between 1 mN/m and 25 mN/m, depending on the membrane composition and experimental conditions [10]. Moreover, our computer model does not include the presence of the bacterial wall, hence the value of the rupture tension in our generic model is not expected to match the experimentally reported values for bacterial envelope rupture. Nevertheless, the trends and physical mechanisms we observe will still be valid.

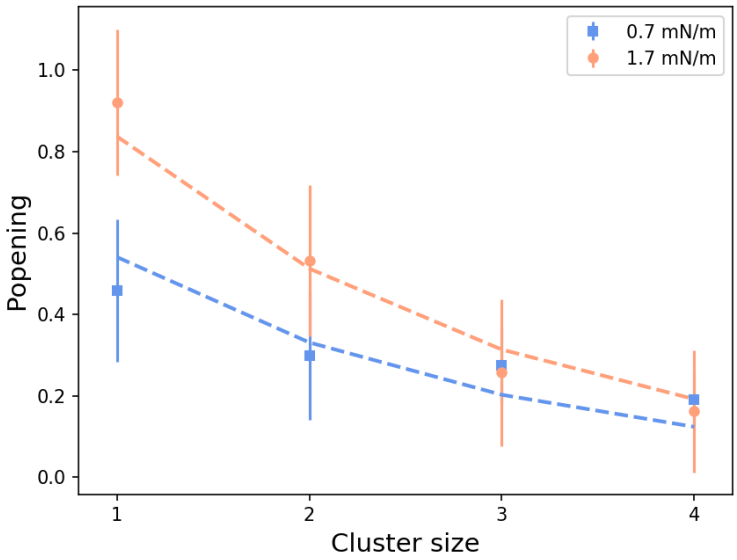

FIG. S3: **Probability of opening per channel versus cluster size at two values of membrane tension.** As the cluster size increases and the tension decreases, the probability of opening per channel decreases.

$P_{formation}(N,\rho,\gamma)$ is the probability of formation of cluster of size N and at a given membrane tension and channel packing fraction, ρ, given as:

$$\rho = N_{MSC} \cdot a_{MSC}/A_c \tag{S14}$$

To obtain $P_{formation}(N,\rho,\gamma)$ we take into account that the computer model developed here, however minimal, does not allow us to collect good statistics for the cluster size distribution in a system of several hundreds of channels (and all at different tensions), which are the values reported in experiments [11]. Thus, to acquire better statistics for $P_{formation}$ we carry a separate set of simulations in which we model the channels as simple disks that interact with each other via a Lennard-Jones potential whose strength and range match the one measured in the membrane channel simulations, and at different values of

membrane tensions. The disks were placed inside a simulation box and allowed to aggregate, similarly to how channels organise into clusters given enough time and a strong enough interaction ($\varepsilon_{protein-protein}$). This allowed an accurate estimation of the distribution of channels into clusters of different sizes. 1089 disks of diameter d = 1σ were inserted inside a square box of side length L. The side length was varied from $L = 100\sigma$ to $L = 500\sigma$ in steps of 100σ and the 2D molecular dynamics simulations were carried out in the NVT ensemble. The channels were allowed to interact through a Lennard-Jones potentials of depth $\varepsilon = 1.0kT$ to $\varepsilon = 2.0kT$ in steps of 0.2 kT. This range of interactions mimics the interactions observed within dimers of channels (Fig. S9). The disks were counted as being in the same cluster if found at distances $d \leq 3\sigma$, which corresponds to the distance at which the disks feel each others attraction in this simulation. The simulations were run for 5 million time steps each. The probability of formation for a cluster of size N showed a non-linear dependence on the packing fractions (or cell volumes in the real system) as shown in Fig. S4. We can fit the observed probability of formation of a cluster of size N to a geometric distribution of the type:

$$P_{formation}(N, L, \varepsilon) = (1-p)^{N-1}p, \tag{S15}$$

where p is the geometric distribution's ratio and related to the probability of formation of a monomer: $P_{formation}(1, L, \varepsilon) = p$. Equation S13 can be rewritten as follows:

$$lnP_{formation}(N, L, \varepsilon) = (N-1)ln(1-p) + lnp \tag{S16}$$

We assume that $p \propto L^2/\varepsilon$. The rationale for this is as follows: (i) if the system's size (for a fix packing fraction) increases, the probability of observing monomers will increase, and (ii) as the interaction energy between channels increases, they tend to reorganize into clusters and the probability of observing monomers will decrease. We can thus substitute p for $p = mL^2/\varepsilon$, where m is a parameter that captures the dependence of the geometric ratio, p, on L^2 and ε:

$$lnP_{formation}(N, L, \varepsilon) = (N-1)ln(1-mL^2/\varepsilon) + ln(mL^2/\varepsilon) \tag{S17}$$

By using a Taylor approximation when $mL^2/\varepsilon << 1$:

$$lnP_{formation}(N, L, \varepsilon) = (N-1)(-mL^2/\varepsilon) + ln(mL^2/\varepsilon), \tag{S18}$$

which can be rewritten as

$$lnP_{formation}(N, L, \varepsilon) = (1-N)mL^2/\varepsilon + ln(L^2/\varepsilon) + lnm, \tag{S19}$$

Then, channel packing fraction, ρ, is inversely proportional to box area L^2:

$$\rho = \frac{N_{disks}\pi d^2}{4L^2}, \tag{S20}$$

So equation S17 becomes:

$$lnP_{formation}(N, \rho, \varepsilon) = (1-N)mN_{disks}\pi d^2/4\rho\varepsilon + ln(1/\rho\varepsilon) + ln(N_{disks}\pi d^2/4) + lnm \tag{S21}$$

Writing the equation S19 only in terms of the three variables N, ρ and ε, it becomes:

$$ln[P_{formation}(N, \rho, \varepsilon)] = (1-N)A/\rho\varepsilon + ln(1/\rho\varepsilon) + B \tag{S22}$$

with A and B being constants to be estimated from the simulations. Fitting the results for $P_{formation}$ for both different ρ and different ε varied in the parameter space described above yielded the coefficients: $A = 0.009kT$ and $B = -8.316$.

We assume there is a correlation between the effective interaction energy between two channels with the surface tension, because higher surface tensions should lead to conformations that are more tilted and less likely to interact with each other. This is indeed observed in Fig. S9 which shows the average interaction energy between two channels if they are close enough from each other (explained in section II F). As the tension is increased, it is observed indeed that the channels tend to interact less strongly. We can then approximate the dependence of the interaction between channels on surface tension on a sigmoid (Fig. S9):

$$\varepsilon = a/(1 + \exp(-c(\gamma - d)) + b, \tag{S23}$$

where a, b, c and d are the parameters determined from the fitting the data in Fig. S9 ($a = 0.587kT$, $b = -1.973kT$, $c = 18.431$ m/mN, $d = 0.743$ mN/m).

We then normalise $P_{formation}$ as follows:

$$\sum_{N=1}^{30} P_{formation}(N, \rho, \gamma) = 1 \tag{S24}$$

We group together clusters larger than *N=30* as $P_{opening}$ and $P_{formation}$ are negligibly small for *N>30*, see Fig S3 and S4.

Lastly, based on our previous experimental results and cell volume recovery model, we scale the parameters of the coarse grained model in equation S22 and S23, such that at 4% cell volume increase all the channels are monomers [6] and a, b, c and d become $a = 19.371kT$, $b = -19.73kT$, $c = 1.675$ m/mN, $d = 3.715$ mN/m, respectively (Fig. S4).

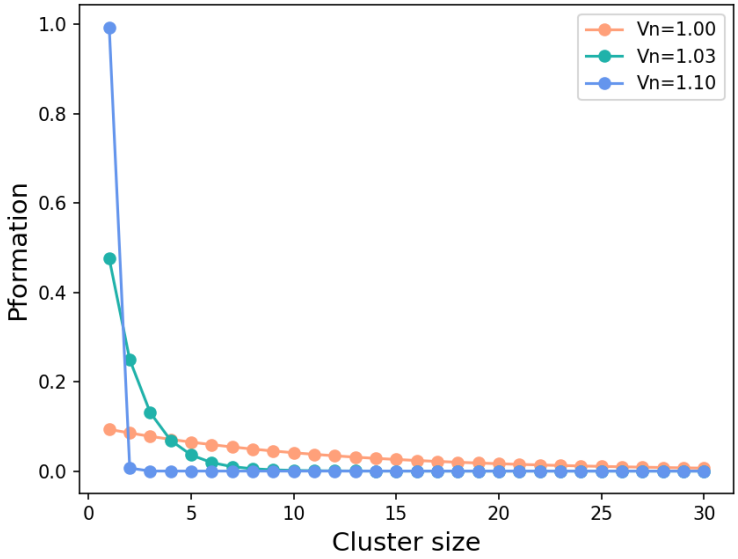

FIG. S4: **Probability of formation of a channel cluster at varying membrane tension.** The probability of formation of a cluster, calculated using Eq S22 at varying normalized cell volumes (V_n), at 0.5% packing fraction.

The Master equations for the cell volume change and solute concentration change (Eq. S10 and S11) can now be written as:

$$\frac{dV}{dt} = (\beta + 1)V_m K R T \left[\left(\frac{n_i}{V} - c_e\right) - e^{\sqrt[3]{\frac{10}{3}}\pi \frac{E_0 l (V^{\frac{1}{3}} - V_0^{\frac{1}{3}})}{\Delta c_0 R T V^{\frac{1}{3}} V_0^{\frac{1}{3}}}} \cdot \Delta c_0 \frac{V_0^{\frac{1}{3}}}{V^{\frac{1}{3}}} \right] \tag{S25}$$

$$\frac{dn_i}{dt} = -\beta \cdot \left(V_m K \cdot \frac{n_i}{V} \cdot e^{\sqrt[3]{\frac{10}{3}}\pi \frac{E_0 l (V^{\frac{1}{3}} - V_0^{\frac{1}{3}})}{\Delta c_0 R T V^{\frac{1}{3}} V_0^{\frac{1}{3}}}} \cdot \Delta c_0 R T \frac{V_0^{\frac{1}{3}}}{V^{\frac{1}{3}}} + \alpha\left(\frac{n_i}{V} - c_0\right)\right). \tag{S26}$$

In Eq S26, $\alpha = D_s N_{MSC} a_{MSC} / l_M V_0$. We fit the parameter values K and α to an experimental representative singe cell volume response as these two parameters are associated with the properties of channels and expect it to be different from the previous estimations [6] and fix the rest of the parameters at values previously determined (see section SI III for details and Supplementary Information of our

previous model [6]). The 0.96 Osmol hypoosmotic shock was achieved by growing *E.coli* in media with elevated NaCl concentration [6] and then suddenly exposing the cells to the same media but without NaCl. Growing in elevated NaCl (specifically 550mM) results in expression of ≈ 1300 MscL [11]. The packing fraction at this experimental condition is 0.5%, calculated based on the area of a single MscL ($24nm^2$ [12]) and surface area of *E.coli* (6 μm^2 based on experimentally obtained cell volume of 1.338 fL [6]). The obtained fit values for K and α are $7.0 \times 10^{-22} molPa^{-1}s^{-1}$ and 0.37 fls^{-1}. To predict the cell responses when the channels existed solely as isolated channels or dispersed, $P_{formation}$ and $P_{opening}$ in Eq.S12 was calculated for $N = 1$.

IV. SUPPORTING RESULTS

A. Membrane tension

The calculation of the membrane tension revealed a linear scaling against the number of solute particles in the simulation box (Fig. S5). The membrane tension was fitted to a linear equation of the form $\gamma = aN_{solutes} + b$, with $a = 0.002$ mN/m and $b = -0.304$ mN/m. The membrane ruptured at tensions greater than 3 mN/m, corresponding to a number of solutes particles greater than 1800. This mapping of the surface tension was used in all subsequent calculations.

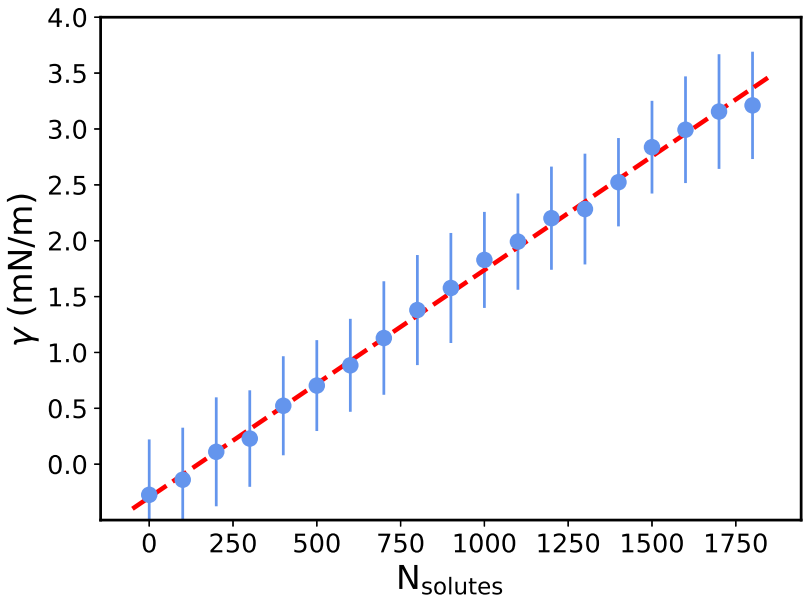

FIG. S5: **Membrane tension against number of solute particles.** The membrane tension scales linearly with the number of solute beads. The surface tension was calculated as an average over one million time steps. The error bars represent one standard deviation. Higher number of solutes (not shown here) led to the fracturing of the membrane.

B. Probability of opening

The opening probability of a single isolated MSC increases monotonically with membrane tension (Fig. S5). This suggests the channel acts as a pressure sensor, more likely to be found in the "open" state at large external pressures. The threshold value of the gyration radius tensor term, above which the channel was considered as "open" in Fig. S6, was 8.2 nm^2.

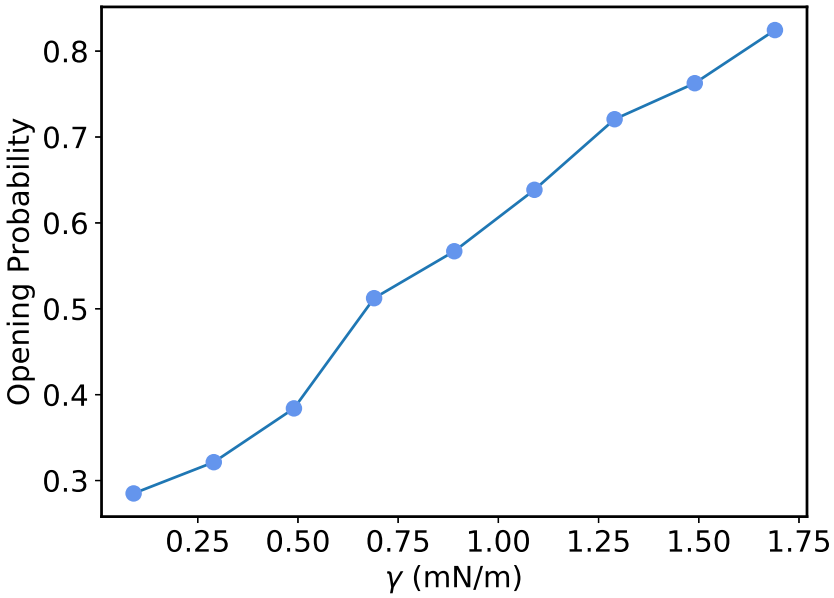

FIG. S6: **Opening probability of a single MSC against membrane tension.** The opening probability of a single isolated channel increases proportionally with the membrane tension. It should be noted that in the context of this model, there is still a finite probability for the channels to open even at low membrane tension. At higher tensions, the channels are more permeable to the solute particles, being found mostly in the open conformation.

C. Interaction of two channels

The potential of mean force (PMF) between two channels was calculated using the Weighted Histogram Analysis Method (WHAM) [13]. A biasing potential of a spring constant $k_{spring} = 1kT/\sigma^2$ was applied to the two channels and 20 different windows were used to extract the potential. In Fig. S7 it can be seen that two channels do not interact through any membrane mediated interactions, their only interaction being the volume exclusion at low separations.

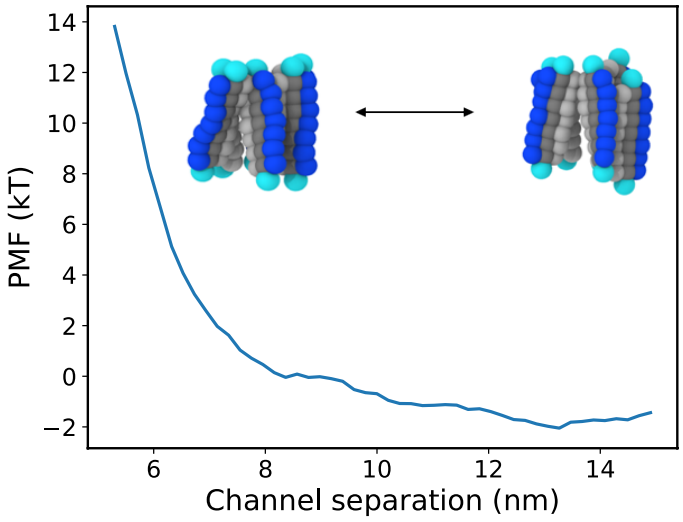

FIG. S7: **Potential of mean force between two non-interacting channels.** The potential of mean force between channels shows a relatively flat profile at large separations. The sudden increase at small separations is caused by the volume exclusion of the two channels.

D. Interaction of two rigid inclusions

Rigid inclusions of length 8 nm were inserted in the membrane to test the attractive effect of the hydrophobic mismatch. These inclusions were constructed similarly to the channels with a hydrophobic core to and head beads. The same potentials were used as for the MscL channels. The inclusions do not have any direct interactions. The potential of mean force (PMF) between two rigid inclusions was calculated from computing the radial distribution function of 10 channels placed on a lipid bilayer of side length $L_x = 40\sigma$, using the formula $PMF(r) = -k_B T ln(g(r))$. The inclusions did not organise into clusters, but showed a slight interaction of approximately 0.5kT (Fig. S8). It can be concluded that, although membrane-mediated interactions might be present in the system, they are too weak to drive the aggregation of channels and thus an attractive Lennard-Jones potential between channels was introduced to model the homophilic protein interactions. The simulations were run for 2 million time steps and 10 different seeds were used to compute the potential of mean force.

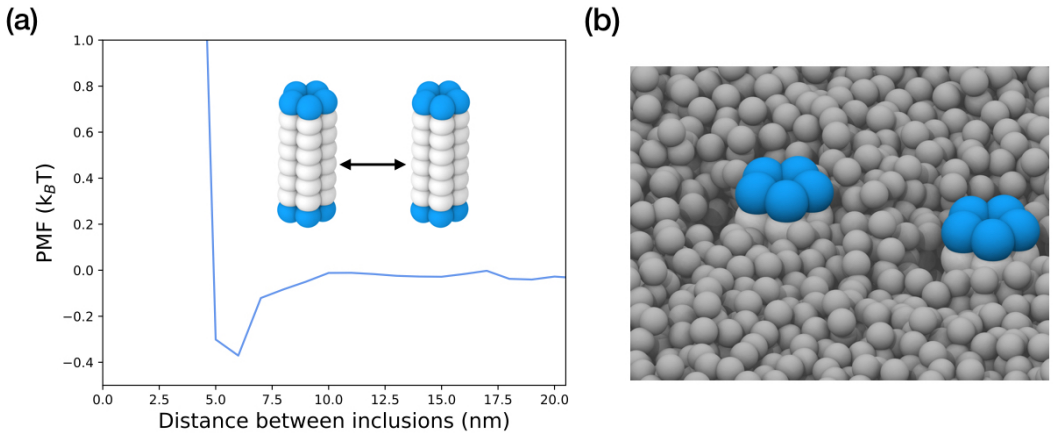

FIG. S8: **Potential of mean force between two rigid cylindrical inclusions of hydrophobic mismatch of 0.5 nm.** (a) The potential of mean force between two rigid cylindrical inclusions of a 0.5 nm hydrophobic mismatch shows weak attractive interactions of ~ 0.5 kT. (b) Simulation snapshot of rigid inclusions embedded in the membrane.

E. Interaction of two attractive proteins

The probability of opening per channel is heavily influenced by the interaction of two adjacent channels. The increase in the direct protein-protein interaction leads to a decrease in the opening probability (Fig. S9). Higher interaction energies act to keep the two channels strongly bound together and allow for less conformational change. The channel has to overcome a larger activation energy barrier in order to rearrange from a compact closed structure into an expanded open one.

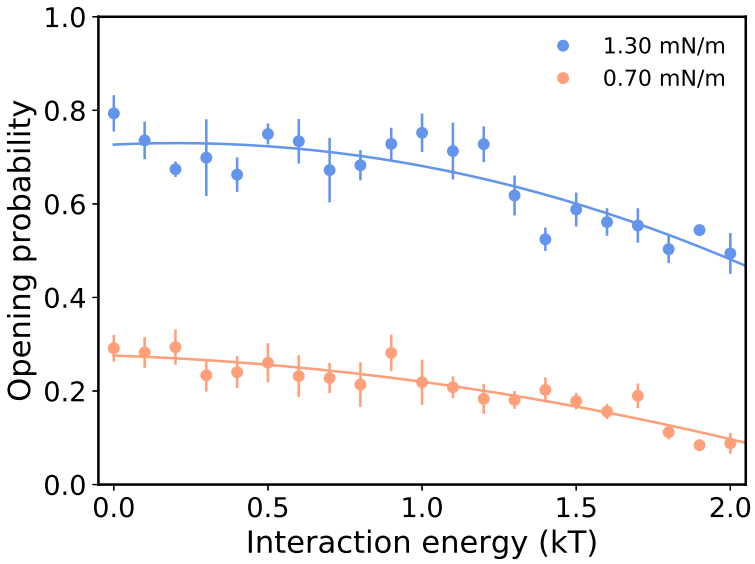

FIG. S9: **Opening probability for a channel against protein interaction energy** $\varepsilon_{protein,protein}$**.** The opening probability per channel of two interacting channels kept at a fixed distance from each other.

The interaction energy between two channels in a dimer was plotted in Fig. S10. The average interaction between channels decreases as the tension is increased. There is a sharp transition in the average interaction within a dimer at a tension of 0.7 mN/m. The behaviour can be attributed to tilting of the channels in the membrane plane at higher tensions, thus reducing the available contact area. Higher tensions will also suppress membrane thermal fluctuations, which induce the unbinding of two channels in a dimer.

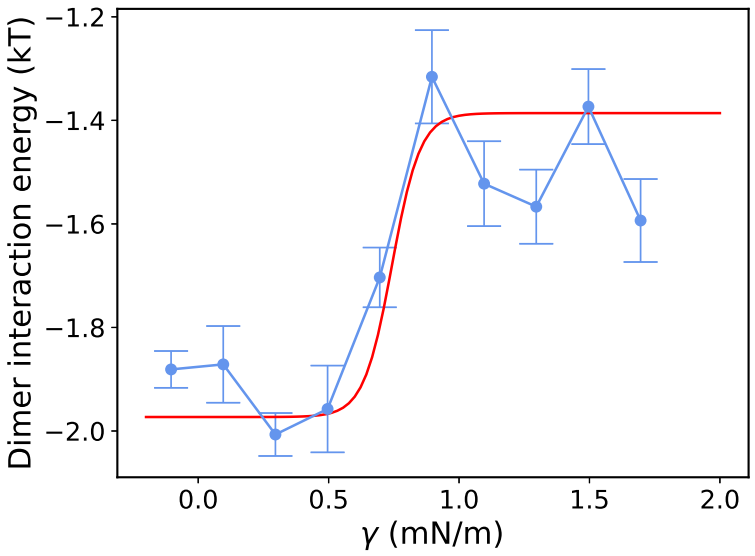

FIG. S10: **The average interaction energy between channels in a dimer depends on the membrane tension.** As the tension is increased, the channels tend to interact less favourably which leads to the disaggregation of protein clusters.

F. Model fit to experimental volume trace

We fit the master equations S25 and S26 to a representative experimental volume trace for 0.96 osmol [6] and physiological packing fraction of 0.5%, at this experimental conditions. The fitted trace was used

to demonstrate the cluster aggregation-disaggregation dynamics as in the main text,Fig. 4a.

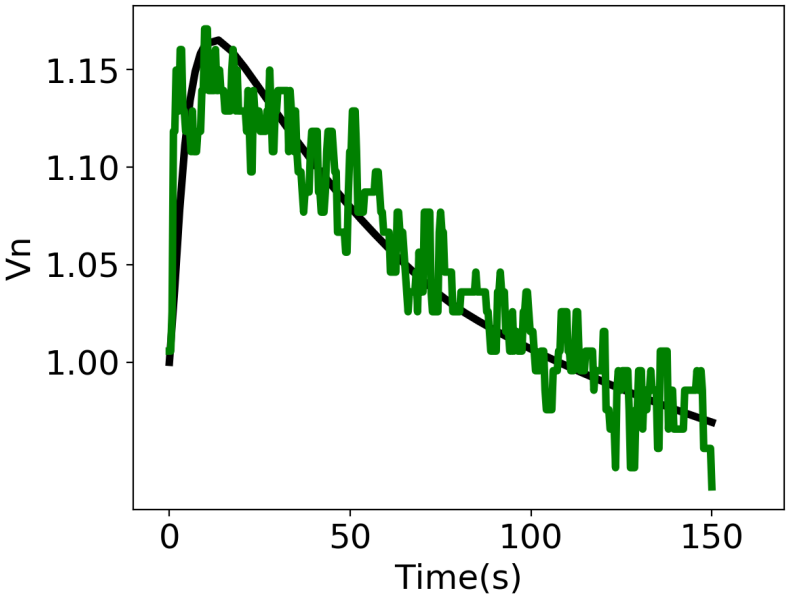

FIG. S11: Model fit (black) to a representative experimental volume trace (green) at 0.96 Osmol hypoosmotic shock and ρ=0.5%.

G. Dynamics of β during hypoosmotic shock

The figure below demonstrates the dynamics of the effective probability of opening, β, (see Eq. S12) upon hypoosmotic shock, when the channels in the model are clustered and dispersed. Effective probability of opening β in the clustered model shows an earlier drop in channel opening attributing to re-aggregation of channel clusters during volume recovery. This early closing of channels results in lesser volume overshoot while compared to the dispersed model (Fig4b).

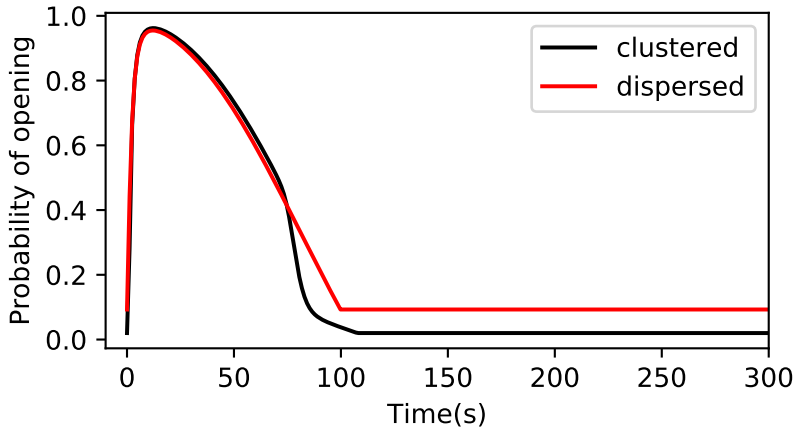

FIG. S12: Comparison of dynamics of the effective probability of opening, β, between a clustered model (black line) and dispersed model(red line) during a 0.96 Osmol hypoosmotic shock and 0.5% channel packing

H. Analysis of trade-offs different amounts of clustering pose on cell pressure and volume regulation

To illustrate the effects of increasing amount of clusters (higher than that predicted by coarse-grained model) on cell volume response (Fig 4b), interaction energy between the channels in Eq. S7 is increased by increasing the scaled constants a and b up to 20 times. The figure below shows the maximum tension on the cell membrane at maximum volume expansion, plotted against the minimum cell volume ($\Delta V_{n,min}$) during volume recovery. At a lower amount of channel clustering, the cells benefit by reducing the volume overshoot without much increasing the maximum tension upon a hyperosmotic shock. At higher amount of clustering, the benefit of further reducing $\Delta V_{n,min}$ is traded off by the burden on cells due to increased cell membrane tension, risking cell lysis. This illustrates that the interchannel interactions have been likely optimized to give the optimal amount of clustering.

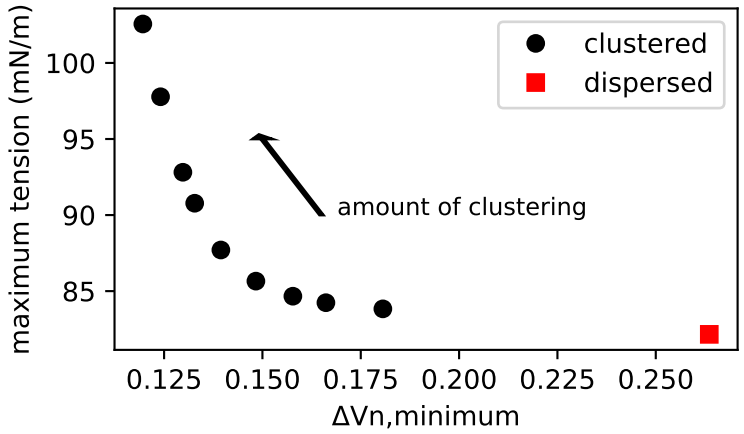

FIG. S13: **Effect of increased amount of clustering on the cell tension and overshoot upon a hypoosmotic shock.** Maximum tension on the cell membrane at maximum volume expansion is plotted against difference in volume overshot below the initial volume ($\Delta V_{n,min}$). The osmotic shock is 0.96 Osmol and packing fraction is set to 0.5%.

I. Supporting Videos

Video 1: Pore size oscillations of a single channel under osmotic shock leading to the membrane tension of 1.1 mN/m (see also Fig. 2b). Solute particles are omitted for clarity.

Video 2: Passage of a solute particle though a channel pore for membrane tension of 1.1 mN/m.

Video 3: Inter-protein attraction leads to channel clustering and cooperative closure; $\varepsilon_{protein,protein} = 0.9kT$ and $\gamma = 1.3$ mN/m (see also Fig. 3a). Solute particles are omitted for clarity.

Video 4: Side view: A preformed cluster made of 12 channels disaggregates under tension of $\gamma = 1.7$ mN/m (see Fig 3c). Here solute particles are explicitly shown (colored in pink).

Video 5: Top view: A preformed cluster made of 12 channels disaggregates under tension of $\gamma = 1.7$ mN/m (see Fig 3c). Solute particles are omitted for clarity.

[1] Ira R Cooke, Kurt Kremer, and Markus Deserno. Tunable generic model for fluid bilayer membranes. *Physical Review E*, 72(1):011506, 2005.
[2] John D Weeks, David Chandler, and Hans C Andersen. Role of repulsive forces in determining the equilibrium structure of simple liquids. *The Journal of chemical physics*, 54(12):5237–5247, 1971.
[3] Steve Plimpton. Fast parallel algorithms for short-range molecular dynamics. *Journal of computational physics*, 117(1):1–19, 1995.
[4] William Humphrey, Andrew Dalke, and Klaus Schulten. VMD – Visual Molecular Dynamics. *Journal of Molecular Graphics*, 14:33–38, 1996.
[5] Jean-Baptiste Fournier and Camilla Barbetta. Direct calculation from the stress tensor of the lateral surface tension of fluctuating fluid membranes. *Physical review letters*, 100(7):078103, 2008.
[6] Renata Buda, Yunxiao Liu, Jin Yang, Smitha Hegde, Keiran Stevenson, Fan Bai, and Teuta Pilizota. Dynamics of escherichia coliâĂŹs passive response to a sudden decrease in external osmolarity. *Proceedings of the National Academy of Sciences*, 113(40):E5838–E5846, 2016.
[7] Yi Deng, Mingzhai Sun, and Joshua W. Shaevitz. Direct measurement of cell wall stress-stiffening and turgor pressure in live bacterial cells. 2011.
[8] Michelle D Edwards, Susan Black, Tim Rasmussen, Akiko Rasmussen, Neil R Stokes, Terri-Leigh Stephen, Samantha Miller, and Ian R Booth. Characterization of three novel mechanosensitive channel activities in escherichia coli. *Channels*, 6(4):272–281, 2012.
[9] Vladislav Belyy, Kishore Kamaraju, Bradley Akitake, Andriy Anishkin, and Sergei Sukharev. Adaptive behavior of bacterial mechanosensitive channels is coupled to membrane mechanics. *The Journal of General Physiology*, 135(6):641–652, 2010.
[10] Evan Evans, Volkmar Heinrich, Florian Ludwig, and Wieslawa Rawicz. Dynamic tension spectroscopy and strength of biomembranes. *Biophysical journal*, 85(4):2342–2350, 2003.
[11] Maja Bialecka-Fornal, Heun Jin Lee, Hannah A. DeBerg, Chris S. Gandhi, and Rob Phillips. Single-cell census of mechanosensitive channels in living bacteria. *PLoS ONE*, 7(3), 2012.
[12] Stephan L Grage, Asbed M Keleshian, Tamta Turdzeladze, Andrew R Battle, Wee C Tay, Roland P May, Stephen A Holt, Sonia Antoranz Contera, Michael Haertlein, Martine Moulin, et al. Bilayer-mediated clustering and functional interaction of mscl channels. *Biophysical journal*, 100(5):1252–1260, 2011.
[13] Shankar Kumar, John M Rosenberg, Djamal Bouzida, Robert H Swendsen, and Peter A Kollman. The weighted histogram analysis method for free-energy calculations on biomolecules. i. the method. *Journal of computational chemistry*, 13(8):1011–1021, 1992.

Bibliography

Akitake, Bradley, Andriy Anishkin, and Sergei Sukharev (2005). “The "dash-pot" mechanism of stretch-dependent gating in MscS”. In: *Journal of General Physiology* 125.2, pp. 143–154. ISSN: 00221295.

Al-Rekabi, Zeinab and Sonia Contera (2018). “Multifrequency AFM reveals lipid membrane mechanical properties and the effect of cholesterol in modulating viscoelasticity”. In: *Proceedings of the National Academy of Sciences* 115.11, pp. 2658–2663. ISSN: 0027-8424.

Arnoldi, Markus et al. (2000). “Bacterial turgor pressure can be measured by atomic force microscopy”. In: *Physical Review E* 62.1, pp. 1034–1044. ISSN: 1063-651X.

Asha, H. and J. Gowrishankar (1993). “Regulation of kdp operon expression in Escherichia coli: Evidence against turgor as signal for transcriptional control”. In: *Journal of Bacteriology* 175.14, pp. 4528–4537. ISSN: 00219193.

Baba, Tomoya et al. (2006). “Construction of Escherichia coli K-12 in-frame, single-gene knockout mutants: the Keio collection.” In: *Molecular systems biology* 2, p. 2006.0008. ISSN: 1744-4292.

Baldwin, W. W. et al. (1995). “Growth and buoyant density of Escherichia coli at very low osmolarities”. In: *Journal of Bacteriology* 177.1, pp. 235–237. ISSN: 00219193.

Balleza, Daniel and Froylan Gómez-Lagunas (2009). “Conserved motifs in mechanosensitive channels MscL and MscS”. In: *European Biophysics Journal* 38.7, pp. 1013–1027. ISSN: 01757571.

Baslé, Arnaud et al. (2006). “Crystal Structure of Osmoporin OmpC from E. coli at 2.0 Å”. In: *Journal of Molecular Biology* 362.5, pp. 933–942. ISSN: 00222836.

Belyy, Vladislav et al. (2010). “Adaptive behavior of bacterial mechanosensitive channels is coupled to membrane mechanics”. In: *The Journal of General Physiology* 135.6, pp. 641–652. ISSN: 0022-1295.

Benz, R., A. Schmid, and R. E.W. Hancock (1985). "Ion selectivity of gram-negative bacterial porins". In: *Journal of Bacteriology* 162.2, pp. 722–727. ISSN: 00219193.

Berrier, C. et al. (1996). "Multiple Mechanosensitive Ion Channels from Escherichia coli, Activated at Different Thresholds of Applied Pressure". In: *Journal of Membrane Biology* 151.2, pp. 175–187. ISSN: 00222631.

Berrier, Catherine et al. (1989). " A patch-clamp study of ion channels of inner and outer membranes and of contact zones of E. coli , fused into giant liposomes ". In: *FEBS Letters* 259.1, pp. 27–32.

Berrier, Catherine et al. (1992). "Gadolinium ion inhibits loss of metabolites induced by osmotic shock and large stretch-activated channels in bacteria". In: *European Journal of Biochemistry* 206.2, pp. 559–565. ISSN: 14321033.

Bialecka-Fornal, Maja et al. (2012). "Single-cell census of mechanosensitive channels in living bacteria". In: *PLoS ONE* 7.3. ISSN: 19326203.

Bialecka-Fornal, Maja, Heun Jin Lee, and Rob Phillips (2015). "The Rate of Osmotic Downshock Determines the Survival Probability of Bacterial Mechanosensitive Channel Mutants". In: *Journal of Bacteriology* 197.1, pp. 231–237. ISSN: 0021-9193.

Bickel, Fabian et al. (2016). "Reversible NaCl-induced aggregation of a monoclonal antibody at low pH: Characterization of aggregates and factors affecting aggregation". In: *European Journal of Pharmaceutics and Biopharmaceutics* 107, pp. 310–320.

Boer, Miriam, Andriy Anishkin, and Sergei Sukharev (2011). "Adaptive MscS gating in the osmotic permeability response in E. coli: The question of time". In: *Biochemistry* 50.19, pp. 4087–4096. ISSN: 00062960.

Booth, Ian R. (2014). "Bacterial mechanosensitive channels: Progress towards an understanding of their roles in cell physiology". In: *Current Opinion in Microbiology* 18.1, pp. 16–22. ISSN: 18790364.

Bootha, Ian R. and Paul Blount (2012). "The MscS and MscL families of mechanosensitive channels act as microbial emergency release valves". In: *Journal of Bacteriology* 194.18, pp. 4802–4809. ISSN: 00219193.

Britten, R J and F T McCLURE (1962). "The amino acid pool in Escherichia coli." In: *Bacteriological reviews* 26, pp. 292–335. ISSN: 0005-3678.

Buda, Renata et al. (2016). "Dynamics of Escherichia coli 's passive response to a sudden decrease in external osmolarity". In: *Proceedings of the National Academy of Sciences* 113.40, E5838–E5846. ISSN: 0027-8424.

Cayley, D. Scott, Harry J. Guttman, and M.Thomas Record (2000). "Biophysical Characterization of Changes in Amounts and Activity of Escherichia coli Cell and Compartment Water and Turgor Pressure in Response to Osmotic Stress". In: *Biophysical Journal* 78.4, pp. 1748–1764. ISSN: 00063495.

Cayley, Scott and M. Thomas Record (2003). "Roles of Cytoplasmic Osmolytes, Water, and Crowding in the Response of Escherichia coli to Osmotic Stress: Biophysical Basis of Osmoprotection by Glycine Betaine". In: *Biochemistry* 42.43, pp. 12596–12609. ISSN: 00062960.

— (2004). "Large changes in cytoplasmic biopolymer concentration with osmolality indicate that macromolecular crowding may regulate protein-DNA interactions and growth rate in osmotically stressed Escherichia coli K-12". In: *Journal of Molecular Recognition* 17.5, pp. 488–496. ISSN: 09523499.

Çetiner, Uğur et al. (2017). " Tension-activated channels in the mechanism of osmotic fitness in Pseudomonas aeruginosa ". In: *The Journal of General Physiology* 149.5, pp. 595–609. ISSN: 0022-1295.

Chang, Geoffrey, Margaret T Barclay, and Douglas C Rees (1998). "Structure of the MscL Homolog from Mechanosensitive Ion Channel Structure of the MscL Homolog from Mycobacterium tuberculosis : A Gated Mechanosensitive Ion Channel". In: *Science* 282, pp. 2220–2227.

Chure, Griffin et al. (2018). "Connecting the Dots between Mechanosensitive Channel Abundance, Osmotic Shock, and Survival at Single-Cell Resolution". In: 200.23, pp. 1–15.

Cruickshank, Christopher C. et al. (1997). "Estimation of the pore size of the large-conductance mechanosensitive ion channel of Escherichia coli". In: *Biophysical Journal* 73.4, pp. 1925–1931. ISSN: 00063495.

Cui, C, D O Smith, and J Adler (1994). "Characterization of mechanosensitive channels in Escherichia coli cytoplasmic membrane by whole-cell patch clamp recording." In: *Journal of Membrane BiologyMembrane B* 144, pp. 31–42.

Culham, Doreen E. et al. (2018). "Dual Role of the C-Terminal Domain in Osmosensing by Bacterial Osmolyte Transporter ProP". In: *Biophysical Journal* 115.11, pp. 2152–2166. ISSN: 15420086.

Dai, Xiongfeng and Manlu Zhu (2018a). " High Osmolarity Modulates Bacterial Cell Size through Reducing Initiation Volume in Escherichia coli ". In: *mSphere* 3.5, pp. 1–12.

Dai, Xiongfeng et al. (2018b). "Slowdown of translational elongation in Escherichia coli under hyperosmotic stress". In: *mBio* 9.1, pp. 1–9. ISSN: 21507511.

Datsenko, Kirill A. and Barry L. Wanner (2000). "One-step inactivation of chromosomal genes in Escherichia coli K-12 using PCR products". In: *Proceedings of the National Academy of Sciences* 97.12, pp. 6640–6645. ISSN: 0027-8424.

Delamarche, Christian et al. (1999). "Visualization of AqpZ-mediated water permeability in Escherichia coli by cryoelectron microscopy". In: *Journal of Bacteriology* 181.14, pp. 4193–4197. ISSN: 00219193.

Deng, Yi, Mingzhai Sun, and Joshua W. Shaevitz (2011). "Direct measurement of cell wall stress stiffening and turgor pressure in live bacterial cells". In: *Physical Review Letters* 107.15. ISSN: 00319007.

Dick, D A T (1966). *Cell water*. Molecular biology and medicine series. Butterworths.

Dinnbier, Ulrike et al. (1988). "Biology of Escherichia coli K-12 to elevated sodium chloride concentrations". In: *Cell*, pp. 348 –357.

Ebrahimi, Pooria and Maurizio Barbieri (2019). "Gadolinium as an Emerging Microcontaminant in Water Resources: Threats and Opportunities". In: *Geosciences* 9.2, p. 93.

Edwards, Michelle D. et al. (2012). "Characterization of three novel mechanosensitive channel activities in Escherichia coli". In: *Channels* 6.4, pp. 272–281. ISSN: 1933-6950.

Erickson, Harold P. (2017). "How bacterial cell division might cheat turgor pressure - a unified mechanism of septal division in Gram-positive and Gram-negative bacteria". In: *BioEssays* 39.8, p. 1700045. ISSN: 02659247.

Ermakov, Yury A. et al. (2010). "Gadolinium ions block mechanosensitive channels by altering the packing and lateral pressure of anionic lipids". In: *Biophysical Journal* 98.6, pp. 1018–1027. ISSN: 15420086.

Evans, Evan et al. (2003). "Dynamic tension spectroscopy and strength of biomembranes". In: *Biophysical Journal* 85.4, pp. 2342–2350. ISSN: 00063495.

Fernandes, Lucas D., Ksenia Guseva, and Alessandro P.S. De Moura (2017). "Cooperative response and clustering: Consequences of membrane-mediated interactions among mechanosensitive channels". In: *Physical Review E* 96.2, pp. 1–6. ISSN: 24700053.

Francisco, Bezanilla and Eduardo Perozo (2002). "Force and voltage sensors in one structure". In: *Science* 298, pp. 1562–1563.

Gary, Decad M and Nikaido Hiroshi (1976). "Outer Membrane of Gram-Negative Bacteria". In: 128.1, pp. 325–336.

Glick, J. and N. Garber (1983). "The Intracellular Localization of Pseudomonas aeruginosa Lectins". In: *Journal of General Microbiology* 129.10, pp. 3085–3090. ISSN: 1350-0872.

Grage, Stephan L. et al. (2011). "Bilayer-mediated clustering and functional interaction of MscL channels". In: *Biophysical Journal* 100.5, pp. 1252–1260. ISSN: 15420086.

Hall, Michael N. and Thomas J. Silhavy (1981). "The ompB locus and the regulation of the major outer membrane porin proteins of Escherichia coli K12". In: *Journal of Molecular Biology* 146.1, pp. 23–43. ISSN: 00222836.

Hancock, R. E.W. (1987). "Role of porins in outer membrane permeability". In: *Journal of Bacteriology* 169.3, pp. 929–933. ISSN: 0021-9193.

Holland, Daryl P. and Anthony E. Walsby (2009). "Digital recordings of gas-vesicle collapse used to measure turgor pressure and cell-water relations of cyanobacterial cells". In: *Journal of Microbiological Methods* 77.2, pp. 214–224. ISSN: 01677012.

Iscla, Irene et al. (2014). "Streptomycin potency is dependent on MscL channel expression". In: *Nature Communications* 5, pp. 1–7. ISSN: 20411723.

Jespers, Laurent et al. (2004). "Crystal structure of HEL4, a soluble, refoldable human VH single domain with a germ-line scaffold". In: *Journal of Molecular Biology* 337.4, pp. 893–903. ISSN: 00222836.

Jiang, Hongyuan and Sean X. Sun (2010). "Morphology, growth, and size limit of bacterial cells". In: *Physical Review Letters* 105.2, pp. 1–4. ISSN: 00319007.

Kennedy, E. P. (1982). "Osmotic regulation and the biosynthesis of membrane-derived oligosaccharides in Escherichia coli". In: *PNAS* 79.17, pp. 1092–1095. ISSN: 00219258.

Koch, A. L., M. L. Higgins, and R. J. Doyle (1981). "The Role of Surface Stress in the Morphology of Microbes". In: *Microbiology* 128.5, pp. 927–945. ISSN: 1350-0872.

Koch, Arthur L (1990). "Growth and Form of the Bacterial Cell Wall". In: 78.4, pp. 327–341.

Krasnopeeva, Ekaterina (2018). "Single cell measurements of bacterial physiology traits during exposure to an external stress". PhD thesis.

Lennon, C and J Pointon (2014). *White Paper : pAVEway ™ expression system for the efficient expression of therapeutic proteins.* Tech. rep., pp. 1–4.

Leontiadou, Hari, Alan E. Mark, and Siewert J. Marrink (2004). "Molecular Dynamics Simulations of Hydrophilic Pores in Lipid Bilayers". In: *Biophysical Journal* 86.4, pp. 2156–2164. ISSN: 00063495.

Levina, N. (1999). "Protection of Escherichia coli cells against extreme turgor by activation of MscS and MscL mechanosensitive channels: identification of genes required for MscS activity". In: *The EMBO Journal* 18.7, pp. 1730–1737.

Li, Xin min et al. (1994). "Effect of lanthanide ions on the phase behavior of dipalmitoylphosphatidylcholine multilamellar liposomes". In: *Journal of Inorganic Biochemistry* 53.2, pp. 139–149. ISSN: 01620134.

Li, Yuezhou et al. (2002). "Ionic regulation of MSCk, a mechanosensitive channel from Escherichia coli". In: *EMBO Journal* 21.20, pp. 5323–5330. ISSN: 02614189.

Link, Andrew J and George M Church (1997). "Methods for Generating Precise Deletions and Insertions in the Genome of Wild-Type". In: *Journal of Bacteriology* 179.20, pp. 6228–6237.

Lonergan, N. E., L. D. Britt, and C. J. Sullivan (2014). "Immobilizing live escherichia coli for AFM studies of surface dynamics". In: *Ultramicroscopy* 137, pp. 30–39. ISSN: 18792723.

M9 minimal medium (standard) (2010). Vol. 2010. 8, pdb.rec12295.

Martinac, B et al. (1987). "Pressure-sensitive ion channel in Escherichia coli." In: *Proceedings of the National Academy of Sciences of the United States of America* 84.8, pp. 2297–301. ISSN: 0027-8424.

McLaggan, Debbie et al. (1994). "Interdependence of K+ and glutamate accumulation during osmotic adaptation of Escherichia coli". In: *Journal of Biological Chemistry* 269.3, pp. 1911–1917. ISSN: 00219258.

Merlin, Christophe, Sean McAteer, and Millicent Masters (2002). "Tools for characterization of Escherichia coli genes of unknown function." In: *Journal of bacteriology* 184.16, pp. 4573–81. ISSN: 0021-9193.

Moe, Paul and Paul Blount (2005). "Assessment of Potential Stimuli for Mechano-Dependent Gating of MscL: Effects of Pressure, Tension, and Lipid Headgroups †". In: *Biochemistry* 44.36, pp. 12239–12244. ISSN: 0006-2960.

Neu, H C and L A Heppel (1965). "The release of enzymes from Escherichia coli by osmotic shock and during the formation of spheroplasts." In: *The Journal of biological chemistry* 240.9, pp. 3685–92. ISSN: 0021-9258.

Nossal, Nancy G and Leon A Heppel (1966). "The Release of Enzymes by Osmotic Shock from". In: *Shock* 241.13, pp. 3055–3062.

Paraschiv, Alexandru et al. (2020). "Dynamic Clustering Regulates Activity of Mechanosensitive Membrane Channels". In: *Phys. Rev. Lett.* 124.4, p. 48102.

Perozo, E et al. (2002a). "Structure of MscL in the open state and the molecular mechanism of gating in mechanosensitive channels". In: *Biophysical Journal* 82.August, 1299 ST –Structure of MscL in the open state and. ISSN: 0006-3495.

Perozo, Eduardo et al. (2002b). "Physical principles underlying the transduction of bilayer deformation forces during mechanosensitive channel gating". In: *Nature Structural Biology* 9.9, pp. 696–703. ISSN: 10728368.

Pilizota, Teuta and Joshua W Shaevitz (2012). "Fast, multiphase volume adaptation to hyperosmotic shock by Escherichia coli." In: *PloS one* 7.4, e35205. ISSN: 1932-6203.

Pilizota, Teuta and Joshua W. Shaevitz (2013). "Plasmolysis and cell shape depend on solute outer-membrane permeability during hyperosmotic shock in E. coli". In: *Biophysical Journal* 104.12, pp. 2733–2742. ISSN: 00063495.

Pilizota, Teuta and Joshua W. Shaevitz (2014). "Origins of escherichia coli growth rate and cell shape changes at high external osmolality". In: *Biophysical Journal* 107.8, pp. 1962–1969. ISSN: 15420086.

Pliotas, Christos et al. (2015). "The role of lipids in mechanosensation". In: *Nature Structural & Molecular Biology* 22.12, pp. 991–998. ISSN: 1545-9993.

Racher, K. I., D. E. Culham, and J. M. Wood (2001). "Requirements for osmosensing and osmotic activation of transporter ProP from Escherichia coli". In: *Biochemistry* 40.24, pp. 7324–7333. ISSN: 00062960.

Record, M. Thomas et al. (1998). "Responses of E. coli to osmotic stress: Large changes in amounts of cytoplasmic solutes and water". In: *Trends in Biochemical Sciences* 23.4, pp. 143–148. ISSN: 09680004.

Reppas, Christos et al. (2015). "Characterization of Contents of Distal Ileum and Cecum to Which Drugs/Drug Products are Exposed during Bioavailability/Bioequivalence Studies in Healthy Adults". In: *Pharmaceutical Research* 32.10, pp. 3338–3349. ISSN: 1573904X.

Reuter, Marcel et al. (2014). "Mechanosensitive channels and bacterial cell wall integrity: Does life end with a bang or a whimper?" In: *Journal of the Royal Society Interface* 11.91. ISSN: 17425662.

Rinas, Ursula and Frank Hoffmann (2004). "Selective leakage of host-cell proteins during high-cell-density cultivation of recombinant and non-recombinant Escherichia coli". In: *Biotechnology Progress* 20.3, pp. 679–687. ISSN: 87567938.

Rojas, E., J. A. Theriot, and K. C. Huang (2014). "Response of Escherichia coli growth rate to osmotic shock". In: *Proceedings of the National Academy of Sciences* 111.21, pp. 7807–7812. ISSN: 0027-8424.

Rojas, Enrique R., Kerwyn Casey Huang, and Julie A. Theriot (2017). "Homeostatic Cell Growth Is Accomplished Mechanically through Membrane Tension Inhibition of Cell-Wall Synthesis". In: *Cell Systems*. ISSN: 24054720.

Rojas, Enrique R. et al. (2018). "The outer membrane is an essential load-bearing element in Gram-negative bacteria". In: *Nature* 559.7715, pp. 617–621. ISSN: 0028-0836.

Romantsov, Tatyana, Ziqiang Guan, and Janet M. Wood (2009). "Cardiolipin and the osmotic stress responses of bacteria". In: *Biochimica et Biophysica Acta - Biomembranes* 1788.10, pp. 2092–2100. ISSN: 00052736.

Rosko, Jerko (2017). "Osmotaxis in Escherichia coli". PhD thesis.

Rumley, M. K. et al. (1992). "Mechanisms of regulation of the biosynthesis of membrane-derived oligosaccharides in Escherichia coli". In: *Journal of Biological Chemistry* 267.17, pp. 11806–11810. ISSN: 00219258.

Sambrook, J, E F Fritsch, and T Maniatis (1989). *Molecular Cloning: A Laboratory Manual*. Molecular Cloning: A Laboratory Manual v. 1-3. Cold Spring Harbor Laboratory Press. ISBN: 9780879693091.

Sands, Jeff M. and Harold E. Layton (2009). "The Physiology of Urinary Concentration: An Update". In: *Seminars in Nephrology* 29.3, pp. 178–195. ISSN: 02709295.

Schneider, J. E et al. (1979). "Structural Studies of the Membrane-derived Oligosaccharides of Escherichia coli". In: 254.20, pp. 10135–10138.

Schumann, Ulrike et al. (2010). " YbdG in Escherichia coli is a threshold-setting mechanosensitive channel with MscM activity ". In: *Proceedings of the National Academy of Sciences* 107.28, pp. 12664–12669. ISSN: 0027-8424.

Sévin, Daniel C. and Uwe Sauer (2014). "Ubiquinone accumulation improves osmotic-stress tolerance in Escherichia coli". In: *Nature Chemical Biology* 10.4, pp. 266–272. ISSN: 15524469.

Stock, J. B., B. Rauch, and S. Roseman (1977). "Periplasmic space in Salmonella typhimurium and Escherichia coli". In: *Journal of Biological Chemistry* 252.21, pp. 7850–7861. ISSN: 00219258.

Stokes, N. R. et al. (2003). "A role for mechanosensitive channels in survival of stationary phase: Regulation of channel expression by RpoS". In: *Proceedings of the National Academy of Sciences* 100.26, pp. 15959–15964. ISSN: 0027-8424.

Strahl, Henrik and Leendert W. Hamoen (2010). "Membrane potential is important for bacterial cell division". In: *Proceedings of the National Academy of Sciences of the United States of America* 107.27, pp. 12281–12286. ISSN: 00278424.

Sudrik, Chaitanya et al. (2017). "Preferential interactions of trehalose, L-arginine.HCl and sodium chloride with therapeutically relevant IgG1 monoclonal antibodies". In: *mAbs* 9.7, pp. 1155–1168. ISSN: 19420870.

Sukharev, Sergei I et al. (1993). "Two Types of mechanosensitive Channels in the Escherichia coli cell envelope: solubilization and functional reconstitution". In: *BioEssays* 65, pp. 177–183.

Sukharev, Sergei I et al. (1994). "A large-conductance mechanosensitive channel in E.coli encoded by mscL alone". In: *Nature* 368.March, pp. 265–268.

Sukharev, Sergei I. et al. (1999). "Energetic and Spatial Parameters for Gating of the Bacterial Large Conductance Mechanosensitive Channel, MscL". In: *The Journal of General Physiology* 113.4, pp. 525–540. ISSN: 0022-1295.

Sun, Yen, Tzu Lin Sun, and Huey W. Huang (2014). "Physical properties of Escherichia coli spheroplast membranes". In: *Biophysical Journal* 107.9, pp. 2082–2090. ISSN: 15420086.

Thompson, Wentworth D'Arcy (1917). *On growth and form*. Cambridge University Press.

Tomasek, Kathrin, Tobias Bergmiller, and Călin C. Guet (2018). "Lack of cations in flow cytometry buffers affect fluorescence signals by reducing membrane stability and viability of Escherichia coli strains". In: *Journal of Biotechnology* 268.January, pp. 40–52. ISSN: 18734863.

Turner, Robert D. et al. (2013). "Cell wall elongation mode in Gram-negative bacteria is determined by peptidoglycan architecture". In: *Nature Communications* 4, pp. 1496–1498. ISSN: 20411723.

Ursell, Tristan et al. (2007). "Cooperative gating and spatial organization of membrane proteins through elastic interactions". In: *PLoS Computational Biology* 3.5, pp. 0803–0812. ISSN: 1553734X.

Van Den Berg, Jonas et al. (2016). "On the mobility, membrane location and functionality of mechanosensitive channels in Escherichia coli". In: *Scientific Reports* 6.September, pp. 1–11. ISSN: 20452322.

Van Den Berg, Jonas, Arnold J. Boersma, and Bert Poolman (2017). "Microorganisms maintain crowding homeostasis". In: *Nature Reviews Microbiology* 15.5, pp. 309–318. ISSN: 17401534.

Vázquez-Laslop, N. et al. (2001). "Molecular sieve mechanism of selective release of cytoplasmic proteins by osmotically shocked Escherichia coli". In: *Journal of Bacteriology* 183.8, pp. 2399–2404. ISSN: 00219193.

Walsby, A. E. (1971). "The pressure relationships of gas vacuoles". In: *Proceedings of the Royal Society of London. Series B.* 178.1052, pp. 301–326. ISSN: 2053-9193.

Wang, Wenjian et al. (2008). "The Structure of an open form of an E.coli mechanosensitive channel at 3.45 Å resolution". In: *Science* 321.5893, pp. 1179–1183.

Whitehead, P (1997). "Ultra-pure water for ion chromatography". In: *Journal of Chromatography A* 770.1-2, pp. 115–118. ISSN: 0021-9673.

Wood, Janet M. (2007). *Bacterial Osmosensing Transporters*. Vol. 428. 07. Elsevier Masson SAS, pp. 77–107. ISBN: 9780123739216.

— (2010). "Bacterial Osmoregulation: A Paradigm for the Study of Cellular Homeostasis". In: *Annual Review of Microbiology* 65.1, pp. 215–238. ISSN: 0066-4227.

Wray, Robin et al. (2016). "Dihydrostreptomycin Directly Binds to, Modulates, and Passes through the MscL Channel Pore". In: *PLoS Biology* 14.6, pp. 1–27. ISSN: 15457885.

Yang, Xian Cheng and Frederick Sachs (1989). "Block of stretch-activated ion channels in xenopus oocytes by gadolinium and calcium ions". In: *Science* 243.4894, pp. 1068–1071. ISSN: 00368075.

Yao, X et al. (1999). "Thickness and elasticity of gram-negative murein sacculi measured by atomic force microscopy". In: *Journal of Bacteriology* 181.22, pp. 6865–6875. ISSN: 0021-9193.

Zoratti, Mario and Valeria Petronilli (1988). "Ion-conducting channels in a Gram-positive bacterium". In: *FEBS Letters* 240.1-2, pp. 105–109. ISSN: 00145793.